

PORTUGALIAE PHYSICA

VOLUME 11
FASCÍCULO 1-2
1980

SOCIEDADE PORTUGUESA DE FÍSICA

PORTUGALIAE PHYSICA

Fundada em 1943 por A. Cyrillo Soares, M. Telles Antunes, A. Marques da Silva e M. Valadares

Director

J. M. Araújo (Faculdade de Ciências, Universidade do Porto)

Comissão Redactorial

- J. M. Araújo (Faculdade de Ciências, Universidade do Porto)
- J. Gomes Ferreira (Faculdade de Ciências, Universidade de Lisboa)
- F. Bragança Gil (Faculdade de Ciências, Universidade de Lisboa)
- M. F. Laranjeira (Faculdade de Ciências e Tecnologia, Universidade Nova de Lisboa)
- F. D. S. Marques (Universidade do Minho)
- A. Farinha Martins (Centro de Física da Matéria Condensada, Lisboa)
- R. Vilela Mendes (Centro de Física da Matéria Condensada, Lisboa)
- A. M. C. Moutinho (Centro de Física Molecular, Lisboa)
- J. Pinto Peixoto (Faculdade de Ciências, Universidade de Lisboa)
- A. Policarpo (Faculdade de Ciências e Tecnologia, Universidade de Coimbra)
- J. da Providência (Faculdade de Ciências e Tecnologia, Universidade de Coimbra)
- F. Carvalho Rodrigues (Laboratório de Física e Engenharia Nucleares, Sacavém).
- F. D. Santos (Faculdade de Ciências, Universidade de Lisboa)
- E. Ducla Soares (Faculdade de Ciências, Universidade de Lisboa)
- O. D. D. Soares (Faculdade de Ciências, Universidade do Porto)
- J. B. Sousa (Faculdade de Ciências, Universidade do Porto)
- A. T. Rocha Trindade (Instituto Superior Técnico, Lisboa)
- L. Alte da Veiga (Faculdade de Ciências e Tecnologia, Universidade de Coimbra)

CDU 53 (469) (05)

PORTUGALIAE PHYSICA

VOLUME 11
1980

117



IMPROVED EXPERIMENTAL METHOD FOR HALF-LIFE MEASUREMENTS BY ELECTRON—ELECTRON DELAYED COINCIDENCES

M. C. ABREU, J. P. RIBEIRO and F. B. GIL

Centro de Física Nuclear da Universidade de Lisboa,
Av. Gama Pinto 2, 1699 Lisboa Codex, Portugal

(Received 25 September 1979)

ABSTRACT—A new method for accurate determination of instrumental time delays in measurements of half-lives using an electron magnetic spectrometer is presented. Lifetimes of the order of 100 ps can be obtained from curves of the centroid vs energy. For the $3/2^+$ level in ^{203}Tl , the remeasured period value is 266 ± 13 ps.

1—INTRODUCTION

The measurement of lifetimes of nuclear excited states is of great importance in experimental nuclear spectroscopy to test the nuclear models.

In the low energy region (≤ 1 MeV) the unstudied decays are complex and the lifetimes expected to be less than a few hundred picosecond. Therefore, the delayed coincidence method by centroid shift (between the radiation that creates the excited state and the radiation that annihilates it) is the best experimental method, provided it obeys the following three conditions:

- i) good resolution in energy;
- ii) time resolution as short as possible;
- iii) use of theoretical and experimental methods which allow the correct calculation of the inevitable shifts in time, connected with the process of measurement and the energy difference between the radiations in study.

A compromise between conditions i) and ii) can be achieved by the delayed coincidence methods in electron - electron cascades using a double lens magnetic spectrometer equipped with plastic crystals associated with photomultipliers and fast electronics.

When the experiments are performed with such a magnetic spectrometer two main methods have been proposed to minimize the error in iii): a) pre - acceleration of the electron emitted by the source in such a way that the coincidences in time are measured between radiations of equal energy [1]; b) theoretical corrections of the shifts in time when the relative difference of the energies ($\Delta E/E$) of the radiations is small. However this method is quite restrictive. For example, for electron energies around 200 keV and differences of $\Delta E = 30$ keV the error introduced is approximately 30 picosecond [2].

We have developed an experimental method to correct those shifts in time, making them independent of $\Delta E/E$. Our method is applicable for electron-electron coincidences and we have made beta - conversion electron coincidences. The energies are in the range 50-600 keV. A similar, though more restrictive method, was used by Lindskog and Svensson [3].

The purpose of this paper is to present our method and the results obtained in the determination of a well known lifetime.

2 — EXPERIMENTAL PROCEDURE

The experimental arrangement is formed by a double lens Gerholm magnetic spectrometer equipped with plastic crystals NE 111 and photomultipliers RCA 8850. Constant fraction time discriminators Ortec 463 and conventional fast-slow coincidences installation with a time-to-amplitude converter Ortec 437 A are used. This allows the determination of the centroid of the fast-slow coincidence curve, by selecting one region of the continuous beta spectrum in coincidence with the internal conversion electron. By systematic selections of successive regions of the continuous beta in one of the lenses and focusing the conversion electrons in the other lens we can measure the shift of the centroid of the fast-slow coincidence curve as a function of the selected beta energy. Reversing the selec-

tion of the energies in the lenses can, then, construct the β - e_k and e_k - β curves of the centroid shift as functions of the selected beta energies. By β - e curves we mean that the start and stop input of the

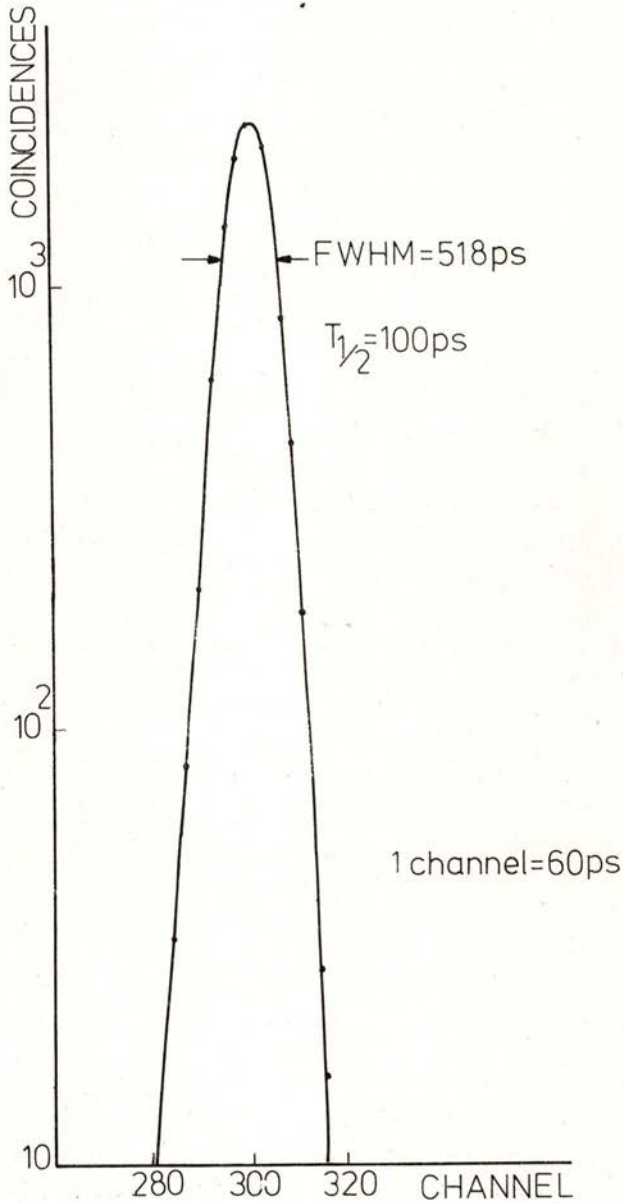


Fig. 1 — Prompt resolution curve obtained with a ^{198}Au source.

TAC are triggered respectively by the β -radiation and the conversion electron beam. In this way we have experimentally determined the systematic errors introduced in the lifetime measurements discussed by Lindskog *et al* [2], i. e., 1) the energy dependence of the scintillator, 2) the time of flight of the electrons in the spectrometer, 3) the transit time variations due to small changes in either the electron momentum or in the magnetic field strength, 4) the electron transit time in the photomultiplier due to changes in the magnetic field.

3 — MEASUREMENTS

The experimental correction curves of the centroid shift in function of the energy were obtained with the cascades beta-conversion electron from the nuclides ^{203}Hg and ^{198}Au . The resolution time of the experimental arrangement was determined from ^{198}Au prompt beta-electron conversion curve (Fig. 1). The resolution time measured is 518 ps and the slope is 100 ps. Fig. 2 shows the results of coincidence experiments between continuous beta and K or L conversion electrons using a source of ^{198}Au . An identical behaviour for the e_K and e_L coincidences in the selected range of energies was obtained.

To cover the mentioned range of energies the cascades of two different nuclides, ^{198}Au and ^{203}Hg , were used. These results (Fig. 3) show the same systematic behaviour as the curve in Fig. 2.

Curves of second order could be well fitted by our experimental values. However to obtain small dispersion in the results of lifetime measurements it is necessary to start the fits with different sets of experimental values. We used four sets and obtained a dispersion of the order of 3%.

Using this correction methods we measured the lifetime of the $3/2^+$ state of ^{203}Tl by centroid shift. In this case the self-comparison technique is not adequate since the beta end point (208 keV) is quite near the electron conversion energy (193 keV). Experimentally we measured the beta (140 keV) — e_K (193 keV) and e_K (193 keV) — beta (140 keV) coincidences. The difference of the centroid positions should give twice the value of the lifetime (τ), if there were no systematic errors due to the differences of the electron energies

focused in each lens on reversing the selected energies. In fact we have

$$2\tau = C_1 - C_1^* + \epsilon_1 + \epsilon_2$$

where C_1 and C_1^* are the centroid positions mentioned above and ϵ_1 and ϵ_2 the values given by the curves of Fig. 3, taking into account the difference of the electron energies selected in each lens. So, ϵ_1 corresponds to the value determined from the curve β - e_K and ϵ_2 to the value determined from the curve e_K - β .

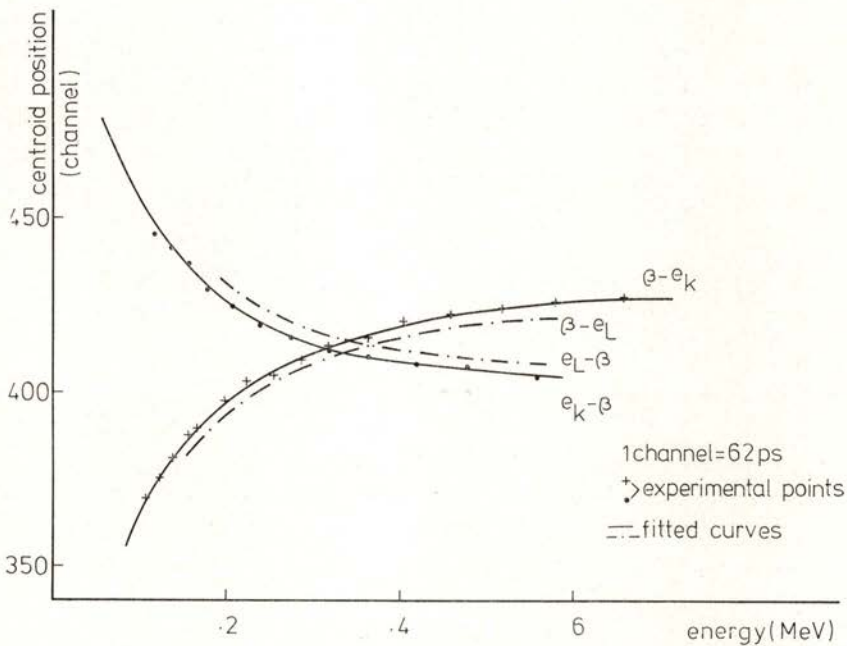


Fig. 2 — Instrumental centroid shift of the fast-slow delayed coincidence curves vs. beta energy. The curves correspond to β -L and β -K conversion electron coincidences.

The average lifetime obtained from the three sets of measurements with different sources is

$$\tau = 384 \pm 18 \text{ ps}$$

and thus

$$T_{1/2} = 266 \pm 13 \text{ ps} \quad ;$$

the overall error includes the error in the calibration with a time calibrator Ortec 462 (1.2 ps), the statistical error and the uncertainty from the determination of the systematic shifts (3%).

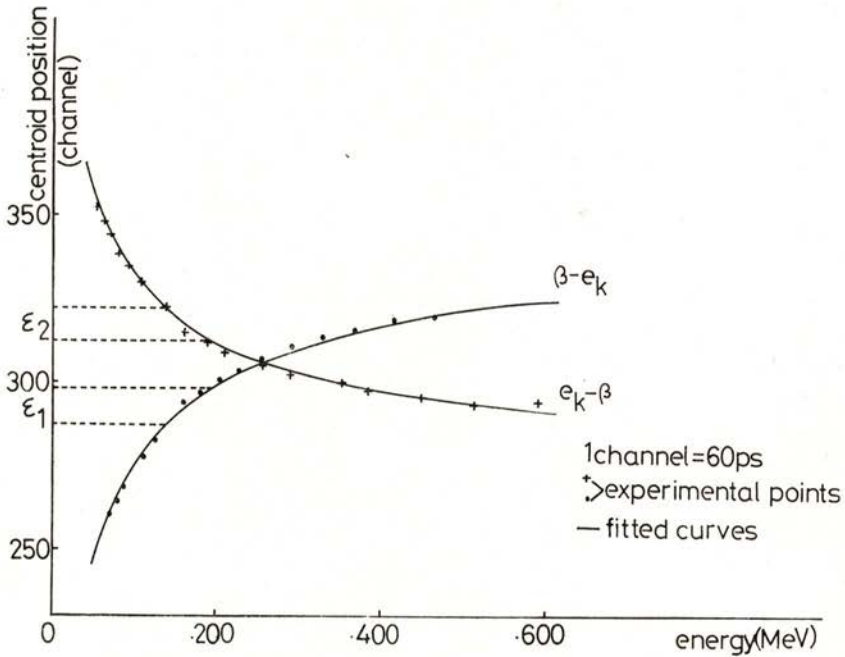


Fig. 3 — Instrumental centroid shift of the fast-slow delayed coincidence curves vs. beta energy. The sources ^{203}Hg and ^{198}Au were used. The curve obtained with ^{203}Hg was normalised to the curve with ^{198}Au , thus covering the range 50-600 keV.

4 — CONCLUSION

The result obtained for the half-life of the $3/2^+$ level in ^{203}Tl is in good agreement with the adopted value (278 ± 2 ps) [4], which we have remeasured by β - γ delay coincidences with NE 111 plastic crystals. The curve of the β - γ coincidences in ^{198}Au was used as reference source. Both the moments and the convolution methods were applied.

The value obtained through the moments method was:

$$T_{1/2} = 275 \pm 8 \text{ ps}$$

The convolution of the curves led us to

$$T_{1/2} = 274 \pm 6 \text{ ps} .$$

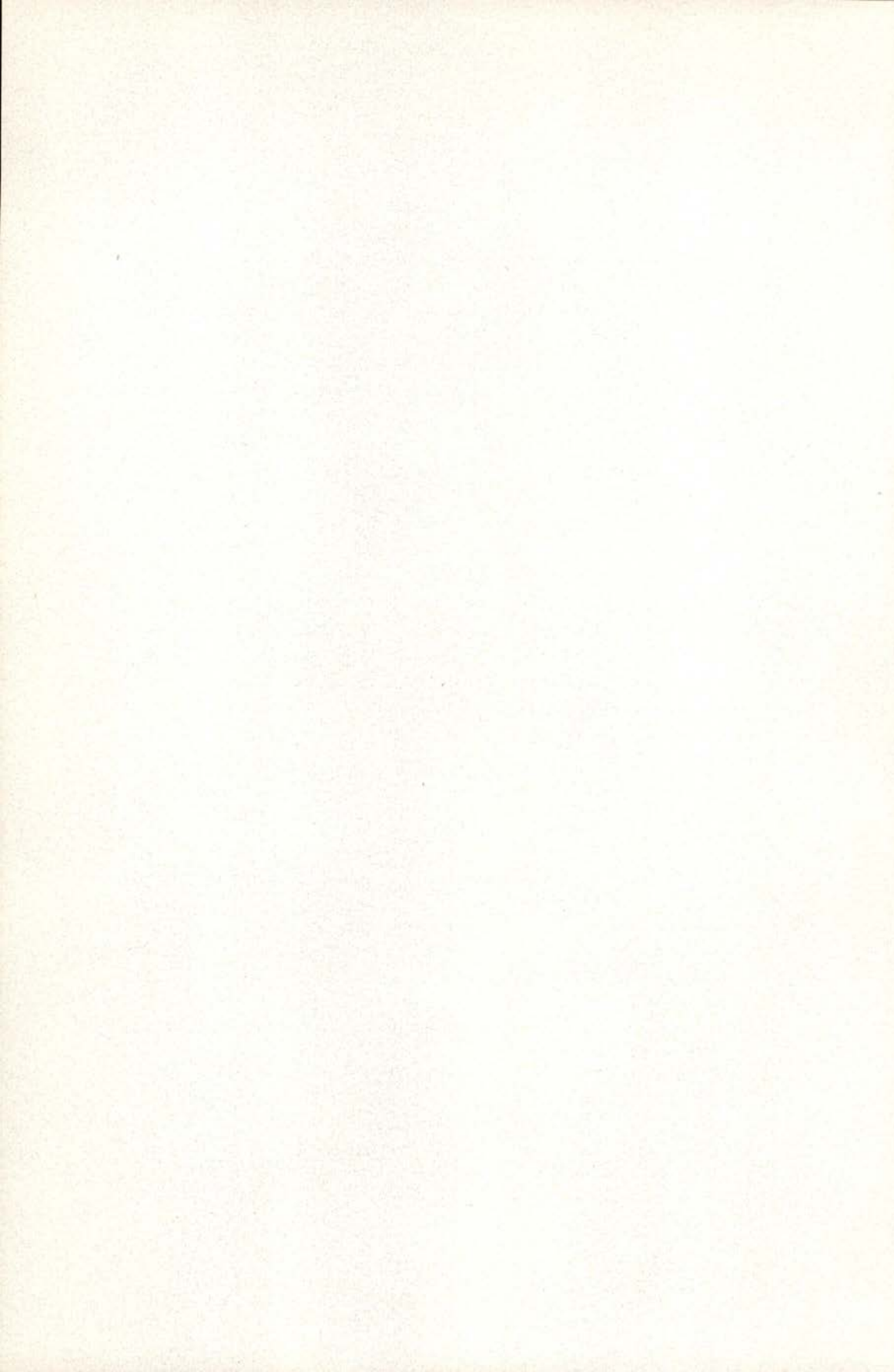
This measurement was performed without the use of the magnetic spectrometer but with the same experimental equipment. It should be noted that it was possible to use such methods and detection processes due to the simplicity of the ^{203}Hg decay scheme; the greater complexity of the majority of the decays requires an accurate energy resolution, which can only be achieved by means of the magnetic spectrometer. We adopted the convolution model discussed in reference [5] though the results were identical if we carried out the calculations according to the Hutcheon model [6]. The model proposed by Kim [7] led us to a higher value (295 ± 6 ps). This seems to be in accordance with the remarks of Lima *et al* [8].

The above described process of measuring the instrumental shifts makes it possible to measure half-lives even when the self-comparison method is not applicable. Moreover it does not require theoretical corrections such as Lindskog's, which have proved inadequate in many cases.

The authors wish to thank Dr. J. C. Soares for many helpful discussions in the course of this work. Financial assistance given by Instituto Nacional de Investigação Científica (INIC) is acknowledged.

REFERENCES

- [1] J. LINDSKOG, P. SPARRMAN, A. MARELUIS and T. SUNDSTROM, *Ark. Fys.*, **32**, 417 (1966).
- [2] J. LINDSKOG and T. SUNDSTROM, *Ark. Fys.*, **24**, 199 (1963).
- [3] J. LINDSKOG and L.-G. SVENSSON, *Nucl. Inst. and Meth.*, **133**, 99 (1976).
- [4] M. R. SCHMORAK, *Nucl. Data Sheets*, **24**, 117 (1978).
- [5] L. BOSTROM, B. OLSEN, W. SCHNEIDER and E. MATHIAS, *Nucl. Inst. and Meth.*, **44**, 61 (1966).
- [6] D. A. HUTCHEON, *Nucl. Inst. and Meth.*, **113**, 221 (1973).
- [7] H. J. KIM and W. T. MILNER, *Nucl. Inst. and Meth.*, **95**, 429 (1971).
- [8] E. DE LIMA, H. KAWAKAMI, A. DE LIMA, R. HICHTWA, A. V. RAMAYYA, J. H. HAMILTON and W. DUNN, *Nucl. Inst. and Meth.*, **151**, 221 (1978).



THE L_1 SUBSHELL FLUORESCENCE YIELD OF Tl (*)

M. I. MARQUES, M. C. MARTINS and J. G. FERREIRA

Laboratory of Physics, Faculty of Science
University of Lisbon, Portugal

(Received 9 July 1980)

ABSTRACT— L_1 fluorescence yield of Tl has been measured by comparing the relative intensities of the K and L_1 -X-ray spectra. The experimental result is $\omega_1 = 0.109 \pm 0.016$

1 — INTRODUCTION

Experimental information of atomic fluorescence yields for L_1 subshell, ω_1 , is scarce mostly for elements in the atomic number region $Z \geq 70$. Particularly, the three experimental values [1, 2, 3] reported for thallium ($Z=81$) do not agree very well.

The purpose of this note is to find ω_1 for Tl by comparison of the K and L_1 X-ray spectra of this element, which is a different method.

We denote by n_K , n_{L_1} , F_K , F_{L_1} , the numbers of primary vacancies in K and L_1 shells respectively and the correspondent number of L X-ray photons; ω_K , ω_1 represent the atomic fluorescence yields of the K and L_1 shells and f_{KL_1} the probability of ionization transfer from the level K to the L_1 level.

The following equations are valid

$$F_K = \omega_K n_K \quad F_{L_1} = \omega_1 (n_{L_1} + f_{KL_1} n_K)$$

or

$$\omega_1 = \omega_K \frac{F_{L_1}}{F_K} \frac{1}{(n_{L_1}/n_K) + f_{KL_1}} \quad (1)$$

(*) This work has been supported by INIC (Portugal); results presented at the Conference of the Portuguese Physics Society (Porto, April 80).

A result for ω_1 of Tl can be obtained from expression (1) as ω_K , n_1/n_K and f_{KL_1} are well known and F_{L_1}/F_K has been measured in the present work.

2 — EXPERIMENTAL PROCEDURE

K and L X-ray spectra of Tl were obtained, following β^- decay of ^{203}Hg , using a Si(Li) X-ray detector, 10 mm in diameter and 5 mm deep, fitted with a 0.025 mm Be window and having a resolution of 210 eV FWHM at 6.4 keV.

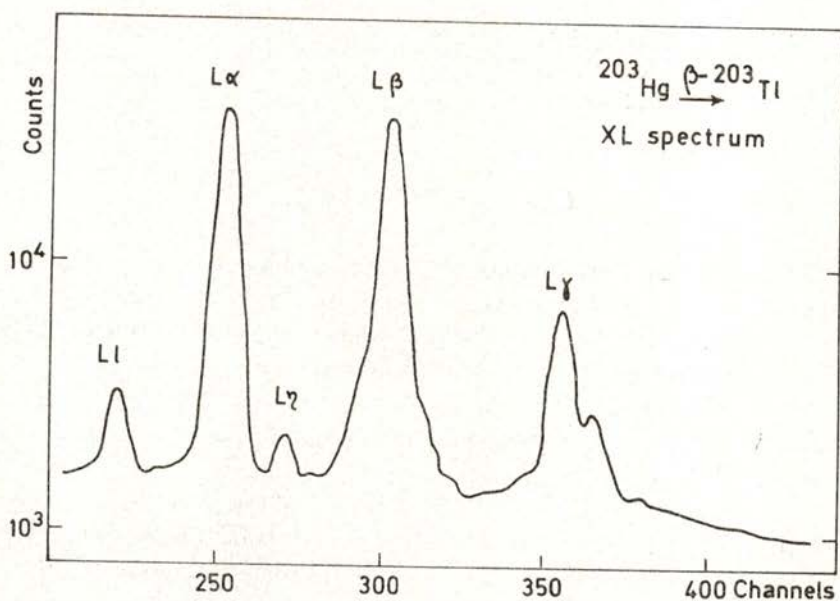


Fig. 1 — L X-ray spectrum of Tl

The source preparation and the method used to obtain the efficiency-absorption curve were previously described [4].

The L_1 X ray spectrum is due to the lines $L\beta_4$, $L\beta_3$, $L\gamma_2$, $L\gamma_3$, $L\gamma_4$ and the contribution of these lines in all the L-X spectrum (Fig. 1) is evaluated by decomposing the $L\gamma$ group in the L_1 and ($L\gamma_2 + L\gamma_6 + L\gamma_3 + L\gamma_4$) lines. Theoretical L radiative rates of Scofield [5] and experimental values of Salem *et al.* [6] were used in this

evaluation. L_{α} of Np (13.9 keV) and γ (14.4 keV) of ^{57}Fe , which have energies very close to $L\gamma_1$ of Tl (14.29) keV were used to obtain the shape of this line.

3 — RESULTS

In table I we present the values of ω_K , f_{KL_1} , and n_1/n_K adopted to determine ω_1 by expression (1); transition rates from Scofield (a) and Salem *et al.* (b) were used in evaluating F_{L_1}/F_K

TABLE I

ω_K [7]	f_{KL_1} [8]	n_1/n_K [9]	F_{L_1}/F_K
0.966	0.0190	0.155	0.0217 (a)
			0.0176 (b)

Table II shows our result $\omega_1 = 0.109 \pm 0.016$ together with values obtained in previous experimental work.

TABLE II

Sujkowski <i>et al.</i> [1]	Wood <i>et al.</i> [2]	Auler <i>et al.</i> [3]	Present work
0.11 ± 0.025	0.07 ± 0.02	0.10	0.109 ± 0.016

REFERENCES

- [1] Z. SUJKOWSKI and O. MELIN, *Ark. Fys.*, **20**, 193 (1961).
- [2] R. E. WOOD, J. M. PALMS and P. V. RAO, *Phys. Rev.*, **187**, 1497 (1969).
- [3] L. T. AULER, A. G. DA SILVA and A. G. PINHO, *Rev. Bras. Fis.*, **4**, 29 (1974).

- [4] M. I. MARQUES, M. C. MARTINS, J. G. FERREIRA, *J. Phys. B.*, **13**, 41, (1980).
- [5] J. M. SCOFIELD, *At. Data and Nucl. Data Tables*, **14**, 121 (1974).
- [6] S. I. SALEM, S. L. PANOSSIAN and R. A. KRAUSE, *At. Data and Nucl. Data Tables*, **14**, 91 (1974).
- [7] M. O. KRAUSE, *J. Phys. Chem. Ref. Data*, **8**, 307 (1979).
- [8] P. V. RAO, M. H. CHEN and B. CRASEMANN, *Phys. Rev.*, **A5**, 997 (1972).
- [9] Table of isotopes, ed. C. M. LEDERER and V. S. SHIRLEY, 7th edition (1978).

PROTON-INDUCED K-SHELL HOLE PRODUCTION ON Ar AND Kr (*)

J. S. LOPES (**), K. KRIEN (***), J. C. SOARES (****)
and F. B. GIL (****)

(Received 30 May 1980)

ABSTRACT— Proton-induced K-shell X-ray production cross sections for Ar and Kr are measured in the incident energy ranges 0.135–2 MeV and 0.5–2 MeV, respectively, using ion implanted targets. The corresponding ionisation cross sections are compared to other experimental results, when available, and to theoretical cross sections calculated in accordance with the PWBA, SCA and BEA models, taking into account effects due to retardation of the projectile by the nuclear Coulomb field of the target, electronic binding energy and polarisation effects and, for Kr, to electronic relativistic effects. Best overall agreement is found with the PWBA corrected values; the agreement is poor for Kr at the lowest energies used, the theoretical cross sections being roughly 50% above the experimental ones.

1 — INTRODUCTION

There is only scant experimental information on the proton-induced K-shell ionisation cross sections of argon and krypton; the published results [1–6] are summarised in the tables of Rutledge and Watson [7] and Gardner and Gray [8]. The measurements have been made on gas targets under single collision conditions with the exception of the work of Lennard and Mitchell [3] who used Kr implanted on Si for their measurements of the Kr cross sections.

(*) Results presented at the Second Conference of the Portuguese Physics Society (Porto, April 1980).

(**) Laboratório de Física e Engenharia Nucleares, 2685 Sacavém, Portugal.

(***) Institut für Strahlen-und Kernphysik, Universität Bonn, Federal Republic of Germany. Present address: Department of Physics, Princeton University, USA.

(****) Centro de Física Nuclear da Universidade de Lisboa, Av. Gama Pinto 2, 1699 Lisboa Codex, Portugal.

In this paper we report on measurements of the Ar and Kr K-shell hole production cross sections using targets made by ion implantation on Be and compare our results to the PWBA [9–11] and SCA [12–13] theories corrected for electron binding and polarization effects, projectile Coulomb retardation and deflection and electronic relativistic effects; a comparison to the Coulomb effect corrected BEA theory [14–15] is also made.

2 — EXPERIMENTAL PROCEDURE

Proton beams from 0.135 to 2 MeV were produced by the 2 MV. Van de Graaff accelerator at Sacavem; the H_3^+ beam was used to obtain the 0.135 MeV incident energy while the other energies below 0.4 MeV were obtained with the H_2^+ beam. The experimental set up has been described previously [16] and only a few specific points are referred here.

The Ar X-rays were detected in a Si(Li) detector with a resolution of 200 eV for Ar and the Kr X-rays in a HP Ge detector with a resolution of 250 eV for Kr. The X-ray detector was placed at an angle of 105° to the beam and accepted radiation within a solid angle of 0.548 msr. X-ray background with a pure Be foil in the target position was negligible for the integrated currents used in each run. The count rate was kept low but where appropriate dead time corrections have been made. X-ray absorption corrections have been made as described previously [16]. The efficiency of the Si(Li) detector for the Ar X-rays has been found following the method proposed by Rosner *et al.* [17] and using $Ca SO_4$.

A silicon surface barrier detector of 13 keV resolution for 1 MeV protons was used to detect backscattered protons within a solid angle of 2.12 msr at 165° degrees to the beam axis. Proton spectra were taken in a multichannel analyser and the peak corresponding to the element under study was integrated to be used in the X-ray production cross section determination. Background counts, coming mainly from the Be (p, α) reaction were at each incident energy subtracted from the proton scattering spectra; at high incident energies an aluminium foil 0.025 mm thick was used in front of the particle detector to stop the alpha particles. A particle spectrum of the Ar target is shown superimposed on a background spectrum (taken with a Be foil with an equal amount of deposited carbon) in Figure 1, where the corres-

ponding difference spectrum, giving a well defined peak, is also displayed; these spectra were taken at 0.2 MeV, thus representing the worst case situation. (The Ar X-ray production cross section at 0.135 MeV was obtained assuming the target thickness determined at an higher energy and measuring the incident charge.) Dead time corrections had to be made but generally did not exceed 10%; they were based on the simultaneous measurement of a peak produced by pulses fed by a mains triggered pulse generator into the particle preamplifier.

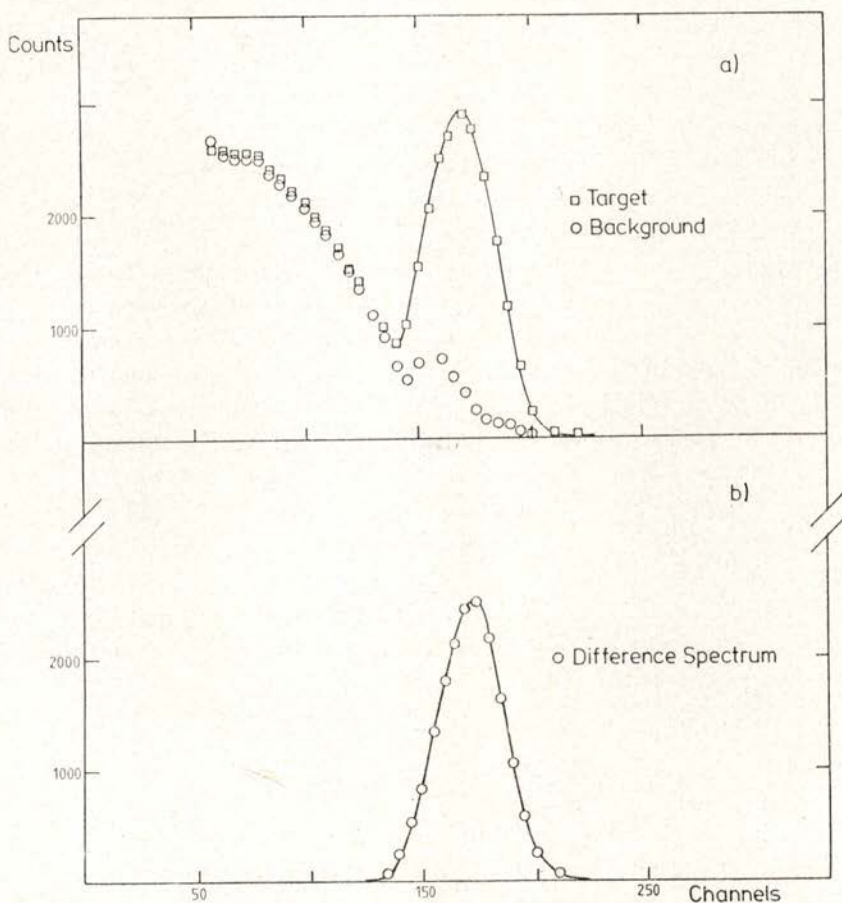


Fig. 1 — Spectra of backscattered protons at 0.2 MeV incident energy. *a)* Spectrum given by the Ar implanted on Be target superimposed on the background spectrum given by a Be foil with the same amount of deposited carbon. *b)* Difference spectrum showing clearly the peak due to the Ar atoms.

Except for Ar at 0.135 MeV, the X-ray production cross sections were determined using the formula

$$\sigma_X(E_i) = 4\pi\sigma_R(E_i, \theta) \cdot (n_X \Omega_p / n_p \Omega_X)$$

where $\sigma_R(E_i, \theta)$ is the Rutherford cross section at energy E_i and detection angle θ , n_X and n_p are the corrected numbers (see below) of simultaneously detected X-rays and protons, and Ω_p and Ω_X are the solid angles subtended by the proton and X-ray detectors, respectively. The number n_X has been corrected for the detection system overall efficiency and for dead time. The number n_p has been corrected for dead time and for the E^{-2} dependence of the Rutherford-scattering law at incident energies where the fact that the implanted ions are below the Be foil surface makes this correction significant.

The targets were implanted in flat Be foils at 80 keV bombarding energy at ISKP, University of Bonn. We used the work of Santry and Werner [18] to obtain the ranges of the implanted ions, finding the values $17 \mu\text{gcm}^{-2}$ for Ar and $8 \mu\text{gcm}^{-2}$ for Kr, with an error estimate of $\pm 25\%$. The targets were positioned at 45° to the beam; thus, assuming negligible range straggling, the proton beam had to pass through Be layers $24 \mu\text{gcm}^{-2}$ and $11.3 \mu\text{gcm}^{-2}$ thick before hitting the Ar and Kr atoms, respectively. At low energies the results have to be corrected for the significant beam energy loss thus produced. The proton stopping power has been obtained from the tables of Northcliffe and Shilling [19]; the energy loss for a $24 \mu\text{gcm}^{-2}$ Be layer at 0.135 MeV bombarding energy is calculated to be 16.2 keV, and at 1 MeV, 5.5 keV. To obtain the X-ray production cross sections at the stated bombarding energy we assumed that the cross section varied as the α power of the energy,

$$\sigma_X(E) = (E/(E - \Delta E))^{\alpha+2} \cdot \sigma_X(E - \Delta E)$$

where E is the bombarding energy and ΔE the energy loss; the term 2 in the exponent comes from the Rutherford scattering law. The value of α has been derived from the corrected theoretical PWBA cross sections. Thus to obtain the cross section value for Ar at 0.135 MeV, the measured value has to be multiplied by 2.04; at 0.2 MeV by 1.54; at 0.5 MeV by 1.09. The corresponding factor for Kr at 0.5 MeV is 1.04. The error in the cross section coming

from a 25% error on the assumed thickness of the Be layer in front of the implanted Ar decreases with increasing incident energy and is roughly 30% at 0.135 MeV, 12% at 0.2 MeV and 6% at 0.3 MeV. The Ar and Kr layers were, of course, very thin, with a density of roughly 5×10^{-16} atoms cm^{-2} .

3 — RESULTS AND DISCUSSION

The results obtained in the present work are shown in Table I together with other available experimental values. For Kr it is seen that our results are almost a factor of 2 smaller than the gas target results of Winters *et al* [2] while being in agreement to within 10–20% with those obtained with a Kr implanted on Si target by Lennard and Mitchel [3]. For Ar all the previous results have been obtained with gas targets and it is seen that there is agreement with the present values to within roughly 10%, except for the value at 2 MeV which is about 25% lower than some of the previous results [5,6].

A comparison of the present data with theoretical values derived from the PWBA, SCA and BEA theories is now made. The PWBA values were calculated following the procedures and using the tables of Basbas *et al.* [11]. Corrections for electron binding and polarisation effects, and for retardation and deflection of the projectile in the Coulomb field of the nucleus are included in the calculated values; electronic relativistic corrections made according to formula 4 of Amundsen *et al* [20] were also included in the theoretical values for Kr. In Figure 2 is plotted the ratio $\sigma_{\text{th}}/\sigma_{\text{exp}}$ for both Ar and Kr against the logarithm of the proton incident energy represented in terms of the scaled energy variable $y = \eta_{\text{K}} / (\zeta_{\text{K}} \theta_{\text{K}})^2$ defined by Basbas *et al* [11], where $\eta_{\text{K}} = (v_1/v_{2\text{K}})^2$ is the square of the projectile velocity in units of the K-shell electron velocity, θ_{K} is the screening parameter given by the ratio of the binding energy to that of a pure hydrogenic system and ζ_{K} is a v_1 -dependent function related to the binding and polarisation effects. For Ar, our incident energy range corresponds to values $0.024 < y < 0.45$; for Kr, to values $0.020 < y < 0.085$. It is seen that over their common y -range the ratios $\sigma_{\text{th}}/\sigma_{\text{exp}}$ for Ar and Kr have their main differences for low values of y , say $y < 0.03$, the calculated PWBA cross sections being, relatively to the experimental ones, larger for Kr than for Ar. In this low energy range use of the Kocbach Coulomb correction

TABLE I

K-shell ionisation cross sections (in barn). The integers in brackets indicate powers of 10. Estimated absolute errors are $\pm 10\%$ above 0.3 MeV, $\pm 15\%$ below 0.3 MeV and $\pm 35\%$ at 0.135 MeV; corresponding estimated relative errors are $\pm 5\%$, $\pm 10\%$ and $\pm 20\%$, respectively. Fluorescence coefficients are taken to be 0.122 and 0.660 for Ar and Kr, respectively.

E_i	Argon		Krypton			
	This work	Previous work	This work	Previous work		
2.0	3.41 (3)	3.75 ^a , 4.29 ^b , 4.00 (3) ^c	1.20 (1)	2.00 ^a , 1.00 (1) ^f		
1.9	3.57 (3)		1.03 (1)			
1.8	3.33 (3)		9.28 (0)			
1.7	3.00 (3)		8.02 (0)			
1.6	2.77 (3)		6.80 (0)		6.20 (0) ^g	
1.5	2.37 (3)		2.61 (3) ^a		5.13 (0)	9.44 (0) ^a
1.4	2.11 (3)	4.53 (0)				
1.3	1.89 (3)	3.22 (0)		3.41 (0) ^g		
1.2	1.65 (3)	2.43 (0)				
1.1	1.39 (3)	1.78 (0)				
1.0	1.21 (3)	1.15 (3) ^d		1.45 (0)	1.51 (0) ^g	
0.9	1.04 (3)	9.67 (2) ^d		1.03 (0)	9.48 (-1) ^g	
0.8	8.16 (2)	7.66 (2) ^d	6.68 (-1)	7.36 (-1) ^g		
0.7	5.73 (2)	5.61 (2) ^d	3.77 (-1)			
0.6	3.94 (2)	3.93 (2) ^d	1.72 (-1)			
0.50	2.46 (2)	2.46 (2) ^d	9.08 (-2)	1.00 (-1) ^f		
0.45	1.84 (2)					
0.40	1.26 (2)	1.30 (2) ^d				
0.35	7.63 (1)					
0.30	4.75 (1)	5.34 (1) ^d				
0.25	2.64 (1)	2.93 (1) ^d				
0.20	1.29 (1)	1.30 (1) ^d				
0.135	3.41 (0)	3.49 (0) ^e				

a: Ref. 2; *b*: Ref. 5; *c*: Ref. 6; *d*: Ref. 4; *e*: Ref. 1; *f*: Refs. 8, 3.

g: Interpolated from the data of Refs. 8, 3.

factor [21] for Kr would slightly improve the agreement with experiment. For Ar the introduction of the polarisation correction [11], an additive correction increasing with energy in this scaled energy range, made a significant improvement in the theory by increasing the calculated value at 2 MeV by about 20% relatively to the low energy values. Thus the more recent paper of Basbas *et al* [11] gives an appreciably better agreement with experiment than the older one [10].

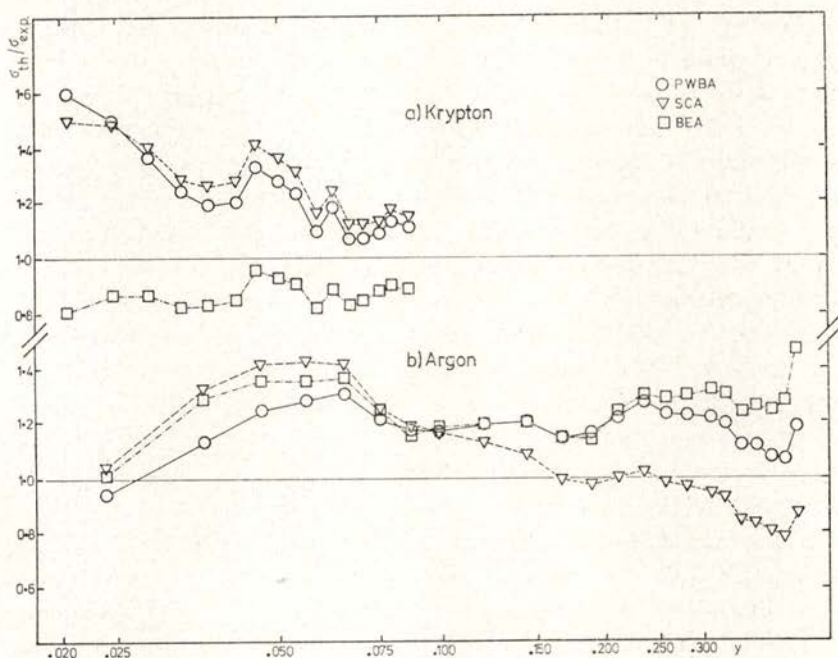


Fig. 2 — Ratio of theoretical to experimental proton-induced ionisation cross sections, σ_{th}/σ_{exp} , for a) krypton and b) argon. The theoretical cross sections correspond to the PWBA, SCA and BEA models and are calculated as described in the text. The abscissa is the logarithm of the scaled energy variable $y = \eta_K / (\xi_K \theta_K)^2$ referred to in the text.

The formulae and procedures presented by Laegsgaard *et al* [13] were used to obtain the SCA cross sections taking into account the effects due to electron binding, Coulomb retardation and, in the case of Kr, the relativistic form of the electron wavefunctions at small distances from the nucleus. The SCA cross sections thus calculated do not allow for polarisation effects which, in the present case, are most important for Ar at the higher end of the incident energy range;

thus one would expect the SCA cross sections for Ar to become significantly smaller than the experimental ones at those energies, as Figure 2 indeed shows. For Kr, the SCA cross sections, like the PWBA ones, are above the experimental values; this is especially so at low scaled incident energies, say $\gamma < 0.03$, where the Coulomb and relativistic corrections are large. One may note here that there is fair agreement between the present results for Kr and those obtained by Lennard and Mitchell [3,8].

In summary, one may say that the corrected PWBA theory gives the best overall fit to the present results (within about $\pm 10\%$ of the average value of the ratio $\sigma_{th} / \sigma_{exp}$ for Ar) and that the inclusion of the polarisation effect provided a significant improvement in the case of Ar. For low values of the scaled energy variable γ the fit is better for Ar than for Kr. The binding energy correction procedure gives, of course, similar correction factors for Ar and Kr and, indeed, seems very accurate if a comparison is made between the results of Ford *et al* [22] using self consistent electron wavefunctions in a second order Born calculation and those obtained following Basbas *et al* [11]. Thus, the fact that at low energies the Ar results are better fitted than those of Kr possibly indicates that the procedures to take into account nuclear Coulomb effects and electronic relativistic effects (which are much smaller for Ar than for Kr) still need to be improved with the net effect of reducing the calculated cross section at low values of the scaled energy variable.

The ratio k_β / k_α for Kr was measured at 1.8 MeV incident proton energy with the results $k_\beta / k_\alpha = 0.178 \pm 0.005$. This ratio has been determined in proton-induced ionisation by other authors with the results 0.189 ± 0.010 [2] and 0.167 ± 0.009 [3]. Multiple ionisation induced by proton impact is expected to be small in this Z-region [23] and this is reflected in the good agreement of the present experimental result with the value $k_\beta / k_\alpha = 0.173$ calculated by Scofield [24] under the assumption that the excited atom is singly ionised.

We would like to thank E. M. Ataíde and M. Lança e Silva for their help in running the accelerator and A. P. Jesus and S. C. Ramos for their assistance in the data analysis. Special thanks are due to Dr. K. Freitag, ISKP, University of Bonn, who kindly prepared the ion implanted targets.

One of us (K. K.) acknowledges the financial support from DAAD, Bonn, and INIC, Lisbon.

REFERENCES

- [1] HARRISON, K. G., TAWARA, H., HEER, F. J., *Physica* **66**, 16 (1973).
- [2] WINTERS, L. M., MACDONALD, J. R., BROWN, M. D., ELLSWORTH, L. D., CHIAO, T., *Phys. Rev.*, **A7**, 1276 (1973).
- [3] LENNARD, W. N., MITCHELL, I. V., *Phys. Rev.*, **A12**, 1723 (1975).
- [4] LANGENBERG, A., VAN ECK, J., *J. Phys.*, **B9**, 2421 (1976).
- [5] RANDALL, R. R., BEDNAR, J. A., CURNUTTE, B., COCKE, C. L., *Phys. Rev.*, **A13**, 204 (1976).
- [6] PRESSER, G., private communication.
- [7] RUTLEDGE, C. H., WATSON, R. L., *At. Data and Nucl. Data Tables*, **12**, 195 (1973).
- [8] GARDNER, R. K., GRAY, T. J., *At. Data and Nucl. Data Tables*, **21**, 515 (1978).
- [9] MERZBACHER, E., LEWIS, H. W., *Handbuch der Physik* (ed. by S. Flugge), Vol. 34, p. 166, Berlin-Göttingen-Heidelberg: Springer (1958).
- [10] BASBAS, G., BRANDT, W., LAUBERT, R., *Phys. Rev.*, **A7**, 983 (1973).
- [11] BASBAS, G., BRANDT, W., LAUBERT, R., *Phys. Rev.*, **A17**, 1655 (1978).
- [12] BANG, J., HANSTEEN, J. M., *K. Dan. Vidensk. Selsk. Mat. Fys. Medd.*, **31**, 1 (1959).
- [13] LAEGSGAARD, E., ANDERSEN, J. U., LUND, M., Proc. 10th Intern. Conf. on the Physics of Electronic and Atomic Collisions (ed. by G. Watel), p. 353, North-Holland Publ. Co. (1978).
- [14] MCGUIRE, J. H., RICHARD, P., *Phys. Rev.*, **A8**, 1374 (1973).
- [15] HANSEN, J. S., *Phys. Rev.*, **A8**, 822 (1973).
- [16] LOPES, J. S., JESUS, A. P., FERREIRA, G. P., GIL, F. B., *J. Phys.*, **B11**, 2181 (1979).
- [17] ROSNER, B., GUR, D., SHABASON, L., *Nucl. Inst. and Meth.*, **131**, 81 (1975).
- [18] SANTRY, D. C., WERNER, R. D., *Nucl. Inst. and Meth.*, **139**, 135 (1976).
- [19] NORTHCLIFFE, L. C., SCHILLING, R. F., *Nucl. Data Tables*, **A7**, 233 (1970).
- [20] AMUNDSEN, P. A., KOEBACH, L., HANSTEEN, J. M., *J. Phys.*, **B9**, L203 (1976).

- [21] KOCBACH, L., *Phys. Norvegica*, **8**, 187 (1976).
- [22] FORD, A. L., FITCHARD, E., READING, J. F., *Phys. Rev.*, **A16**, 133 (1977).
- [23] SEE e.g. RICHARD, P., *Atomic Inner-Shell Processes* (ed. by B. Crasemann), p. 73, New York, Academic Press (1975).
- [24] SCOFIELD, J. H., *Atomic Inner-Shell Processes* (ed. by B. Crasemann), p. 265, New York, Academic Press (1975).

ULTRASONIC STUDY OF ANTIFERROMAGNETIC DOMAINS IN DYSPROSIUM

G. N. BLACKIE and S. B. PALMER

Department of Applied Physics, University of Hull
HU6 7RX, United Kingdom

(Received 7 February 1980)

ABSTRACT— Measurements of thermal hysteresis in the elastic constant C_{33} and its associated ultrasonic attenuation α_{33} for single crystal dysprosium have been carried out using CdS thin film transducers. The results are very similar to earlier ones using quartz transducers bonded with epoxy resin. The anomalous behaviour is interpreted in terms of antiferromagnetic spiral spin domains and this view is supported by thermal cycling studies.

INTRODUCTION

The heavy rare earth metals display a wide range of magnetic spin structures, one of the most fascinating being the antiferromagnetic spiral spin or helical structure. The magnetic moments are confined to the basal planes of the hexagonal structure and in a particular plane all the moments are ferromagnetically aligned. As one moves along the hexagonal c-axis, however, the moments rotate from basal plane to basal plane by a constant angle, θ , the turn angle. Among the elements, Tb, Dy and Ho have a spiral spin state as do the intra-rare earth alloys Tb-Ho and Gd-Y. The antiferromagnetic order commences at the Néel Temperature T_N and disappears at the Curie Temperature T_c . Values of T_N and T_c for the elements and for selected alloys are shown in Table I.

TABLE I

Material	T_N	T_c
Tb	226 K	219 K
Dy	180 K	~ 85 K
Ho	139 K	20 K
Tb - 50 % Ho	185 K	~ 85 K
Gd - 40 % Y	183 K	~ 95 K

The spiral spin structure has attracted a great deal of interest in recent years and it was soon realised that a single crystal sample containing a continuous spiral of magnetic moments would act as a polarizer of an incident neutron flux. However, no such preferential

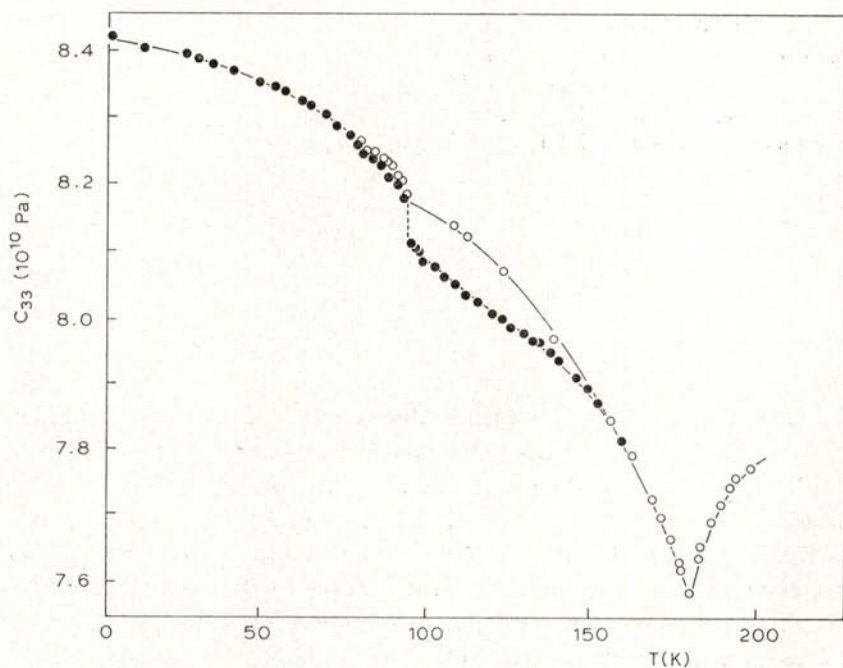


Fig. 1 — Temperature dependence of the elastic constant C_{33} (in units of 10^{10} Pa) for Dysprosium [using quartz transducers]

- Temperature decreasing
- Temperature increasing

polarization was observed and it was therefore assumed that a particular sample is divided into regions where the spiral twists either clockwise or anticlockwise with respect to the *c*-axis.

Further evidence for the presence of these two types of region or domain was provided by studies of the ultrasonic propagation in the heavy rare earths. The elastic constant C_{33} , measured by propagating compressional waves down the hexagonal axis, and its asso-

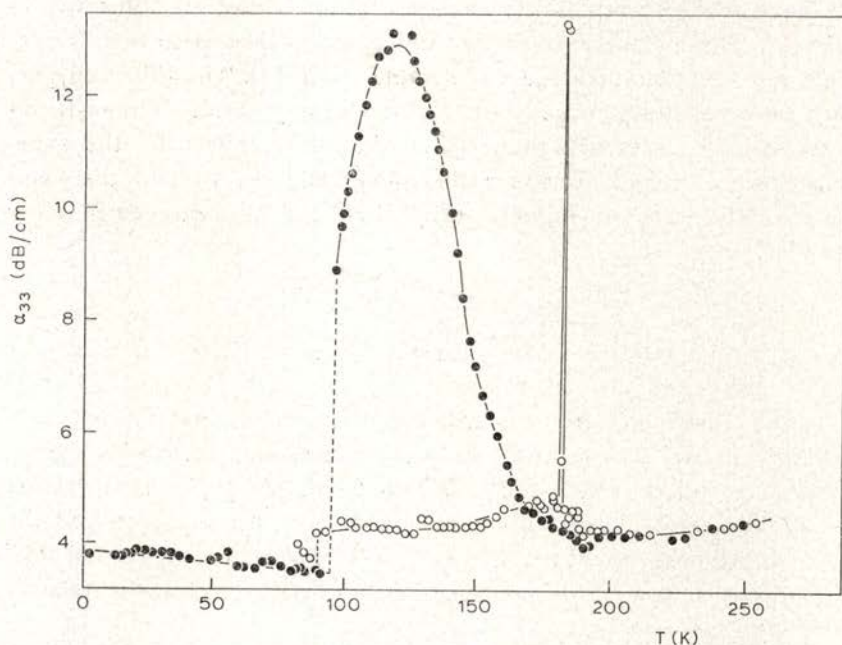


Fig. 2 — Temperature dependence of the ultrasonic attenuation α_{33} (db/cm) for Dysprosium [using quartz transducers]

- Temperature decreasing
- Temperature increasing

ciated ultrasonic attenuation α_{33} display marked thermal hysteresis in the spiral spin regime of Dy, Tb-50% Ho and Gd-40% Y [1]. The measurements reported in [1] show an anomalous drop in C_{33} and a sharp rise in α_{33} when the sample is warmed from below T_c . Figures 1 and 2 show the results obtained for Dy. The ultrasound was generated and detected with quartz transducers which were bonded to the sample with Araldite epoxy resin. The epoxy resin bond was neces-

sary because the large differential thermal expansion between the rare earth sample and the quartz transducer was sufficient to break weaker bonding agents.

It is possible, however, that the use of quartz transducers and Araldite bonds will clamp the relatively soft rare earth sample preventing it from developing its full strain. This clamping could affect the *c*-axis lattice parameter and hence the inter-layer turn angle of the magnetic spiral. To check the reliability of the measuring technique we have replaced the quartz transducers with CdS thin film transducers [2]. These have been shown to adhere to rare earth metals over wide ranges of temperature and sample strain [3]. The thin film puts very little constraint on the sample and simply breaks into 'island' areas at high states of strain. Dysprosium was chosen for the experiment since it had a wide antiferromagnetic region and the sample available was of higher purity than the intra-rare earth alloy samples.

EXPERIMENTAL DETAILS AND RESULTS

The elastic constant C_{33} was calculated from measurements of the velocity of longitudinal waves, propagating down the *c*-axis, using a standard pulse echo overlap technique [5,6]. Temperature variation was achieved with a standard gas flow cryostat and the temperature was measured by a 0.03% Fe in Au versus chromel thermocouple to an absolute accuracy of ± 0.5 K, while the relative accuracy was ± 0.1 K.

The single crystal of Dy was in the form of a cylinder, 5 mm in diameter and 35 mm long, cut with its faces perpendicular to the *c*-axis. It was grown by zone flotation at Metals Research Ltd. and had a purity of better than 99 atomic %. The CdS transducers were vacuum evaporated onto the surface of the sample with a sufficient thickness to allow operation at 15 MHz. Since this was the resonant frequency of the quartz transducers it allowed direct comparison with the earlier measurements [1].

The measurements of C_{33} and α_{33} for Dy taken while the temperature was reduced to 4.2 K and while it was increased from 4.2 K, i.e., from the ferromagnetic region, to room temperature are shown in Figs. 3 and 4. The results obtained for C_{33} are very similar to the previous measurements and exhibit a nearly identical hysteresis when

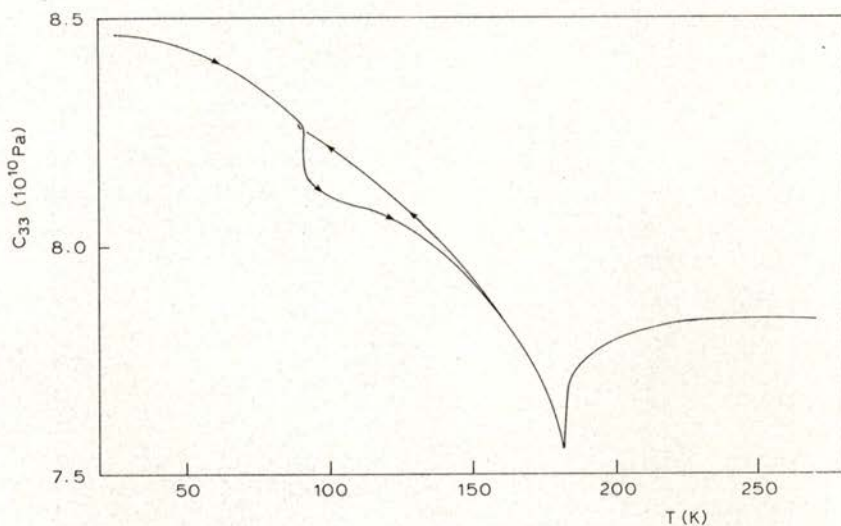


Fig. 3 — Temperature dependence of the elastic constant C_{33} (in units of 10^{10} Pa) for Dysprosium, [using CdS transducers]. Arrows indicate direction of temperature change.

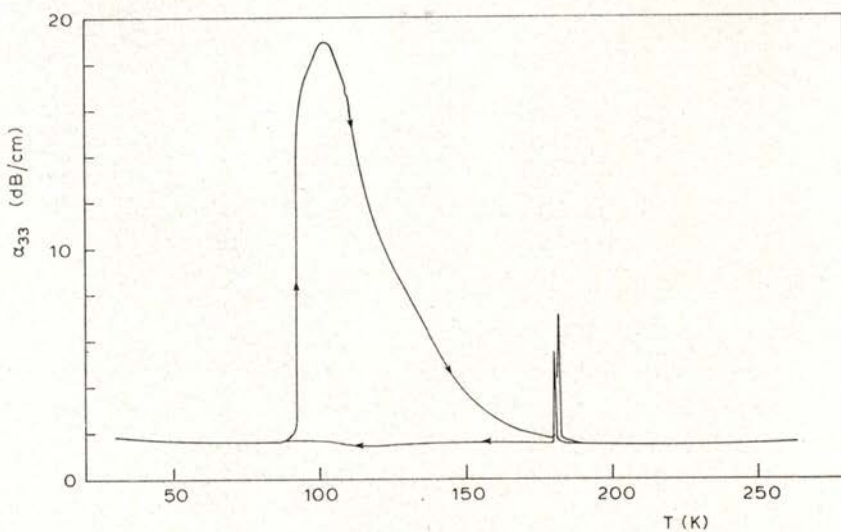


Fig. 4 — Temperature dependence of the ultrasonic attenuation α_{33} (dB/cm) for Dysprosium [using CdS transducers]. Arrows indicate direction of temperature change.

warming from below T_c . The results for α_{33} are again similar except that the phase change at T_c is not seen when cooling and the anomalous attenuation peak is much higher with CdS transducers.

Figure 5 shows the ultrasonic attenuation close to T_N . The hysteresis of 1.5K in T_N is of interest since it is well outside the experimental error associated with thermal equilibrium of the sample. However, more important in the present context is the presence of thermal hysteresis in α_{33} below T_N which tends to zero as T_N is

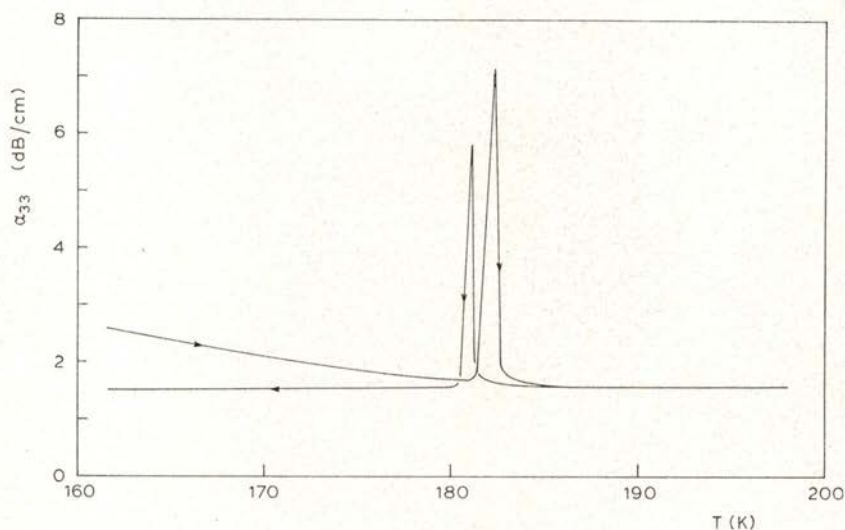


Fig. 5 — Temperature dependence of the ultrasonic attenuation α_{33} (db/cm) for Dysprosium in the vicinity of T_N . The arrows indicate the direction of temperature change.

approached. It should be noted (Fig. 6) that the thermal hysteresis in C_{33} does not extend above 160K.

Figure 7 shows in more detail the sharp rise in α_{33} close to T_c associated with the onset of the spiral spin state. Figure 8 (a) shows the effect of thermal cycling in the region of T_c . The sample is first cooled below T_c into the ferromagnetic phase and then warmed into the spiral spin phase where C_{33} drops as expected. The warming of the sample was then halted at three separate temperatures, 100K, 109K and 123K and the sample cooled below T_c while the behaviour of C_{33} was monitored (Fig. 8 (a, b)).

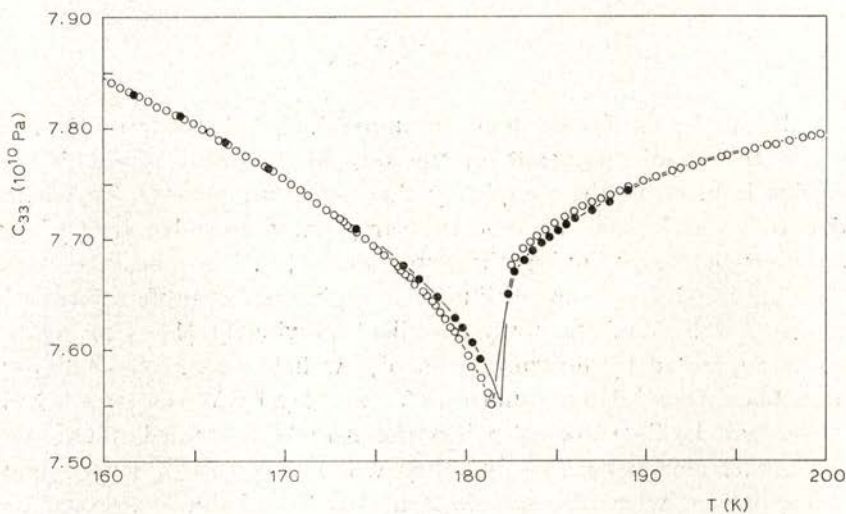


Fig. 6 — Temperature dependence of the elastic constant C_{33} (10^{10} Pa) for Dysprosium in the vicinity of T_N .

- Temperature decreasing
- Temperature increasing

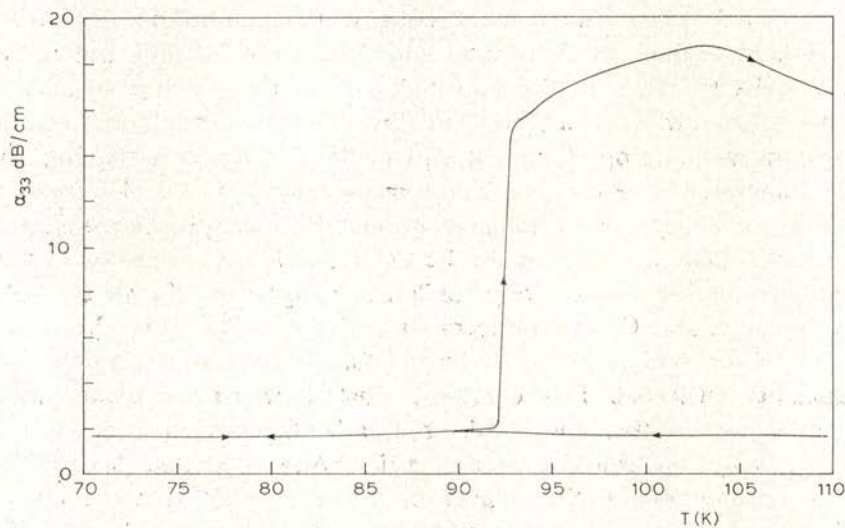


Fig. 7 — Temperature dependence of the ultrasonic attenuation α_{33} (dB/cm) for Dysprosium in the vicinity of T_e .

DISCUSSION

It can be confirmed that the anomalous behaviour of C_{33} and α_{33} in the spiral spin state of the rare earth metals is not due to strains induced in the sample by the measuring process. To ensure that this was indeed the case the sample was annealed at 60°C for an hour before beginning the experiments [7]. The rise in α_{33} and the fall in C_{33} can be attributed to spiral spin antiferromagnetic domains (SSD) of the form described previously [1]. This analysis is supported by measurements of low field (a.c.) susceptibility and thermal modulation studies in Tb and Dy by Wilson *et al* [8, 9]. There will be SSD present when the sample is cooled down into the antiferromagnetic state but they will be far less numerous than those present when the sample is heated from below T_c . Extra SSD will be nucleated from the ferromagnetic Bloch walls in a manner described earlier [1]. The domain boundaries between SSD will be ferromagnetic and the lowering of the elastic constant C_{33} will be caused by the well known « ΔE » effect. The applied stress of the acoustic wave produces rotation of the magnetisation in the domain wall developing a magnetostrictive strain that adds to the elastic strain reducing the elastic constant below its non-magnetic value.

The ferromagnetic domain walls will be pinned to impurities and imperfections in the crystal and the ultrasonic wave will cause the walls to move in the potential well of the pinning site. This phenomenon will obviously lead to ultrasonic attenuation and the attenuation will be proportional, at a particular frequency, to the number of domains. Hence the attenuation measurements in Fig. 4 infer that there are always more domains present in a sample warmed from below T_c than would normally be the case, although close to T_N the numbers of domains are very similar. A comparison of Figs. 2 and 4, with quartz and CdS transducers respectively, indicate that the clamping of the sample produced by the former reduces the number of domains nucleated. This comment must, however, be treated with caution as the attenuation peak itself varies from run to run.

Finally one would expect from the « ΔE » effect that the drop in C_{33} is proportional to the number of domains present. Hence in Fig. 8 the maximum number of domains are nucleated close to T_c and this number decreases as T_N is approached. However, when the temperature is lowered from an intermediate value the number of domains

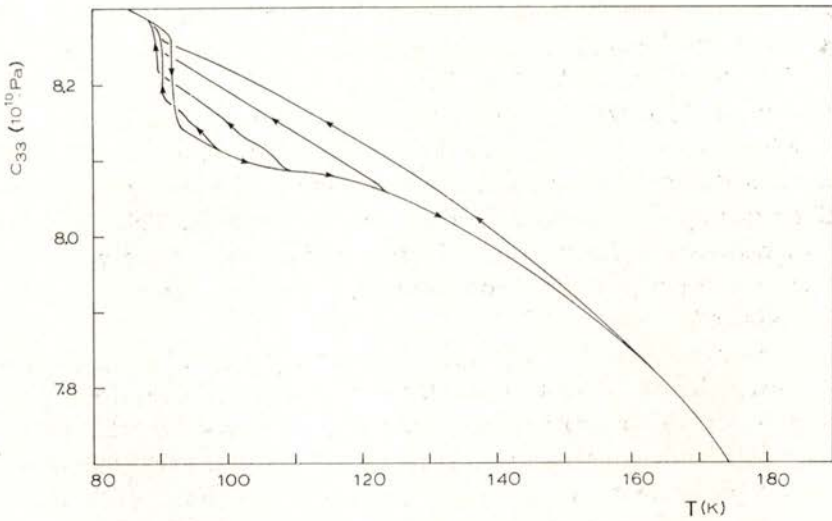


Fig. 8(a) — Temperature dependence of the elastic constant C_{33} (10^{10} Pa) for Dysprosium in the vicinity of T_c .

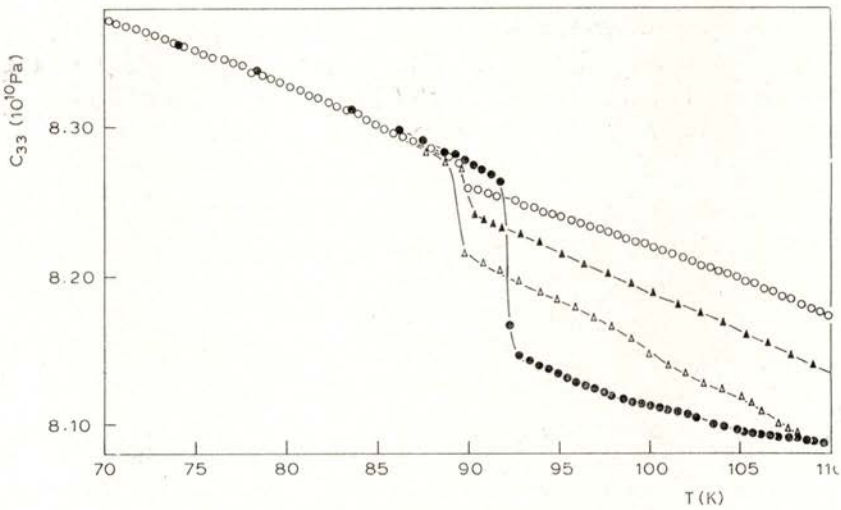


Fig. 8(b) — Enlarged version of 8(a) in the region of T_c .

○ Temperature decreasing from 300 K.

● Temperature increasing from 4 K.

Temperature increase from below T_c followed by:

△ Temperature decreasing from 109 K.

▲ Temperature decreasing from 123 K.

remains essentially constant, with all four curves being very nearly parallel, until the Curie temperature is reached.

We have available, therefore, a technique for increasing the number of SSD, whereas the requirement for a neutron polarizer is to reduce the number of domains present. It is probable that fewer domains can only be produced by improving the purity and crystalline quality of the single crystal samples available. This improvement will reduce the number of pinning sites for domain walls and hence the number of domains, especially when the sample is cooled from above T_N .

The hysteresis in T_N , (Figs. 5,6) probably arises from the different strain levels present in the Dy crystal when cooling from room temperature and warming from below 100K. It was reported previously [7] that the ordering temperatures of the rare earth metals are strongly dependent on the state of strain in the sample. It should be noted that the measurement of ultrasonic attenuation associated with spin fluctuation scattering at the phase change is a remarkably sensitive technique for defining the transition temperature and therefore studying any hysteresis.

The authors would like to thank Mr. Stuart Lawson of the Physics Department, University of Lancaster, for evaporating the CdS transducer. The financial support of SRC is also acknowledged as is the provision of a studentship to one of us (N. B.).

REFERENCES

- [1] S. B. PALMER, *J. Phys. F: Metal Physics*, **5**, 2370 (1975).
- [2] J. D. LLEWELLYN, H. M. MONTAGUE-POLLAK and E. R. DOBBS, *J. Phys. E. (Sci. Inst.)*, **2**, 535 (1974).
- [3] S. B. PALMER, *J. Phys. Chem. Solids*, **37**, 1069 (1976).
- [4] F. H. SPEDDING, *Handbook of Chemistry and Physics* 52nd edition Cleveland: *The Chemical Rubber Co.* (1971).
- [5] J. E. MAY, *I.R.E. Nat. Conv. Rep.*, **6**, pt 2, 134 (1958).
- [6] E. P. PAPADAKIS, *J. Appl. Phys.*, **35**, 1474 (1964).
- [7] S. B. PALMER and R. D. GREENOUGH, *J. Mag. Mag. Mat.*, **1**, 310 (1976).
- [8] T. J. MCKENNA, S. J. CAMPBELL, D. H. CHAPLIN and G. V. H. WILSON, *J. Phys. F: Met. Phys.* (in press) (1979).
- [9] T. J. MCKENNA, S. J. CAMPBELL, D. H. CHAPLIN, G. H. J. WANTENAAR and G. V. H. WILSON, *J. de Physique*, **40**, C-5-22 (1979).

MAGNETIC PHASE TRANSITIONS IN TERBIUM SINGLE CRYSTALS (*)

M. M. AMADO, J. B. SOUSA, M. F. PINHEIRO, R. P. PINTO,
M. E. BRAGA, J. M. MOREIRA

Centro de Física da Universidade do Porto, 4000 Porto, Portugal

D. HUKIN, G. GARTON, P. WALKER

Clarendon Laboratory, Univ. Oxford, OX1 3PU, United Kingdom

(Received 15 June 1980)

ABSTRACT—New high precision measurements of the electrical resistivity and its thermal derivative for a high quality terbium single crystal along a basal direction are presented and discussed in connection with the para-antiferromagnetic and anti-ferromagnetic transitions.

In terbium, the charge distribution of 4f-electrons is toroidal in character, originating a number of interesting effects and a succession of two magnetic transitions. As the temperature is monotonically decreased Tb goes from the para- to the antiferromagnetic phase at $T_N = 229$ K (2nd order), the localized ionic spins (\vec{S}_i ; site \vec{R}_i) presenting then an helicoidal arrangement:

$$S_i^x = S \cos(\vec{q} \cdot \vec{R}_i) \quad , \quad S_i^y = S \sin(\vec{q} \cdot \vec{R}_i) \quad , \quad S_i^z = 0 \quad (1)$$

\vec{q} characterizes the helix period along the \vec{c} -axis ($2\pi/q$) and $qc/2$ gives the rotation angle of S_i from an atomic plane to the next along \vec{c} ($\approx 20^\circ$).

A second transition, of the order-order type, takes place at $T_c = 221$ K, where Tb goes into a simple ferromagnetic state ($\vec{q} = 0$)

(*) Work supported by INIC and NATO Research Grant 1481; results presented at the Conference of the Portuguese Physics Society (Porto, April 1980).

in eq. 1). Spins \vec{S}_i are still in the basal plane, but they now point everywhere in the same direction.

These magnetic transitions received considerable attention in the past [1], through extended measurements of thermodynamic (specific heat, magnetization, susceptibility; *no* latent heat measurements) and transport properties, namely electrical and thermal resistivity, thermopower, ultrasonic attenuation.

In spite of this, most properties did not reveal clearly the order-order transition at T_c . Electrical resistivity studies have been most informative, and for that reason we restrict ourselves here to this type of measurements.

The temperature dependence of the electrical resistivity $\rho(T)$ has been studied by Hegland *et al* [2] along *a*- and *c*-crystallographic directions and from 4 – 300 K. The considerable anisotropy is apparently enhanced in the paramagnetic phase which is a rather surprising result.

(i) *Along the c-axis*, the onset of the antiferromagnetic phase at T_c originates a sharp rise in ρ , as shown in Fig. 1 (from ref. 2): The increase in ρ is due to the formation of magnetic superzones caused by the new periodicity in the system (helix structure; wave vector \vec{q} along \vec{c}); this produces new gaps, reducing the effective

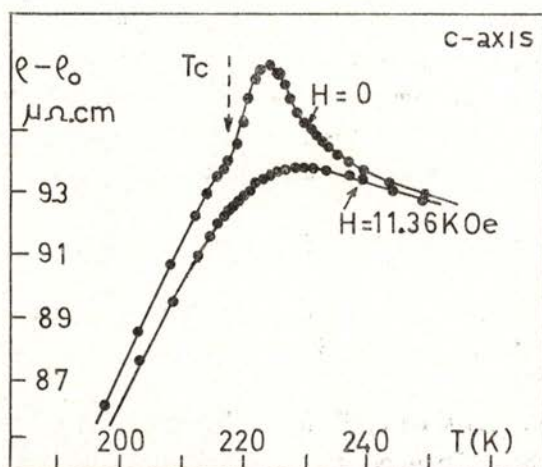


Fig. 1 — Temperature dependence of ρ for Terbium along the *c*-axis in transverse (along *b*) external magnetic field (from ref. [2]).

number of electrons to carry the current along the c-axis. Since T_c is close to the temperature at which magnetic order is suppressed (T_N), such gaps are relatively small and the anomaly $\Delta\rho/\rho$ at T_c becomes correspondingly small (≈ 0.04). Part of the jump at T_c may also come from a change in magnon dispersion. Superzone effects in the antiferromagnetic phase naturally produce the well developed hump observed in ρ (Fig. 1). This hump can be suppressed if the helical phase is destroyed by application of an external magnetic field along a basal direction, as shown in the same figure ($H \geq 11$ kOe; interlayer rotation suppressed; spins \vec{S}_i frozen along \vec{H}).

A clear identification of the Néel temperature is difficult from simple $\rho(T)$ measurements. A better insight can be gained with measurements of the temperature derivative ($d\rho/dT$), as performed by Meaden *et al* [3] in the vicinity of T_N .

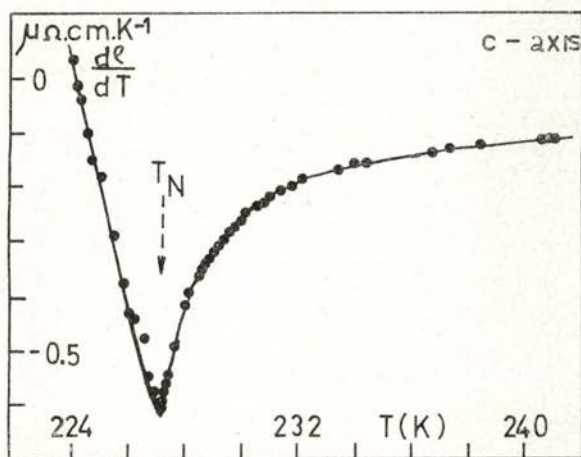


Fig. 2 — Temperature dependence of $d\rho/dT$ for Terbium along the c-axis (from ref. [3]).

As shown in Fig. 2, a sharp minimum occurs in $d\rho/dT$ at $T_N = 227.2$ K. The critical behaviour reveals a log-divergence for $0.6 \leq T - T_N \leq 3$ K, whereas for $T - T_N \geq 3$ K one has a $(T - T_N)^{-1/2}$ dependence. For $T - T_N < 3$ K the specific heat also diverges practically in a logarithmic way [3]. As will be seen later, this result has interesting consequences regarding the critical behaviour.

(ii) *Along a basal direction*, previous measurements [2] revealed a rather uninteresting behaviour in ρ : a simple knee in the curve at the Néel point and no obvious anomaly around T_c . Besides that, no experimental data seem available for $d\rho/dT$, neither attempts to analyze the critical behaviour near T_N and T_c .

In view of this we decided to perform very accurate measurements of ρ and $d\rho/dT$ along a basal direction (a-axis). For the first time, we believe, a sharp anomaly has been detected in ρ_a and $(d\rho/dT)_a$ near T_c and new information obtained for the critical behaviour of the basal-resistivity of Tb near T_N . The anomalously large $(d\rho/dT)_a$ values in the ferromagnetic phase are also analyzed here.

Fig. 3 shows our results for ρ_a and $(d\rho/dT)_a$:

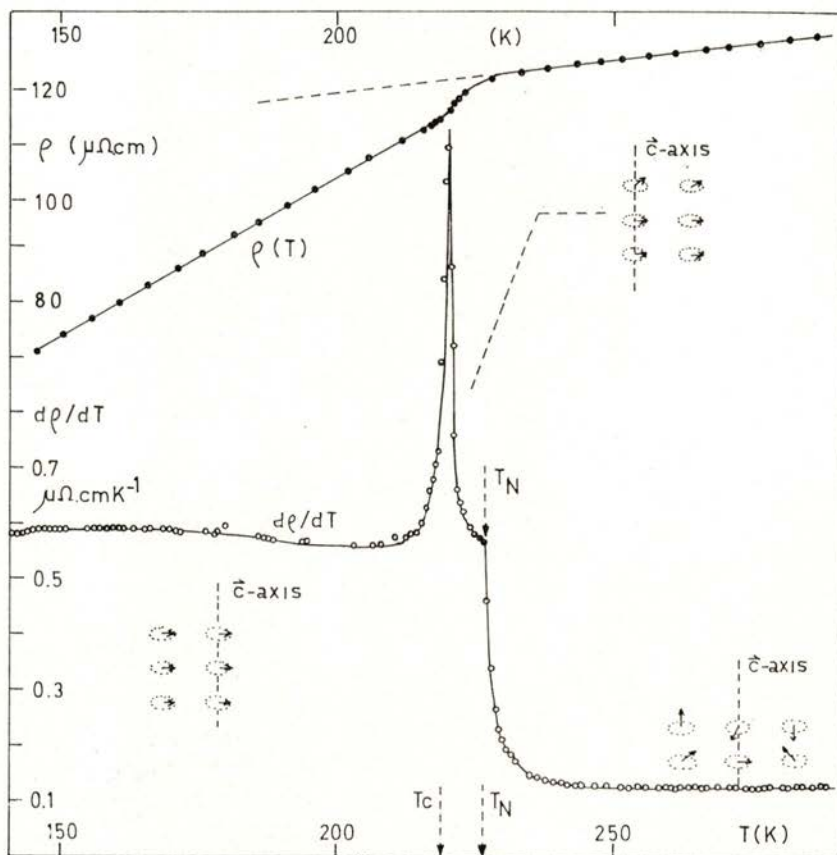


Fig. 3 — Temperature dependence of ρ and $d\rho/dT$ for Terbium along the a-axis.

The usual knee in ρ_a at the Néel point is confirmed in Fig. 3, but our data also reveal a neat kink in ρ_a at T_c . While in previous investigations the latter anomaly is hardly observed (see e.g. the specific heat C_m in ref. 4), it is exuberantly present in our $d\rho/dT$ curve, where a very sharp peak appears just at the ferro-antiferromagnetic transition (T_c). The Néel temperature is also well defined, by the sudden and sharp decrease in $d\rho/dT$. Above T_N , $d\rho/dT$ rapidly reaches a constant value of $\sim 0.13 \mu\Omega \cdot \text{cm} \cdot \text{K}^{-1}$, attributable to electron-phonon scattering.

The critical behaviour of $(d\rho/dT)_a$ near T_N has been analyzed in detail for $T > T_N$. Our data closely follow a logarithmic dependence:

$$(d\rho/dT)_a = A \cdot \ln(T - T_N) + B \quad (2)$$

with $A = -0.078$, $B = 0.2834$ ($\mu\Omega \cdot \text{cm} \cdot \text{K}^{-1}$ units), $T_N = 226.9 \text{ K}$; the fit is valid down to reduced temperatures $\sim 10^{-3}$ (i.e. $T - T_N \approx 0.3 \text{ K}$). This result confirms that $(d\rho/dT)_a$ and $(d\rho/dT)_c$ have the same functional (log) dependence near T_N , as expected within the universality hypothesis. Since the specific heat practically diverges as $\ln(T - T_N)$ near the Néel point it also follows that:

$$(d\rho/dT)_a \sim C_m(T) \quad (3)$$

This relation is expected to hold when short-range fluctuations dominate the electrical resistivity near T_N [5]: large-momentum transfer to the electrons.

A brief comment is now in order on the qualitative shapes of $(d\rho/dT)_a$ and $(d\rho/dT)_c$ near T_N (Figs. 2 and 3): whereas along c the shape is characteristic of typical antiferromagnets (e.g. chromium; $d\rho/dT < 0$), for the a -axis it rather looks like usual ferromagnetic systems ($d\rho/dT > 0$; see Fig. 4).

In physical terms, what really happens is that electrons flowing along a basal plane in Tb always 'see' the corresponding spins in the *same* direction. This is exactly a ferromagnetic-like situation, which, of course, appears reflected in the shape of the $(d\rho/dT)_a$ curve for terbium. As an illustration, Fig. 4 shows the similarities between $d\rho/dT$ anomalies for Tb near T_N (a -axis) and for gadolinium near the Curie temperature [6].

A striking feature in terbium is the anomalously high $(d\rho/dT)_a$ derivative in the ferromagnetic phase, even for $T \ll T_c, T_N$. In simple ferromagnets like Ni, Fe $(d\rho/dT)$ decreases rather fast below T_c , due

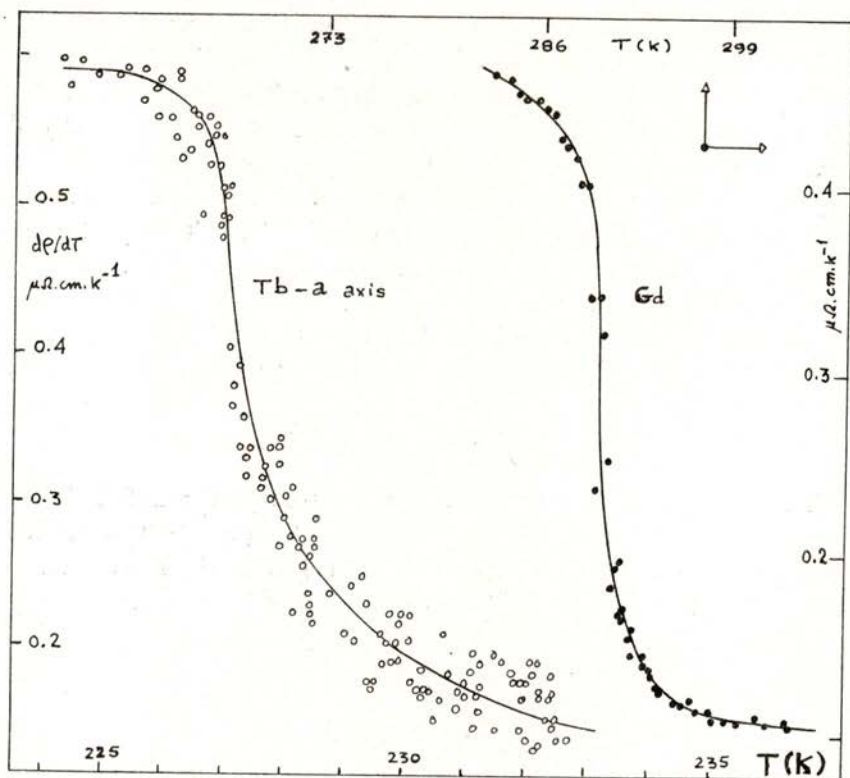


Fig. 4 — Comparison between the qualitative shape of $d\rho/dT$ along the a -axis for Terbium and $d\rho/dT$ for Gadolinium.

to the increasing magnetic order in the system. In Tb, we believe that the high $(d\rho/dT)_a$ values are due to the unusually rapid variation of the magnetization with temperature:

$$M(0) - M(T) = A \cdot T^{3/2} \cdot e^{-\Delta/kT} \quad (4)$$

with $M(0) = 325 \text{ emu} \cdot \text{g}^{-1}$, $A = 0.03595 \text{ emu} \cdot \text{g}^{-1} \cdot \text{K}^{-3/2}$, $\Delta/k = 20 \text{ K}$ [7]. For order of magnitude calculations, let us use a mean field model for the magnetic resistivity:

$$\rho_m(T) = \rho_\infty [1 - (M(T)/M(0))^2] \quad (5)$$

where $\rho_\infty \approx \rho(T_N) = 123 \text{ } \mu\Omega \cdot \text{cm}$. We then find $d\rho_m/dT = 0.37 \text{ } \mu\Omega \cdot \text{cm} \cdot \text{K}^{-1}$ at $T = 120 \text{ K}$, and $d\rho_m/dT = 0.39 \text{ } \mu\Omega \cdot \text{cm} \cdot \text{K}^{-1}$ for $T = 150 \text{ K}$. If one

adds the phonon contribution to the resistivity derivative ($d\rho_p/dT \sim 0.13 \mu\Omega \cdot \text{cm} \cdot \text{K}^{-1}$) we get $d\rho/dT = 0.50; 0.52 \mu\Omega \cdot \text{cm} \cdot \text{K}^{-1}$ at $T = 120$ and 150 K , respectively, whereas experiment gives correspondingly: $d\rho/dT = 0.58$ and $0.59 \mu\Omega \cdot \text{cm} \cdot \text{K}^{-1}$. In view of the approximate nature of our calculations, the results are indeed quite good.

The high-quality terbium single crystal used in this work has been purified by solid state electron transport, and our high accuracy data on $d\rho/dT$ were obtained with a quasistatic method previously described in the literature [8].

Work is now in progress to investigate the critical behaviour of the thermoelectric power and thermal conductivity in the same Tb single crystal.

The financial support of INIC and NATO (Res. Grant 1481) is gratefully acknowledged. The technical assistance of Eng. Jaime Bessa is also deeply appreciated.

REFERENCES

- [1] SEE e.g. R. J. ELLIOTT (ed.) in *Properties of Rare Earth Metals*, Plenum Press 1972, p. 245.
- [2] HEGLAND, D. E., LEVGOLD, S., SPEDDING, F. H., *Phys. Rev.*, **131**, 158 (1963).
- [3] MEADEN, G. T., SZE, N. H., JOHNSTON, J. R., in *Dynamical Aspects in Critical Phenomena*, Budnick and Kawatra (ed.), Gordon and Breach 1972, p. 315.
- [4] JENNINGS, L. D., STANTON, R. M., SPEDDING, F. H., *J. Chem. Phys.*, **27**, 909 (1957).
- [5] ALEXANDER, S., HELMAN, J. S., BALBERG, I., *Phys. Rev.*, **B13**, 304 (1976).
- [6] DAMAS, A. M., RESTIVO, M. T., SOUSA, J. B., *Anais da Faculdade de Ciências do Porto*, **LIX**, 1 (1976).
- [7] MACKINTOSH, A. R., *Physics Letters*, **4**, 140 (1963).
- [8] SOUSA, J. B., AMADO, M. M., BRAGA, M. E., PINTO, R. P., MOREIRA, J. M., HUKIN, D., *Communications on Physics*, **2**, 95 (1977).



THERMOPOWER IN RARE EARTH INTERMETALLIC COMPOUNDS AND THE VALIDITY OF s-f SCATTERING MODELS (*)

R. P. PINTO, J. B. SOUSA, J. M. MOREIRA, M. M. AMADO,
M. F. PINHEIRO, M. E. BRAGA

Centro de Física da Universidade do Porto, 4000 Porto, Portugal

P. MORIN

Laboratoire Louis Néel, 166 X 38042 Grenoble Cedex, France

(Received 15 June 1980)

ABSTRACT—The s-f scattering models of Kasuya and Abel'skii—Irkhin are tested against experimental data on the thermopower of several rare-earth intermetallic compounds (Gd Zn, Gd Cd, Tb Zn). Good agreement is obtained for Gd Zn but not for Tb Zn; for Gd Cd the present data are inconclusive.

The s-f interaction of strength G between conduction electrons (spin \vec{s}) and localized ionic spins (\vec{S}_i) in rare earth systems,

$$G \delta(\vec{r} - \vec{R}_i) \vec{s} \cdot \vec{S}_i \quad (1)$$

changes sign for conduction electrons with spin up or down, making the corresponding relaxation times different when a net magnetic polarization \vec{M} exists in the system ($T < T_c$; T_c = Curie point). Pronounced anomalies then arise in the thermopower Q , as was first shown by Kasuya [1]. For temperatures not too low compared to T_c , Kasuya expression can be written:

$$Q(T) = (k^2 \pi^2 / 3 e E_F) T + \frac{+ (2k(g-1) \zeta / e E_F) G \langle J_z \rangle \cdot (1 - e^{-x}) / (1 + e^{-x})}{}, \quad (2)$$

(*) Work supported by INIC, NATO Res. G. 1481 (Porto), and CNRS (Grenoble); results presented at the Conference of the Portuguese Physics Society (Porto, April 1980).

$\langle J_z \rangle$ being the z-axis expectation value of the total angular momentum \vec{J} , g the Landé factor, $x = 3[J(J+1)]^{-1} \cdot (T_c/T) \cdot \langle J_z \rangle$, ζ the fraction of magnetic ions in the system, E_F the Fermi level, and k the Boltzmann constant. The first term in $Q(T)$ is the normal diffusion electronic contribution, and the second term characterizes the magnetic anomaly, with a magnitude controlled by the parameter (G/E_F) .

The shape of the anomaly depends on the sign of G , which rises (or lowers) the energy of each electron group (\uparrow or \downarrow), making electrons to flow preferentially to one (or the other) of the thermoelectric junctions. The thermopower measurements can be used to obtain the sign of G , in contrast to the case of the electrical resistivity ρ [1] which depends on the square of G .

Fig. 1 summarizes the different types of Q -anomalies expected in ferromagnetic systems near T_c , according to the possible signs of e and G :

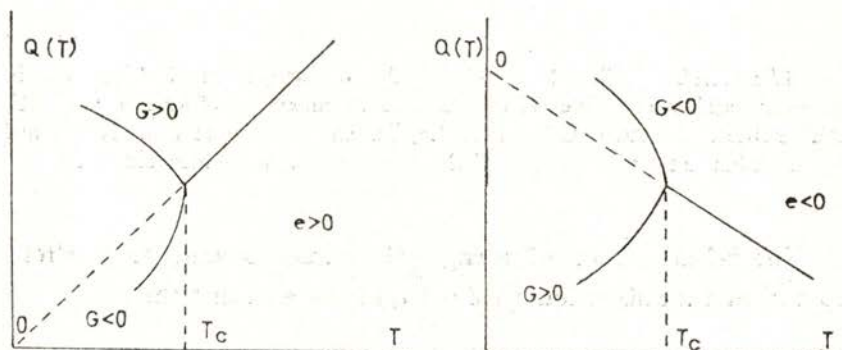


Fig. 1 — Different types of thermoelectric power (Q) anomalies expected in ferromagnetic systems near T_c , according to the possible signs of e and G .

Kasuya model has been improved by Abel'skii-Irkhin [2], through inclusion of electron-phonon scattering and more accurate calculations. The following mean-field expression for $Q(T)$ near or above T_c is obtained:

$$Q(T) = A_1 T \cdot F_1(t, z; J, \gamma) + A_2 z \cdot F_2(t, z; J, \gamma) \quad (3)$$

where $A_1 = \text{const}(kT/E_F)$, $A_2 = \text{const}(G/E_F) \zeta J$, $t = T/T_c$, $z = M(T)/M(0)$ and F_1, F_2 are simple functions of t, z, J, γ , with $\gamma = (\rho_s / \beta T_c) [J(J+1)]^{-1}$, where $\rho_s, \beta T$ are the total spin and phonon resistivities, respectively.

The second term in (3), which vanishes above T_c , becomes the dominant magnetic contribution below T_c . The first term is a diffusion-like contribution which entirely determines $Q(T)$ in the paramagnetic phase.

Expressions (2) and (3) describe reasonably well the shape of $Q(T)$ in ferromagnets, but quantitative tests in rare earth systems are rather scarce, and practically limited to the case of Gd[1,3]. For this reason we report now on a detailed investigation of the validity of the s-f model to describe the Q -anomalies in rare earth ferromagnets. To avoid the complexities of uniaxial crystals, we have chosen a series of intermetallic compounds with the simple CsCl structure, of the type RM, where R=heavy rare earth, M=Zn, Cd. Here we select three of these compounds (GdZn, TbZn, GdCd), one presenting a very *large* Q -anomaly (TbZn), the other a *moderate* one (GdZn) and the last one presenting only a *small* Q -anomaly near T_c (GdCd).

Fig. 2 shows $Q(T)$ for TbZn and GdZn:

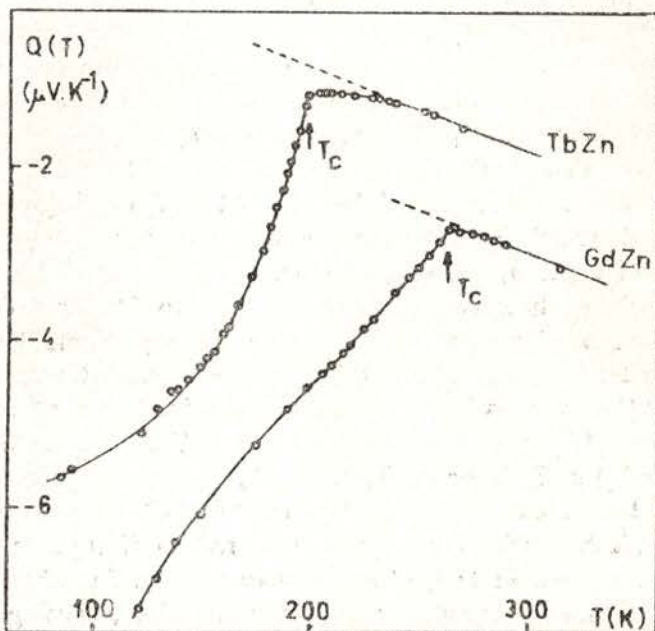


Fig. 2 — Temperature dependence of thermoelectric power ($Q(T)$) for TbZn and GdZn.

In the paramagnetic phase Q has a negative slope ($e < 0$), approaching gradually a quasi-linear behaviour (a small quadratic term is present), as expected from (3) in terms of a diffusion-like electronic contribution to Q :

$$Q_{\text{para}} = (k^2 \pi^2 / 3 e E_F) T (3/2 + r_1 \beta T / \rho + r_2 \rho_s / \rho) \quad (4)$$

where r_1 , r_2 characterize the energy dependence of the electron relaxation times for phonon and spin scattering $\tau \propto E^{r_1}$, E^{r_2} respectively. Of course, the experimental curve bends progressively as T approaches T_c from above, due to the increasing role of the critical fluctuations, which are not accounted for in the above (mean-field) models.

For numerical calculations we use the standard values $r_1 = 3/2$, $r_2 = -1/2$; $J = 7/2$, $g = 2$ (Gd); $J = 6$, $g = 3/2$ (Tb); $\zeta = 1/2$. From accurate electrical resistivity studies we obtained $\beta = 0.136 \mu\Omega \cdot \text{cm} \cdot \text{K}^{-1}$, $\rho_s = 52.5 \mu\Omega \cdot \text{cm}$, $T_c = 265 \text{ K}$ for GdZn, and $\beta = 0.119 \mu\Omega \cdot \text{cm} \cdot \text{K}^{-1}$, $\rho_s = 36.3 \mu\Omega \cdot \text{cm}$, $T_c = 199.6 \text{ K}$ for TbZn. [4].

From eq(4) we then obtain $E_F = 4.4, 6.9 \text{ eV}$ for GdZn and TbZn respectively. Since Q gets more negative below T_c (and $e < 0$, we also conclude that G is positive both in TbZn and GdZn.

We are now in a position to test eq. (3) in the ferromagnetic phase. For GdZn, a good fit to our experimental data can be obtained if one assumes $G = 0.18 \text{ eV}$, as shown in Fig. 3 (heavy line; the broken line shows the paramagnetic-like line, as given by eq. (2).

The G value obtained appears quite reasonable and fairly close to the quoted values for pure Gd (0.17–0.20 eV) [5]. It gives a ratio $G/E_F \sim 0.04$, which is of the same order of magnitude as previously obtained for Gd from $Q(T)$ measurements [3].

For TbZn, however, it is not possible to fit our $Q(T)$ data using 'reasonable' values for G ($\sim 10^{-1} \text{ eV}$); they would lead to a much smaller anomaly than found experimentally. Within the assumption that Q -anomalies below T_c are entirely due to the s-f exchange interactions [1,2] one would require $G \sim 7 \text{ eV}$ to match the steep decrease of Q in TbZn below T_c ($G/E_F \sim 1$).

An alternative approach is, of course, to admit the possible dominance of factors which are not considered in Kasuya and Abel'ski-Irkhin models. In fact, other mechanisms besides phonon and normal spin scattering might be operative in TbZn, causing Q_{exp} to decrease more sharply below T_c . An interesting case is the possible effect of quadrupole ordering below T_c [6] and of the tetragonal

lattice distortion which arises at the onset of the ferromagnetic phase in TbZn [7]. Both features are absent in GdZn, which might justify the good agreement between experiment and theory found in this compound. Effects due to the possible non-s character of the conduction band in TbZn should also be carefully investigated.

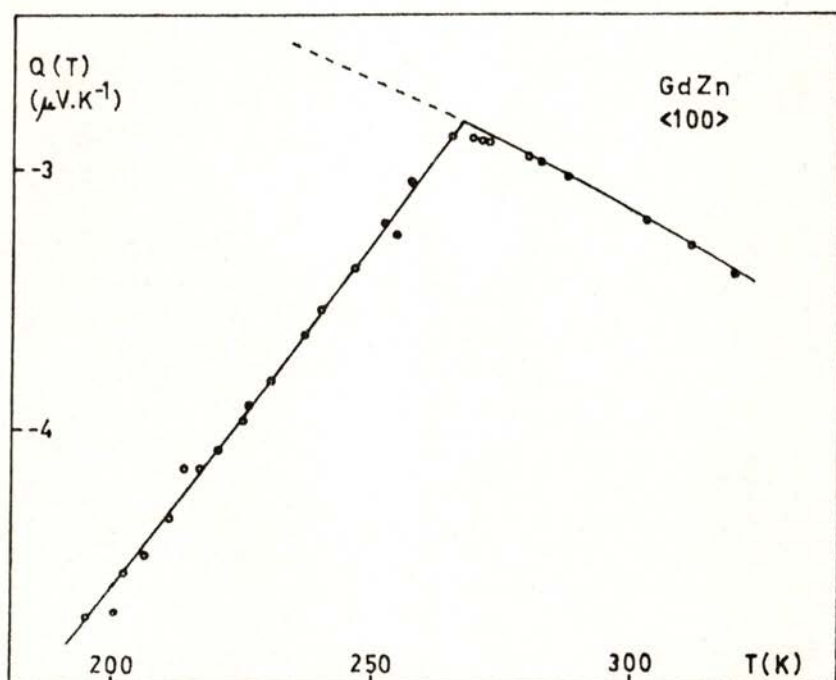


Fig. 3 — Fitting of the experimental data of thermoelectric power (Q) for GdZn $\langle 100 \rangle$ to equation (2), assuming $G = 0.18$ eV.

Finally we show in Fig. 4 the temperature dependence of the thermoelectric power for GdCd.

The anomaly is now much smaller than in previous samples, although with the same qualitative features as in GdZn and TbZn, since $dQ/dT < 0$ in the paramagnetic state, and below T_c we have Q depressed with respect to the linear extrapolation from the paramagnetic state [8]. However, due to the smallness of the anomaly in this sample and the existence of a second transition below T_c [8], work is still in progress for the detailed analysis in this sample.

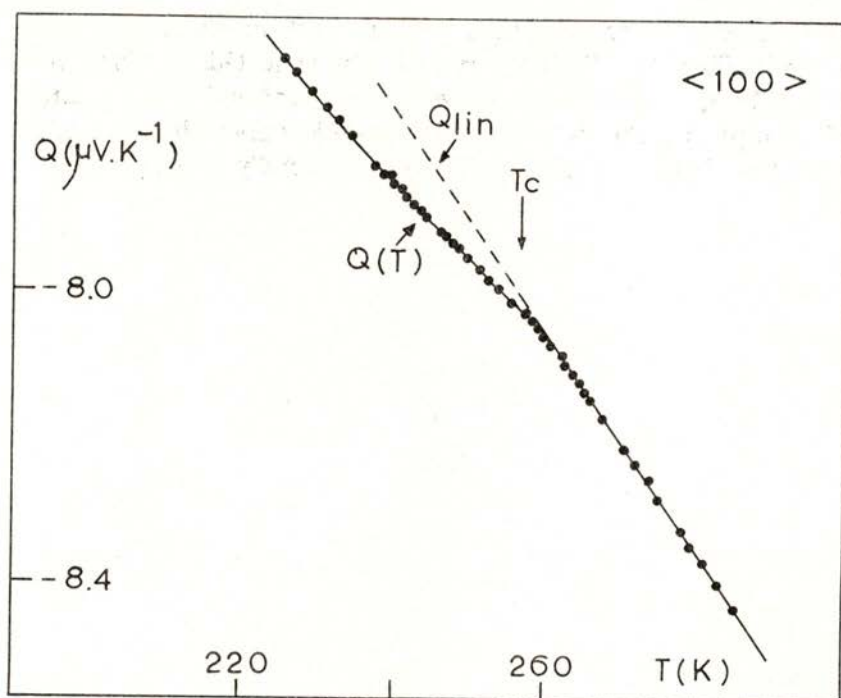


Fig. 4 — Temperature dependence of thermoelectric power $Q(T)$ for GdCd near T_c .

Financial support by INIC (National Institute for Scientific Research, Portugal) NATO (Res. Grant 1481) and CNRS is gratefully acknowledged. Technical aid of J. Bessa is deeply appreciated.

REFERENCES

- [1] KASUYA, T., *Prog. Theor. Phys.*, **22**, 227 (1959).
- [2] ABEL'SKII, SH. SH., IRKHIN, YU. P., *Sov. Phys. Sol. St.*, **13**, 2035 (1972).
- [3] SOUMURA, T., MAEDA, T., *J. Phys. Soc. Japan*, **41**, 1544 (1976).
- [4] SOUSA, J. B., PINTO, R. P., AMADO, M. M., MOREIRA, J. M., BRAGA, M. E., MORIN, P., *J. Phys. F. Metal Phys.* 1980 (in press).
- [5] LIU, S., *Phys. Rev.*, **123**, 470 (1961).
- [6] LEVY, P. M., MORIN, P., SCHMITT, D., *Phys. Rev. Lett.*, **42**, 1417 (1979).
- [7] MORIN, P., *Thèse doctorat, Univ. Grenoble* (1975).
- [8] SOUSA, J. B., PINTO, R. P., AMADO, M. M., MOREIRA, J. M., BRAGA, M. E., MORIN, P., ALEONARD, R., Proc. Fargo 14th Rare Earth Conf. 1979 (in press).

CORRELATION BETWEEN TWIST VISCOSITY AND DIELECTRIC RELAXATION IN NEMATIC LIQUID CRISTALS (*)

A. C. DIOGO and A. F. MARTINS

Centro de Física da Matéria Condensada (INIC)
Av. Gama Pinto 2, 1699 Lisboa Codex, Portugal

(Received 16 June 1980)

ABSTRACT— We compare experimental data on the low-frequency dielectric relaxation time $\tau_{||}^{(1)}$ with data on the twist viscosity γ_1 for the nematic phase of the elements with $n=4$ to 7 in the homologous series of 4,4'-di-n-alkoxyazobenzene, using the relation

$$\tau_{||}^{(1)} \approx 1/\nu_o = (\pi^2 V^* / k T) \cdot \gamma_1$$

which was proposed by us in a previous paper; here, V^* is a molecular volume and T is the temperature.

This relation is verified to within the experimental uncertainties in all cases studied.

1—INTRODUCTION

In previous papers [1], we proposed a molecular statistical theory of the twist viscosity in nematic liquid crystals which involves the frequency ν_o of the rotational jumps performed by the nematic molecules about an axis normal to their preferred orientation \mathbf{n} , between two equilibrium positions separated by π radians. This quantity was related to the twist viscosity coefficient γ_1 by the following expression [1]:

$$\frac{1}{\nu_o} = \frac{\pi^2 V^*}{k T} \cdot \gamma_1 \quad (1)$$

(*) Presented at the Second Conference of the Portuguese Physics Society (Porto, April 16-18, 1980).

where V^* is the molecular volume at the temperature T , as extrapolated from the isotropic phase, and k is the Boltzmann constant. It was suggested in ref. [1] that

$$\frac{1}{\nu_0} \simeq \tau_{||}^{(1)} \quad (2)$$

or

$$\gamma_1 \simeq \frac{k T}{\pi^2 V^*} \cdot \tau_{||}^{(1)} \quad (3)$$

which is a relation between twist viscosity and dielectric relaxation since $\tau_{||}^{(1)}$ is the low-frequency dielectric relaxation time, measured when the electric field \mathbf{E} is parallel to the nematic director \mathbf{n} . This low frequency relaxation observed in nematics, was attributed [2] to the reorientation of the component of the molecular dipole parallel to the long molecular axis, which is hindered by the nematic mean-field potential. Therefore, a check of relation (3) may provide information about the molecular processes that contribute both to the low frequency dielectric relaxation and to the twist viscosity.

The validity of relation (3) was demonstrated in ref. [1] for the case of *p*-azoxyanisole, which is the first element in the homologous series of 4,4'-di-*n*-alkoxyazoxybenzenes (nOAB). Here, the result of [1] is extended to the elements of this series with aliphatic chains ranging from $n=4$ (butoxy) to $n=7$ (heptyloxy). In the next section we compare the values of $1/\nu_0$ computed from our experimental data on the twist viscosity [3] with the dielectric relaxation times $\tau_{||}^{(1)}$ quoted from refs [4-6], and discuss the results. Section 3 displays our main conclusion together with a suggestion for further work.

2 — EXPERIMENTAL DATA AND DISCUSSION

Figures 1 to 4 show the plots of $\log \tau_{||}^{(1)}$ and $\log (1/\nu_0)$ versus $1/T$, respectively for the homologues 4OAB, 5OAB, 6OAB, and 7OAB. The dielectric data are quoted from refs. [5] and [6], and ν_0 was computed from our data on twist viscosity [3], using expression (1). In computing ν_0 we used the actual molecular volume in the nematic phase V_N [7], instead of V^* , due to the lack of enough data on the density of these materials in the isotropic phase. This

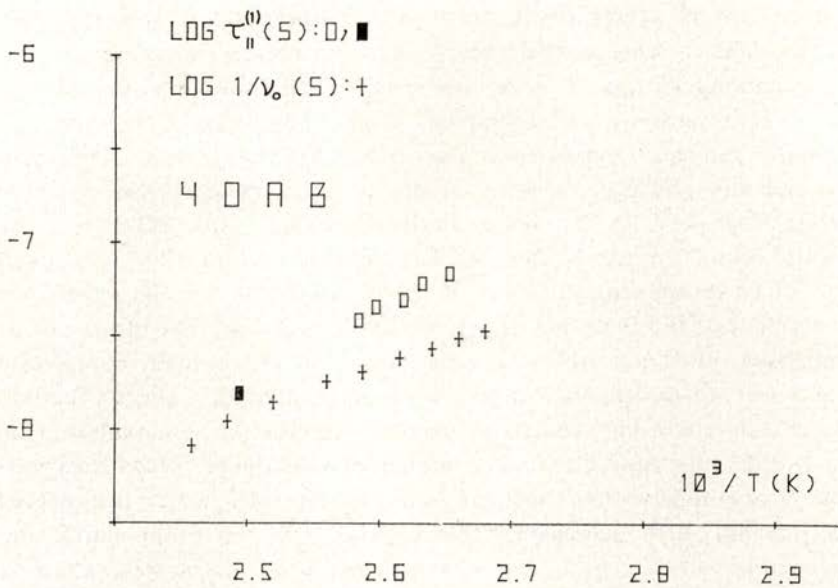


Fig. 1 — $\text{Log } \tau_{||}^{(1)}$ and $\text{log } 1/\nu_0$ versus $10^3/T$ for 4OAB. Data points: + : values of $1/\nu_0$ computed from the twist viscosity data of [3]; ■ : $\tau_{||}^{(1)}$ quoted from [5]; □ : $\tau_{||}^{(1)}$ quoted from [6].

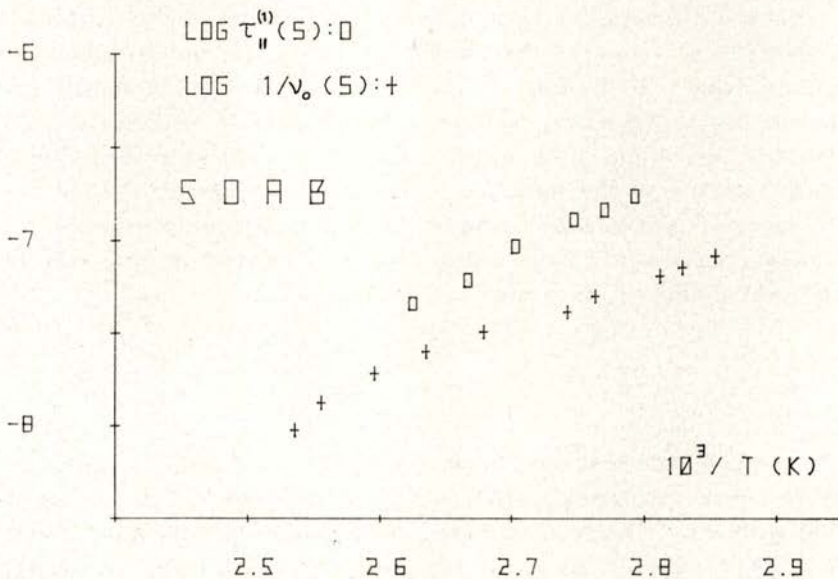


Fig. 2 — $\text{Log } \tau_{||}^{(1)}$ and $\text{log } 1/\nu_0$ versus $10^3/T$ for 5OAB. Data points: + : values of $1/\nu_0$ computed from the twist viscosity data of [3]; □ : $\tau_{||}^{(1)}$ quoted from [6].

approximation seems to be not very important due to the smallness of the density jump at the nematic-isotropic phase transition.

Looking at figs. 1 to 4, one sees that the simple expression (2) is in reasonably good agreement with experience along the full nematic range of these materials. In the low temperature region of the nematic phase of these materials, $\tau_{||}^{(1)}$ appears to increase slightly faster than $1/\nu_o$ as the temperature decreases. This effect may be partly due to the use of the nematic molecular volume $V_N(T)$ instead of $V^*(T)$ in the computation of ν_o , because the thermal expansion coefficient of the isotropic phase is usually less than that of the nematic phase. Most probably, however, this will not explain completely the observed discrepancy, and a sounder explanation should include some differences between twist viscosity and dielectric relaxation. One such difference may stand on the distinct sensitivities of both experimental methods to the short range molecular order, which is expected to increase with decreasing temperature. On the other hand, the calculation of $\tau_{||}^{(1)}$ from the observables in dielectric relaxation is always based on some model and is subject to a number of approximations that are difficult to control. The values obtained are model-dependent to an extent that could be used to explain the observed discrepancy [8].

The agreement between $1/\nu_o$ and $\tau_{||}^{(1)}$ shown by figs. 1 to 4 supports our view [1] that a simple model of molecular jumps between the two minima of the nematic mean-field potential can account for the essential features of both the twist viscosity and the dielectric relaxation, although it may be somewhat surprising due to the complexity of the microscopic behaviour involved in these two processes. This is specially true in the high temperature region of the nematic phase, near the nematic-isotropic transition temperature, where $1/\nu_o$ and $\tau_{||}^{(1)}$ have nearly the same value.

3 — CONCLUSION

We conclude that the available dielectric relaxation data about $\tau_{||}^{(1)}$ in the nematic materials 4OAB, 5OAB, 6OAB and 7OAB is compatible with eq. (3) which is based on a molecular statistical theory of $\gamma_1(T)$ proposed by us [1, 3]. Our viscosity measurements discussed here are the first set of data on γ_1 obtained from one homologous series of nematic liquid crystals. In order to test more closely the

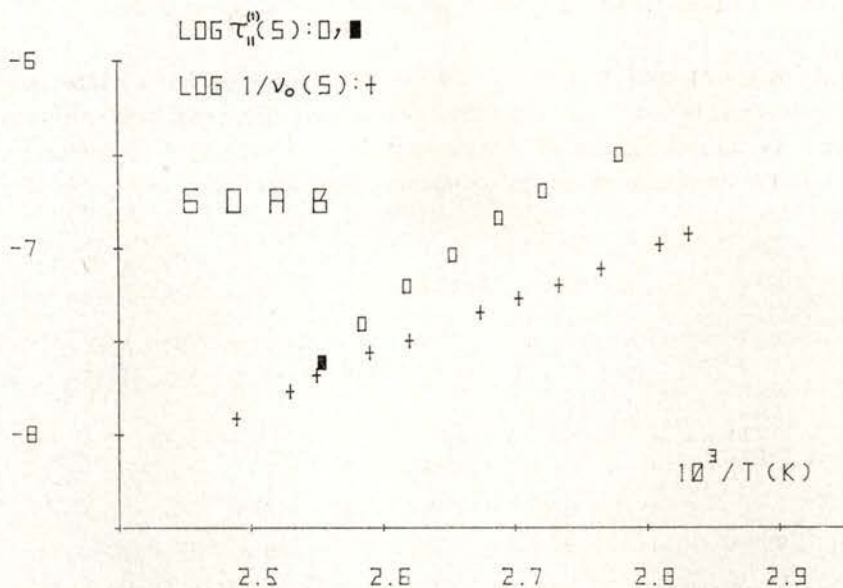


Fig. 3 — Log $\tau_{||}^{(1)}$ and log $1/\nu_0$ versus $10^3/T$ for 6OAB. Data points: + : values of $1/\nu_0$ computed from the twist viscosity data of [3]; ■ : $\tau_{||}^{(1)}$ quoted from [5]; □ : $\tau_{||}^{(1)}$ quoted from [6].

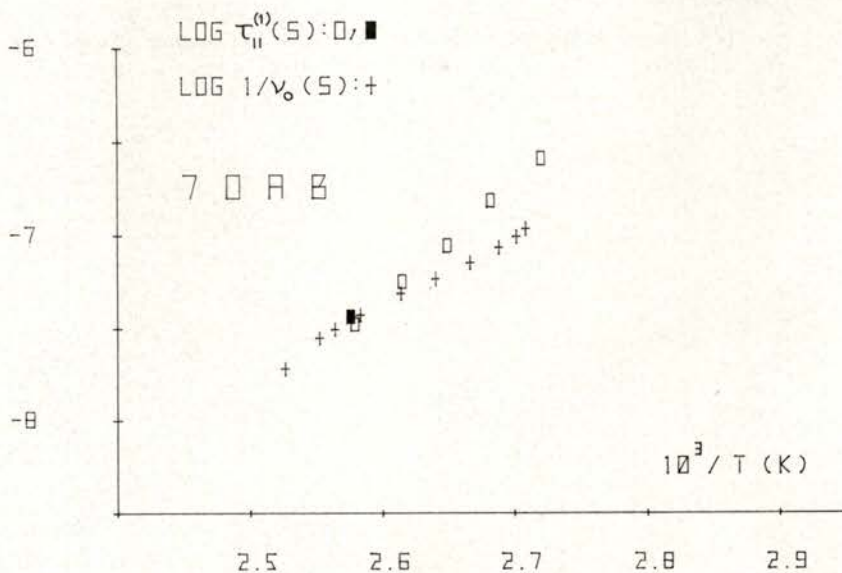


Fig. 4 — Log $\tau_{||}^{(1)}$ and log $1/\nu_0$ versus $10^3/T$ for 7OAB. Data points: + : values of $1/\nu_0$ computed from the twist viscosity data of ref [3]; ■ : $\tau_{||}^{(1)}$ quoted from [5]; □ : $\tau_{||}^{(1)}$ quoted from [6].

relations (2) and (3) it should be interesting to have systematic measurements on both dielectric relaxation and twist viscosity, as well as measurements of the density, as a function of temperature, for other homologous series of nematic liquid crystals.

REFERENCES

- [1] A. F. MARTINS and A. C. DIOGO, *Portgal. Phys.*, **9**, 129 (1975); A. F. MARTINS, A. C. DIOGO and N. P. VAZ, *Ann. Physique* **3**, 361 (1978).
- [2] G. MEIER and A. SAUPE, *Mol. Cryst.*, **1**, 515 (1966); A. J. MARTIN, G. MEIER and A. SAUPE, *Symp. Farad. Soc.* n.º 5, 119 (1971).
- [3] A. C. DIOGO and A. F. MARTINS, to be published.
- [4] W. MAIER and G. MEIER, *Z. Naturforschg.* **16-a**, 1200 (1961).
- [5] H. WEISE and A. AXMANN, *Z. Naturforschg.* **21-a**, 1316 (1966); A. AXMANN, *Z. Naturforschg.* **21-a**, 615 (1966).
- [6] A. MIRCEA-ROUSSEL and F. RONDELEZ, *J. Chem. Phys.*, **63**, 2311 (1975).
- [7] V_N was computed through the density data of F. LINSERT, Master Thesis, Halle (1945).
- [8] See for instance W. H. DE JEU, *Solid State Physics, Suppl.* **14**, 109 (1978).

RADIOLUMINESCENCE OF RARE GASES

(review article)

M. SALETE S. C. P. LEITE

Departamento de Física, Universidade de Coimbra
3000 Coimbra, Portugal

(Received 8 April 1980)

CONTENTS

- 1 — Introduction.
- 2 — Interaction of ionizing particles with matter, with particular reference to rare gases.
- 3 — Evolution of primary states.
 - 3.1 — Spectra observed.
 - 3.2 — Electronic structure and potential curves of diatomic molecules of rare gases.
 - 3.3 — Ion recombination. Creation and evolution of molecular ions.
 - 3.3.1 — Radiative recombination.
 - 3.3.2 — Recombination ion-electron with participation of a neutral atom.
 - 3.3.3 — Dissociative recombination.
 - 3.4 — Deexcitation of excited atomic states.
 - 3.4.1 — Radiative deexcitation.
 - 3.4.2 — Deexcitation by diffusion and collision with the container walls.
 - 3.4.3 — Collisional transfer of electronic energy.
 - 3.4.4 — Formation of excimers through three-body collisions.
 - 3.4.5 — Associative ionization — Hornbeck-Molnar reactions.
- 4 — Mechanism of luminescence.
 - 4.1 — The origin of two continua.
 - 4.2 — Atomic precursors of the excimers.
 - 4.2.1 — Low pressure conditions ($\ll 1$ atm).

4.2.2 — High pressure conditions (> 1 atm).

4.2.2.1 — Low electronic density ($n_e \ll 10^{10}/\text{cm}^3$).

4.2.2.2 — High electronic density ($n_e > 10^{10}/\text{cm}^3$).

5 — Concluding remarks.

6 — References.

1 — INTRODUCTION

The passage of an ionizing radiation through a material medium gives rise to the ionization and excitation of its atoms or molecules. The electronic energy of excitation is then dissipated non radiatively through collisional processes or internal extinction, or is radiatively emitted as photons. This luminescence excited by an intense flux of ionizing radiation, or radioluminescence, is a well known phenomenon since the early days of radioactivity. However it was not until the fifties that the radioluminescence of gases, particularly that of rare gases, started being used on a new particle detector—the scintillation counter—a system essentially formed by the association of a cell containing the gaseous scintillator and a photomultiplier. Its development was extremely fast due to the considerable progresses achieved in the construction of new photomultiplier tubes: higher gain, spectral sensitivity of the photocathode enlarged towards UV and IR, lower noise, etc. [1].

In the last few years, much work was devoted to the development of these detectors and to the improvement of its performance, leading to detectors with excellent characteristics from the point of view of linearity, time and energy resolution and count rate capabilities. However, most of the published works in this area have an essentially technological nature and it was not until recently that some more detailed spectroscopic studies have been performed trying to elucidate the fundamental mechanisms involved in the radioluminescence of rare gases.

A clear understanding of the processes occurring when the ionizing radiation interacts with the matter is essential for the development of the scintillation gas counters or for any other devices making use of the same effect. The knowledge of the spectral distribution of the emitted luminescence, of its mechanism, the influence of pressure and of electric and magnetic fields is fundamental to optimize the

response from those systems. In the last few years, due to the large increase in the range of applications of radioluminescence of rare gases, such as, among others, the use of the scintillation gas counters as particle detectors in several fields of physics, the development of new gaseous lasers [2], particularly nuclear pumped rare gas lasers, the detection of ultratraces of atmospheric materials and harmful heavy metals through radioluminescence [3], the study of the mechanism and kinetics of the processes involved became an urgent task to be performed [4].

Considerable progresses were obtained in the last few years in this field, and although the mechanism and kinetics are not yet fully established [5]-[8] one thinks that the physics of the processes involved is now understood, at least qualitatively.

The main purpose of the present work is to briefly review the elementary processes occurring when rare gases are submitted to an ionizing radiation, and to consider the evolution of the atomic states directly excited, that is, the path of the excitation energy. From a review of the literature, a probable mechanism for the radioluminescence of rare gases is established. This review covers the most relevant works published in this field, though in no way trying to be exhaustive.

2—INTERACTION OF IONIZING PARTICLES WITH MATTER, WITH PARTICULAR REFERENCE TO RARE GASES

Light emission in a medium submitted to the action of a charged particle is the last stage of a complex set of elementary phenomena, that can be analysed considering three main steps:

— in the first one, very brief ($\sim 10^{-9}$ s in a gas at atmospheric pressure), the primary particle and the secondary electrons released from the material by ionization are slowed down and they create primary states of activation having a large energy

— in the second stage, the directly excited and ionized states either go into the emitting states (radiative states) or deexcite through other channels

— finally the decay of the radiative states.

When a particle moves through a gaseous medium its energy is lost essentially by elastic and inelastic collisions with the atoms and/or molecules of the medium and by radiative losses (bremstrahlung). Elastic collisions are efficient only for heavy particles at the end of their paths (cross section varies with V_0^{-2} , V_0 being the particle velocity), while bremstrahlung emission is significant only when the kinetic energy of the particle is very much larger than its energy at rest. The interaction of charged particles with matter takes place mainly with atomic electrons, so that the primary products are atoms or molecules excited or ionized and electrons liberated in the ionization process [9] [10]. These electrons, on the other hand, can also ionize and excite the medium until they become sub-ionization or sub-excitation electrons, respectively. The energy of the sub-excitation electrons is finally lost in elastic collisions (or even in inelastic collisions others than those involving electronic excitations, such as vibrational and rotational excitations in molecules) until they are thermalized and eventually recombine in the medium or at the cell walls. It is a well known fact that the kinetic energy of the electrons liberated in the ionization processes directly induced by the primary particle constitutes the largest part of the energy dissipated in the medium. Usually there is no distinction between the effects of the incident particle and those of the secondary electrons, and a considerable amount of the final effects (specially electronic excitations) are due to the secondary electrons [11].

The knowledge of the excitation and ionization cross sections as a function of the nature and kinetic energy of the incident particles would allow the determination of the species formed and their relative proportions [12]. Unfortunately, this detailed and explicit information is scanty [12]-[18]. Calculated values come usually from the Born-Bethe approximation [15]; according to this approximation, cross sections for the electronic transitions under swift particles collision are proportional to f/E , f being the optical oscillator strength for the transition under consideration and E its energy. This cross section varies with the velocity of the incident particle as $V_0^{-2} \log V_0$. In the rare gases, most of the oscillator strength lies in the ionization continuum, so ionized atoms are expected to largely exceed excited atoms. For Ar, for example, the Kuhn-Thomas rule gives a theoretical total oscillator strength of 18, and according to Samson and Kelly [19] 83% lies in the ionization continuum.

The knowledge of the oscillator strengths for several energy levels would allow the population of these states to be determined. Oscillator strengths are not at all easy to calculate theoretically, and the values presently known for some levels of a few rare gases (for others there are no calculated values at all) are currently being improved by the introduction of new techniques of calculation and more correct approximations for the wave functions of the states concerned.

The role of the secondary electrons in the production of primary states of activation is essential, particularly in the creation of excited states. The energy spectra of these electrons (degradation spectra) is generally not well known though Platzman's calculations for He [17], [20]-[24] emphasize the large range of energies involved; so the calculation of the primary states of activation is a very complicated task [25] [26] inasmuch as electrons can also induce (through electron exchange) optically forbidden transitions, although these are significant only for slow electrons. Detailed calculations involving an energy bookkeeping from the incident particles and the secondary electrons would be of extreme utility, but to our knowledge it has been tried only for He [17] [20] [24]. In fig. 1 and table I [27] are

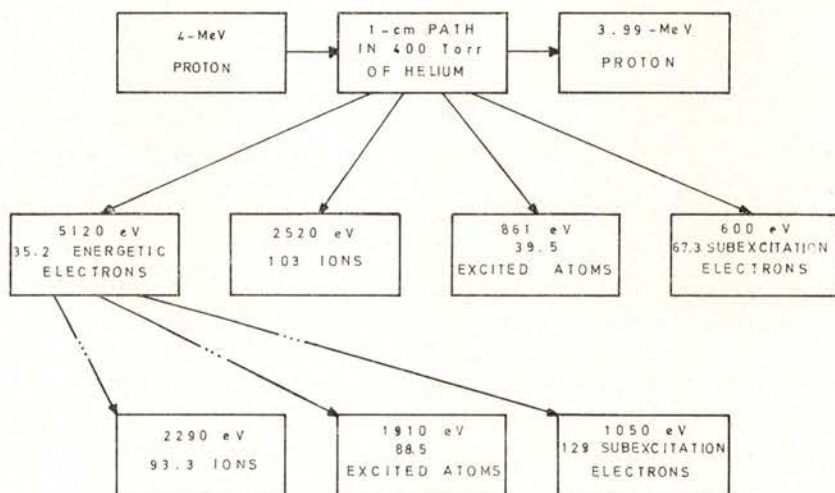


Fig. 1 — Calculated energy degradation when a 4-MeV proton loses a fraction of its energy in helium. The energies given are the portions of the 9101 eV lost by the proton that appear in the species indicated. The numbers of those species produced are also indicated (taken from ref. [27]).

represented, as an illustration, the number of ions and excited states obtained when a 4 MeV proton traverses 1 cm in He at 400 torr. The dominant role of secondary electrons is well underlined.

TABLE I—Average populations resulting when a 1 MeV-proton has a 1-cm path in 400 torr of helium (from ref. [27]).

Products	Primary proton	Secondary electrons
2 1S	1.40	8.82
3 1S	0.31	1.71
2 1P	25.30	27.60
3 1P	6.24	6.32
3 1D	0.07	1.03
2 3S	—	16.00
2 3P	—	1.56
3 3P	—	8.67
3 3D	—	1.77
Other atomic levels	6.08	1.85
Total	39.40	88.53
Ions	103	93.3

Experimental values of cross sections for ionization and excitation come, in general, from measurements of energy losses by electron impact [12]. The strong and detailed correlation of the results at high energies with the optical absorption coefficients for a given gas confirms that the observed peaks of the high energy spectra correspond to optically allowed transitions; at low energies, some additional peaks appear due to forbidden transitions [12] [28]. For argon, for example, excited under 50 KeV electrons impact, the levels preferentially reached are those represented in table II [28] [29]. Agreement between relative values of peak intensities and f/E relative values is quite good [16] if uncertainties in oscillator strengths are kept in mind.

In fig. 2 [30] observed cross-sections for excitation of the 3^1P state of helium by electron impact are compared with the ones calculated from the Born-Bethe approximation: agreement is good for high energies (usually for energies > 200 eV) but poor for low ener-

TABLE II — Comparison of oscillator strengths for some discrete levels of argon with relative intensities of loss peaks under electron impact

Loss Peaks Energy E (eV) ref. [12]	Atomic States ref. [12]	Relative Intensity of Loss Peaks ref. [22]	Experimental Oscillator Strength (f_{exp}) ref. [16]	Theoretical Oscillator Strength (f_{theor}) ref. [16]	f_{exp}/E	f_{theor}/E	$(f_{\text{exp}}/E)_{\text{rel}}$	$(f_{\text{theor}}/E)_{\text{rel}}$
11.62	$4s\ ^3P_1$	0.31	0.0633 (0.059–0.067)	0.059 (0.049–0.080)	0.0055	0.0051	0.26	0.20
11.83	$4s\ ^1P_1$	1.00	0.250 (0.228–0.280)	0.300 (0.200–0.300)	0.021	0.025	1.00	1.00
14.10	$5s\ ^3P_1, 3d\ ^3D_1$	0.27	0.130	0.112	0.0092	0.0079	0.43	0.32
14.26	$5s\ ^1P_1$	0.23	0.130	0.112	0.0091	0.0079	0.43	0.31
14.86	$6s\ ^3P_1, 4d\ ^3D_1$	0.11	0.06	0.053	0.0040	0.0036	0.19	0.14

Note: Values of f_{exp} and f_{theor} in brackets stress the uncertainties in oscillator strengths

gies. We must stress, however, the fact that for low energies cross sections are poorly known and there are no satisfactory theories [30].

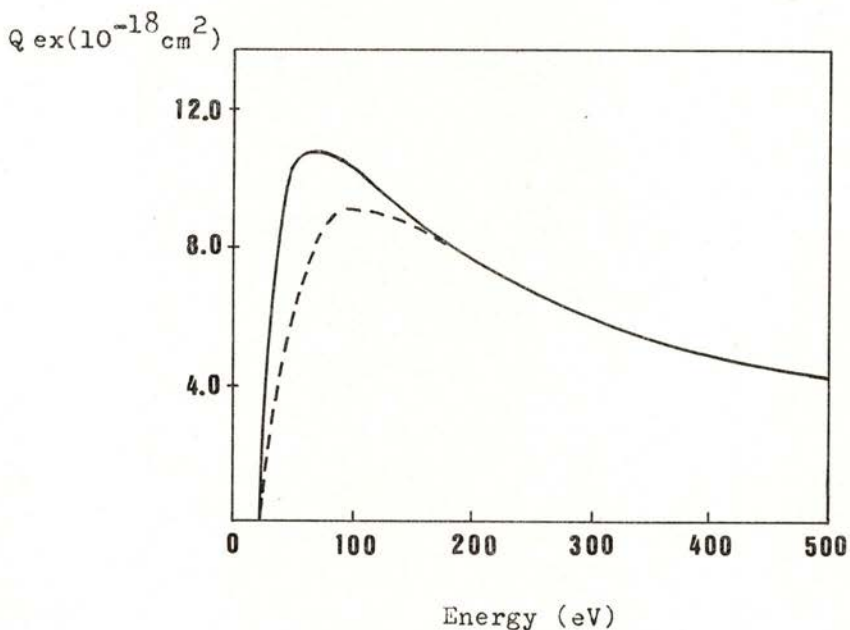


Fig. 2 — Comparison of cross sections for excitation of the $3 \ ^1P$ state of helium by electron impact

——— calculated
 - - - - - observed

(taken from ref. [30]).

In fig. 3 [31] curves for the variation of ionization cross section for single, double and total ionization as a function of the energy of the incident electrons are represented for the lighter rare gases. For He and Ne, the usual approximation of neglecting the formation of multiple charge ions is justifiable, but not so much for Ar: recent measurements under 2 KeV electron impact [32] indicate a relation $Ar^{++}/Ar^+ = 5\%$. The effect is still more pronounced for Kr and Xe [32]. In fig. 4 are indicated cross sections of excitation and ionization

of He by α particles [33]. It is clear that the amount of energy spent in the formation of ions is larger than the one used for the excitation of several levels, and that the level preferentially excited is the state 2^1P , bound to the ground state by the largest oscillator strength.

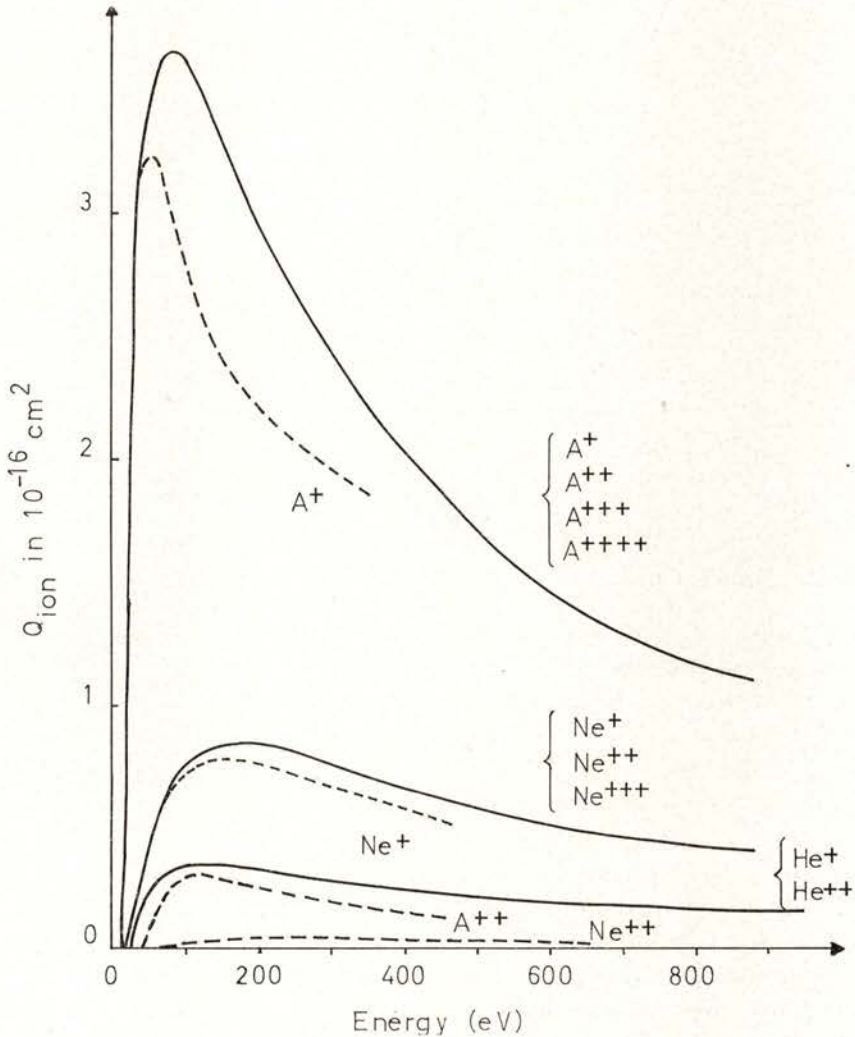


Fig. 3 — Cross sections for single and multiple ionization of helium, neon and argon by electron impact (taken from ref. [31]).

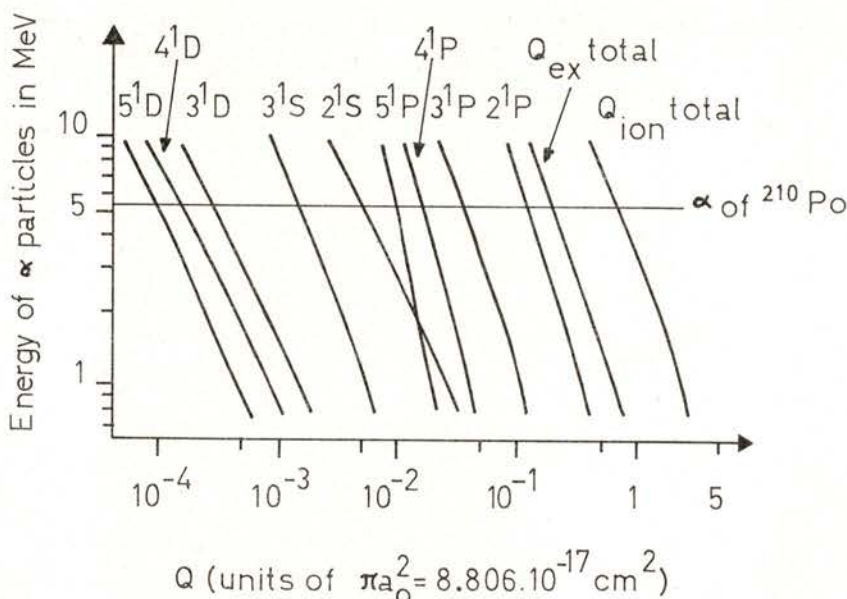


Fig. 4 — Cross sections for excitation and ionization of helium by α -particles (Born approximation) (taken from ref. [33]).

3—EVOLUTION OF THE PRIMARY STATES

3.1 — Spectra observed

After the first stage, during which the primary activated states are created, the medium contains:

- ions, excited or not, mostly singly charged
- excited atoms in several levels
- electrons
- neutral atoms.

In the absence of atomic collisions (gas at very low pressure) excited atoms would deexcite radiatively with a probability inversely proportional to the lifetime of the excited state; but in a gas under pressure, collisions due to thermal agitation become very important. The primary activated atoms participate then in binary and ternary reactions, that compete with the emission of atomic lines, reducing the natural lifetime of the excited states; other species may then be created whose radiative deactivation contributes to the observed radioluminescence [10], [33] - [35].

For the rare gases excited by swift charged particles, most of the irradiated energy lies in the VUV [36]. The specific luminescence $d\varepsilon/dx$, defined as the energy radiated per unit distance along the particle track, is taken very often as a measure of the luminescent yield, as well as the luminescence yield $d\varepsilon/dE$, defined as the energy radiated per unit of energy lost in the medium by the ionizing particle. According to Hurst [36], $d\varepsilon/dx$ for the noble gases is an appreciable fraction of the total stopping power dE/dx . For argon at 400 torr, for instance, under excitation by impact with 4 MeV protons, 29% of the energy lost by the protons appears as emission in the VUV, though this value tends to be lower for the other rare gases.

Recent measurements [37] under 5.5 MeV α -particles impact tend to corroborate this high efficiency for argon. However, if we keep in mind that the number of excited atoms formed on passage of a charged particle through argon is 40% of the number of ions created [20], and taking 26.2 eV as the energy required to form an ion-pair in argon [36], a scintillation efficiency of 29% would require ion-electron recombination as an additional source of excited atoms [36] [37]. Dissociative recombination (see section 3.3.3) can indeed be important and increase significantly the intensity luminescence at high pressures, particularly for the heavier rare gases [38] [39]. At pressures lower than 1 atm, however, particularly for the lighter rare gases, the effect does not seem to be so important [34] [35] [40] though experimental evidence of recombination does exist [41]. Experimental work in this field is scanty. Preliminary work in this Department tends to show that recombination at pressures lower than 1 atm is observable for Kr and Xe but unimportant for Ar, but further work on this subject is to be carried on.

The emission spectrum of a gas observed on the sequence of excitation is characteristic of the gas used, of its pressure and of the excitation process. The emission spectrum of the rare gases (except He) in the VUV presents two reasonably sharp lines in the wavelength region of their first excited states that are resonance radiation and two continua emissions at longer wavelengths, known as the first and the second continuum. The relative amount of those spectral components depends on the pressure as well as on the excitation conditions.

In fig. 5 [42] are represented the VUV spectra for the rare gases under proton impact. The first continuum, that (at very low pressure) exhibits structure, follows immediately the resonance radiation, and the second continuum lies at longer λ . At higher pressure

(a few hundred torr) the second continuum dominates the whole spectrum.

It is now well known that these continua are due to transitions taking place from the lowest excited diatomic levels (excimers) to the repulsive molecular ground state [43].

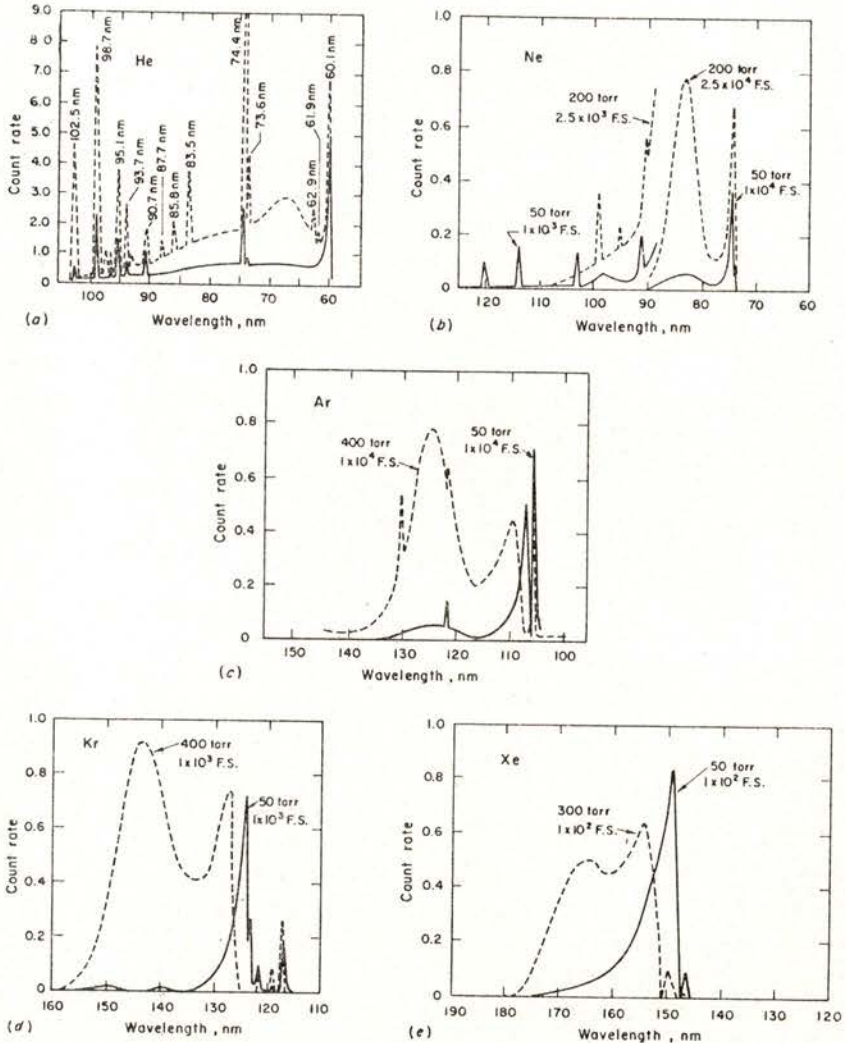


Fig. 5 — Samples of the emission spectra of various noble gases. Note the effect of impurities in He. Data taken at various fractions of full-scale (F. S.) count rates as indicated. (taken from ref. [36]). Reprinted by permission of John Wiley & Sons, Inc.

It was also observed experimentally that the spectra obtained under excitation by charged particles (α , p , e) are identical, irrespective of the kind of particle used, but they differ from the ones obtained on gas discharges [41].

In the visible and infrared, the emission observed so far is atomic in nature and attributed to cascade transitions ending at the $1s$ levels (Paschen), the most important being the transitions $2p-1s$ [3], [43]-[47].

Very few results regarding this spectral region have been published, and the present paper is concerned only with the VUV region, partly for the above mentioned reason but mainly because the VUV is the region potentially more interesting as most of the emission lies on this region. However, a detailed study of the visible and IR regions is essential for a complete understanding of the mechanism of radioluminescence [3].

The physical processes leading to the continuous emission are thought to be understood today, at least qualitatively; however, quantitatively they are not yet fully established and they are the subject of current investigation.

3.2 — *Electronic structure and potential curves of diatomic molecules of rare gases*

The knowledge of the electronic structure of the rare gas dimers is the clue to the understanding of most of the relaxation processes that lead the atomic ions and excited atoms to the lowest bound state of the excimers.

Although the ground state of these species is repulsive (except for a weak Van der Waals binding) [48], all rare gases form positive molecular diatomic ions reasonably stable, and by addition of one electron in a Rydberg molecular orbital, they should originate numerous molecular excited states, bound and unbound in correspondence to the molecular ion.

Potential curves for the rare gases are more or less known from the work of Mulliken, though more qualitatively than quantitatively; lately, better theoretical approximations and more experimental data have contributed to a better understanding of them [18], [25], [26], [49] - [55].

Except for He, electronic structure of rare gases is rather uniform, the main difference being the value of the principal quantum number, n , from the electrons belonging to the outer shell. Most of the systematic differences observed between the atomic spectra of these elements arise from the monotonic increase of the spin-orbital coupling as one goes from Ne to Xe (table III [31] and fig. 6 [56]) [57]; a similar behaviour is expected for the molecular states, so that potential curves for any one should be representative (qualitatively) of the ones for the other gases.

TABLE III — Some energy levels of the rare gases (eV) (from. ref. [56]).

	3P_2	3P_1	3P_0	1P_1	$^2P_{3/2}$	$^2P_{1/2}$	R_2^+
Xe	8.31	8.43	9.44	9.57	12.13	13.43	11.16
Kr	9.91	10.03	10.56	10.64	14.00	14.66	13.00
Ar	11.56	11.62	11.72	11.82	15.75	15.93	14.71
Ne	16.61	16.67	16.71	16.84	21.56	21.66	20.9
He	(2^3S) 19.81	(2^1S) 20.61		(2^1P) 21.21	(2^2S) 24.58		23.3

To a given pair of rare gas atoms in contact in the electronic configuration of the ground state $\dots ns^2 np^6$ (atomic term 1S_0), corresponds the electronic molecular configuration $\dots (\sigma_g ns)^2 (\sigma_u ns)^2 (\sigma_g np)^2 (\pi_u np)^4 (\pi_g np)^4 (\sigma_u np)^2$. This configuration should lead to a repulsive molecular state $^1\Sigma_g^+$, that represents the ground state of the rare gas molecules.

In fig. 7 [48], due to its relevance to the present work, are represented the potential curves of some excited molecular states of Xe_2^* , precisely those curves corresponding to the electronic molecular states that dissociate to the four $1s$ states of Paschen. They are the most relevant to the processes originating the radioluminescence of rare gases [8].

A few points deserve a comment:

1) An important characteristic of the structure of the molecular state of rare gases is the existence of two strongly attractive states

of the excimer, $^3\Sigma_u^+$ and $^1\Sigma_u^+$ lying very close together and dissociating respectively to $^3P_2 + ^1S_0$ and $^3P_1 + ^1S_0$. They are the lowest excited molecular states. They are practically Rydberg states originating from the R_2^+ ion core [48] [58]. The excited electron in $^3\Sigma_u^+$ and $^1\Sigma_u^+$ is loosely bound and has little effect on the molecular binding

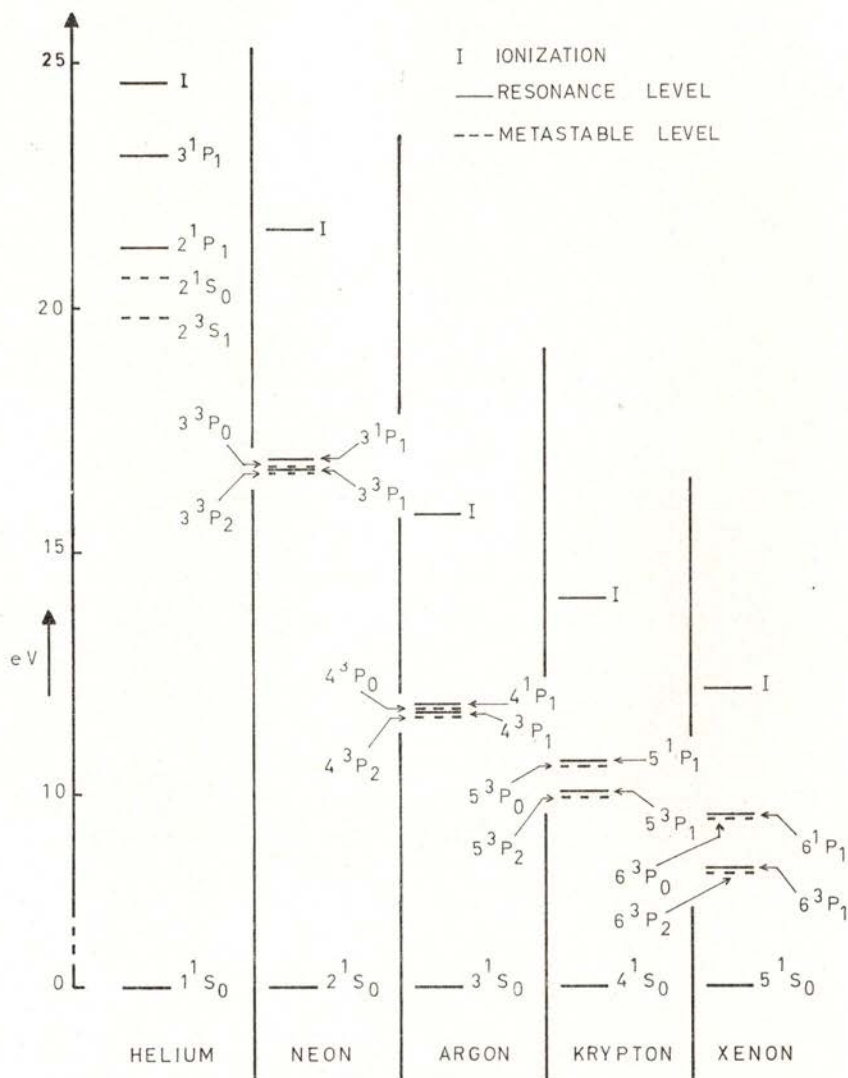


Fig. 6 — Ionization potential and lowest resonance and metastable levels of rare gases (taken from ref. [31]).

energy. Thus the general features of R_2^+ systems are expected to be repeated in various states of R_2^* with respect to binding energy, shape of the potential surface and location of the energy minimum [57]. Theoretical calculations as well as experimental results from scattering measurements [49] [52] [59] tend to confirm this expectation [50] [53] [60].

2) The molecular states $^3\Sigma_g^+$ and $^1\Sigma_g^+$ have potential curves showing small bumps or potential barriers that may eventually pre-

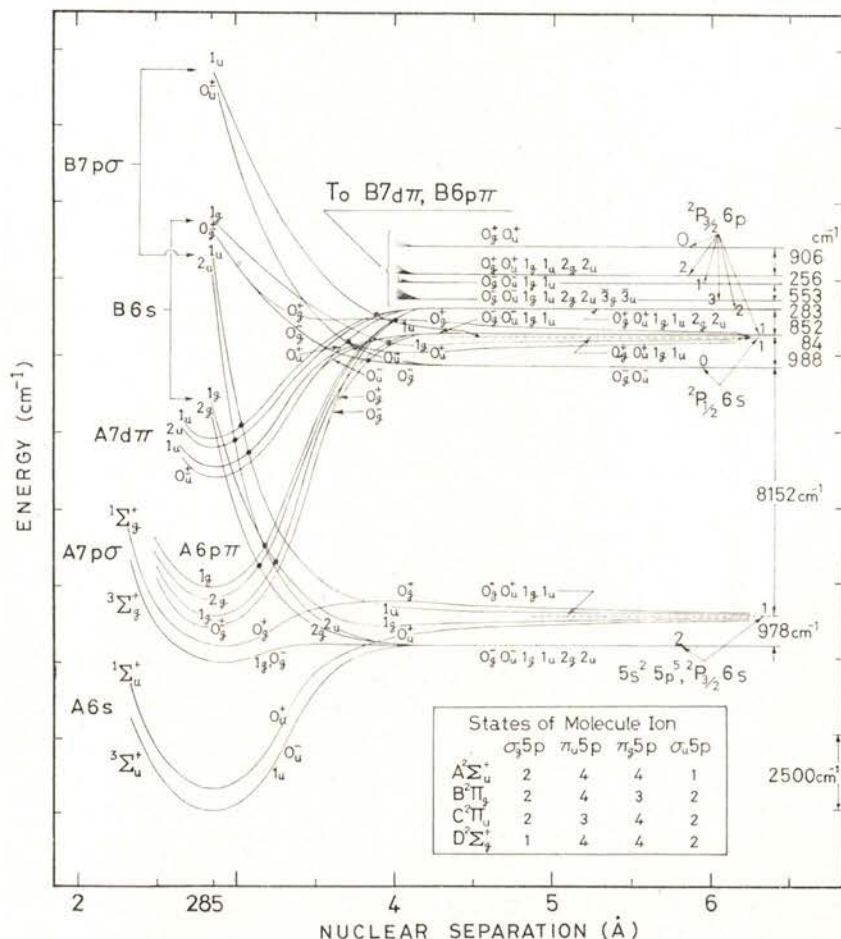


Fig. 7 — Estimated potential curves for some of the lower excited states (Rydberg states) of Xe_2 (taken from ref. [48]).

vent its population by thermal collisions. They are weakly bound states, having small potential wells.

3) In every $1s$ state of Paschen, except at 3P_0 , converge both attractive and repulsive potential curves; the 3P_0 state does not form attractive molecular states through collision with 1S_0 [48].

4) Both ${}^3\Sigma_u^+$ and ${}^3\Sigma_g^+$ have two substates, respectively $(1_u, 0_u^-)$ and $(1_g, 0_g^-)$.

5) 1P_1 can form, through collisions with 1S_0 a strongly attractive state, 0_g^+ and another less attractive state, 0_u^+ , among others.

It is a well known fact that from the interaction of excited atoms with identical atoms on the ground state, continua spectra can be obtained. These are the result of a Franck Condon transition in the diatomic collision complex and are classified as recombination spectra or dissociative spectra according to the stability of the final molecular state. The VUV continua of the rare gases are dissociative continua corresponding to transitions from the excited states of the excimers to the ground state, but the transitions involved occur at internuclear distances very small, where the potential curve is purely repulsive.

According to the selection rules, the transition ${}^1\Sigma_u^+(0_u^+) \rightarrow {}^1\Sigma_g^+(0_g^+)$ is fully allowed, having a large oscillator strength and a small lifetime. The transition ${}^3\Sigma_u^+(1_u) \rightarrow {}^1\Sigma_g^+(0_g^+)$ is also allowed, although with a smaller probability, then longer radiative lifetime. The transition ${}^3\Sigma_u^+(0_u^-) \rightarrow {}^1\Sigma_g^+(0_g^+)$ is forbidden by the selection rules.

The states ${}^3\Sigma_u^+$ and ${}^1\Sigma_u^+$ are so close in energy and the ground state potential curve is so steep that the radiation originating in the transition from those states to the ground state appears as a unique band that cannot be spectroscopically resolved in two components. In argon, for example, according to the last theoretical calculations [52] to estimate the spin-orbital effect, the excimer ${}^1\Sigma_u^+$ lies $600-800 \text{ cm}^{-1}$ ($0.075-0.1 \text{ eV}$) above ${}^3\Sigma_u^+$. Experimental work on the luminescence of gaseous argon following an electrical discharge [61] and excitation by α -particles [62] indicate for the separation ${}^1\Sigma_u^+ - {}^3\Sigma_u^+$ a value of 0.04 eV and 0.052 eV , respectively, while experimental work on solid argon [63] indicates a value of 0.03 eV . According to Jortner et al. [58] the emission spectra of argon is practically identical in the

gaseous, liquid and solid phase. For xenon, Mulliken [48] [64] estimated for the energy gap $^1\Sigma_u^+ - ^3\Sigma_u^+$ a value of 2000 cm^{-1} (0.24 eV), while Lorents [52] [65] calculated a value of 0.2 eV. However, recently Keto [66] estimated from experimental work a value of 0.04–0.08 eV for a temperature range of 200–300 K, in good agreement with the experimental values of 0.03 eV determined by Collier on solid xenon [67] and 0.04 ± 0.02 eV by Zimmerer also on solid xenon [63]. Though not exactly known, the energy difference of those levels is surely a small value that should not vary too much among the heaviest rare gases [65], and contributes less to the bandwidth of the emission than the slope of the repulsive potential curve. Still according to theoretical calculations, for small internuclear distances the energy difference between the 0_u^- and 1_u sublevels of the $^3\Sigma_u^+$ state must be very small: $\text{Ne}_2^* < 1 \text{ cm}^{-1}$, $\text{Ar}_2^* < 3 \text{ cm}^{-1}$, $\text{Kr}_2^* < 25 \text{ cm}^{-1}$, $\text{Xe}_2^* < 80 \text{ cm}^{-1}$ [65]. The value in Xe_2^* agrees with other reports [68]. So, the two emissions $^3\Sigma_u^+ - ^1\Sigma_g^+$ and $^1\Sigma_u^+ - ^1\Sigma_g^+$ cannot be distinguished on an energy base, but they should be distinguishable on a time base, as the radiative lifetimes of both transitions are very different (ns and μs) and this leads to two components in the time decay curves, as experimentally observed.

3.3 — Ion recombination.

Creation and evolution of molecular ions

The ions formed upon the passage of the ionizing radiation through a material [20] [35] [69] have a certain probability of being neutralized by recombination from various processes, from which we stress:

3.3.1 — Radiative recombination

It is a reaction of the kind



The recombination process is described by a recombination coefficient α_e , defined from the equation

$$dn_e/dt = -\alpha_e n_e n_+$$

where n_+ is the ion density and n_e is the electron density.

[Illegible text]

When the state reached is the ground state, the process is just the reverse of photoionization and the value of α_0 can then be deduced. Theoretical calculations (mainly for H) show that cross sections are small, about 10^{-19} cm², leading to recombination coefficients $\alpha_0 = 10^{-12}$ cm³ s⁻¹ [34] [35], so that this process is negligible under the usual experimental conditions ($n_e \sim 10^{11}$ cm⁻³). It is however very important under special conditions, for example in gas nebulae.

3.3.2 — *Recombination ion-electron with participation of a neutral atom*

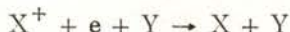
It is a reaction of the kind



or



or



In this process, the excess of internal energy of the recombination collision is removed by a neutral atom or by a molecule of the same or of other kind. At very high pressures, the probability of the presence of a neutral atom in the vicinity of the ion-electron system is large enough so as to make this process important, and its recombination coefficient is larger than the preceding one. This collision is treated in detail in ref. [69]. Defining the recombination coefficient α for this process from the equation

$$dn_+ / dt = -\alpha n_e n_+$$

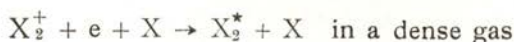
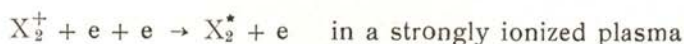
α is now a function of the pressure p . Representative values of α are of the order of 10^{-11} p cm³ s⁻¹ for He [35] reaching a saturation value at a pressure of $\sim 10^4$ torr [69]. For argon at 1 atm, $\alpha \sim 10^{-8}$ cm³ s⁻¹ [34]. If we calculate the fraction of ions neutralized after a period of 10^{-6} s, a value of $\sim 10^{-3}$ is obtained [34]. So, the number of excited atoms formed from the recombination ion-electron upon ternary collisions is also negligible for argon and similarly for the other rare gases except at very high pressures and electronic densities.

3.3.3 — Dissociative recombination

It is a perfectly well known fact that at very low pressures the ions present in a gas are monoatomic, but at high and even moderate pressures the ions that recombine are mostly from the molecular type X_2^+ , formed upon a three-body collision of the type



On the other hand, photoexcitation of rare gases for atomic levels above a threshold result in formation of the diatomic ion (section 3.4.5) and the appearance potential of the molecular ion is lower by about 1–2 eV than the one of the corresponding atomic ions (table III [56]). These molecular ions participate then in recombination reactions of the kind



The excited atoms produced by dissociative recombination can also form excited molecules. The emission of these molecules is the cause of the recombination component of the scintillation light experimentally observed [41] (section 3.1). The dissociative recombination has been recognized since several years as being capable of taking place at a much higher speed than the recombination processes considered so far. It represents probably the main contribution for the recombination rates measured in weakly ionized gases and in the upper atmosphere. The rate equation for this process is

$$\frac{1}{n_+} \frac{dn_+}{dt} = -KN^2$$

K being the rate constant, n_+ the density of X^+ and N the density of atoms X .

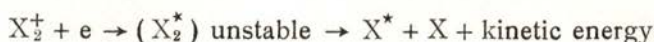
Values of K for the various rare gases have been obtained by several processes. With a typical value of $10^{-31} \text{ cm}^6 \text{ s}^{-1}$ [70] a posi-

tive atomic ion is converted to a molecular ion within a time of $\sim 10^{-8}$ s at a pressure of 1 atm. For argon, $K = 2 \times 10^{-31} \text{ cm}^6 \text{ s}^{-1}$ [71], and the reaction is efficient even at low pressures ($p > 10$ torr) [45]. The fast conversion of atomic ions to molecular ions is followed by the process of dissociative recombination [72]. The rate equation for this process is

$$\frac{1}{N_+} \frac{dN_+}{dt} = -\alpha n_e$$

N_+ being the density of X_2^+ , α the recombination coefficient and n_e the electronic density. References [35] and [72] contain tables of experimental values of α for the rare gases. For a typical value of $10^{-7} \text{ cm}^3 \text{ s}^{-1}$ and an electronic density of 10^{11} cm^{-3} , the rate of recombination for a molecular positive ion is 10^4 s^{-1} [36]. An experimental value of $\sim 10^{-5}$ s is indicated [38] for the recombination of a thermalized electron and an ion in xenon for a range of pressures of 5–50 atm. From the exposed, it is to be expected that when a heavy charged particle creates a large density of ion-pairs in a noble gas at 1 atm pressure, the ions X^+ are converted to X_2^+ in about 10^{-8} s. A much longer time ($10^{-4} - 10^{-5}$ s) is necessary for the molecular ion to recombine with an electron in a process of dissociative recombination. This process becomes very important at high values of pressure and n_e , but it is probably unimportant at low pressure (< 1 atm) (section 3.1).

The mechanism of dissociative recombination



is well illustrated in the work of Bardsley and Biondi [72]. This process is fast only if the final potential curve crosses the one of the diatomic ion near its minimum. This is the case for the rare gases other than He [36]. Fig. 8 shows some relevant potential curves for Ar_2 [52] that illustrate the proposed mechanism [72]. The excited atomic states preferentially populated are the 2p states (Paschen) that in Ar correspond to the $3p^5 4p$ states [73] [74].

The dissociation can be followed by emission of atomic and/or delayed molecular radiation. For He, according to Mulliken, the mole-

cular potential curves resulting from the combination of a ground state atom and an excited atom lie below the ones belonging to the diatomic ion He_2^+ , so that they do not provide a dissociative pathway. The excited molecules formed upon radiative combination can afterwards emit radiation for lower states. This cascade radiation has indeed been observed experimentally [36].

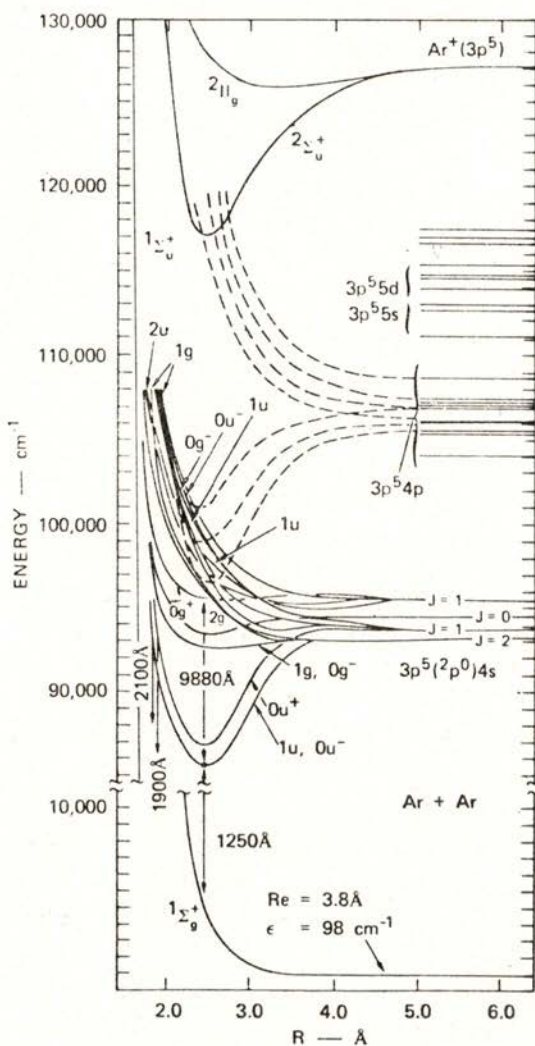


Fig. 8 — Argon intermolecular potential curves (taken from ref. [52]).

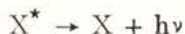
3.4 — Deexcitation of excited atomic states

The primary activated states created in the sequence of the passage of a charged particle through a gas evolve to the excitation levels responsible for the light emission following pathways that depend on the nature of the radiative and collisional processes that take place. It should be stressed that the levels involved in these processes can be obtained through direct excitation, or as a result of cascades or in the sequence of collisions, or through ion-electron recombination, and this makes the kinetics of the process and its dependence on temperature and pressure very complicated.

The main pathways for deexcitation of excited atomic states are summarized below. Numerical values are indicated for argon that is representative of the remaining heavy rare gases.

3.4.1 — Radiative deexcitation

For optical and resonant states emission can take place respectively through cascading or directly to the ground state:



The resonant emission occurs both from 1P_1 , and 3P_1 to S_0 , but it is strongly reabsorbed and reemitted [75] (radiation retention) leading to an increase in the duration of these excited states that may last a few μ s (as the metastables 3P_2 and 3P_0) though its radiative lifetime is of a few nanoseconds [76]. They are then able to participate in collisional deactivation processes.

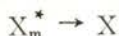
Radiation retention has been treated by Holstein [75]. It depends both on pressure and geometry of the medium. For argon, for example, for a 1.2 cm diameter cell, radiation retention is already well noticeable at pressures < 10 torr [36]. For pressures ~ 400 torr, the transmitted resonance radiation is already negligible due both to radiation retention and collisional competition [77].

The most important cascade transitions for the rare gases are the $2p-1s$. Some of these are tabulated for Ar in ref. [45] together with its wavelength and oscillator strength, when known. Lifetimes for these transitions are of the order of 20–30 ns [78] and they lie, as for the other rare gases, in the infrared, their extreme values of λ being 6677 and 10470 Å. They are easily observed at low pressures, but they are inhibited even at medium pressures through competition with collisional processes. Arai and Firestone [46] still observe the $2p-1s$ emission in argon at 1031 torr, though atomic emission in the visible, IR and UV represents a negligible fraction of the total excitation [33]. According to Bennett et al [79] for argon at 1 atm 90% of the total emission is centered in the second continuum.

The $3p-1s$ transitions, with lifetimes of 100–200 ns [45], lie in the visible, but they are observed only at low pressures. For Ar, λ situates between 3900 and 4700 Å. They are clearly observed [43] at 200 torr.

Above 10 torr all atomic emission from states higher than the appearance potential of the diatomic ion disappear [8], [45]-[47] due to the inhibition of the process by the known Hornbeck-Molnar effect [44] [80] (section 3.4.5).

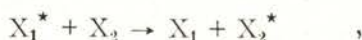
3.4.2 — *Deexcitation by diffusion and collision with the container's walls*



This is the dominant process for metastable states at low pressures. For $p > 100$ torr, collisional processes are already dominant [81].

3.4.3 — *Collisional transfer of electronic energy*

It is a reaction of the kind



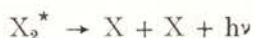
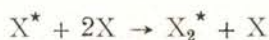
X_1 and X_2 being the same atomic species.

This process is also called a second kind collision. Its cross section σ depends on the energy difference ΔE between X_1^* and

X_2^* . For the 1s states of Ar, $\Delta E \sim 0.1$ eV, $\sigma \sim 10^{-20} - 10^{-21}$ cm², so for $p=1$ atm the frequency of collisions taking place (per particle) is $\sim 10^3 - 10^4$ s⁻¹ [30]. These collisions tend to redistribute the energy of the primary levels among the electronic levels of identical energy, so that the most populated tend to be those of lower energy. However, this coefficient of 'collisional mixture' is small.

For higher levels, for example the 2s levels, $\Delta E \sim kT$ (0.025 eV at room temperature), $\sigma \sim 10^{-15}$ cm² [30], so for $p=1$ atm the number of collisions per second is $2 \cdot 10^9$ and the mixture is efficient [34].

3.4.4 — Formation of excimers through three-body collisions



This process is the dominant one even at relatively low pressures (~ 50 torr), and is more important than second kind collision. Typical values of rate constants for these reactions are $\sim 10^{-32}$ cm⁶ . s⁻¹ [34] so that at 1 atm the frequency of collision is $\sim 7 \times 10^6$ s⁻¹, rather higher than for binary processes.

3.4.5 — Hornbeck-Molnar reactions — Associative ionization processes



Any excited atom whose energy lies between the appearance potential of the molecular ions and the ionization potential of the atom is susceptible of creating, through binary collisions with neutral atoms, a molecular ion [80]. For every atom there is a threshold state; for argon it is the state $3p^5 4d$, and it is observed that every excited state of higher energy can originate the molecular ion [82]. The threshold states for the rare gases are summarized in reference [36] together with the threshold energies. A very recent determination of the appearance potential of Ar_2^+ via associative ionization indicates the value 14.6 ± 0.2 eV [83].

The mechanism of the Hornbeck-Molnar reactions is well understood from the potential curves. However, it should be noted that the

efficiency of Hornbeck-Molnar processes is not unity, as there is experimental evidence [82] that it competes with a reaction of the type



Fig. 9 summarizes all the deexcitation processes mentioned above in a kinetic scheme. Their relative importance depends on the pressure and electronic density conditions, but the origin of the atomic lines and of the continua of the rare gases emission in the VUV is qualitatively understood.

Of course, additional processes of deexcitation occur in the presence of impurities or mixtures of rare gases. These include energy transfer processes [36] [43] [84] [85], formation of mixed excimers or mixed diatomic ions [83], [85] - [88] but this field is out of the scope of the present work.

4 — MECHANISM OF LUMINESCENCE

In the establishment of the mechanisms of luminescence it is particularly relevant the study of the time dependence of the emission spectrum in a large range of pressure. This study, individually made for every line and band of the emission spectrum, would give valuable information for the establishment of the atomic precursors of the continua emission, as well as for the pathways of deexcitation and cross sections for these processes.

Of course, the evolution of the atomic states initially excited will depend strongly on the pressure through the collisional processes taking place. It is common practice to divide kinetic studies into two classes: the low pressure region (≤ 1 atm) and the high pressure region (> 1 atm). The last one, where collisional processes are very fast, is the region of potential interest for lasers. Besides, two further classes can be distinguished, according to the density of deposition of energy or the density of excitation and the resulting electronic density. For low electronic densities ($n_e \leq 10^{10} \text{ cm}^{-3}$) the ion-electron recombination processes are slow relative to the rates of formation and relaxation of the excimers, and as a result only processes originating at neutral excited atoms are interesting. For high electronic densities ($n_e \geq 10^{14} \text{ cm}^{-3}$) not only is recombination a fast process but the thermalized electrons play an important role in the relaxation

This is the situation we shall deal with firstly. At high pressures, there are measurements made in conditions of both high and low electronic density, which we shall consider afterwards.

For low pressures, there is information for every rare gas, though a detailed and exact mechanism for the formation and decay of a large variety of atomic and molecular excited species is still to be established. The behaviour of the heavier rare gases is identical, so we shall take argon as representative of all the others.

Argon presents in the VUV region a sharp resonance line at 1048 Å, the first continuum originating apparently at the other resonance line at 1067 Å, and a second continuum, broad, roughly gaussian, centered at 1270 Å.

At very low pressures (< 10 torr) only the two resonance lines are observed, but at about 25 torr the two continua emissions are well noticeable [8] [89]. As the pressure increases, the second continuum tends to dominate the whole spectrum, this being the situation at a few hundred torr.

Work done by Michaelson and Smith [53] at very low pressures (4-20 torr) and low temperatures ($125 \text{ K} < T < 200 \text{ K}$), showed that the first continuum has structure and begins at 1074 Å, the energy of the forbidden transition $^3P_2 - ^1S_0$. Recently, Tanaka et al [54] [55] studied the emission spectra of the argon dimer in the pressure range 0.1 - 70 torr. They observed, in addition to the second continuum, four emission band systems. According to them, the so called first continuum could be a combination of these.

4.1 — The origin of the two continua

It has been generally accepted, according to a proposition by Mulliken based on theoretical considerations, that the first continuum corresponds to transitions taking place from the higher vibrational levels of $^1\Sigma_u^+$ and $^3\Sigma_u^+$, the molecular states related to the lowest atomic states 3P_1 and 3P_2 , while the second continuum takes place from the vibrationally relaxed level ($\nu=0$) of those molecular states to the same repulsive ground state $^1\Sigma_g^+$ [43]. The transitions from the upper vibrational levels occur mainly near the classical turning point on the attractive branch of the potential curve [54]. However, according to Tanaka et al [54] [55], three of the four observed emission band systems in the region of the first continuum could be attributed to

transitions from $^1\Sigma_u^+$, $^3\Sigma_u^+$ and B 5 p σ (0_u^+) to the repulsive ground state, while the origin of the fourth one is still unknown. This being so, the origin of the first continuum is not clear at this time [54].

Table IV lists some experimental values of lifetimes for both $^1\Sigma_u^+$ and $^3\Sigma_u^+$ [52].

TABLE IV — Radiative lifetimes of excimer states (mainly taken from ref. [52])

Excimer	$^1\Sigma_u$ (ns)	$^3\Sigma_u$ (μ s)	Ref.
Ne ₂ *	—	5.1	[7]
	2.8	11.9	[107]
	—	12 ± 6	[65]
Ar ₂ *	—	6.62	[8]
	—	2.8	[41]
	—	3.7	[92]
	4.2 ± 0.1	3.2 ± 0.3	[98]
	—	4.0 ± 2.0	[65]
Kr ₂ *	—	3.22	[8]
	—	1.7	[92]
	—	0.3	[108]
	—	0.36 ± 0.16	[65]
	—	0.35	[8]
Xe ₂ *	5.5 ± 1.0	0.096 ± 0.005	[98]
	—	0.140 ± 0.05	[65]
	6.22 ± 0.80	0.100 ± 0.002	[66]

4.2 — Atomic precursors of the excimers

4.2.1 — Low pressure conditions ($\ll 1$ atm)

Although it is generally accepted today that both continua have their origin at $^1\Sigma_u^+$ and $^3\Sigma_u^+$, and experimental values of the radiative lifetimes of these states are known with a reasonable degree of agreement, there are still some doubts as to the mechanism of their formation, i.e., on their atomic precursors and its evolution to those molecular states. There are nevertheless a set of experimental observations that, together with theoretical considerations, allow a few conclusions to be drawn, forming a good support for the elaboration

of a plausible mechanism of evolution of the atomic precursors of the radiative excimers, as summarized in fig. 10. This table deserves a few comments regarding the participation of the four 1s levels:

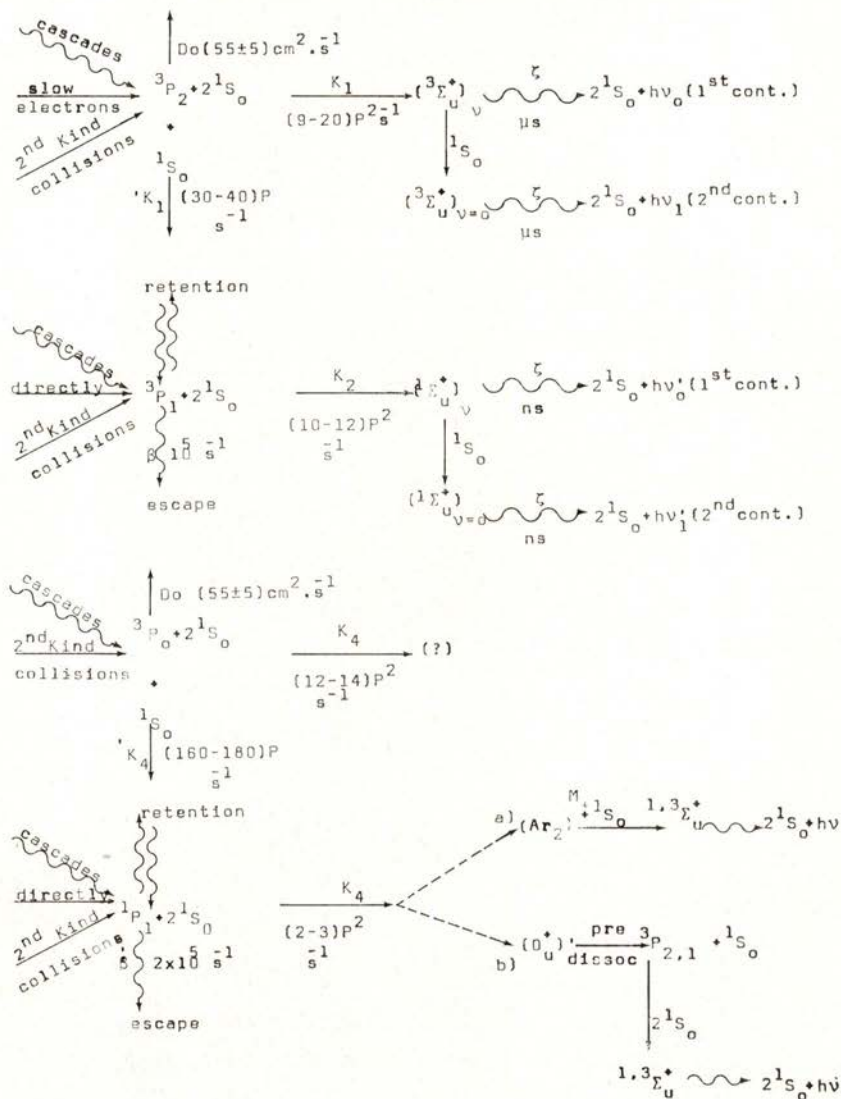


Fig. 10 — Schematic diagram of the creation of the lowest excited states of rare gases after charged particles impact and its evolution to the radiative levels of the excimer. Numerical values of rate constants are indicated for argon. 'Do' is the diffusion coefficient. Remaining symbols as referred in text.

1) Participation of 3P_2

a) Theoretical considerations show that 3P_2 is the direct atomic precursor of $^3\Sigma_u^+$, whose dissociation limit is $^3P_2 + ^1S_0$; $^3\Sigma_u^+$ can be formed upon ternary collisions $^3P_2 + 2 ^1S_0$.

Experimental observations show that the evolution of the metastable state 3P_2 takes place indeed by a mechanism involving binary and ternary collisions. Every experimental observation agrees in this point, although the values of the rate constants are widely different as shown in table V. Ternary collisions are dominant even at low pressures.

b) Time dependent measurements made in the sequence of electrical discharges that populate preferentially 3P_2 point to this state as being the main precursor of the radiative excimers, as the decay rate of the continua is consistent with the rate of disappearance of 3P_2 , i. e., the rate of production of $^3\Sigma_u^+$ agrees well with the rate of disappearance of 3P_2 at low pressures (up to 50 torr) [41], [66], [90]-[93]. According to Michaelson and Smith [53] the first continuum decays at a rate comparable to that of 3P_2 . For $p > 50$ torr, three body collisions involving the other atomic states feeding the excimer levels become increasingly important [93], and that relationship is blurred.

c) On excitation under fast heavy charged particles, 3P_2 is not directly excited. Its importance under these conditions is certainly much lower than under discharges, where it is the most populated of the 1s states due to the high proportion of slow electrons, but its population cannot nevertheless be ignored as 3P_2 can be populated by three main processes:

- on the sequence of radiative cascades from the excited states 2p (and in a less extent from 3p),
- collisions of the second kind,
- collisions with slow electrons

2) Participation of 3P_1

Theoretical considerations show that 3P_1 is the direct atomic precursor of $^1\Sigma_u^+$, whose dissociation limit is $^3P_1 + ^1S_0$; $^1\Sigma_u^+$ can be

TABLE V — Collisional rate constants for argon

Reaction	Experimental values of K						
K_1 ${}^3P_2 + 2\,{}^1S_0 \rightarrow \text{Products}$	9	13.5	20 ± 2	7.6 ± 0.5	8.3	18.0 ± 0.2	9 20 5.2
Ref.	[113]	[114]	[91]	[115] [116]	[92]	[93]	[117] [118] [94]
K'_1 ${}^3P_2 + {}^1S_0 \rightarrow \text{Products}$	40		31 ± 6	29		45 ± 5	60 78
Ref.	[113]		[91]	[115] [116]		[93]	[114] [119] [120]
K_2 ${}^3P_1 + 2\,{}^1S_0 \rightarrow \text{Products}$	10.6	12.5	10	3.5	21.4		
Ref.	[94]	[89]	[93]	[98]	[118]		
K_3 ${}^3P_0 + 2\,{}^1S_0 \rightarrow \text{Products}$	12.0						
Ref.	[91]						
K'_3 ${}^3P_0 + {}^1S_0 \rightarrow \text{Products}$	160						
Ref.	[91]						
K_4 ${}^1P_1 + 2\,{}^1S_0 \rightarrow \text{Products}$			2.20 ± 0.05		11.4		
Ref.			[41] [121]		[118]		

K ($\text{cm}^3 \text{s}^{-1}$) = K' ($\text{torr}^{-1} \text{s}^{-1}$) · 760/L, K ($\text{cm}^3 \text{s}^{-1}$) = K' ($\text{torr}^{-2} \text{s}^{-1}$) · (760/L)², L = Loschmidt number (2.6871×10^{19} at cm^{-3})

formed upon ternary collisions ${}^3P_1 + 2 {}^1S_0$, that compete with the resonance emission for the deexcitation of 3P_1 . Experimental observations confirm that the deexcitation of 3P_1 occurs indeed by radiative emission and by ternary collisions [41] [93] [94].

3) Participation of 3P_0

According to Mulliken, 3P_0 does not form, upon collision, stable molecular states, as it forms only O_g^- and O_u^- . However, its destruction, occurs also partly by two- and three-body collisions [91]. Its eventual participation in the process is not clear and it has not been included in a kinetic scheme so far, as under swift charged particle excitation its importance is much less than that of 3P_2 due to its much smaller population, although recent work [95] tends to show that 3P_0 is more populated than it is generally supposed to be.

4) Participation of 1P_1

The excited states 1P_1 , bound to the ground state by the largest oscillator strength are the most populated under fast charged particle excitation. Its deexcitation must include some form of emission. The intensity of its resonant emission decreases strongly with increasing pressure, and this decrease is accompanied by an increase of the continuum intensity [36]. There is a qualitative relation between the intensities of both emissions, well revealed in the spectra of fig. 5. Though 1P_1 does not form directly ${}^{1,3}\Sigma_u^+$ upon collision with ground state atoms, there are several reasons that point out to considering 1P_1 as an important precursor of the continuous emission:

a) Fig. 11 [41] shows the time evolution of the second continuum of argon at several pressures, as well as the resonant radiation of 1P_1 under excitation with charged particles. Regarding the continuum it is interesting to remark that its intensity goes on increasing after the excitation pulse has ended and the peak is reached only about 0.3-10 μ s after the end of the excitation pulse. This time delay decreases with increasing pressure. It can be seen as well that the decay of the resonance radiation takes place within the rising time of the second continuum, suggesting [41] the possibility of that atomic state being

one of the contributors to the formation of the continuum. This suggestion is corroborated by the observation that the time interval necessary to reach the peak of the 1250 Å continuum decreases with increasing pressure, and this may relate to the decreasing lifetime of 1P_1 at high pressures. However, the time delay of the peak emission seems to suggest that this does not occur only through Franck-Condon

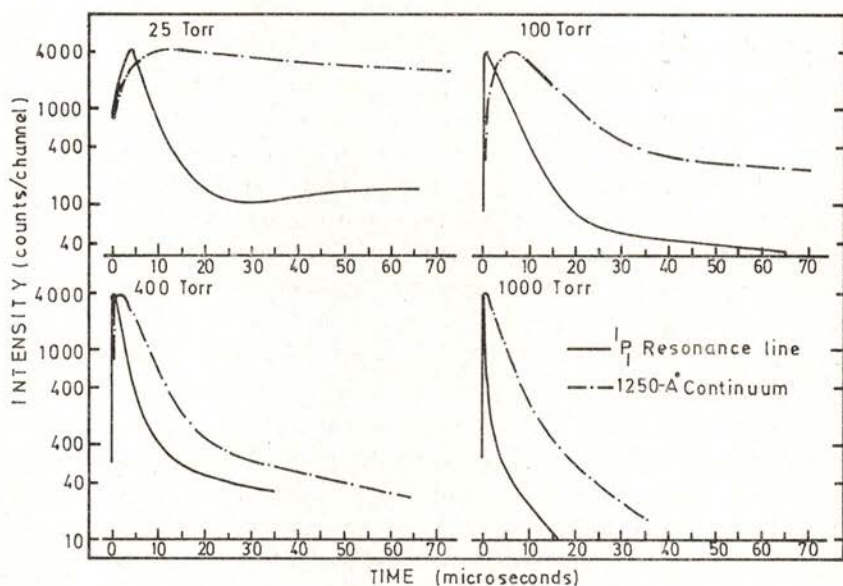


Fig. 11 — Comparison of time dependence of the 1P_1 resonance level and the 1250 Å continuum from 25 to 1000 torr.

— 1P_1 resonance line
 - · - · - 1250 Å continuum

25 torr data taken with 0.4 μ s excitation; 100 to 1000 torr data taken with 0.5 μ s excitation (from ref. [41]).

emission, but it also depends on a process of collision that transfers energy from a state initially excited to an intermediate state [36]. For $p > 3$ atm the rising time of the second continuum cannot be determined as it is of the same order of the excitation pulse.

b) 1P_1 does not form, upon direct collision with 1S_0 , the radiative states $^1,^3\Sigma_u^+$ of the excimer [48]. However, it can form a 0_u^+ state,

almost unstable, having a small potential well [36]. This state could radiate to the ground state $^1\Sigma_g^+$ through an allowed transition whose wavelength should be shorter than $^3P_2 - ^1S_0$. Emission band system III from Tanaka et al [54] [55] beginning at 1048 Å could possibly account for it. However, most of the VUV continuous emission comes from the $^{1,3}\Sigma_u^+$ radiative states [36]. This means that, if the 0_u^+ state is formed upon collision, it must also decay in another way. Two channels have been suggested to account for the participation of 1P_1 in the formation of radiative excimers, as shown schematically in fig. 10: channel a) proposed by Hurst et al [36] consists in the formation of a metastable molecule that further collisions would convert to a radiative molecule. This scheme does not seem to be corroborated from the potential curves. Besides, the rising time of the second continuum is too fast to occur via a metastable molecule. Scheme b) [36] [96], consistent with the potential curves, is more likely to describe the correct mechanism. The 0_u^+ state formed from 1P_1 can predissociate through potential curve crossing to the atomic levels $^3P_{1,2}$, this predissociation being followed by the formation of a new molecule. This mechanism could explain (at least qualitatively) the observed behaviour in the time evolution of the continua and of 1P_1 and its dependence on pressure, but it still awaits experimental confirmation.

Besides the channels indicated in fig. 10, that must contain the main modes of formation of radiative excimers, others have been suggested starting from 3P_2 and 1P_1 . Some of these are indicated in fig. 12. However, it must be stressed that they all await experimental confirmation, that must include measurements in the infrared region that, to our knowledge, have not been tried so far.

These mechanisms deserve a few comments:

1) Measurements made under certain conditions following electrical discharges in rare gases seem to suggest that 3P_2 could be related to the continuous emission originating from $^1\Sigma_u^+$: if this suggestion is correct, mechanism 1 in fig. 12 could explain it; 3P_2 does not form $^1\Sigma_u^+$ upon direct collision but it could form this state from an intermediate state. Through the collision, a molecular state dissociating to $^3P_2 + ^1S_0$ could be formed and upon potential curve crossing it could go to a high vibrational level of $^1\Sigma_u^+$, the radiative state [53]. This intermediate state could be the $^3\Sigma_g^+$ state. The presence of a third body could remove symmetry restrictions. Tanaka and Yoshino [10] studied the higher vibrational levels of $^3\Sigma_u^+$ and

$^1\Sigma_u^+$ and their results indicate that there is a vibrational level of $^1\Sigma_u^+$ only 14 cm^{-1} above the dissociation limit $^3P_2 + ^1S_0$.

2) The second channel in fig. 12 suggests another way of participation of 1P_1 that still needs experimental confirmation. To our knowledge, the infrared studies that it involves have not been done so far.

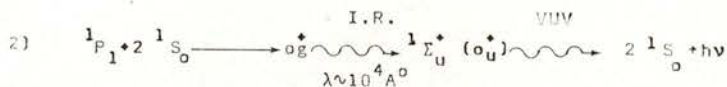
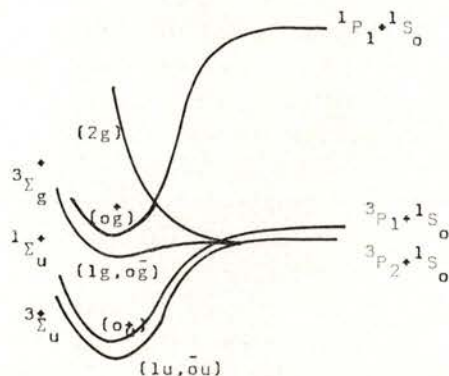
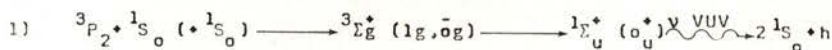


Fig. 12 — Additional pathways of formation of the $^1\Sigma_u^+$ radiative level.

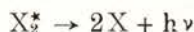
It must be emphasized that the analysis of the experimental results including all possible precursors, or at least 3P_1 , 3P_2 , 1P_1 has not been attempted so far, and it is a task calling for urgent realization. The analysis done by Hurst et al [41] (including only 3P_2 and 1P_1 via channel a)) and that of Mortier et al [92] [97] (including 3P_2 and 3P_1) cannot be considered conclusive.

4.2.2— *High pressure conditions (>1 atm)*

At high pressure, the high collision frequency establishes a vibrational relaxation in a short time relative to the radiative lifetime of the excited states. The only emission to be observed is the second continuum, as expected. Formation of excimers through ternary collisions is also very fast relatively to the radiative decay of the excited atoms.

4.2.2.1— *Low electronic density ($n_e \ll 10^{10} \text{ cm}^{-3}$)*

Fig. 13 summarizes the dominant reactions in the system under these conditions. The kinetics of the second continuum emission is simple and well represented by the equations



Relevant work is due to Keto et al [66] [98] under electron impact, for $1 \text{ atm} < p < 32 \text{ atm}$. From the analysis of the rising and decay of the radiation following an excitation pulse, the rate constants were obtained. For argon they are displayed on fig. 13. The two excimers radiate independently, so their collisional mixture is negligible. An upper limit for the cross section of the reaction



was established as $6 \cdot 10^{-18} \text{ cm}^2$

4.2.2.2. — *High electronic density ($n_e > 10^{14} \text{ cm}^{-3}$)*

This situation has been treated in great detail by Lorents [52] [65]. The main processes taking place are summarized in fig. 14. The electronic density is high and the recombination ion-electron takes place at a rate comparable to the kinetics of neutral species and is an important source of excited atoms. Under the conditions

stated, all initial ionization and excitation decay very rapidly to the levels of the excimers and the system can radiate most of the available energy in a very short time.

As Lorents points out, reactions involving collision of two excited species (either dimeric or monoatomic) or absorption of the

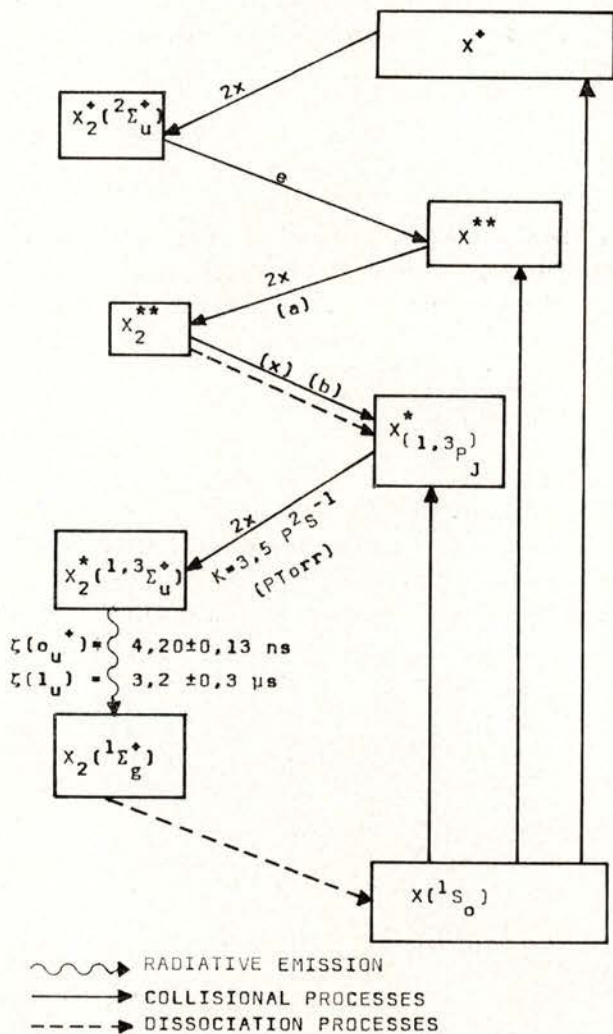


Fig. 13 — Schematic diagram of the collision kinetics for dense rare gases at low electronic densities ($p > 1 \text{ atm}$; $n_e \ll 10^{10} \text{ cm}^{-3}$) following charged particles impact. Numerical values of rates constants are indicated for argon.

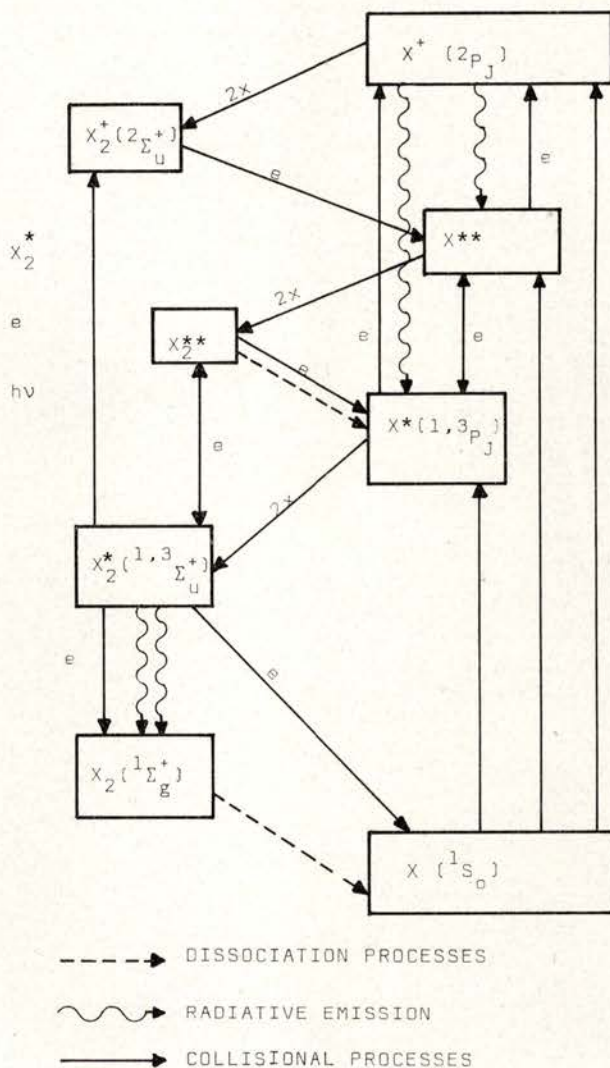


Fig. 14 — Schematic diagram of collision kinetics for dense rare gases at high electronic densities ($p > 1$ atm; $n_e > 10^{14}$ cm $^{-3}$) following electron impact.

excimer radiation by an excited atom or excimer resulting in ion-pair formation may be significant. Rate constants estimated for some of these reactions are indicated in table VI.

TABLE VI — Rate constants for some reactions in argon and xenon

Reaction	Ar	Ref.	Xe	Ref.
$X^* + 2X \rightarrow X_2^* + X$	${}^3P_2 (1.6 - 0.5) \times 10^{-32} \text{ cm}^6 \text{ s}^{-1}$ ${}^3P_1 (1.7 - 0.3) \times 10^{-32} \text{ cm}^6 \text{ s}^{-1}$ ${}^3P_0 \quad 1.0 \times 10^{-32} \text{ cm}^6 \text{ s}^{-1}$ ${}^1P_1 (0.9 - 0.17) \times 10^{-32} \text{ cm}^6 \text{ s}^{-1}$	} See Table V	$4 \times 10^{-32} \text{ cm}^6 \text{ s}^{-1}$ $\sim 5 \times 10^{-32} \text{ cm}^6 \text{ s}^{-1}$	[67] [65]
$X_2^* \rightarrow 2X + h\nu$	${}^1\Sigma_u^+ \zeta = 4.20 \pm 0.13 \text{ ns}$ ${}^3\Sigma_u^+ \zeta = 2.88 \pm 0.06 \mu\text{s}$ $k \ll 10^{-13} \text{ cm}^3 \text{ s}^{-1}$ $< 10^{-14} \text{ cm}^3 \text{ s}^{-1}$ $-k \ll 10^{-15} \text{ cm}^3 \text{ s}^{-1}$		[66] [66] [52] [66] [8]	$\zeta = 6.22 \pm 0.80 \text{ ns}$ $\zeta = 100 \pm 2 \text{ ns}$
${}^1\Sigma_u^+ + X \xrightleftharpoons[k]{k} {}^3\Sigma_u^+ + X$	$< 1.8 \times 10^{-15} \text{ cm}^3 \text{ s}^{-1}$ $(2.5 - 1.5) \times 10^{-31} \text{ cm}^6 \text{ s}^{-1}$	[66] [111] [112]	$(1.25 \pm 0.68) \times 10^{-13} \text{ cm}^3 \text{ s}^{-1}$ $(6.6 \pm 1.08) \times 10^{-15} \text{ cm}^3 \text{ s}^{-1}$ $2.5 \times 10^{-31} \text{ cm}^6 \text{ s}^{-1}$	[66] [66] [66]
$X^+ + 2X \rightarrow X_2^+ + X$	$3,4 T_e^{-0.67} \times 10^{-5} \text{ cm}^3 \text{ s}^{-1}$ $(7 \times 10^{-8} \text{ cm}^3 \text{ s}^{-1} \text{ at } 10^4 \text{ K})$	[72]	$(2.0 - 3.6) \times 10^{-31} \text{ cm}^6 \text{ s}^{-1}$ $2.4 T_e^{-0.5} \times 10^{-5} \text{ cm}^3 \text{ s}^{-1}$ $(2 \times 10^{-7} \text{ cm}^3 \text{ s}^{-1} \text{ at } 10^4 \text{ K})$	[109] [110] [72]
$X^{**} + 2X \rightarrow X_2^{**} + X$			$10^{-31} \text{ cm}^6 \text{ s}^{-1}$	[52]

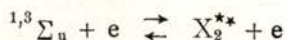
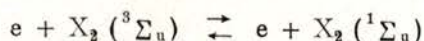
TABLE VI — (Cont.)

Reaction	Ar	Ref.	Xe	Ref.
$X_2^{**} + (X) \rightarrow X^* + X + (X)$			$10^{-11} \text{ cm}^3 \text{ s}^{-1}$	[52]
$X_2^* + X_2^* \rightarrow 2X + X_2^+ + e$	$\sim 10^{-9} \text{ cm}^3 \text{ s}^{-1}$	[52]	$\sim 0.5 \times 10^{-9} \text{ cm}^3 \text{ s}^{-1}$	[52]
$X_2^* + hv \rightarrow X_2^+ + e$	$\sigma \sim 10^{-19} \text{ cm}^2$	[65]	$\sigma \sim 10^{-18} \text{ cm}^2$	[65]
$X(^3P_J) + e \xrightarrow{k'} X(^3P'_J) + e$	(a) $10^{-6} - 10^{-7} \text{ cm}^3 \text{ s}^{-1}$	[52]	$10^{-6} - 10^{-7} \text{ cm}^3 \text{ s}^{-1}$	[52]
$^3\Sigma_u^+ + e \xrightarrow{k'} ^1\Sigma_u^+ + e$	(a) $10^{-6} - 10^{-7} \text{ cm}^3 \text{ s}^{-1}$	[52]	$10^{-6} - 10^{-7} \text{ cm}^3 \text{ s}^{-1}$	[52]
$X_2^{**} (^3\Sigma_u^+) + e \xrightarrow{k'} X_2^{**} + e$	(a) $10^{-6} - 10^{-7} \text{ cm}^3 \text{ s}^{-1}$	[52]	$10^{-6} - 10^{-7} \text{ cm}^3 \text{ s}^{-1}$	[52]
$X_2^{**} + e \rightarrow X_2^* + e$	(a) $10^{-6} - 10^{-7} \text{ cm}^3 \text{ s}^{-1}$	[52] [65]	$10^{-6} - 10^{-7} \text{ cm}^3 \text{ s}^{-1}$	[52]
$X_2^* + e \rightarrow X_2^+ + 2e$	(a) $10^{-6} - 10^{-7} \text{ cm}^3 \text{ s}^{-1}$	[52] [65]	$10^{-6} - 10^{-7} \text{ cm}^3 \text{ s}^{-1}$	[52] [65]
$X_2^* + e \rightarrow 2X + e$	(a) $10^{-7} - 10^{-8} \text{ cm}^3 \text{ s}^{-1}$	[52] [65]	$10^{-7} - 10^{-8} \text{ cm}^3 \text{ s}^{-1}$	[52]
$X_2^{**} \rightarrow X^* + hv$	$\sim 10^{-9} \text{ cm}^3 \text{ s}^{-1}$	[52] [65]	$\sim 10^{-9} \text{ cm}^3 \text{ s}^{-1}$	[52]
$X_2^{**} + X \rightarrow X^+ + X + e$			$1.5 \times 10^7 \text{ s}^{-1}$	[65]
$X_2^{**} + X_2^{**} \rightarrow X_2^+ + 2X + e$			$5 \times 10^{-10} \text{ cm}^3 \text{ s}^{-1}$	[65]
$X_2^* + X^+ \rightarrow X^+ + X + e$			$5 \times 10^{-10} \text{ cm}^3 \text{ s}^{-1}$	[65]
			$5 \times 10^{-10} \text{ cm}^3 \text{ s}^{-1}$	[65]

(a) Estimate dependent on T_e (ref. [52]).

A double star indicates a highly excited state.

Another kind of peculiar reactions, that may become very important are inelastic and superelastic collisions with excited species. Reactions such as



originate a mixing of states and have rate constants of the order of $10^{-6} - 10^{-7} \text{ cm}^3 \text{ s}^{-1}$. Electronic states with energy differences of the order of 0.1 eV are completely mixed up and can be regarded as a unique state relaxing through the fastest way available for any one [52]. The excimer can be formed from $^3,^1P_{2,1,0}$ but only the highest rate of formation is observed.

Experimental data for xenon and argon [52] [66] [99] [100] show that there is only a radiative lifetime that goes to a constant value as the pressure increases: a similar behaviour is expected for the other rare gases [52] and this is a result of the effect of the mixing reactions just mentioned.

The rate constants corresponding to the various reactions for this kinetic model for Xe and Ar are listed in table VI. This table was mainly taken from ref. [52] [65]. For some rate parameters, there are experimental values. For others, the values indicated are computed from the kinetic scheme displayed on fig. 14. Of course, cross sections of interaction of electrons with excited atoms or molecules are not known, and so there is still a lot of work to do in order to establish reliable rate constants for many reactions. Nevertheless, a reasonable understanding of the processes concerned is now believed to have been achieved.

5 — CONCLUDING REMARKS

As a conclusion, it must be emphasized as it comes out from the exposed, that the physical processes involved in the main mechanisms of production of both continua emission are thought to be known; however, their atomic precursors are not unequivocally established nor are the specific rate constants and/or cross sections of the

reactions concerned, and for this reason a detailed and safe mechanism is still to be established. Very little spectroscopic information exists on the higher atomic excited states of the rare gases, the same being true for the higher excited states of the excimers. Mulliken has suggested [48] that radiative transitions could occur from higher excited molecular states (formed upon collision from the excited levels $2p$ or even $3p$) to the levels $^3\Sigma_u^+$ and $^1\Sigma_u^+$. Experimental observations of these transitions do not practically exist [52] [99] except for the work of Firestone [46]. We must also remark that two other continua emission have been reported for argon by several authors, at 1900 \AA and 2200 \AA , weaker than those in the VUV [33], [57], [101] - [104].

While the first one is believed to belong to some impurity emitting in that region [99], the second one seems to have in fact a molecular origin, but conclusive studies are still lacking [101] [105]. It could be a recombination continuum [99] [105]. Huffman et al [106] observed a weak continuum emission at 850 \AA which could correspond to direct emission from Ar_2^{**} to the repulsive ground state. To a clear understanding of the full process is essential more experimental work in a wider spectral region, including the $2p-1s$ and $3p-1s$ spectral lines.

We thank Prof. A. Policarpo for useful discussions.

Permission granted for the reproduction of the figures and tables taken from published work, as signaled 'in loco', is gratefully acknowledged.

Financial support given by Instituto Nacional de Investigaçao Ciêntifica (Centro de Física da Radiação e dos Materiais) is fully acknowledged.

REFERENCES

- [1] J. B. BIRKS, *The Theory and Practice of Scintillation Counting*, Pergamon 1964.
- [2] C. K. RHODES, *IEEE J. Quant. Elect.* **QE9**, 647 (1973).
- [3] P. E. THIESS, G. H. MILEY, *IEEE Trans. Nucl. Sci.*, **NS21**, 125 (1974).
- [4] R. D. ANDRESEN, E. A. LEIMANN, A. PEACOCK, *Nucl. Instr. and Meth.* **140**, 371 (1977).

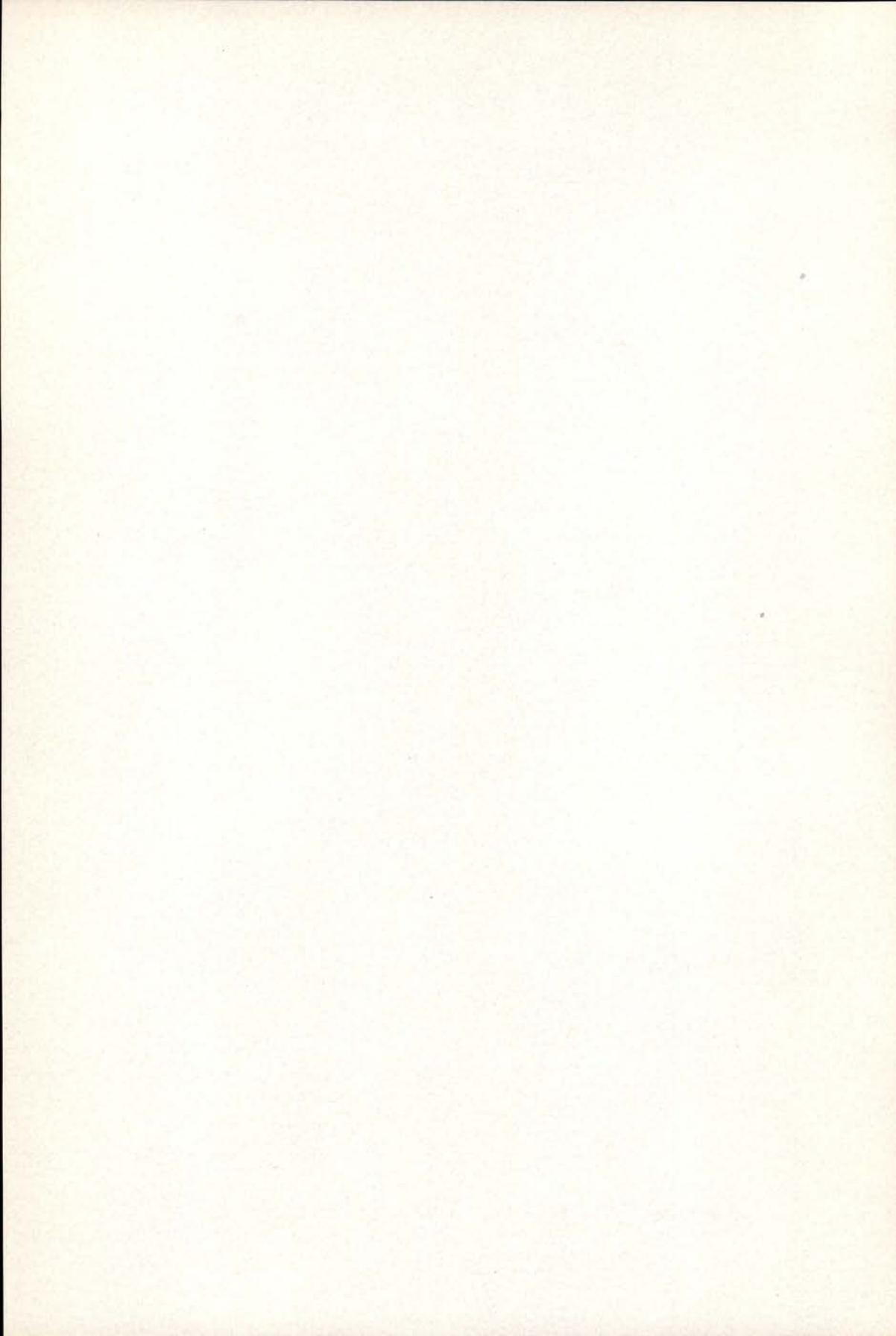
- [5] J. R. McNEELY, G. S. HURST, E. B. WAGNER, M. G. PAYNE, *J. Chem. Phys.*, **63**, 2717 (1975).
- [6] T. E. STEWART, G. S. HURST, D. M. BARTELL, J. E. PARKS, *Phys. Rev.*, **A3**, 1991 (1971).
- [7] P. K. LEICHER, *Phys. Rev.*, **A8**, 815 (1973).
- [8] T. OKA, K.U.S. RAMA RAO, J. L. REDPATH, R. F. FIRESTONE, *J. Chem. Phys.*, **61**, 4740 (1974).
- [9] L. G. CHRISTOPHOROU, Atomic and Molecular Radiation Physics, Wiley-Interscience, 1971.
- [10] Y. TANAKA, K. YOSHINO, *J. Chem. Phys.*, **53**, 2012 (1970).
- [11] G. A. ERSKINE, *Proc. Roy. Soc.*, **A224**, 362 (1954).
- [12] L. R. PETERSON, J. E. ALLEN JR., *J. Chem. Phys.*, **56**, 6068 (1972).
- [13] D. E. GERHART, *J. Chem. Phys.*, **62**, 821 (1975).
- [14] M. INOKUTI, Y. K. KIM, R. L. PLATZMAN, *Phys. Rev.*, **164**, 55 (1967).
- [15] M. INOKUTI, Y. ITIKAWA, J. E. TURNER, *Rev. Mod. Phys.*, **43**, 297 (1971); *ibid*, **50**, 23 (1978).
- [16] E. EGGARTER, *J. Chem. Phys.*, **62**, 833 (1975).
- [17] U. FANO, *Radiat. Res.*, **64**, 217 (1975).
- [18] C. E. KLOTS, H. WRIGHT, *Int. J. Radiat. Phys. Chem.*, **2**, 191 (1970).
- [19] J. A. R. SAMSON, F. L. KELLY, «Planetary Physics III: Photoionization Cross Sections of the Rare Gases» Geophysics Corporation of America Report GCA 64-3-N, Washington D. C., 1964.
- [20] R. L. PLATZMAN, *Int. J. Appl. Radiat. Isot.*, **10**, 116 (1961).
- [21] R. L. PLATZMAN, *J. Phys. Rad.*, **21**, 843 (1960).
- [22] R. L. PLATZMAN, *Voltex*, **23**, 372 (1962).
- [23] R. L. PLATZMAN, *Radiat. Res.*, **3**, 340 (1955); *ibid*, **2**, 1 (1955); *ibid*, **17**, 419 (1962); *ibid*, **32**, 383 (1967).
- [24] R. L. PLATZMAN, Radiation Biology and Medicine, ch. 2, Addison-Wesley, Reading, Mass. (1958).
- [25] K. M. SANDO, *Mol. Phys.*, **23**, 413 (1972).
- [26] B. I. SCHNEIDER, J. S. COHEN, *Radiat. Res.*, **59**, 363 (1974).
- [27] D. M. BARTELL, G. S. HURST, E. B. WAGNER, *Phys. Rev.*, **A7**, 1068 (1973).
- [28] E. N. LASSETTRE, A. SKERBARLE, M. A. DILLON, K. J. ROSS, *J. Chem. Phys.*, **48**, 5066 (1968).
- [29] H. BOERSCH, J. GEIGER, H. HELLWIG, *Phys. Letters.*, **3**, 64 (1962).

- [30] N. F. MOTT, H. S. W. MASSEY, *The Theory of Atomic Collisions*, Oxford 1965.
- [31] R. HENCK, Doctoral Thèse (Strasbourg 1966).
- [32] V. SCHMIDT, N. SANDNER, H. KUNTZEMÜLLER, *Phys. Rev.*, **A13**, 1743 (1976).
- [33] W. R. BENNETT JR., *Ann. Phys.*, **18**, 367 (1962).
- [34] R. HENCK, R. VOLTZ, *J. Phys.*, **29**, 149 (1968).
- [35] J. B. HASTEED, *Physics of Atomic Collisions*, Butherworths 1972.
- [36] G. S. HURST, C. E. KLOTS, *Advan. Rad. Chem.*, **5**, 1 (1976).
- [37] J. SEGUINOT, T. Y. YPSILANTIS, *Nucl. Inst. and Meth.*, **142**, 377 (1977).
- [38] B. A. DOLGOSHEIN, V. N. LEBEDENKO, A. M. ROGOZHIN, B. U. RODIONOV, E. N. SHUVALOVA, *Soviet Physics JETP* **29**, 619 (1969).
- [39] S. KONNO, T. TAKAHASHI, *Nucl. Inst. Meth.*, **150**, 517 (1978).
- [40] S. KUBOTA, T. TAKAHASHI, T. DOKE, *Phys. Rev.*, **165**, 225 (1968).
- [41] N. THONNARD, G. S. HURST, *Phys. Rev.*, **A5**, 1110 (1972).
- [42] T. E. STEWART, G. S. HURST, T. E. BORTNER, J. E. PARKS, F. W. MARTIN, H. L. WEIDNER, *J. Opt. Soc. Am.*, **60**, 1290 (1970).
- [43] A. GEDANKAN, J. JORTNER, B. RAZ, A. SZÖKE, *J. Chem. Phys.*, **57**, 3456 (1972).
- [44] P. E. THIESS, Doctoral Thesis (Illinois 1975).
- [45] ODILE DUTUIT, Thèse (docteur 3^{ème} Cycle) (Orsay 1974).
- [46] S. ARAI, R. F. FIRESTONE, *J. Chem. Phys.*, **50**, 4575 (1969).
- [47] P. E. THIESS, G. H. MILEY, *Tran. Am. Nucl. Soc.*, **18**, 70 (1974).
- [48] R. S. MULLIKEN, *J. Chem. Phys.*, **52**, 5170 (1970).
- [49] D. C. LORENTS, R. E. OLSON, G. M. CONKLIN, *Chem. Phys. Letters*, **20**, 589 (1973).
- [50] T. L. GILBERT, A. L. WAHL, *J. Chem. Phys.*, **55**, 5247 (1971).
- [51] I. M. PARSON, P. E. SISK, Y. T. LEE, *J. Chem. Phys.*, **56**, 1511 (1972).
- [52] D. C. LORENTS, *Physica*, **82C**, 19 (1976).
- [53] R. C. MICHAELSON, A. L. SMITH, *J. Chem. Phys.*, **61**, 2567 (1974).
- [54] Y. TANAKA, W. C. WALKER, K. YOSHINO, *J. Chem. Phys.*, **70**, 380 (1979).
- [55] D. E. FREEMAN, K. YOSHINO, Y. TANAKA, *J. Chem. Phys.* **71** 1780 (1979).
- [56] B. BROCKLEHURST, *Radiat. Res. Reviews*, **1**, 223 (1968).
- [57] M. MARTIN, *J. Chem. Phys.*, **54**, 3289 (1971).

- [58] O. CHESHNOVSKY, B. RAZ, J. JORTNER, *Chem. Phys. Letters*, **15**, 475 (1972).
- [59] H. U. MITTMANN, H. P. WEISE, *Z. Naturforsch.*, **29a**, 400 (1974).
- [60] W. ABERTH, D. C. LORENTS, *Phys. Rev.*, **144**, 109 (1966).
- [61] G. KLEIN, M. J. CARVALHO, CRN/CPR 79-2.
Centre de Recherches Nucleaires et Université Louis Pasteur,
Strasbourg.
- [62] M. J. CARVALHO, G. KLEIN, *J. Luminescence*, **18/19**, 487 (1979).
- [63] G. ZIMMERER, *J. Luminescence*, **18/19**, 875 (1979).
- [64] R. S. MULLIKEN, *Radiat. Res.*, **59**, 357 (1974).
- [65] D. C. LORENTS, D. J. ECKSTROM, D. HUESTIS, Excimer Formation
and Decay Processes in Rare Gases.
Final Report MP 73-2, Contract N00014-72-C-0457, SRI Project
2018, Stanford Research Institute, Menlo Park Ca (1973).
- [66] J. W. KETO, R. E. GLEASON Jr., T. D. BONIFIELD, G. K. WALTERS,
F. K. SOLEY, *Chem. Phys. Letters*, **42**, 125 (1976).
- [67] E. COLLIER, International Conference on VUV, Montpellier 1977.
- [68] U. HAHN, N. SCHWENTNER, G. ZIMMERER, *Opt. Communic.*, **21**,
237 (1977).
- [69] H. S. W. MASSEY, E. H. S. BURHOP, H. B. GILBODY, Electronic and
Ionic Impact Phenomena. Oxford University Press.
- [70] E. C. BEATY, P. PATTERSON, 6th Intern. Conf. on Ionization Pheno-
mena in Gases, **1**, SERMA Paris, 289 (1963).
- [71] F. LIU WEI-CHENG, D. C. CONWAY, *J. Chem. Phys.*, **60**, 784 (1974).
- [72] J. N. BARDSLEY, M. A. BIONDI, Advances in Atomic and Molecular
Physics, **6** (1970). Editors D. R. Bates, I. Estermann. Academic
Press, New York.
- [73] J. Y. SHIU, M. A. BIONDI, *Phys. Rev.*, **A17**, 868 (1978); *ibid* **A16**,
1817 (1977).
- [74] Y. J. SHIU, M. A. BIONDI, D. P. SIPLER, *Phys. Rev.*, **15**, 494 (1977).
- [75] T. HOLSTEIN, *Phys. Rev.*, **72**, 1212 (1947); *ibid*, **83**, 1159 (1951).
- [76] G. M. LAWRENCE, *Phys. Rev.*, **175**, 40 (1968).
- [77] P. G. WILKINSON, *Can. J. Phys.*, **45**, 1715 (1967).
- [78] R. A. NODWELL, J. MEYER, T. JACOBSON, *J. Quant. Spectrosc.*
Radiat. Transfer, **10**, 335 (1970).
- [79] J. R. BENNETT, A. J. L. COLLINSON, *J. Phys.*, **B2**, 571 (1969).
- [80] J. A. HORNBECK, J. P. MOLNAR, *Phys. Rev.*, **84**, 621 (1951).

- [81] G. S. HURST, T. E. STEWART, J. E. PARKS, *Phys. Rev.*, **A2**, 1717 (1970).
- [82] R. E. HUFFMAN, D. H. KATAYAMA, *J. Chem. Phys.*, **45**, 138 (1966).
- [83] H. HELM, K. STEPHAN, T. D. MÄRK, *Phys. Rev.*, **A19**, 2154 (1979).
- [84] O. CHESHNOVSKY, B. RAZ, J. JORTNER, *J. Chem. Phys.*, **59**, 3301 (1973).
- [85] Y. TANAKA, K. YOSHINO, D. E. FREEMAN, *J. Chem. Phys.*, **62**, 4484 (1975).
- [86] D. E. FREEMAN, K. YOSHINO, Y. TANAKA, *J. Chem. Phys.*, **67**, 3462 (1977).
- [87] N. LEE, J. B. FENN, *Rev. Sci. Instr.*, **49**, 1269 (1978).
- [88] P. M. DEHMER, J. L. DEHMER, *J. Chem. Phys.*, **68**, 3462 (1978).
- [89] G. S. HURST, E. B. WAGNER, M. G. PAYNE, *J. Chem. Phys.*, **61**, 3680 (1974).
- [90] R. C. MICHAELSON, A. L. SMITH, *Chem. Phys. Letters*, **6**, 1 (1970).
- [91] E. ELLIS, N. D. TWIDDY, *J. Phys.*, **B2**, 1366 (1969).
- [92] R. BOUCIQUE, P. MORTIER, *J. Phys.*, **D3**, 1905 (1970).
- [93] W. WIENNE, J. WIENNE-LENAERTS, *Phys. Letters*, **47A**, 37 (1974).
- [94] R. F. FIRESTONE, Report No **C00-1116-20**, Ohio State University (1972).
- [95] J. LE CALVÉ, R. A. GUTCHECK, O. DUTUIT, *Chem. Phys. Letters*, **47**, 470 (1977).
- [96] M. G. PAYNE, (unpublished results — see ref. [36]).
- [97] P. MOERMAN, R. BOUCIQUÉ, P. MORTIER, *Phys. Letters*, **49A**, 179 (1974).
- [98] J. W. KETO, R. E. GLEASON JR., G. K. WALTERS, *Phys. Rev. Letters*, **33**, 1365 (1974).
- [99] H. A. KOEHLER, L. J. FERBERDER, D. L. READHEAD, P. J. EBERT, *Phys. Rev.*, **A9**, 768 (1974).
- [100] J. B. GERARDO, A. W. JOHNSON, *J. Quant. Elect.* **QE9**, 748 (1973).
- [101] G. S. HURST, T. E. BORTNER, T. D. STRICKLER, *Phys. Rev.*, **49**, 2460 (1968); *ibid*, **178**, 4 (1969).
- [102] J. JORTNER, L. MEYER, S. A. RICE, E. G. WILSON, *J. Chem. Phys.*, **42**, 4250 (1965).
- [103] T. D. STRICKLER, E. T. ARAKAWA, *J. Chem. Phys.*, **41**, 1783 (1964).
- [104] J. R. BENNETT, A. J. L. COLLINSON, *J. Phys.*, **B2**, 571 (1969).
- [105] J. A. VIECELLI, UCRL Report No **UCRL-51374** (1973), (unpublished).

- [106] R. E. HUFFMAN, Y. TANAKA, J. C. LARRABEE, *J. Opt. Soc. Am.*, **52**, 851 (1962).
- [107] B. SCHNEIDER, J. S. COHEN, *J. Chem. Phys.*, **61**, 3240 (1974).
- [108] P. K. LEICHNER, R. J. ERICSON, *Phys. Rev.*, **A9**, 251 (1974).
- [109] D. SMITH, A. G. DEAN, I. C. PLUMB, *J. Phys.*, **B5**, 2134 (1972).
- [110] A. P. VITOLS, H. J. OSKAM, *Phys. Rev.*, **A8**, 1860 (1973).
- [111] D. SMITH, P. R. CROMEY, *J. Phys.*, **B1**, 638 (1968).
- [112] C. B. KRETSCHMER, H. L. PEDERSON, *J. Appl. Phys.*, **34**, 3209 (1963).
- [113] A. V. PHELPS, J. P. MOLNAR, *Phys. Rev.*, **89**, 1202 (1953).
- [114] A. H. FUTCH, F. A. GRANT, *Phys. Rev.*, **104**, 356 (1956).
- [115] J. LE CALVÉ, M. BOURÈNE, *J. Chem. Phys.*, **58**, 1446 (1973).
- [116] M. BOURÈNE, J. LE CALVÉ, *J. Chem. Phys.*, **58**, 1452 (1973).
- [117] L. COLLI, *Phys. Rev.*, **95**, 892 (1954).
- [118] M. BOURÈNE, O. DUTUIT, J. LE CALVÉ, *J. Chem. Phys.*, **63**, 1668 (1975).
- [119] N. SADEGUI, IV Coll. Nat. Phys. Collisions Atomiques et Electroniques, Brest (1970).
- [120] R. A. GUTCHEK, E. C. ZIPF, *Bull. Am. Phys. Soc.*, **17**, 395 (1972).
- [121] M. G. PAYNE, J. E. TALMAGE, G. S. HURST, E. B. WAGNER, *Phys. Rev.* **A9**, 1050 (1974).



SOCIEDADE PORTUGUESA DE FÍSICA
AV. REPÚBLICA 37-4.º, 1000 LISBOA, PORTUGAL

PORTUGALIAE PHYSICA publishes articles or research notes with original results in theoretical, experimental or applied physics; invited review articles may also be included.

Manuscripts, with an abstract, may be written in English or French; they should be typewritten with two spaces and in duplicate. Figures or photographs must be presented in separate sheets and be suitable for reproduction with eventual reduction in size; captions should make the figures intelligible without reference to the text. Authors are requested to comply with the accepted codes concerning references.

There is no page charge. Author(s) will get 50 free reprints (without covers); these are to be shared among all the authors of the article. Authors interested in more reprints should say so when sending their manuscripts; quotations shall be sent with the proofs.

Subscription rates for volume 11:

1,000 Escudos (US\$20) — individuals
2,500 Escudos (US\$50) — libraries

PORTUGALIAE PHYSICA may also be sent on an exchange basis; we welcome all suggestions to such effect.

All mail to be addressed to

PORTUGALIAE PHYSICA

C/O LABORATÓRIO DE FÍSICA, FACULDADE DE CIÊNCIAS
PRAÇA GOMES TEIXEIRA
4000 PORTO PORTUGAL

PORTUGALIAE PHYSICA

VOL. 11 · NUMB 1/2 · 1980

CONTENTS

NUCLEAR PHYSICS

- Improved Experimental Method for Half-Life Measurements by Electron — Electron Delayed Coincidences
M. C. ABREU, J. P. RIBEIRO, F. B. GIL 1
- The L_1 Subshell Fluorescence Yield of Tl
M. I. MARQUES, M. C. MARTINS, J. G. FERREIRA 9
- Proton-Induced K-Shell Hole Production on Ar and Kr
J. S. LOPES, K. KRIEN, J. C. SOARES, F. B. GIL 13

MOLECULAR AND CONDENSED MATTER PHYSICS

- Ultrasonic Study of Antiferromagnetic Domains in Dysprosium
G. N. BLACKIE, S. B. PALMER 23
- Magnetic Phase Transitions in Terbium Single Crystals
M. M. AMADO, J. B. SOUSA, M. F. PINHEIRO, R. P. PINTO,
M. E. BRAGA, J. M. MOREIRA, D. HUKIN, G. GARTON,
P. WALKER 33
- Thermopower in Rare Earth Intermetallic Compounds and the Validity of s-f Scattering Models
R. P. PINTO, J. B. SOUSA, J. M. MOREIRA, M. M. AMADO,
M. F. PINHEIRO, M. E. BRAGA, P. MORIN 41
- Correlation Between Twist Viscosity and Dielectric Relaxation in Nematic Liquid Crystals
A. C. DIOGO, A. F. MARTINS 47
- Radioluminescence of Rare Gases (review article)
M. SALETE S. C. P. LEITE 53

PORTUGALIAE PHYSICA

VOLUME 11
FASCÍCULO 3-4
1980

SOCIEDADE PORTUGUESA DE FÍSICA

PORTUGALIAE PHYSICA

Fundada em 1943 por A. Cyrillo Soares, M. Telles Antunes, A. Marques da Silva e M. Valadares

Director

J. M. Araújo (Faculdade de Ciências, Universidade do Porto)

Comissão Redactorial

J. M. Araújo (Faculdade de Ciências, Universidade do Porto)

J. Gomes Ferreira (Faculdade de Ciências, Universidade de Lisboa)

F. Bragança Gil (Faculdade de Ciências, Universidade de Lisboa)

M. F. Laranjeira (Faculdade de Ciências e Tecnologia, Universidade Nova de Lisboa)

F. D. S. Marques (Universidade do Minho)

A. Farinha Martins (Centro de Física da Matéria Condensada, Lisboa)

R. Vilela Mendes (Centro de Física da Matéria Condensada, Lisboa)

A. M. C. Moutinho (Centro de Física Molecular, Lisboa)

J. Pinto Peixoto (Faculdade de Ciências, Universidade de Lisboa)

A. Policarpo (Faculdade de Ciências e Tecnologia, Universidade de Coimbra)

J. da Providência (Faculdade de Ciências e Tecnologia, Universidade de Coimbra)

F. Carvalho Rodrigues (Laboratório de Física e Engenharia Nucleares, Sacavém).

F. D. Santos (Faculdade de Ciências, Universidade de Lisboa)

E. Ducla Soares (Faculdade de Ciências, Universidade de Lisboa)

O. D. D. Soares (Faculdade de Ciências, Universidade do Porto)

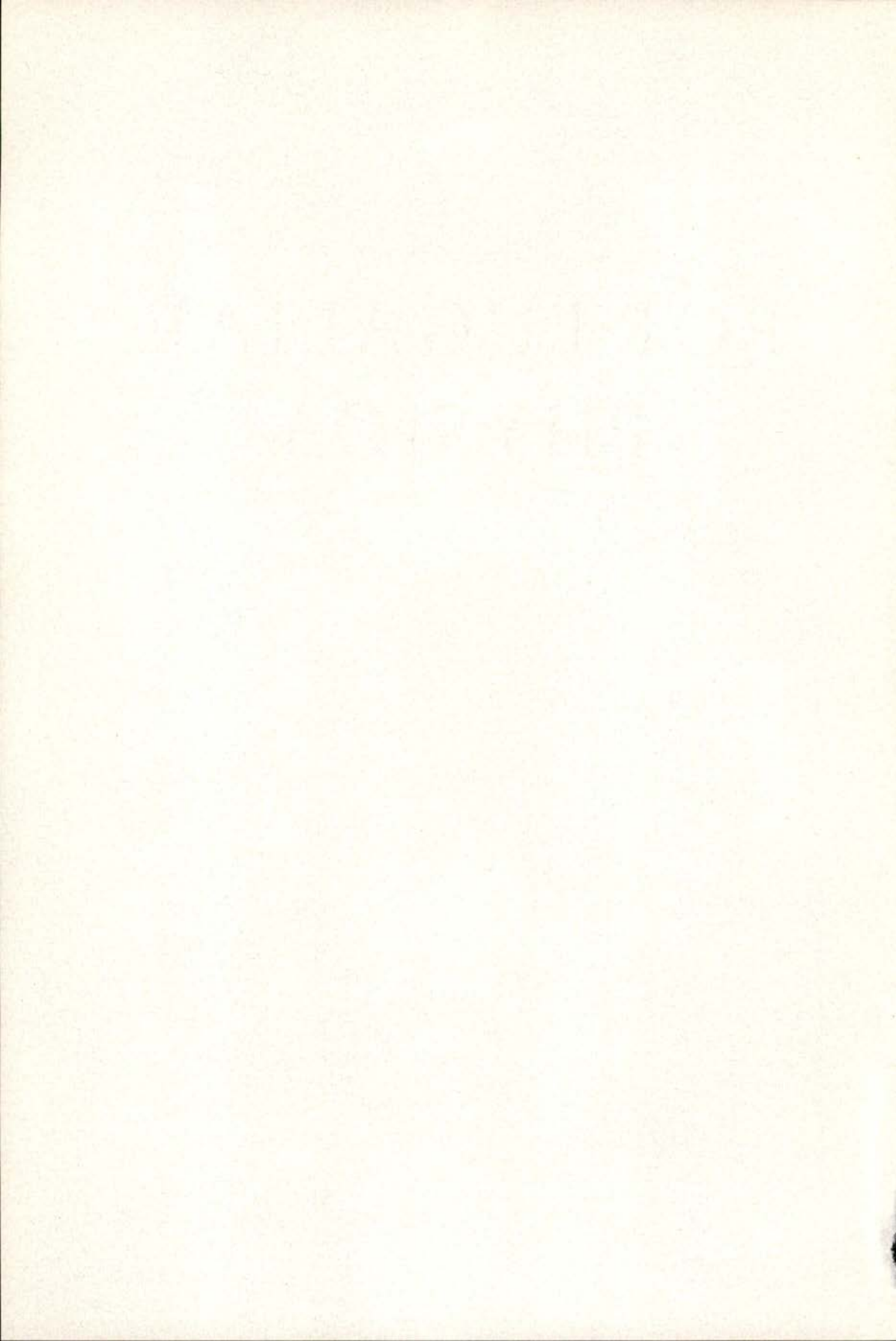
J. B. Sousa (Faculdade de Ciências, Universidade do Porto)

A. T. Rocha Trindade (Instituto Superior Técnico, Lisboa)

L. Alte da Veiga (Faculdade de Ciências e Tecnologia, Universidade de Coimbra)

PORTUGALIAE
PHYSICA

VOLUME 11
FASCÍCULO 3-4
1980



A SET OF NUCLEAR STOPPING CORRECTION FACTORS

M. F. DA SILVA, P. BORDALO *, J. VARELA, P. M. CORRÊA **,
and J. M. G. CARAÇA ***

Laboratório Nacional de Engenharia e Tecnologia Industrial,
Estrada Nacional n.º 10, 2685 Sacavém, Portugal

(Received 1 September 1980)

ABSTRACT

A set of nuclear Stopping correction factors to be used in the analysis of D.S.A. experiments by means of the LSS theory is presented. The results are derived from experimental determinations of the slowing down of ^{28}Si ions in several backings, ranging from carbon to uranium.

1 — INTRODUCTION

The problem of extracting nuclear lifetimes from Doppler shifted γ -rays has been haunting experimentalists for more than a decade, especially when no measured stopping powers are available and in consequence (some) theoretical estimates have to be used in the analysis. The question assumes further importance at low recoil energies due to: (i) the difficulty of measuring stopping powers in this range, and (ii) the complexity of the energy transfer mechanism which leads to the stopping of the recoiling ions.

Usually this has been handled by means of a distinction between two different stopping processes, namely a nuclear (or atomic)

(*) Permanent address: Instituto Superior Técnico, Lisboa, PORTUGAL.

(**) Present address: Companhia Nacional de Petroquímica, Lisboa, PORTUGAL.

(***) Present address: Junta Nacional de Investigação Científica e Tecnológica, Lisboa, PORTUGAL.

process and an electronic process, both concurring to the actual stopping. Nuclear (or atomic) stopping contributes appreciably to the total energy loss at low recoil velocities ($v/c < 0.5\%$), whereas for recoils of higher energy electronic stopping is the dominant slowing down mechanism. The stopping cross sections employed in the analysis are usually taken from the theory of Lindhard, Scharff and Schiøtt (LSS) [1] which is based upon the Thomas-Fermi statistical model of the atom. The mathematical treatment developed by Blaugrund [2] has also been widely used, as a straightforward means of deducing lifetime values from experimentally measured energy shifts.

However, the reliability of this method has been questioned practically since its inception [3]. To overcome this situation, which assumed particular relevance when no measured stopping powers were available for the actual experimental conditions, different approaches have been introduced [4].

Neither of them can be said to have been successful in the attempt to explain the slowing down process. Da Silva *et al.* [5] show it clearly at low recoil energies, by means of a careful study of the well-known lifetime of the second excited state of ^{28}Si [6] using different backing materials, ranging from carbon to uranium.

We also chose the low energy region because this is the situation encountered in the experiments performed with the 2MV Van de Graaff accelerator located at Sacavém. Further, atomic (or nuclear) stopping is the dominant process at these recoil energies.

2 — RESULTS AND DISCUSSION

Up to the present, statements expressing that available potentials lead to an overestimate of atomic (or nuclear) stopping are abundant in the literature. More scarce are, however, adequate estimates of that deviation. Nevertheless, one has to be sure that the lifetimes extracted in a D.S.A. experiment are correct, even if no measured stopping powers are at hand. The experimental results obtained by da Silva *et al.* [5] mentioned above, warrant the adoption of such a coherent set of nuclear stopping correction factors, which enable the use of straightforward methods, such as the Blaugrund one.

The analysis of D.S.A. experiments by this method proceeds usually through the introduction of corrective factors f_e and f_n , for the electronic and atomic (or nuclear) stopping components, respectively. Further, at low recoil energies, as the atomic component is the main contributor to the stopping, f_e can be safely assumed to equal unity without concern.

The data were reanalysed by varying f_n from 1.0 down to 0.1 in order to obtain lifetime values which were compatible with the adopted value of (63 ± 6) fs [6] for each case selected (the backings used were: C, Al, Cu, Zr, Ta and U), the initial velocity being $v/c = 0.14\%$ in all cases.

Fig. 1 shows the nuclear stopping powers for ^{28}Si ions in carbon and uranium in the Thomas-Fermi case and the corresponding curves used in the analysis (after correction by the multiplicative factors f_n).

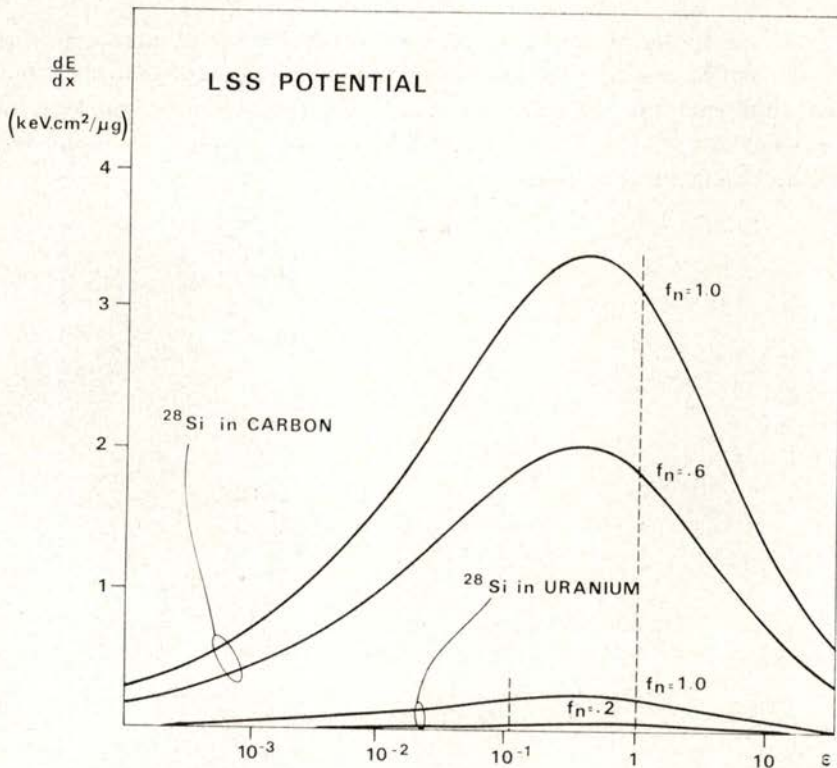


Fig. 1 — Nuclear stopping for ^{28}Si ions recoiling in carbon and uranium. Vertical lines correspond to ϵ initial in each case (ϵ as defined in ref. 1).

In Table 1, the whole set of corrective f_n 's is presented.

TABLE 1 — Multiplicative correction factors, f_n

Material	Z	τ ($f_n = 1.0$) in fs	f_n for τ_{adopted} (*)
carbon	6	47 ± 8	$.6 \pm .1$
aluminium	13	44 ± 2	$.5 \pm .1$
copper	29	33 ± 4	$.3 \pm .1$
zirconium	40	42 ± 5	$.4 \pm .1$
tantalum	73	31 ± 8	$.3 \pm .1$
uranium	92	25 ± 7	$.2 \pm .1$

(*) $\tau_{\text{adopted}} = (63 \pm 6)$ fs [6]

From these values, a curve that covers the recoil of silicon ions in the entire region encountered in similar experiments can be inferred, thus enabling the selection of a value for the multiplicative f_n to be used in a D.S.A. lifetime analysis employing the Blaugrund method. The curve is shown in fig. 2.

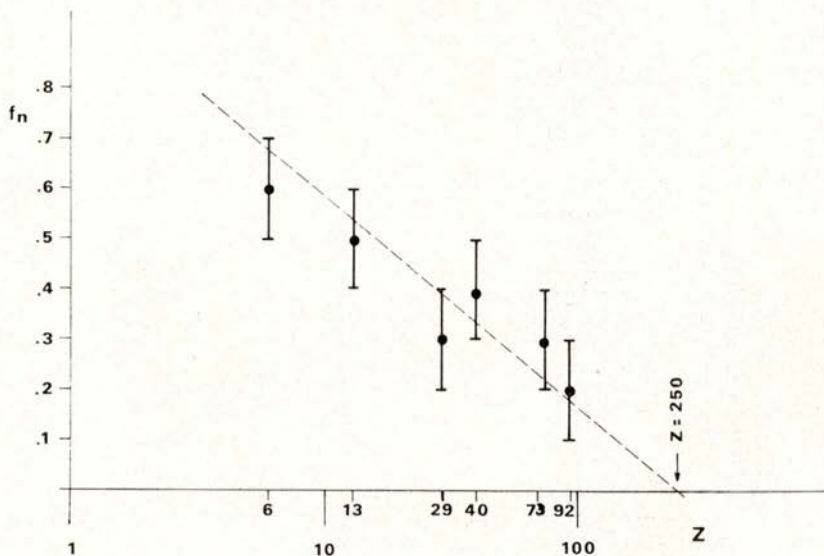


Fig. 2 — Values of the multiplicative factor f_n for silicon ions recoiling in different backings.

The physical meaning of this procedure is possibly hard to perceive [7]. It is however conceivable, at the present state of our investigations, that it conveys solely the indication that a silicon ion recoiling in $Z=250$ would not lose energy significantly through any other process than an 'electronic' one.

REFERENCES

- [1] J. LINDHARD, M. SCHARFF and H. E. SCHIÖTT, *Mat. Fys. Medd. Dan. Vid. Selsk.* **33**, n.º 14 (1963).
- [2] A. E. BLAUGRUND, *Nucl. Phys.* **88** (1966) 501.
- [3] W. M. CURRIE, L. G. EARWAKER and J. MARTIN, *Nucl. Phys.* **A135** (1969) 1295, J. M. G. CARAÇA, R. D. GILL, P. B. JOHNSON and H. J. ROSE, *Nucl. Phys.* **A176** (1971) 273.
- [4] W. M. CURRIE, *Nuc. Instr. and Meth.* **73** (1969) 173, B. M. LATTA and P. J. SCANLON, *Phys. Rev.* **A10** (1974) 1638, W. D. WILSON, L. G. HAGGMARK, and J. P. BIERSACK, *Phys. Rev.* **B15** (1977) 2458.
- [5] M. F. DA SILVA, P. BORDALO, J. VARELA and P. M. CORRÊA, paper contributed to the «2.^a Conferência Nacional de Física», Porto, April 1980.
- [6] P. M. ENDT and C. VAN DER LEUN, *Nucl. Phys.* **A130** (1978) 1.
- [7] P. M. CORRÊA and J. M. G. CARAÇA, *Phys. Lett.* **A70** (1979) 391.

THE POSITION LINEARITY OF PHOTO-IONIZATION DETECTORS

M. ALEGRIA FEIO and A. J. P. L. POLICARPO

Departamento de Física, Universidade de Coimbra
3000 Coimbra, Portugal

(Received 3 December 1980)

ABSTRACT

Data are presented for the linearity of photoionization detectors coupled to scintillators, mainly for gas proportional scintillation counters and also for other detecting media. The influence of electronic noise for low charge gain is considered.

1—INTRODUCTION

The coupling of multiwire proportional chambers as photoionization detectors (PID) to gas scintillation proportional counters (GSPC) [1, 2, 3, 4], giving rise to the so called PIPS chambers, takes profit essentially of the vacuum ultraviolet nature of the emitted photons [4, 5].

Many gaseous scintillators and condensed noble element media feature the same characteristic [4, 6] and its coupling to PIDs is being considered, in particular in the fields of fission fragments and heavy ions work, gamma ray detection, etc. [7]. Active research is going on trying to find crystals that would scintillate in regions suitable to its coupling to PIDs [8, 9]. PIDs are then of interest in the detection of events that correspond to energy deposits of several tens of eV to several GeV, mainly when simultaneous information in energy, position and time is required, over large areas of detection, together with multiple hit capabilities.

There is a revival of the research in the field of photoionization and the tetraminoethylenes and the organo-metallic compounds known

as the ocenes may prove useful for detection of the ultraviolet light; recent results significantly lowered the longest wavelength detectable with photoionization vapours, up to 2313 Å, featuring very large photoionization efficiencies [3, 9].

Profit is being taken of the scanty knowledge of the mechanisms of light emission to shift the spectra to favourable regions of the photoionization vapours [4, 5, 10], looking for cheaper or more convenient detection media and, reversely, the very narrow bandwidths of some photoionization vapours may lead to selected detection of special components, of eventual interest, for example, for time resolution.

Some of the predicted features for energy and position resolution have been confirmed, although only preliminary experimental information is available concerning this last parameter [2]. Previous calculations [11] showed that either the position resolution would be dominated by straggling in windows, range effects associated with photoelectrons or Auger electrons, etc., or the position resolution, although not limited by the physics of the interaction, was better than that of competing instruments. The linearity response of the system for position determination is then of importance, no information either computed or experimental is available, and it is the aim of this work to provide data in this subject, assuming realistic values of the relevant parameters, both intrinsic and instrumental. Charge division techniques [12], based on centroid determinations, make the use of this very usual method even faster, simpler and cheaper and it is then considered in this work.

Also, in particular because for low energies the use of lower noise amplifiers can be considered and some suitable photoionization vapours seem to be not very stable from the point of view of avalanche build-up, the influence of the electronic noise, for relatively low gains in the PID, is considered.

2 — MAIN FEATURES

Fig. 1 shows the geometry of the chamber. When looking for the secondary scintillation, it is assumed that the interaction region is in the absorption gap and it is either punctual or a segment of a line of force.

Calculations were made assuming that krypton, around atmospheric pressure, is the detecting medium [13] and that the photo-ionization vapour is triethylamine. As before [11] using a Monte-Carlo technique the mean number \bar{T}_i of photoelectrons, per photon produced in the scintillation gap, detected at the anode i of the PID, of coordinate x_i , in the direction orthogonal to the anode wires, was determined. Electron diffusion both in the absorption and scintillation gaps [14], spectral distribution of the emitted light [15] and the variation of the window transparency (LiF window) and the photo-ionization efficiency within the molecular emission band, and transparencies of the grids were taken into account [16]. Isotropy of photon emission was assumed.

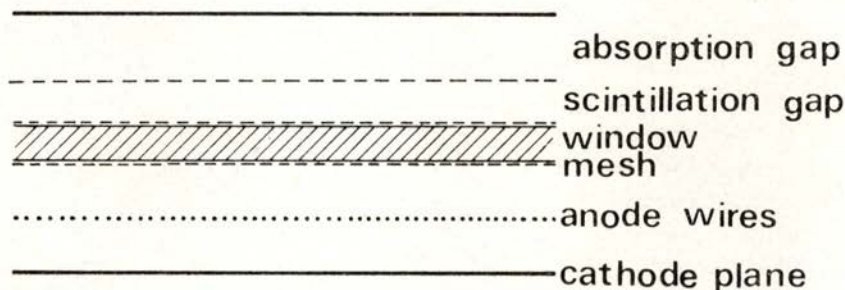


Fig. 1 — Schematic diagram of a photoionization proportional scintillation chamber. Dashed lines represent crossed wire meshes. Coordinates along the anode wire direction can be extracted from the centroid of the induced charge distribution on the strips of the cathode plane.

The number of ions pairs produced by an incident particle corresponding to a full energy deposition is well known, and some information is also available concerning its fluctuations [17]. The realistic assumption is made that to all anode wires corresponds the same charge gain k (relative variances are assumed as in [18]) the same r.m.s. noise charge in number of electrons, σ_0 , and the same electronic bias b . The mean charge collected in wire i , \bar{P}_i , can then be calculated provided that the mean number of photons produced by one drifting electron in the scintillation gap, \bar{H} , is known. For krypton, for 3600 volts across 10 mm, at one atmosphere

$\bar{H} = 340$ [13]. Fluctuations in P_i , arising from a cascade of events [19], were generated taking into account fluctuations in the number of ion pairs associated with the interaction of the particle, fluctuations of the charge gain in the PID, and assuming that HT_i obeys a Poisson distribution. The electronic noise was also considered. For each simulated event $\Sigma_i(P_i - b)$ and $x_M = \Sigma_i x_i (P_i - b) / \Sigma_i (P_i - b)$ were calculated, with the restriction that if $P_i < b$, $P_i - b$ is taken as zero. Mean values and standard deviations of these quantities allow the determination of the energy and position resolution, as well as the position linearity of the system.

3 — RESULTS AND DISCUSSION

Fig. 2 shows \bar{T}_i distributions assuming that the distance between anode wires in the PID is 11 mm, for three different positions x_F of the beam of incident particles. The thickness of the scintillation gap is 20mm, the distance of the bottom grid of the GSPC to the LiF window is 1mm, and the thickness of this window is 5mm. The thickness of the scintillation gap and VUV window contributes to the relatively large width of the distributions ~ 20 mm. This can be compared for example with widths of ~ 8 mm for the spread of the induced charges in multiwire proportional chambers using cathode strips read out [20]. By itself this is a strong indication that indeed the system should possess very good position resolution capabilities, as using pulses induced in cathode strips, position resolutions $\sigma \sim 6 \mu\text{m}$ have been obtained. Of course the use of thinner scintillation gaps and VUV windows would reduce the width of the \bar{T}_i distribution, but lower voltages would have to be used, with a small loss in energy resolution.

Data concerning the linearity of the device are presented in Figs. 3 and 4. The geometrical structure of the GSPC, the voltage applied to the scintillation gap and the nature of the detection medium are the same in both cases and have been described relatively to Fig. 2; a charge gain $\bar{k} = 10^4$ is assumed in the multiwire proportional chamber.

Fig. 3 shows the variation of the difference between computed and real positions (in mm) as a function of the real position of the incident beam, in units of anode wires distance, in the direction orthogonal to the anode wires, for an electronic bias $b = 2\%$ of the total

collected charge and for $\sigma_e = 1000$, for each amplifier. Clearly the linearity of the detector depends strongly on the distance between anode wires of the PID as could be expected in general terms. The larger contribution of the total electronic noise associated with the decrease

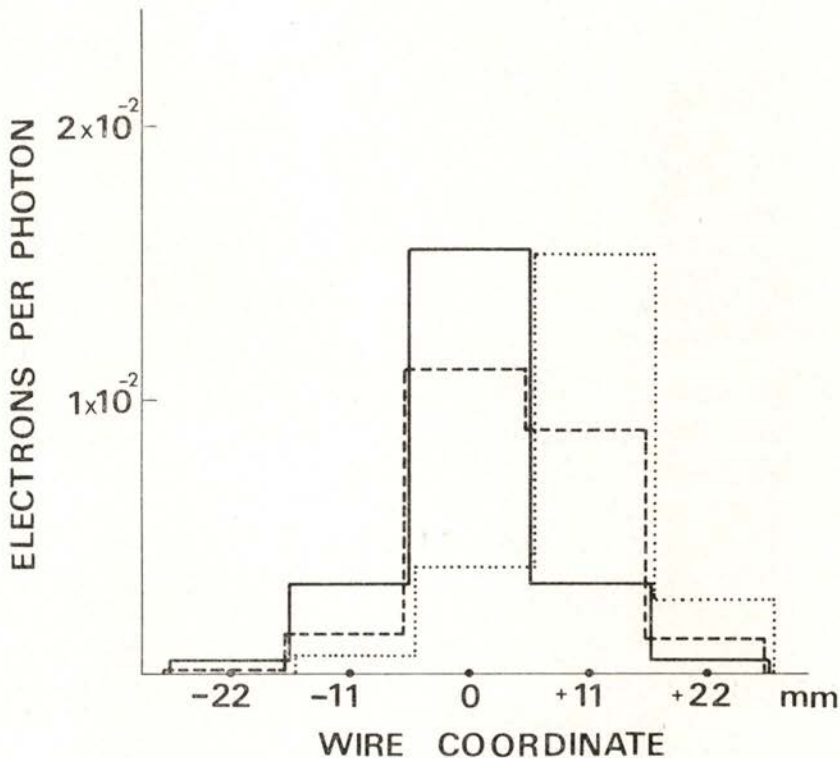


Fig. 2 — Spatial distributions of photoelectrons on the PID per photon, for a scintillation gap thickness $\Delta = 20$ mm and an applied voltage of 7200V. Full lines correspond to $x_F = 0$, dashed lines to $x_F = 5$ and dotted lines to $x_F = 10$ mm.

in the spacing between the anode wires does not affect significantly $\sigma_{x_M}^-$ from 20 keV to 2 keV. And this even for an electronic noise σ_e , that although relatively low for large size systems, is in no way an unrealistic value. For the higher energy even for a 5mm distance between anode wires the non linearity is significant. But it should be noticed that for the lower energy region the non linearity is negligible

and the very simple analog technique referred in ref. [12] is then of special importance.

Fig. 4 displays the variation of the difference between computed and real position as a function of the real position for two values of the electronic bias b (full curve corresponds to 2% and dashed curve

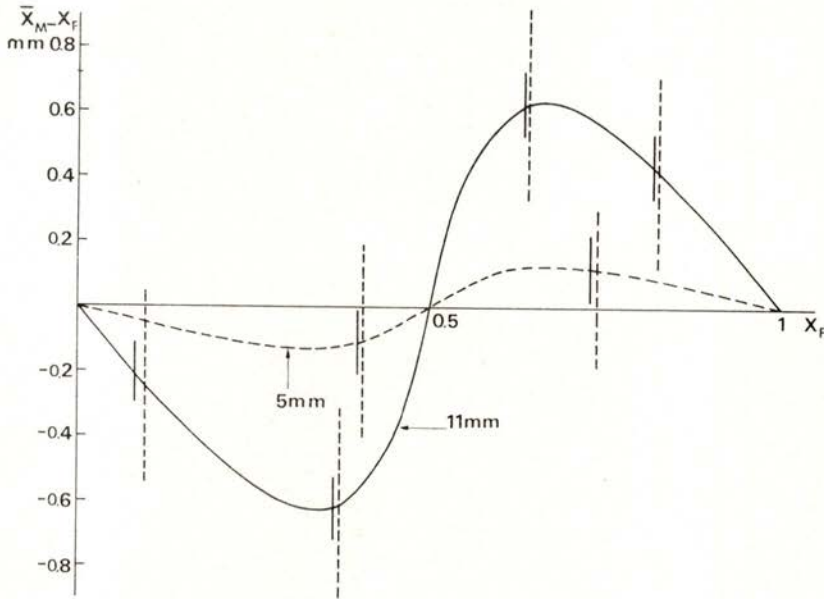


Fig. 3 — Linearity of the detector: \bar{x}_M computed position, x_F real position (the coordinate x_F is expressed in unites of the distance between anode wires). Full curves correspond to a distance between anode wires of 11 mm and dashed curves to 5 mm. Full bars correspond to $\pm \sigma_{x_M}$ for 20 keV and dashed bars $\pm \sigma_{x_M}$ for 2 keV.

to 10% of the total charge collected in the multiwire proportiona chamber). Calculations were made for an energy deposit of 20 keV and the differences between both curves are within the computed values of $\sigma_{x_M} \approx 0.1$ mm, even for this large light output of the system. For energies lower than about 20 keV, then within the position accuracy of the system, a wide band of b can be used without appreciable change of its linearity, the effect of the 'far away' anode wires being negligible.

All data referred till now assume proper proportional counter operation of the PID. Specially difficult conditions are now considered, that could very well be related to vapours featuring instability for avalanche build-up, and the low charge gain $\bar{k} = 10^2$ is assumed

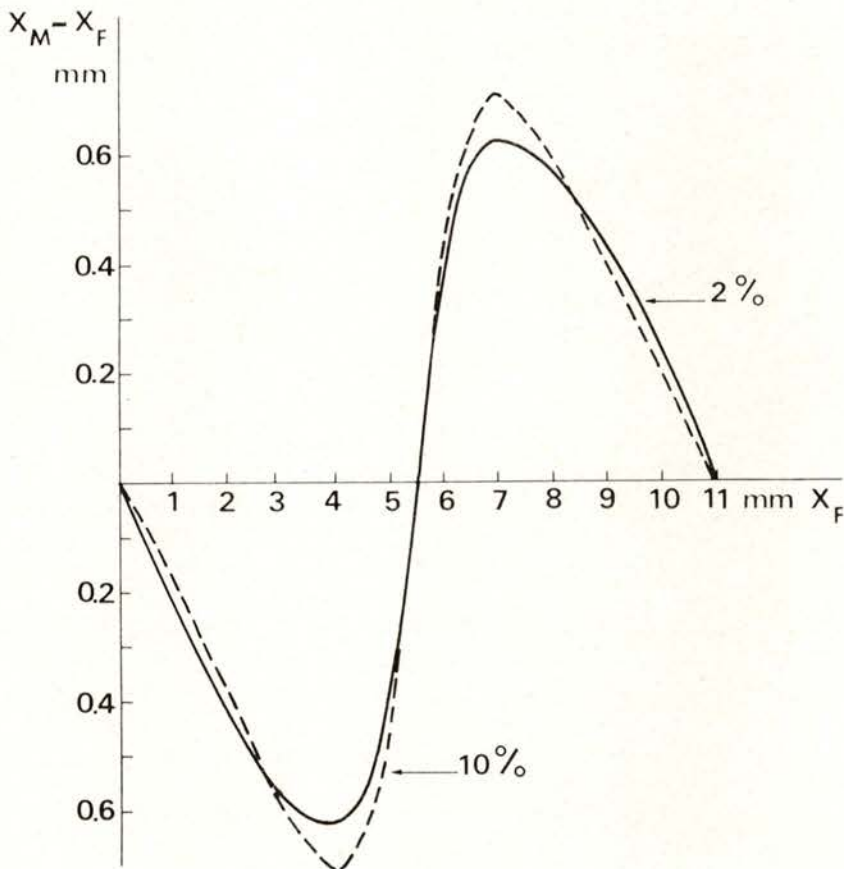


Fig. 4 — Linearity of the detector. Full curve corresponds to a bias b of 2% of the total charge collected in the PID; the dashed curve is for a bias of 10%.

in the data shown in Fig. 5 Again as referred under 2., $\bar{H} = 340$ and $b = 2\%$. The low values of \bar{k} and \bar{H} , together with a Fano factor $F = 0.17$ as well as the relatively low value of 31% for the mean photoionization efficiency of TEA imply energy resolutions

(dashed lines) and position resolutions (full lines) that, for the lower energies, depend strongly on the electronic noise σ_e . Values of $\sigma_e=3000$, 1000 and 140 are considered, this last value implying the use of low noise, but room temperature, preamplifiers.

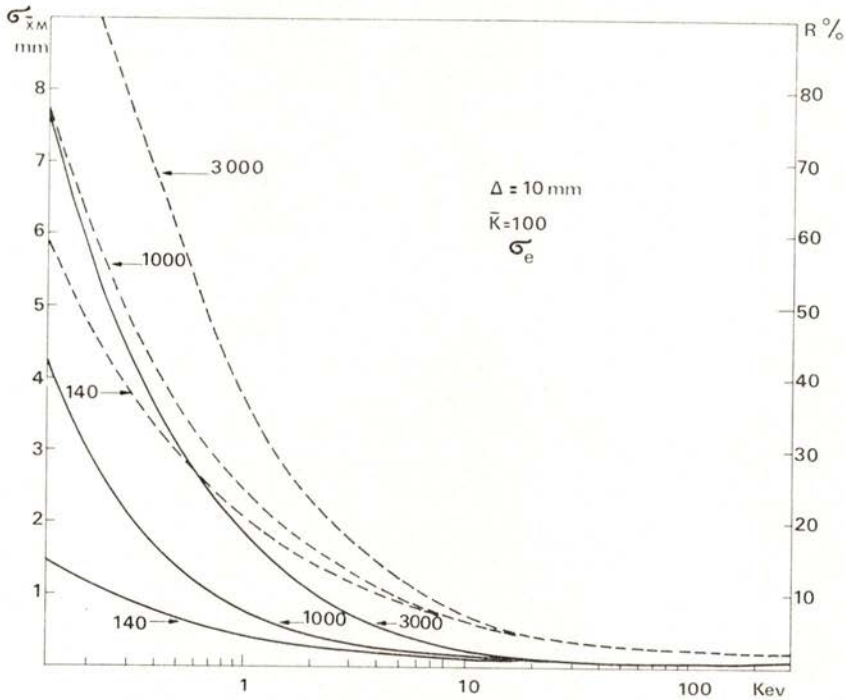


Fig. 5 — Intrinsic position (full lines) and energy (dashed lines) resolutions versus energy of the incident particles, for three values of σ_e , the r.m.s. noise (in number of electrons) of each amplifier.

4 — CONCLUSION

The data presented concerns directly operation of the device based on secondary light emission. For the low energy region, $\lesssim 2 \text{ keV}$, of interest to astrophysics [21] and to the study of muonic X-rays [22] for example, the system is linear within its position resolution, provided that the spacing between anode wires is $\lesssim 5 \text{ mm}$. This is of interest not only because lower spacing between anode

wires is a common feature of multiwire proportional chambers, but also because larger distances between the anode and cathode planes can be used, leading to the possibility of working with vapours of lower photoabsorption cross sections.

For higher energies the system is non linear and adequate corrections have to be introduced. This is more important for the 11 mm spacing, that on the other hand would have the advantage of being a minimum reasonable distance compatible with a multiproportional counter configuration rather than a multiwire chamber. The importance of the non linearity effect can be made very clear, noticing, for example, that even for $\bar{H} = 50$, $\sigma_{\bar{x}_m} = 12 \mu\text{m}$ at 10 MeV and $1 \mu\text{m}$ at 1 GeV [11].

For very difficult conditions of operation, the use of low noise preamplifiers for energies $\lesssim 5$ keV, restores the good energy and position resolution of the system and demonstrates the versatility of the device.

Within a good approximation the data shown concerning the linearity of the system can also be used for primary scintillations of higher energy particles, provided that the track of the particle coincides with a line of force of the scintillation gap, both for gaseous and condensed media. If this condition is roughly satisfied, and even neglecting range effects associated with δ rays, photoelectrons ranges, attenuation lengths of X rays associated with the physics of the interaction, etc., the system should be approximately linear up to energy deposits of a few MeV if one considerer scintillators of photon yields similar to liquid xenon, for example [23]. This covers fields like positron annihilation, nuclear medicine, industrial radiography, lower energy heavy ions physics, etc. For higher energies, its non-linearity would, of course, be again significant.

REFERENCES

- [1] A. J. P. L. POLICARPO, *Nucl. Instr. Meth.* **153**, 389 (1978).
- [2] G. CHARPAK, A. POLICARPO, F. SAULI, *IEEE Trans. Nucl. Sci.* **NS-27** n.º 1, 212 (1980); WILLIAM H. M. KU and CHARLES J. HAILEY, «Properties of an imaging gas scintillation proportional counter», submitted for publication in *IEEE Trans. Nucl. Sci.* Out. 1980.
- [3] D. F. ANDERSON, «Xenon gas scintillation proportional counter coupled to a photoionization detector», to be published in *Nucl. Instr. Meth.*

- [4] M. SALETE S. C. P. LEITE, A. J. P. L. POLICARPO, M. ALEGRIA FEIO and M. A. F. ALVES, «The use of rare gas mixtures in photoionization proportional scintillation chambers», to be published in *Nucl. Instr. Meth.*
- [5] M. SALETE S. C. P. LEITE, *Portugal. Phys.* **11**, 53 (1980); A. J. P. L. POLICARPO, «Light production and gaseous detectors», to be published in *Physica Scripta*.
- [6] J. L. TEYSSIER and D. BLANC, *L'Onde Electrique*, **44**, 458 (1964); M. MUTTERER, J. PANNICKE, H.-P. SHELHAAS J. P. THEOBALD J. C. VAN STADEN, *IEEE Trans. Nucl. Sci.* **NS-26**, n.º 1, 382 (1979).
- [7] J. P. THEOBALD, M. MUTERER, Institut für Kernphysik, Darmstadt, private communication; T. DOKE, Waseda University, private communication.
- [8] G. CHARPAK, F. SAULI, CERN, private communication.
- [9] D. F. ANDERSON, «A photoionization detector for the detection of xenon light», submitted for publication in *IEEE Trans. Nucl. Sci.* 1980.
- [10] R. D. ANDRESEN, E. A. LEIMANN, A. PEACOCK, *Nucl. Instr. Meth.* **140**, 371 (1978).
- [11] M. ALEGRIA FEIO and A. J. P. L. POLICARPO, «Position and energy resolution of the photoionization proportional scintillation (PIPS) chamber», submitted to *Nucl. Instr. Meth.*
- [12] E. MATHIESON, G. C. SMITH and P. G. GILVIN, *Nucl. Instr. Meth.* **174**, 221 (1980).
- [13] M. ALEGRIA FEIO and A. J. P. L. POLICARPO, G. CHARPAK and F. SAULI, «Scintillation efficiency of gas proportional scintillation counters», to be published in *Nucl. Instr. Meth.*
- [14] J. J. LOWE and S. H. PARKER, *Phys. Rev.*, **181**, 302 (1969).
- [15] M. SUZUKI and KUBOTA, *Nucl. Instr. Meth.* **164**, 197 (1979).
- [16] T. YPSILANTIS, CERN, private communication.
- [17] G. D. ALKHAZOV, A. P. KOMAR and A. A. VOROB'EV, *Nucl. Instr., Meth.* **48**, 1 (1967).
- [18] D. G. ALKHAZOV, *Nucl. Instr. Meth.* **89**, 155 (1970).
- [19] W. SCHOCKLEY and J. R. PIERCE, *Proc. I. R. E.* **26**, 321 (1938).
- [20] A. BRESKIN, G. CHARPAK, C. DEMIERRE, S. MAJEWSKI, A. POLICARPO, F. SAULI and J. C. SANTIARD, *Nucl. Instr. Meth.* **143**, 29 (1977).
- [21] G. MANZO, A. PEACOCK, R. D. ANDRESEN and B. G. TAYLOR, *Nucl. Instr. Meth.* **174**, 301 (1980).

- [22] J. BÖKIN, F. DITTUS, R. FERREIRA MARQUES, H. HOFER, F. KOTTMAN, R. SCHÄREN, D. TAQUU, M. WÄLCHLI, W.-D. HEROLD, H. KASPAR, «A large area Xenon gas scintillation proportional counter (GSPC) with timing information for the detection of low energy muonic X-rays», in *Wire Chamber Conference*, Vienna, Feb. 27-29 (1980).
- [23] S. KUBOTA, A. NAKAMOTO, T. TAKAHASHI, T. HAMADA, F. SHIBAMURA, M. MYAJIMA, K. MASUDA and T. DOKE, *Phys. Rev.* **B 17**, 2762 (1978).



K-AND L-SHELL IONIZATION IN ALPHA DECAY

J. P. RIBEIRO and F. B. GIL

Centro de Física Nuclear da Universidade de Lisboa
Av. Gama Pinto 2, 1699 Lisboa Codex, Portugal

(Received 30 December 1980)

ABSTRACT

The probabilities per α particle of shake-off in the K and L shells of ^{210}Po have been determined by α -X ray coincidence experiments. The results $P_K = (2.3 \pm 0.2) \times 10^{-6}$ and $P_L = (6.2 \pm 0.3) \times 10^{-4}$ are simultaneously compared with other experimental results and with the latest theoretical predictions. The number of Pb L X-rays arising from shake-off in the α decay of ^{210}Po is $(2.3 \pm 0.1) \times 10^{-4}$ per α decay and the agreement with other results is satisfactory.

1 — INTRODUCTION

The shell ionization of an atom can be produced during the α -decay of its nucleus by the emerging α -particle. The outgoing α spectrum associated with the ejected electron from a particular shell will have a maximum energy equal to the α -particle initial energy less the binding energy of the electron. The X-rays for each shell of the daughter element result either from the contribution of the 'shake-off' phenomenon, in which the atomic electron is excited into the continuum, or of the 'shake-up', in which the atomic electron is excited to an unoccupied bound state. The latter effect is the smallest of the two and, in this context, can be neglected. The degrees of ionization of the K-and L-shells are given by the ionization probabilities P_K and P_L which are the probabilities to create vacancies in those shells. The best way to determine experimentally these probabilities is by doing either X-ray- α coincidences or X-ray-electron coincidences in a pure α -emitter. The theory of the 'shake-off' phe-

nomenon was first treated by Migdal [1], Feinberg [2], Levinger [3] and lately by Hansen [4], Scott [5], Watson [6], Law [7]; agreement between the results is unsatisfactory. The latest experimental results [8-13] seem to favour Hansen's theoretical interpretation.

On the other hand, in the same experimental results [9] P_L values obtained by X-ray- α coincidences and X-ray-electron coincidences are not in agreement. Fischbeck and Freedman [9] have raised the possibility that some electrons may be captured by the He^{++} ions and emerge like He^+ . As most of the detectors do not distinguish He^{++} from He^+ , the number of X-ray- α coincidences is not changed by the existence of the phenomenon but the number of X-ray-electron coincidences will be affected by the capture of the electron. So far, however, the errors in the P_L values do not allow us to reach definitive conclusions. The work reported here — a measurement of the ionization probabilities of the K- and L-shells of ^{210}Po — was undertaken because there are important discrepancies between theoretical and experimental results and some more values for P_L can contribute to choose the correct theoretical approach. On the other hand, our value for P_L determined by L X-ray- α coincidences is absolutely necessary to investigate the possibility of electron capture by He^{++} , which is one of our objectives. This phenomenon is now being studied and we hope to say something more later on.

2 — EXPERIMENTAL PROCEDURE

2.1 — X-ray side

The K X-ray energy range goes from 73 keV to about 87 keV and so they were recorded in a coaxial Ge(Li) detector which has a volume of 22.5 cm³, a full width at half maximum (FWHM) 2.4 keV for a 1.33 MeV γ -ray. The source-to-detector distance was variable and we have worked with a solid angle $\Delta\Omega_x = (2.10 \pm 0.17) \times 10^{-1}$ sr.

The L X-ray energy goes from 10.5 keV to about 14.8 keV and they were recorded in a solid state detector of hyperpure Ge which has an active diameter of 6 mm, an active depletion depth of 5 mm, a full-width at half maximum of 225 eV for a 5.9 keV and a 5 μm thick beryllium window. The working solid angle was $(4.51 \pm 0.24) \times 10^{-4}$ sr.

2.2 — α -Side

The ^{210}Po α -particles with an energy of 5.306 MeV were recorded in a surface barrier detector, of 50 mm² surface area, of 100 μm depletion depth and a resolution of 17 keV for an 5.486 MeV energy.

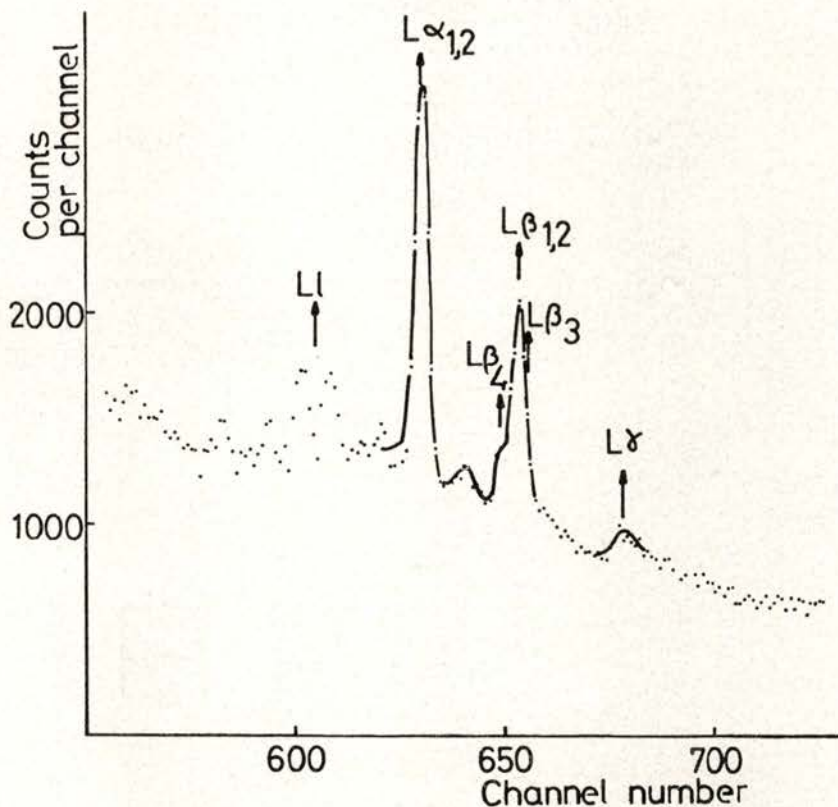


Fig. 1 — The Pb L X-ray spectrum.

This detector and the ^{210}Po source were housed in a small vacuum chamber which has a very thin mica window for the X-ray detection.

2.3 — Source preparation

The ^{210}Po was purchased from Radiochemical Centre (Amersham, England). The ^{210}Po activity was deposited by evaporation onto a

mylar film. The source diameter was about 2 mm and its thickness was controlled to minimize the α -particle energy loss. The source purity was confirmed by the LX-ray spectrum shown in Fig. 1.

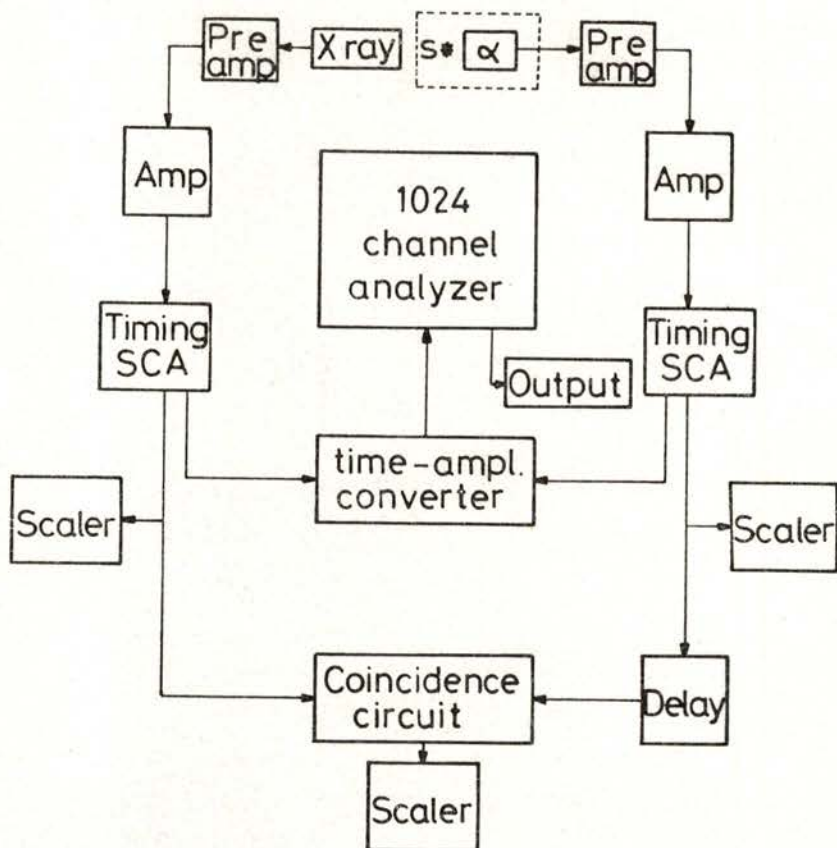


Fig. 2 — Block diagram of the electronic system.

2.4 — Electronic setup

The experimental results were obtained with a conventional coincidence installation associated with an Ortec time-amplitude converter according to the block diagram shown in Fig. 2. The X-ray spectra and the α spectrum were controlled daily in a 1024 multichannel analyser.

3 — RESULTS

3.1 — *K*-shell ionization probability P_K

The coincidence rates obtained with the ^{210}Po source were measured by the coincidence unit and by the time-amplitude converter (TAC) for a total run time of about 31 days. The spectrum of the KX-rays in coincidence with α -particles and registered in the TAC is shown in Fig. 3.

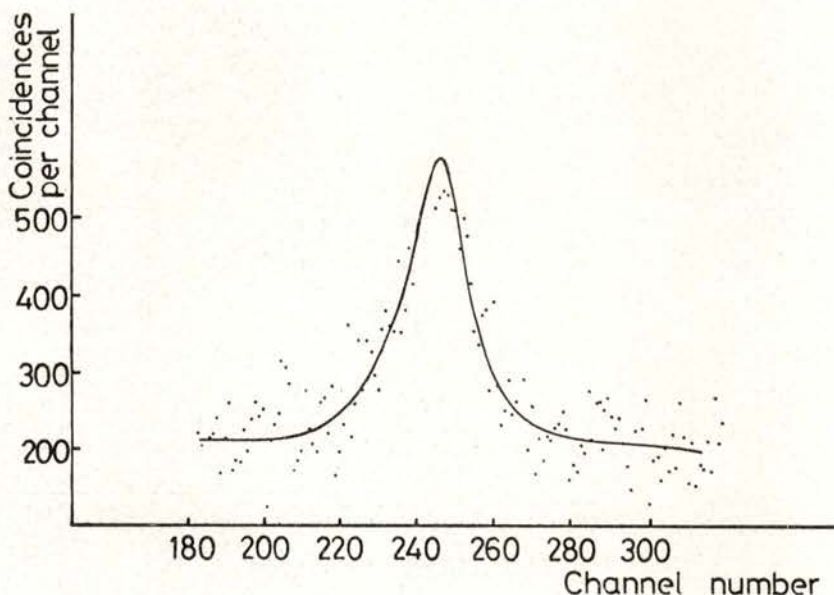


Fig. 3 — K X-ray- α particle coincidence spectrum registered in the TAC.

The ionization probability P_K , that is, the probability to create a vacancy in the K-shell, was determined from the expression:

$$N_c = N_\alpha \Delta\Omega_\alpha \varepsilon_\alpha P_K \omega_K \Delta\Omega_x \varepsilon_x \quad (1)$$

where N_c is the number of coincidences per time unit, N_α is the number of α particles per time unit, ε_α , ε_x are the α -particle and the X-ray detector efficiencies and ω_K is the fluorescence yield of the

K-shell. Using the value of N_0 taken from Fig. 3, the value of $\Delta\Omega_x$ referred in 2.1 and the value $\omega_K = 0.972 \pm 0.008$ [16] we determined

$$P_K = (2.3 \pm 0.2) \times 10^{-6}$$

3.2 — L-shell ionization probability P_L

The spectrum of L X-rays in coincidence with the α -particles is shown in Fig. 4. From this spectrum and from an expression similar

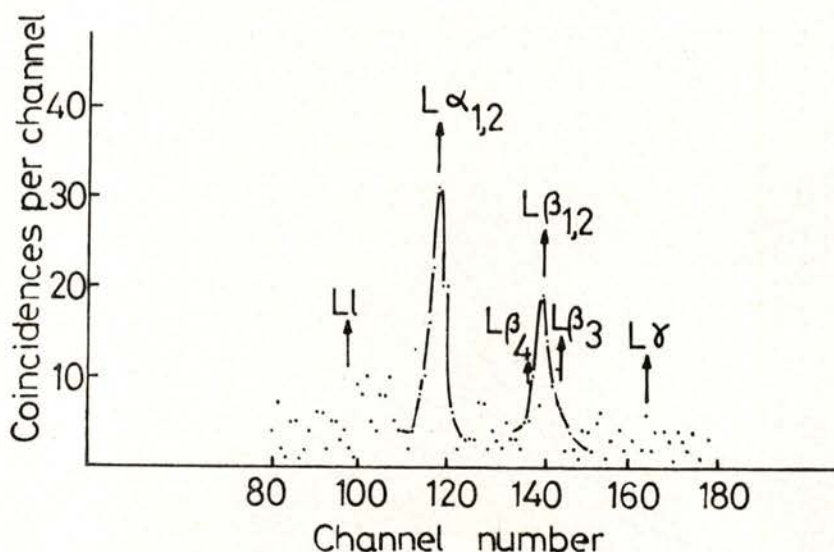


Fig. 4 — Pb L X-ray spectrum in coincidence with α particles.

to (1) we may calculate the probabilities $P_{L\alpha}$, $P_{L\beta}$, $P_{L\gamma}$, P_{LI} . These probabilities have the following meanings: $P_{L\beta}$, for example, is the probability per α particle of emitting an L X-ray belonging to the $L\beta$ peak. To have good statistics we performed three runs of about 17 days each and the results shown below are the average value of these runs. The single L X-rays and the α spectra were controlled daily. The results for the L X-rays of Pb, expressed for α decays of ^{210}Po , are:

$$P_{L\alpha} = (1.09 \pm 0.08) \times 10^{-4}$$

$$P_{L\beta} = (0.95 \pm 0.07) \times 10^{-4}$$

$$P_{L\gamma} = (0.18 \pm 0.03) \times 10^{-4}$$

$$P_{LI} = (0.06 \pm 0.01) \times 10^{-4}$$

Therefore the total number P_{LX} of Pb L X-rays arising from shake-off in the α -decay of ^{210}Po is

$$P_{LX} = (2.3 \pm 0.1) \times 10^{-4}$$

Assuming that the fluorescence yield in the L shell is $\bar{\omega}_L = 0.37$ [16] we found for the ionization probability P_L the value

$$P_L = (6.2 \pm 0.3) \times 10^{-4}$$

This probability can also be written in terms of the P_{LI} , P_{LII} , P_{LIII} subshell probabilities and these values can be deduced from the expressions

$$P_{L\alpha} = [P_{LIII} + P_{LII} f_{23} + P_{LI} (f_{13} + f_{12} f_{23})] \omega_3 F_{3\alpha},$$

$$P_{L\beta} = [P_{LIII} + P_{LII} f_{23} + P_{LI} (f_{13} + f_{12} f_{23})] \omega_3 F_{3\beta} +$$

$$+ (P_{LII} + P_{LI} f_{12}) \omega_2 F_{2\beta} + P_{LI} \omega_1 F_{1\beta},$$

$$P_{L\gamma} = (P_{LII} + P_{LI} f_{12}) \omega_2 F_{2\gamma} + P_{LI} \omega_1 F_{1\gamma},$$

where f_{12} , f_{13} and f_{23} are the values of the Coster-Kronig yields, ω_1 , ω_2 and ω_3 are the values of the subshell fluorescence yields and F_{ij} is the fraction of radiative transitions in the L_j peak connected with filling a vacancy in the L_i subshell. The radiative rates are taken from Scofield tables [15] and the f_{ij} and ω_i from Bambynek *et al* tables [16]. By solving the previous system of equations we may write P_{LI} , P_{LII} , P_{LIII} in terms of $P_{L\alpha}$, $P_{L\beta}$, $P_{L\gamma}$. Thus, for example, $P_{LI} = a P_{L\alpha} + b P_{L\beta} + c P_{L\gamma}$ and the coefficients a , b , c , depend on the f_{ij} , ω_i , F_{ij} parameters. Unfortunately the coefficients a, b, c can be of different signs and therefore they can generate large uncertainties in the P_{LI} , P_{LII} , P_{LIII} values and consequently in the

P_L value. For this reason we have chosen to evaluate P_L from the total photon yield per α particle, P_{LX} , using the mean L-shell fluorescence yield $\bar{\omega}_L = 0.37$.

4 — DISCUSSION

In tables I, II, and III, we have summarized the theoretical and latest experimental results and compared them with our values.

TABLE I — Theoretical and experimental K-electron emission probability per α decay.

Theory	Reference	Experiment	Method	Reference
2.5×10^{-6}	1	$(2.0 \pm 0.5) \times 10^{-6}$	α -KX coinc.	8
2.02×10^{-6}	4	$(1.65 \pm 0.16) \times 10^{-6}$	α -KX coinc.	10
1.81×10^{-6}	7	$(2.6 \pm 0.5) \times 10^{-6}$	α -KX coinc.	9
2.24×10^{-6}	7	$(2.5 \pm 0.7) \times 10^{-6}$	Elect-KX coinc.	9
2.34×10^{-6}	7	$(2.3 \pm 0.2) \times 10^{-6}$	α -KX coinc.	This work
2.88×10^{-6}	7			

The results of ref. 7 are obtained with different approximations for the α -nucleus potential.

TABLE II — Theoretical and experimental L-electron emission probability per α decay

Theory	Reference	Experiment	Method	Reference
1.13×10^{-4}	1	$(2.83 \pm 0.45) \times 10^{-4}$	α -LX coinc.	9
5.9×10^{-4}	4	$(3.05 \pm 0.46) \times 10^{-4}$	Elect-LX coinc.	9
1.29×10^{-4}	7	$(8.6 \pm 2.2) \times 10^{-4}$	α -LX coinc.	8
2.74×10^{-4}	7	$(7.23 \pm 0.65) \times 10^{-4}$	α -LX coinc.	16
1.27×10^{-4}	7	$(6.2 \pm 0.3) \times 10^{-4}$	α -LX coinc.	This work
2.69×10^{-4}	7			

The P_K value is very close to the other experimental values and the agreement with the theoretical results is quite satisfactory.

The unexpected value of $(2.83 \pm 0.45) \times 10^{-4}$ for P_L obtained by Fischbeck and Freedman [9] is not reinforced by our result. This seems, in fact, to confirm the experimental results obtained by many

TABLE III — Theoretical and experimental L-total photon yield per α decay

Theory	Reference	Experiment	Reference
1.83×10^{-4}	4	$(2.93 \pm 0.44) \times 10^{-4}$	14
0.477×10^{-4}	7	$(3.2 \pm 0.8) \times 10^{-4}$	8
1.01×10^{-4}	7	$(3.03 \pm 0.19) \times 10^{-4}$	9
0.470×10^{-4}	7	$(2.37 \pm 0.21) \times 10^{-4}$	10
0.995×10^{-4}	7	$(2.6 \pm 0.4) \times 10^{-4}$	12
		$(2.3 \pm 0.1) \times 10^{-4}$	This work

The results of ref. 7 are obtained from table II assuming $\bar{\omega}_L = 0.37$.

other authors and the theoretical value calculated by Hansen [4]. The recent theory due to Law [7] is not confirmed by our experimental result. Since our values have been obtained by α -L X coincidences, the electron capture hypothesis can not be discussed. This will be a matter for study in the near future. On the other hand, as the values of P_{L_I} , $P_{L_{II}}$, $P_{L_{III}}$ depend strongly on the theoretical model, an experimental set of accurate values for those subshell probabilities will be important to test those models.

The authors wish to thank Dr. A. Barroso for helpful discussions in the course of this work. Financial assistance given by Instituto Nacional de Investigação Científica (INIC) is acknowledged.

REFERENCES

- [1] MIGDAL A., *J. Phys. (USSR)* **4**, 449 (1941).
- [2] FEINBERG E. L., *J. Phys. (USSR)* **4**, 423 (1941).
- [3] LEVINGER J. S., *Phys. Rev.* **90**, 11 (1953).
- [4] HANSEN J. S., *Phys. Rev.* **A9**, 40 (1974).
- [5] SCOTT R. D., *J. Phys.* **A7**, 1171 (1974).
- [6] WATSON R. L., *Phys. Rev.* **A12**, 2628 (1975).
- [7] LAW J., *Nucl. Phys.* **A286**, 339 (1977).
- [8] BRIAND J. P., CHEVALLIER P., JOHNSON A., ROZET J. P., TAVERNIER M., and TONATI A., *Phys. Rev. Lett.* **33**, 266 (1974).

- [9] FISCHBECK H. J., and FREEDMAN M. S., *Phys. Rev. Lett.* **34**, 173 (1975) and *Phys. Rev.* **A15**, 162 (1977).
- [10] RAPAPORT M. S., ASARO F., and PERLMAN I., *Phys. Rev.* **C11**, 1740 (1975) and *Phys. Rev.* **C11**, 1746 (1975).
- [11] DYER P., BURCH D., FISCHBECK H. J., and FREEDMAN M. S., *Phys. Rev. Lett.* **36**, 903 (1976).
- [12] SCOTT R. D., and WELLUM R., *J. Phys.* **G3**, 67 (1977).
- [13] SCOTT R. D., *J. Phys.* **G4**, 1353 (1978).
- [14] RUBINSON W., and BERNSTEIN W., *Phys. Rev.* **86**, 545 (1952).
- [15] SCOFIELD J. H., *Phys. Rev.* **179**, 9 (1969).
- [16] BAMBYNECK W., CRASEMAN B., FINK R. H., FREUND H. U., MARK H., SWIFT C. D., PRICE R. E., and RAO P. V., *Rev. Mod. Phys.* **44**, 716 (1972).

ENHANCED NUCLEAR MAGNETISM IN HoVO_4 (*)

B. BLEANEY

Clarendon Laboratory, Oxford OXI 3PU, England

(Received 30 October 1980)

ABSTRACT — HoVO_4 is a Van Vleck paramagnet with a susceptibility which is large perpendicular to the tetragonal crystal axis, but very small parallel to this axis. The nuclear magnetic resonance spectrum of the single stable isotope ^{165}Ho ($I=7/2$) shows a corresponding anisotropy in the magnetogyric ratio, which is enhanced by a factor of about 170 in the plane normal to the tetragonal axis. The interactions between the enhanced nuclear moments are predominantly dipolar, with a small anti-ferromagnetic component. On this basis the nuclear spins are predicted to order at about 4 to 5 mK in a novel anti-ferromagnetic arrangement. This is consistent with nuclear orientation measurements at temperatures down to 1 mK obtained by magnetic self-cooling. The anisotropy in the γ -ray emission from $^{160\text{m}}\text{Ho}$ ($I=7$) confirms the existence of a 'spin-flop' phase, and the nuclear magnetic moment of this isomer is determined as $3.60 \pm 0.06 \mu_N$. The sign of the nuclear electric quadrupole parameter of ^{165}Ho in HoVO_4 is shown to be positive, $(P/h) = +25.9 \pm 0.3$ MHz.

1—INTRODUCTION

In a paramagnetic solid compound, the various levels of the magnetic ion are split by interaction with the 'crystal electric field' set up by the ligand ions around the magnetic ion. Such splittings vary from ten to several hundred cm^{-1} , but do not necessarily raise all the degeneracy. For an ion with an odd number of electrons, a

(*) Results presented at the Conference of the Portuguese Physical Society (Porto, April 1980).

two-fold degeneracy ('Kramers degeneracy') must remain, which can only be lifted by the application of a magnetic field. Under such circumstances, the magnetic susceptibility, at low temperatures where only a pair of such levels is occupied, follows Curie's law (with a modified value of the Curie constant), until, below some characteristic temperature determined by the interactions between the magnetic ions, an ordered magnetic state sets in. In contrast, for ions with an even number of electrons ('non-Kramers ions'), all the degeneracy may be removed, or at least the ground state is a singlet. Such a singlet state can have no permanent magnetic moment, and at temperatures so low that only this level is populated, the susceptibility reaches a constant value, independent of temperature. This condition is often known as 'Van Vleck paramagnetism', since the explanation was first given by Van Vleck [1]. If the ground state has large matrix elements of the Zeeman interaction with other low-lying states (say at 10 to 20 K), this temperature independent susceptibility may be quite sizeable. Such a situation is most likely to occur for ions of the 4f group, where a magnetic moment per ion of order 1 Bohr magneton can be induced in the singlet state by the application of a field of one tesla.

In such a magnetization, no entropy is removed, and it follows that no magnetic cooling is possible by adiabatic demagnetization in such a simple electronic system. However, the nucleus of such an ion may possess a spin I and a nuclear magnetic moment, with a nuclear entropy of $R \ln (2I+1)$. When an electronic moment is induced by the application of an external magnetic field, the magnetic hyperfine interaction produces a field at the nucleus which, for a 4f ion, may approach 10^3 tesla for an electronic moment of $1 \mu_B$. The nuclear levels are then split through the action of this hyperfine field \mathbf{B}_e by an amount which is much larger than that produced by the external field \mathbf{B} . For moderate values of \mathbf{B} , the induced electronic moment \mathbf{m} is proportional to the applied field \mathbf{B} , and since \mathbf{B}_e is proportional to \mathbf{m} , the net field $(\mathbf{B} + \mathbf{B}_e)$ acting on the nuclear moment is also proportional to \mathbf{B} . The nuclear Zeeman energy is

$$-\mathbf{m}_n \cdot (\mathbf{B} + \mathbf{B}_e) = -\mathbf{m}_n \cdot \mathbf{B} (1 + K) = -[\mathbf{m}_n (1 + K)] \cdot \mathbf{B}$$

This equation shows that the Zeeman energy, and the resultant splitting of the nuclear levels, arises from the field $(\mathbf{B} + \mathbf{B}_e) = \mathbf{B} (1 + K)$,

but it can equally well be regarded as resulting from the interaction of \mathbf{B} with an abnormally large nuclear magnetic moment $\mathbf{m}_n (1+K)$. The latter is called the enhanced nuclear magnetic moment, and K is often called the 'enhancement factor'. In special cases K may be over 100, and the 'enhanced nuclear magnetic moment' may be some tenths of a Bohr magneton.

2—ENHANCED NUCLEAR MAGNETIC RESONANCE

Magnetic resonance offers the most precise method of measuring a nuclear magnetic moment, and it can obviously be applied to find the size of the enhanced moment. In this section the nature of the resonance spectrum is considered. The discussion is restricted to ions of the 4f group, for which the Hamiltonian may be written as

$$\mathcal{H} = \mathcal{H}_{c.f.} + \mu_B \mathbf{B} \cdot (g_J \mathbf{J} - g_I \mathbf{I}) + A_J (\mathbf{I} \cdot \mathbf{J}) + \mathcal{H}_Q \quad (1)$$

provided that only terms within the ground manifold J are included. The terms in (1) represent respectively the crystal field interaction, the Zeeman interaction (both electronic and nuclear), together with the magnetic dipole and electric quadrupole hyperfine interactions.

Within a singlet state, the expectation values of the operators J_x, J_y, J_z are all zero. This is no longer true when matrix elements to higher levels are included. In second order, perturbations from the matrix elements of J_x in the Zeeman and magnetic hyperfine terms produce an effective Hamiltonian for the ground singlet of the form

$$\mathcal{H}_x = - a_x (1/2 g_J^2 \mu_B^2 B_x^2 + g_J \mu_B A_J B_x I_x + 1/2 A_J^2 I_x^2) \quad (2a)$$

$$- g_I \mu_B B_x I_x + \mathcal{H}_Q \quad (2b)$$

together with similar terms in y, z . The parameter a_x in (2a) consists of a sum of terms, each containing the square of a matrix

element $\langle e | J_x | g \rangle$ between the ground state $| g \rangle$ and an excited state $| e \rangle$, divided by the difference in energy $(W_e - W_g)$:

$$a_x = 2 \sum \langle e | J_x | g \rangle^2 / (W_e - W_g).$$

The three terms in (2a) are respectively the induced electronic Zeeman energy, the enhanced nuclear Zeeman interaction, and a term in I_x^2 which behaves like a quadrupole interaction but is a second order effect of the magnetic hyperfine term $A_J (J_x I_x)$. By differentiation with respect to B_x , one finds that the induced electronic moment along the x-axis is

$$m_x = a_x g_J^2 \mu_B^2 B_x, \quad (3)$$

and the effective nuclear magnetic moment operator, enhanced through the hyperfine interaction, is

$$(a_x g_J A_J + g_I) \mu_B I_x = \gamma_x \hbar I_x. \quad (4)$$

The nuclear terms in (2) can now be expressed by the Hamiltonian

$$\mathcal{H}_n = \sum_{x,y,z} (-\gamma_x \hbar B_x I_x + P_x I_x^2) + \mathcal{H}_Q. \quad (5)$$

The quantity $(\gamma_x / 2\pi)$ gives the enhanced nuclear resonance frequency for $B_x = 1$, when $P_x = 0$. In the absence of any enhancement the frequency would be $(\gamma_I / 2\pi)$, where $\gamma_I \hbar = g_I \mu_B$, so that

$$(\gamma_x - \gamma_I) \hbar = a_x g_J A_J \mu_B \quad (6)$$

is the contribution from the electronic moment through the hyperfine interaction.

In (2a) the terms all contain the one parameter a_x , so that they can be expressed in terms of one measured quantity γ_x . From eq. (3), (6) we have

$$m_x / (\mu_B B_x) = (g_J / A_J) \hbar (\gamma_x - \gamma_I) \quad (7)$$

and this gives the electronic moment in Bohr magnetons induced by unit flux density. Similarly,

$$P_x = -1/2 a_x A_J^2 = -1/2 (A_J / g_J \mu_B) \hbar (\gamma_x - \gamma_{\parallel}). \quad (8)$$

In general the values of $\gamma_x, \gamma_y, \gamma_z$ will be all different, depending on the local symmetry at the magnetic ion. If this symmetry is axial, the complete nuclear Hamiltonian may be written in the form

$$\mathcal{H}_n = -\gamma_{\parallel} \hbar B_z I_z - \gamma_{\perp} \hbar (B_x I_x + B_y I_y) + P [I_z^2 - 1/3 I(I+1)], \quad (9)$$

where $P = P_1 + P_2 + P_3$ is the sum of three contributions. The second of these arises from the second order effect of the magnetic hfs; from eq. (8) we have

$$P_2 = P_z - 1/2 (P_x + P_y) = 1/2 (A_J / g_J \mu_B) \hbar (\gamma_{\perp} - \gamma_{\parallel}). \quad (10)$$

P_1 and P_3 arise from \mathcal{H}_Q , and represent interactions of the nuclear electric quadrupole moment with the electric field gradients of the 4f electron cloud and of the lattice respectively. They are given by the standard formulae [2]:

$$P_1 = -\frac{3e^2 Q \langle r^{-3} \rangle}{4I(2I-1)} \langle J \parallel \alpha \parallel J \rangle \langle 3J_z^2 - J(J+1) \rangle, \quad (11)$$

where $\langle 3J_z^2 - J(J+1) \rangle$ is the expectation value for the ground singlet state, and

$$P_3 = -\frac{3Q A_2^2}{I(2I-1)} (1 - \gamma_{\infty}). \quad (12)$$

The advantage of an enhanced n. m. r. experiment is that it can measure the principal values $\gamma_x, \gamma_y, \gamma_z$ for each ion. For axial symmetry these reduce to two, $\gamma_{\parallel} = \gamma_z$, and $\gamma_{\perp} = \gamma_x = \gamma_y$. Then the induced electronic moment per unit field can be calculated by using equation (7), which shows it will have similar anisotropy to γ . Also, the 'pseudo-quadrupole' interaction can be found by using (8), or, with

axial symmetry, eq. (9). These calculations require only the values of g_J and A_J , which for lanthanide (4f) ions are known with precisions of order 1%. This means that P_2 is in general known much more accurately than P_1 or P_3 .

3—RESONANCE MEASUREMENTS ON HoVO₄.

HoVO₄ has the tetragonal zircon structure, in which all the Ho³⁺ ions are magnetically equivalent with tetragonal symmetry about the crystal c-axis, which we take to be the z-axis. The ground state of the Ho³⁺ ion is 4f¹⁰, ⁵I₈; thus $J=8$, and $g_J = 1.242$. For the single stable isotope ¹⁶⁵Ho, $I=7/2$, and $A_J = +812$ MHz, $(\gamma_I/2\pi) = 9.0$ MHz T⁻¹. The crystal field acting on the Ho³⁺ ion has tetragonal symmetry, and splits the $(2J+1) = 17$ states into 9 singlets and 4 doublets. Optical spectroscopy [3] has shown that the ground state is a singlet, which in a good approximation can be characterized as $|J_z = 0\rangle$. The first excited state is a doublet at 21 cm⁻¹ = 30 K, which on the same basis can be written as $|J_z = \pm 1\rangle$. For the singlet, matrix elements of J_z (with levels above 200 cm⁻¹) are small; on the other hand there are large matrix elements of J_x, J_y (or J_+, J_-) with the doublet at 21 cm⁻¹. Thus at helium temperatures the electronic susceptibility should be independent of temperature, very small along the c-axis but large in the plane normal to this axis, as found by Swithenby [4].

Enhanced n.m.r. measurements [5] have been made at frequencies up to 500 MHz on single crystal samples of HoVO₄, and on diluted crystals containing 2% and 0.1% of Ho in YVO₄. In the latter two samples, the value of $(\gamma_I/2\pi)$ at 2 K is 1526 ± 3 MHz T⁻¹, while $|P/h|$ is 25.3 ± 0.2 MHz; no precise measurement of $(\gamma_{||}/2\pi)$ could be obtained, but it is estimated to be about 15 to 20 MHz T⁻¹. From these results the corresponding values of the induced electronic moment are calculated using eq. (7) above to be $2.32 \mu_B$ per tesla perpendicular to c-axis, and $\sim 0.02 \mu_B$ per tesla parallel to this axis. This confirms that the anisotropy is very large, about 100 to 1. The sign of P cannot be determined in such a resonance experiment, but the three contributions to (P/h) are $(P_2/h) = +35.3 \pm 0.1$ MHz, $(P_1/h) = -34 \pm 1$ MHz, and $(P_3/h) = +5$ to $+10$ MHz. The first of these is the most accurate, being calculated using eq. (8) above;

the last contribution, from the lattice, is the most uncertain and should be of the order of 25 MHz to account for the observed value of $|P/h| = 25.9 \pm 0.3$ MHz for HoVO₄.

The magnetic resonance spectrum of ¹⁶⁵Ho is shown in fig. 1 for 2% Ho in YVO₄ and for concentrated HoVO₄. In the latter case the measured values of $(\gamma_{\perp}/2\pi)$ range from 1625 MHz T⁻¹ down to

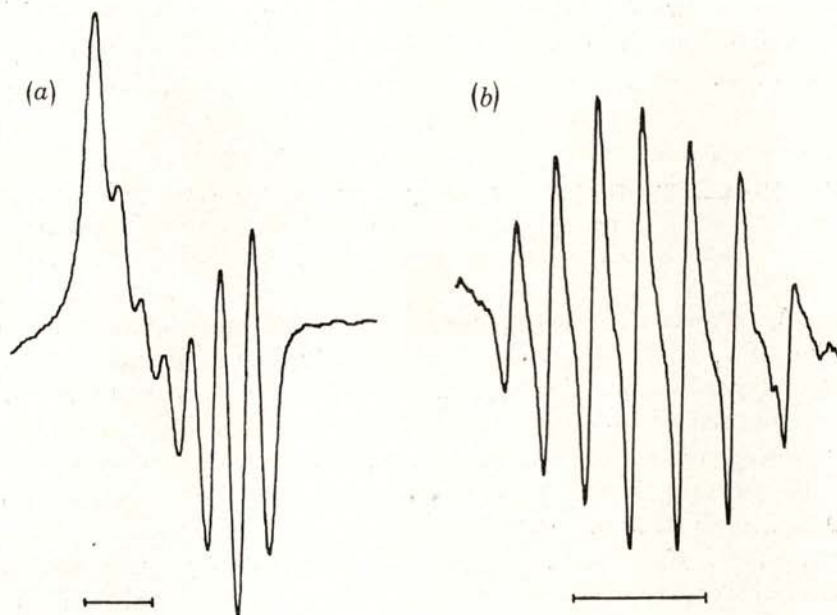


Fig. 1 — The nuclear magnetic resonance spectrum of ¹⁶⁵Ho ($I=7/2$) at a temperature of 4.2 K and at a frequency of 500 MHz in (a) HoVO₄ and (b) (2% Ho,Y)VO₄. The magnetic field is parallel to [110] and the solid line corresponds to an increment of 0.05 T.

1260 MHz T⁻¹, depending on the shape of the sample. This shows that the internal field has values up to $\pm 10\%$ of the applied field. The apparent variation of γ_{\perp} with sample shape arises from changes in the demagnetizing field, and the results confirm that these are in excellent agreement with the values calculated from the induced moment of $2.32 \mu_B$ per tesla quoted above. On the other hand the value of $|P/h|$ is independent of shape and the same as in the diluted crystals. In view of the large contribution

to P from P₂, which is directly proportional to γ_{\perp} (see eq. (10)), it is reasonable to assume that γ_{\perp} is really the same in the concentrated as in the dilute crystals. This is an important deduction, because there is no other way in which the true value of γ_{\perp} (i.e., the value it would have if the internal field were zero) can be ascertained without making some assumption about the nature of the interactions between the ions. These interactions are mainly dipolar, but by taking the actual value of γ_{\perp} to be the same as in the dilute crystals, it can be shown from the measured values of γ_{\perp} that there is a small contribution to the internal field from anti-ferromagnetic exchange interaction.

4 — THE NUCLEAR MAGNETIC MOMENT OF ^{166m}Ho.

An immediate consequence of the large enhancement of the value of γ_{\perp} is that it becomes comparatively easy to produce a large nuclear polarization. For $(\gamma_{\perp}/2\pi) = 1.5 \text{ GHz T}^{-1}$, a field of 2 T perpendicular to the c-axis of the crystal results in a splitting between successive nuclear levels of 3 GHz, which in temperature units is equivalent to 144 mK. In thermal equilibrium at a temperature of 40 mK, over 95% of the ¹⁶⁵Ho nuclei will occupy the extreme state with $|I_z| = I$. Under such conditions the emission of γ -rays following the decay of a radioactive holmium nucleus such as ^{166m}Ho ($I = 7$) will be highly anisotropic. A study of the rate at which the anisotropy grows as a function of the size of the applied field should give an accurate ratio of the nuclear magnetic moment of the radioactive isotope relative to that of ¹⁶⁵Ho. Measurements of this type have been carried out in Oxford by the nuclear orientation group of Dr. N. J. Stone [6].

Neutron irradiation of a single crystal of HoVO₄ produces ¹⁶⁶Ho ($I = 0$), which has a half-life of 27 hours and decays relatively quickly, together with the isomeric state ^{166m}Ho, with a half-life of 1200 years. This isomer decays to ¹⁶⁶Er by emitting a β^- particle, followed by a rather complex cascade of γ -rays. The anisotropy of six of these γ -rays, with energies ranging from 184 to 752 keV, have been studied using a single crystal attached to the cold finger of a dilution refrigerator. Measurements of the anisotropy for two of the

γ -rays, together with the theoretical fits, are shown in fig. 2. A complete analysis of the data for all six γ -rays gives the magnetic moment of ^{166m}Ho as $(+)$ $3.60 \pm 0.06 \mu_N$, assuming that of ^{165}Ho to be $+4.125 \pm 0.044 \mu_N$, as determined by an atomic beam experiment [7].

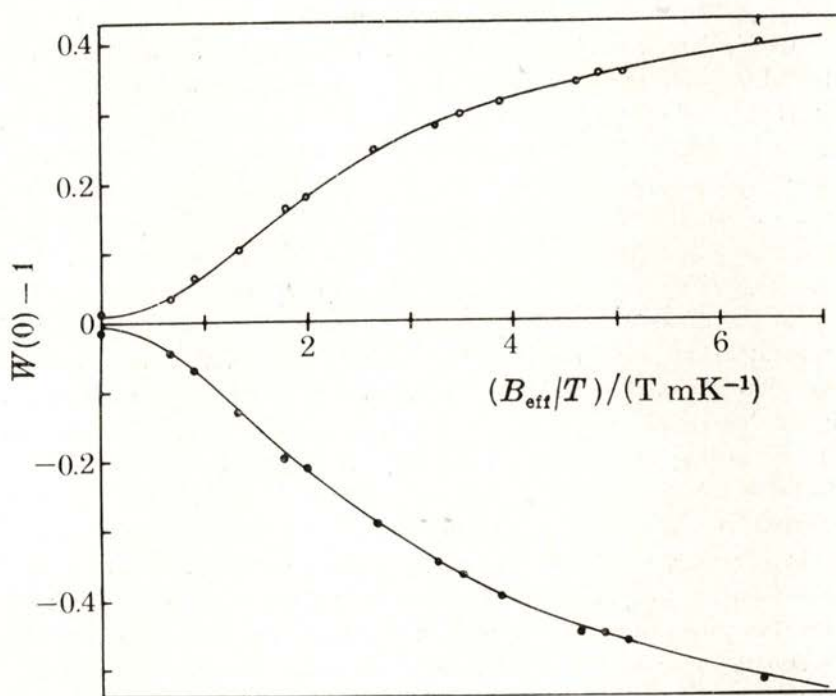


Fig. 2 — Anisotropy in the emission of the 280.5 keV (below) and the 711.7 keV (above) γ -rays from ^{166m}Ho in HoVO_4 as a function of B_{eff}/T . B_{eff} is the total magnetic field (applied + hyperfine) acting on the nuclear moment, in tesla, and the temperature is in units of milliKelvin.

5 — NUCLEAR MAGNETIC ORDERING

The conditions of $B = 2$ tesla and $T = 40$ mK under which the nuclei are almost completely polarized are of course just those under which the nuclear entropy, which in zero field is $R \ln(2I + 1) =$

$= R \ln 8$ for ^{165}Ho , has been reduced almost to zero. It follows that an adiabatic demagnetization from such starting conditions must cool the ^{165}Ho nuclei to such a low temperature that they enter a magnetically ordered state. The nature of the ordering depends on the interactions between the Ho nuclear spins. Fortunately, the size of these interactions can in large measure be deduced from the n.m.r. experiments at 2 to 4 K, as can be seen from the following discussion.

In HoVO_4 the observed n.m.r. frequency is shifted by the internal field set up by the induced electron moments on the surrounding Ho^{3+} ions, discussed in § 3. In § 2 it has been shown that there is a simple direct relation (eq. (7)) between the induced electronic moment per unit field, and the enhancement of the nuclear moment. By the use of this relation it can be shown [8] that the interactions between the enhanced nuclear moments are mainly dipolar, together with a small anti-ferromagnetic contribution. Since the shift in the nuclear resonance frequency depends only on the *sum* of the local fields, a similar limitation must be present in the information which can be derived about the inter-nuclear interactions. The dipolar interactions can be calculated for every pair of nuclei, but the exchange interactions cannot. It is therefore necessary to introduce an assumption in the latter case. Each Ho ion has four equidistant nearest neighbours, to each of which the bond is similar, involving a path containing only one oxygen ion. It is therefore assumed that the exchange interaction is the same with each of these four neighbours, and zero with all other neighbours, which are considerably further away. On this basis it turns out that the interactions with the four nearest neighbours are still mainly dipolar in origin, and no serious error is introduced by the assumption that interactions with more distant neighbours are completely dipolar.

The large anisotropy in γ means that interactions involving the z-components of the enhanced nuclear moments, which are proportional to γ_{\parallel}^2 , are negligible compared with those involving γ_{\perp}^2 . The nuclei must therefore order, in the plane perpendicular to the c-axis. The four nearest neighbours (nn) lie at equal distances along the x- and y-axes, two above and two below the xy-plane; for the purposes of discussion it is a convenient simplification to treat them as if actually in this plane. Two equivalent ordered spin systems, based on predominantly dipole interactions, are shown in fig. 3. The

'end-on' positions are occupied by dipoles parallel to the central dipole; and the 'broadside-on' positions by anti-parallel dipoles; thus the fields of all four nn add at the centre. Interactions with dipoles outside the diamond shown in the figure are small compared with those inside, and the arrangement gives the largest field at the centre, parallel to the central dipole, and hence the lowest energy.

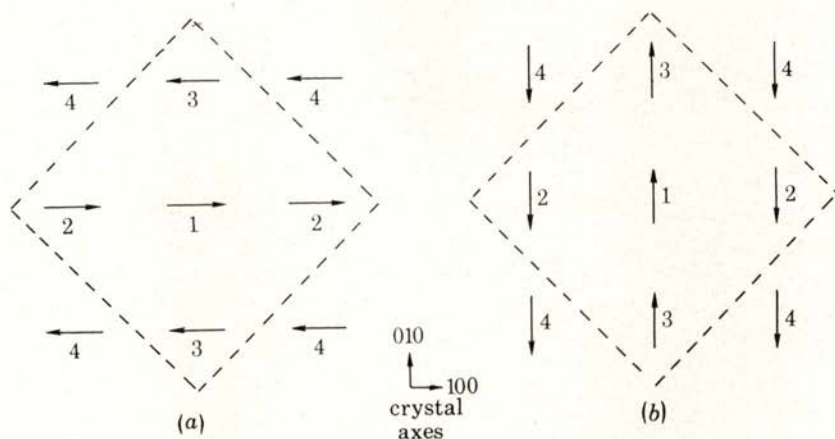


Fig. 3—Two equivalent anti-ferromagnetic arrangements of the nuclear moments in HoVO_4 which give the minimum energy when the interactions between the moments are predominantly dipolar. The largest interactions are those between an ion and its four nearest neighbours lying within the diamond indicated by the broken lines.

Any dipole in the lattice has the same arrangement of neighbours, so that the correct translational symmetry is preserved. The system corresponds to a simple two sub-lattice anti-ferromagnet. If a moment of $1 \mu_B$ exists on each site, the 'molecular field' at each site in this arrangement is $B_{a.f.} = 0.0734$ tesla. An interesting feature of the arrangement is that $B_{a.f.}$ is independent of the size of the anti-ferromagnetic exchange, since two nn are parallel and two anti-parallel, so that their exchange fields cancel. Of course, this occurs only because the dipole forces predominate. If the anti-ferromagnetic exchange were larger by a factor of about four, the stable ordered arrangement would become one in which all four nn are anti-parallel.

A more detailed investigation [8] reveals that there exists a whole range of four sub-lattice 'puckered' arrangements of the type shown in fig. 4. Here the dipoles still all lie in the (001) plane, and each is equally inclined to the four-fold crystal axes. Calculation shows that the energy is independent of the angle β , and is the same as for the arrangements of fig. 3, which correspond to the

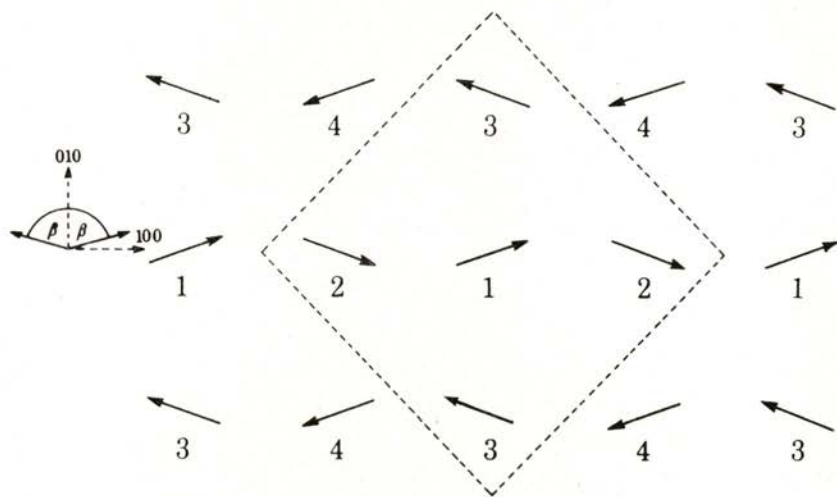


Fig 4 — A 'puckered' arrangement of the nuclear moments. Ions 1,2,3,4 lie on four different sub-lattices. The energy is independent of the angle β , and is the same as for the two sub-lattice configurations of fig. 3, which are special cases corresponding to $\beta=0^\circ$ and 90° .

special cases where $\beta=0$ and 90° . However, as soon as an external field is applied along one of the four-fold axes, these 'puckered' arrangements become unstable, and the system changes to a simple two sub-lattice anti-ferromagnetic arrangement in which the dipoles are perpendicular to the applied field ('spin-flop'). As the applied field B is increased the dipoles turn towards it, becoming parallel to it when B exceeds a certain critical value. For purely dipolar interactions, the value of this critical field is 0.0146 tesla per μ_B , but when the anti-ferromagnetic exchange interaction is included, it becomes 0.035(8) tesla per μ_B .

6—CALCULATION OF THE NÉEL TEMPERATURE

On a molecular field model, the condition for an ordered state to set in can be derived as follows. In each sub-lattice, the magnetic moment is given by

$$m = \chi (B + B_{a.f.} m) \quad (13)$$

where m , χ are the magnetic moment and susceptibility and $B_{a.f.}$ is the molecular field per unit moment calculated for the ordered state. (To avoid problems about units, we work always in μ_B per ion; thus the unit of χ is μ_B per tesla). Eq. (13) may be written in the form

$$m (1 - \chi B_{a.f.}) = \chi B, \quad (14)$$

from which it appears that when $\chi B_{a.f.} = 1$, a finite value of m (spontaneous magnetization) can exist when $B = 0$. Thus an ordered state sets in at temperatures below the point at which χ exceeds $(B_{a.f.})^{-1}$, and no assumption is made about the way in which χ varies with temperature.

In this relation χ is the sum of the enhanced nuclear susceptibility χ_n , calculated for zero interaction between the spins, and the temperature-independent contributions from the induced electron moments. The latter is $2.32 \mu_B$ per tesla, while the former can be calculated from the values of γ_{\perp} and P . If P were zero, χ_n would follow Curie's law; however, the overall quadrupole splitting is $12 (P/h) = 310$ MHz, which is equivalent to about 14 mK, so that departures from Curie's law become significant in the mK region. The n.m.r. results provide the values of γ_{\perp} and of $|P|$, but do not determine the sign of P , though it is probably positive. The nuclear susceptibility can readily be calculated for either sign of P , and the results are shown in fig. 5, where the contribution from the induced electron moment has also been included. If P is negative, the lowest nuclear levels are $I_z = \pm 7/2$, which have no moment perpendicular to the c -axis; χ_n therefore reaches a value almost independent of temperature below about 10 mK. If P is positive the lowest levels are $\pm 1/2$, which have large perpendicular moments; χ_n therefore rises

above the Curie's law value, as shown in fig. 5. The Néel temperature occurs when λ attains the value $(B_{a.f.})^{-1} = (0.0734)^{-1}$, giving $T_N = 4.8$ mK if P is positive. This prediction has been confirmed

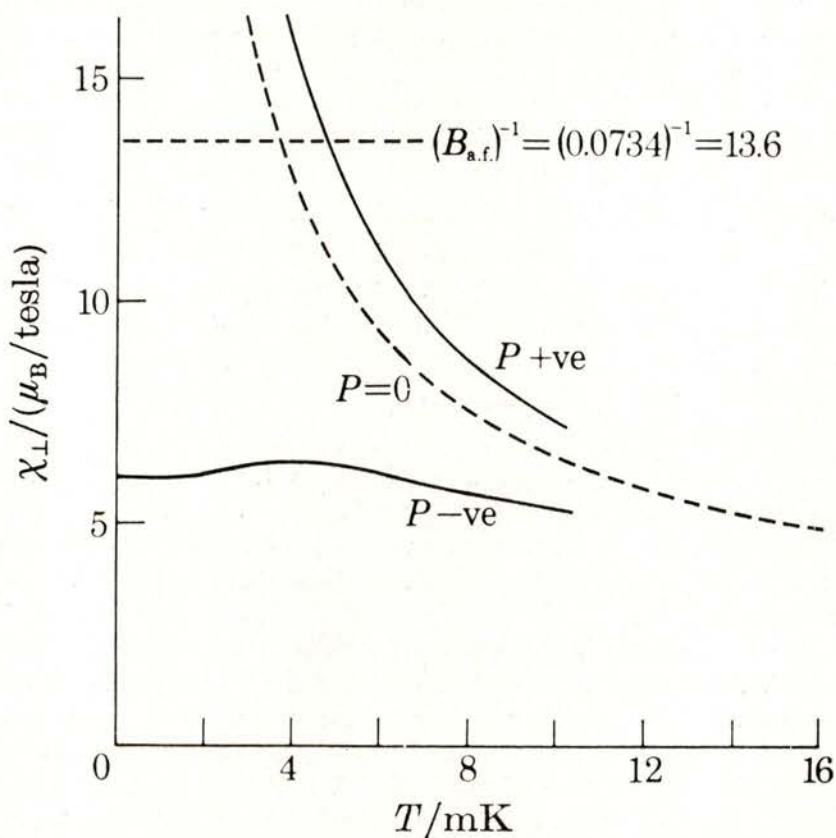


Fig. 5 — The perpendicular susceptibility of HoVO₄ in the mK region. $\lambda(T) = 2.32 + F(T)$, where $2.32 \mu_B$ per tesla is the induced electron moment and $F(T)$ is calculated from the spin Hamiltonian (eq. 9) for $P/h = + 25.9$ MHz and for $P/h = - 25.9$ MHz. For $P = 0$, $F(T) = 41.9 \mu_B$ per tesla. The Néel temperature is given by the intersection of the broken horizontal line with the calculated susceptibility curve.

experimentally by measurements of the radio-frequency susceptibility after adiabatic demagnetization [9], which show a maximum in the region 4 to 5 mK. This confirms that P is positive, since fig. 5 shows that there is no anti-ferromagnetic solution when P is negative.

Fig. 5 shows also that the main part of the susceptibility below 20 mK arises from the enhanced nuclear moments, since the electronic term is constant at $2.32 \mu_B$ per tesla. As T tends to zero, the limiting value of the enhanced nuclear moment reaches $(7/2) \gamma_1 \hbar$, which is equal to $0.38 \mu_B$. To this the induced electronic moment adds an amount $2.32 B_{a.f.} = 0.08 \mu_B$, giving a total moment of $0.46 \mu_B$. The true nuclear moment is only $0.0022 \mu_B$, confirming that the main part of the enhanced nuclear moment is electronic in origin. From the value of the total moment, the size of the applied field as $T \rightarrow 0$ needed to produce orientation of all the dipoles parallel to it (as in a ferromagnet or saturated paramagnet) is $0.46 \times 0.035 = 0.016$ tesla, where 0.035 tesla per μ_B is the critical field per unit moment given at the end of § 5.

7 — NUCLEAR ORIENTATION MEASUREMENTS IN THE ANTI-FERROMAGNETIC PHASE.

In conclusion, we discuss investigations [6] of the anti-ferromagnetic phase of HoVO_4 using nuclear orientation techniques. These consist of measurements of the anisotropy in the emission of γ -rays from $^{166\text{m}}\text{Ho}$ ($I=7$) in the temperature region reached by magnetic self-cooling of the ^{165}Ho nuclear system. A single crystal of HoVO_4 is attached to the cold finger of a dilution refrigerator, and magnetized in a field of 1.8 tesla at a temperature of 35 mK. This removes nearly all the nuclear entropy, and on demagnetization final temperatures of 1 mK are reached (estimated from entropy calculations). In the residual field (0.002 T) of the superconductive magnet, a large anisotropy in the γ -ray emission is observed, with axial symmetry about the c -axis of the crystal. This is precisely what would be expected from a pure quadrupole splitting of the nuclear levels, if the crystal remained in a paramagnetic state. However, just the same result would be obtained in the anti-ferromagnetic phase, either with equal numbers of domains oriented in the two directions shown in fig. 3, or with the puckered arrangements of fig. 4., provided that all values of the angle β are equally probable. These observations do not therefore necessarily imply the existence of magnetic order. The latter is, however, confirmed by the following experiments.

A number of measurements were made in which the nuclear demagnetization ended at final fields of up to 0.042 T, applied along

an a-axis of the crystal. With $B = 0.042$ T, a large anisotropy in the emission of γ -rays appears in the plane normal to the crystal c-axis. This shows that ferromagnetic alignment of the spins, parallel to the applied field, has been achieved, and confirms that the temperature is still about 1 mK. In experiments at smaller final fields, such as 0.012 T, the spins orient themselves at right angles to the applied field. This confirms the existence of a 'spin flop' phase, which is consistent only with anti-ferromagnetism in the nuclear spin system.

8— CONCLUSION.

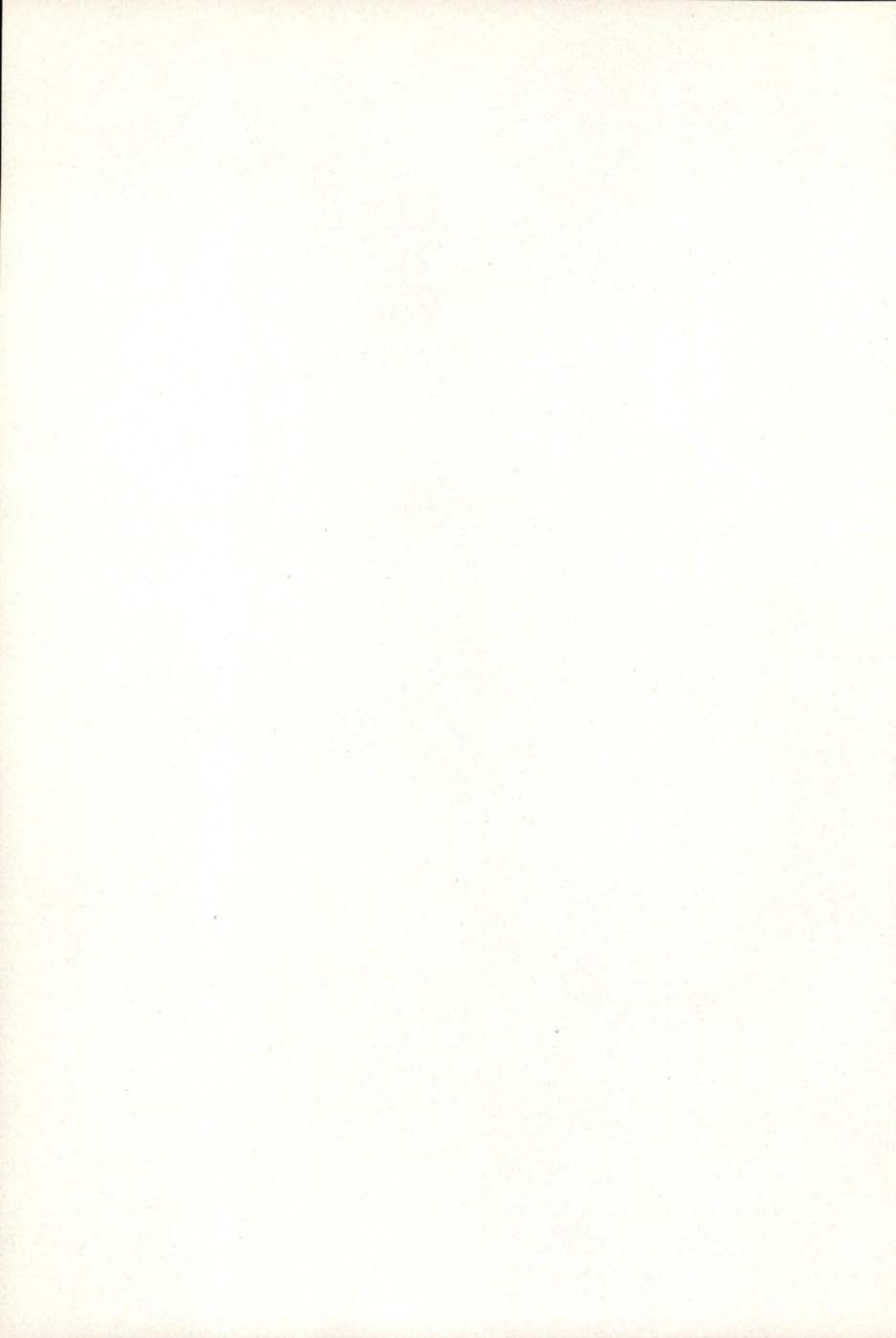
This paper gives a short review of the experimental information which has been obtained on enhanced nuclear magnetism in single crystals of HoVO_4 . The starting point is an investigation at liquid helium temperatures using nuclear magnetic resonance [5]. This gives, for the stable isotope ^{165}Ho ($I=7/2$), the size and anisotropy of the enhancement of the nuclear magnetic moment, together with the nuclear electric quadrupole interaction. The experiments show also that the interactions between the nuclear spins and the induced electron moments of the Ho^{3+} ions are close to those calculated for purely dipolar forces, together with a small contribution from anti-ferromagnetic exchange interaction. Independent measurements of the nuclear susceptibility at temperatures down to 100 mK have been shown to be in excellent agreement with the n.m.r. results, in a paper [10] not discussed above.

From the n.m.r. experiments, predictions can be made [8] about the nature of the ordered phase in the nuclear spin system, and the ordering temperature T_N . The interactions between the enhanced nuclear moments are shown to be mainly dipolar, and novel types of spin arrangements are expected, with a variety of anti-ferromagnetic configurations. These predictions are consistent with the results obtained in nuclear orientation experiments [6] using the γ -ray emission from $^{166\text{m}}\text{Ho}$ ($I=7$), and the value of the nuclear magnetic moment of this isomer is obtained with an accuracy of about 2%.

The author wishes to thank the Portuguese Physical Society and the British Council for their financial assistance. The written version of this paper has been prepared during the tenure of a Leverhulme Emeritus Fellowship, for which the author is indebted to the Leverhulme Trust Fund.

REFERENCES

- [1] J. H. VAN VLECK, *Electric and Magnetic Susceptibilities*, Oxford University Press (1932).
- [2] A. ABRAGAM and B. BLEANEY, *Electron Paramagnetic Resonance*, Oxford University Press (1969).
- [3] J. M. BATTISON, A. KASTEN, M. J. M. LEASK and J. B. LOWRY, *Phys. Lett.*, **55A**, 173 (1975).
- [4] S. J. SWITHEBY, D. Phil. thesis, Oxford (1974).
- [5] B. BLEANEY, F. N. H. ROBINSON and M. R. WELLS, *Proc. R. Soc. Lond.*, **A362**, 179 (1978).
- [6] A. L. ALLSOP, B. BLEANEY, G. J. BOWDEN, N. NAMBU DRIPAD, N. J. STONE and H. SUZUKI, *Proc. R. Soc. Lond.* **A372**, 19 (1980).
- [7] R. A. HABERSTROH, T. I. MORAN and S. PENSELIN, *Z. Phys.* **252**, 421 (1972).
- [8] B. BLEANEY, *Proc. R. Soc. Lond.*, **A370**, 313 (1980).
- [9] H. SUZUKI, N. NAMBU DRIPAD, B. BLEANEY, A. ALLSOP, G. J. BOWDEN, I. A. CAMPBELL and N. J. STONE, *J. Phys. Paris*, **39**, C6-800 (1978).
- [10] B. BLEANEY, K. V. LOFTUS and H. M. ROSENBERG, *Proc. R. Soc. Lond.*, **A372**, 9 (1980).



CRITICAL BEHAVIOUR OF DARK CURRENT IN FERROELECTRIC $\text{Bi}_{0.08}\text{Sb}_{0.92}\text{SI}$ (*)

M. RENATA CHAVES and M. HELENA AMARAL

Laboratório de Física, Universidade do Porto, 4000 Porto, Portugal

S. ZIOLKIEWICZ

Laboratoire d'Ultrasons (**), de l'Université P. et M. Curie, 75230 Paris Cedex 05, France

(Received 17 November 1980)

ABSTRACT — Dark current as a function of temperature has been used to study the ferro-paraelectric phase transition in $\text{Bi}_{0.08}\text{Sb}_{0.92}\text{SI}$.

A simple model is proposed to account for the correlation between the temperature dependence of the activation energy of the impurity levels and the temperature dependence of the intrinsic absorption edge in a one-dimensional structure which $\text{Bi}_{0.08}\text{Sb}_{0.92}\text{SI}$ closely resembles.

1 — INTRODUCTION

Some $\text{A}_V\text{B}_{VI}\text{C}_{VII}$ compounds exhibit a ferro-paraelectric phase transition of displacive nature, accompanied by a change in the coefficient of the temperature dependence of the width of the forbidden gap (E_g) at the critical temperature (T_c); if the transition is of first order there is also a discontinuity in the intrinsic absorption edge at T_c [1]. In SbSI , for instance, this discontinuity is about 0.03 eV; also $(\partial E_g^+ / \partial T) \simeq -9 \times 10^{-4} \text{ eV K}^{-1}$ and $(\partial E_g^- / \partial T) \simeq -2.2 \times 10^{-3} \text{ eV K}^{-1}$

(*) Supported by J.N.I.C.T. Res. Grant 106.79.27., J.N.I.C. (Portugal) and NATO Res. Grant 1824.

(**) Associated with the C.N.R.S. (France).

in the paraelectric and ferroelectric regions, respectively [2]. A similar behaviour is also observed in SbSBr and BiSBr [2].

These effects should lead to anomalies in the temperature dependence of dark current in the critical region due to the change in the activation energy of the impurity levels, as it was in fact observed in SbSI [3,4].

In the following we have studied the critical behaviour of dark current in ferroelectric mixed compound $\text{Bi}_{0.08}\text{Sb}_{0.92}\text{SI}$ and a simple model is proposed to account for the correlation between the temperature dependence of the activation energy of the impurity levels and the temperature dependence of E_g in a one-dimensional structure which $\text{Bi}_{0.08}\text{Sb}_{0.92}\text{SI}$ closely resembles.

2 — EXPERIMENTAL PROCEDURE

Experimental results were obtained by using needle-shaped crystals, 10–15 mm in length and about 0.2 mm² in cross section, as determined by microscope measurements. Silver or gold paste contacts were used. The crystals were polarised with a d.c. field (200–400 V cm⁻¹) while being cooled down slowly to a temperature well below the critical temperature; care was taken never to subject them to thermal shock. The samples were then heated at constant rates of approximately 1 mK s⁻¹ far from the transition while, near the critical temperature, this rate was less than 0.5 mK s⁻¹. Dark current along the c-axis was measured with a Keithley 610 C electrometer under d.c. fields over a range 200–400 V cm⁻¹. The entire apparatus system was shielded from external electric fields.

3 — EXPERIMENTAL RESULTS AND DISCUSSION

In figure 1 we plotted dark current (*I*) versus inverse temperature for $\text{Bi}_{0.08}\text{Sb}_{0.92}\text{SI}$; this figure clearly shows a different behaviour of *I* above and below critical temperature. Temperature dependence of dark current and its temperature derivative near T_c are shown in

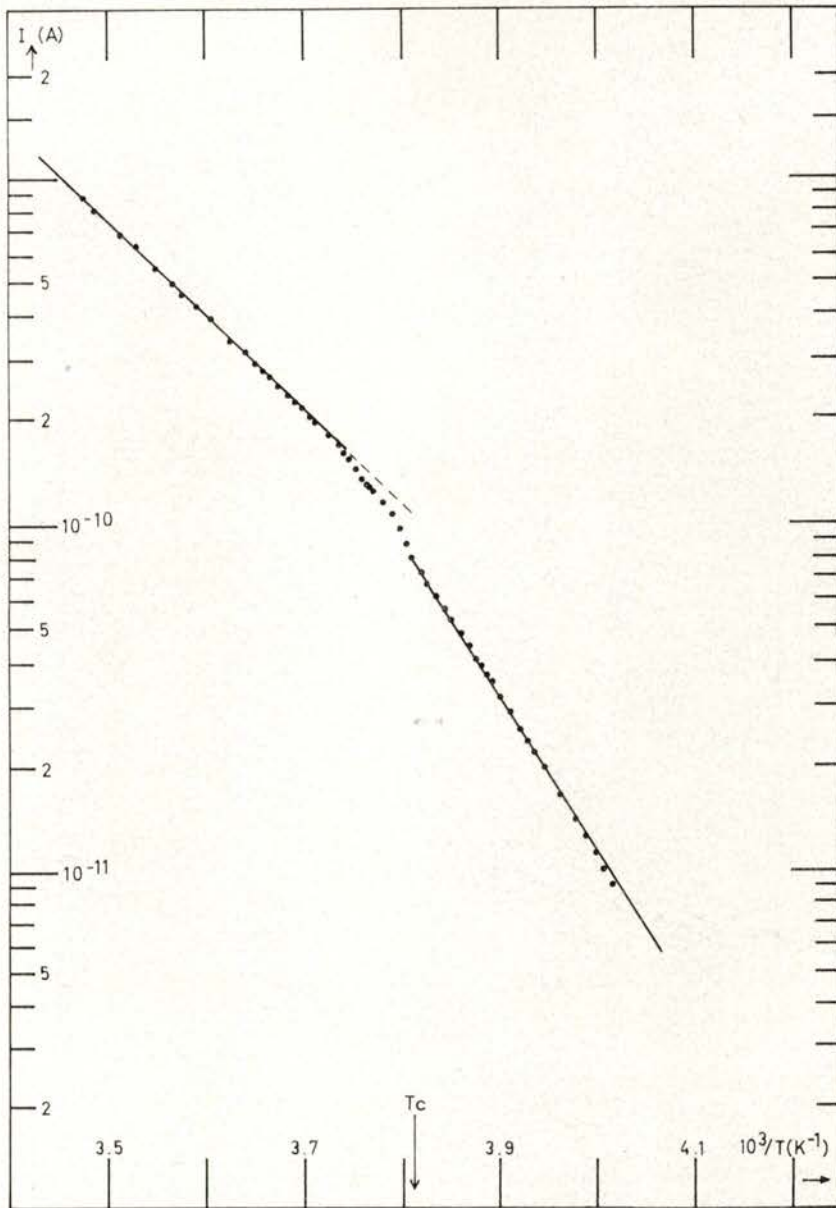


Fig. 1—Dependence of dark current (I) (logarithmic scale) on the inverse temperature near the critical point.

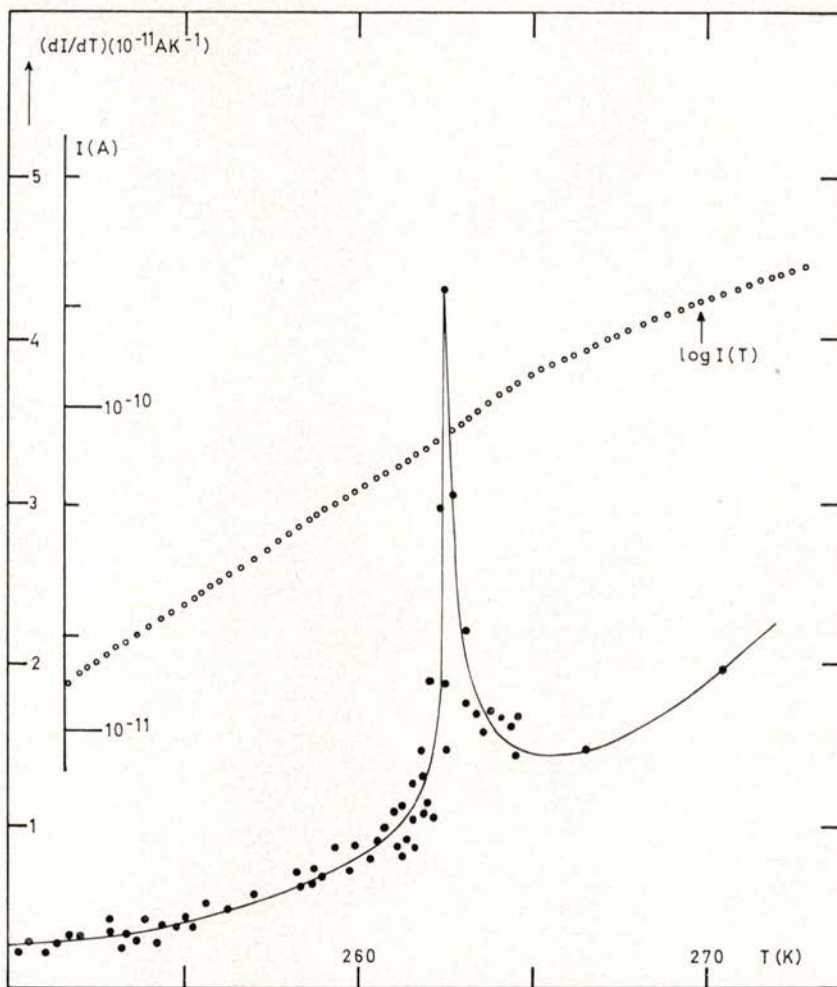


Fig. 2 — Temperature dependences of the dark current (I) (logarithmic scale) and of the temperature derivative of dark current near the critical temperature, $T_c = 262.4$ K.

figure 2. A method of sliding averages was used to calculate the first derivative of I [5]. We take, as usual, the relative maximum of (dI/dT) as the critical temperature (T_c) and for $\text{Bi}_{0.08}\text{Sb}_{0.92}\text{SI}$ we find $T_c \approx 262.4$ K, lower than the values reported for SbSI , as expected [6, 7].

From figure 1 we can see that the dark current above (I_+) and below (I_-) T_c obeys the relations

$$I_{\pm} = A_{\pm} \exp (-E_{\pm}^* / kT) \quad (1)$$

where A_{\pm} are constants, E_{\pm}^* are the effective activation energies of the impurity levels and k is the Boltzmann constant. We determined:

$$E_{+}^* \simeq 0.54 \pm 0.01 \text{ eV} ; A_{+} \simeq 2.670 \text{ A} ;$$

$$E_{-}^* \simeq 0.90 \pm 0.01 \text{ eV} ; A_{-} \simeq 1.789 \times 10^7 \text{ A}$$

If the changes in mobility and effective mass of free carriers can be taken as relatively small, the anomalous variation of dark current at the critical region will be mainly associated with the free carrier concentration. Then for a semiconductor with an impurity level of activation energy E , we have $I(T) = A \exp (-E/kT)$.

It seems plausible, as we have assumed for $SbSI$ [4] that the activation energies of impurity levels vary with temperature accompanying a width variation of the forbidden band. Taking into account the experimental results concerning the temperature dependence of dark current, E must be a linear function of temperature in both phases, at least in the range of temperatures we have studied. So

$$\begin{aligned} E_{+} &= E_{0+} - a_{+}(T - T_c) & \text{for } T > T_c \\ E_{-} &= E_{0-} - a_{-}(T - T_c) & \text{for } T < T_c \end{aligned}$$

where E_{0+} and E_{0-} are the activation energies of the impurity levels at T_c in the paraelectric and ferroelectric phases, respectively, and a_{+} , a_{-} are constants, Accordingly,

$$I_{\pm} = A \exp (a_{\pm} / k) \cdot \exp [-(E_{0\pm} + a_{\pm} T_c) / kT]$$

and by comparison with (1)

$$E_{\pm}^* = E_{0\pm} + a_{\pm} T_c ; A_{\pm} = A \exp (a_{\pm} / k)$$

The shift of the activation energy (ΔE_c) at the critical temperature is given by

$$I_+(T_c) / I_-(T_c) = \exp(\Delta E_c / kT_c)$$

From our data we obtain:

$$I_+(T_c) = 1.16 \times 10^{-10} \text{ A} ; I_-(T_c) = 9.60 \times 10^{-11} \text{ A} ; \\ \Delta E_c = |E_{0+} - E_{0-}| = 0.0041 \text{ eV} ; |a_+ - a_-| = 13.6 \times 10^{-4} \text{ eV K}^{-1}.$$

The relation $|a_+ - a_-| = k \ln(A_-/A_+)$ would, naturally, lead to the same value, $13.6 \times 10^{-4} \text{ eV K}^{-1}$.

These results show that the change in the effective activation energy of the impurity levels at T_c is approximately 0.36 eV whereas the actual shift of the activation energy ΔE_c has a much lower value, about 0.0041 eV. This difference seems to support our assumption that 0.54 and 0.90 eV are not the actual values for the activation energies of the impurity levels.

Experimental results reported for $\text{Bi}_x\text{Sb}_{1-x}\text{SI}$ suggest that one of the effects of the atomic substitution of Sb by Bi is the existence of a tricritical point in the (x, T) plane, localized around $x \simeq 0.17$ and $T_t \simeq 211 \text{ K}$ [8, 9]. Therefore, as long as the phase transition remains of first order, a decreasing shift of the intrinsic absorption edge at T_c with increasing x is expected. We have found $\Delta E_c = 0.011 \text{ eV}$ for SbSI which is a higher value than that observed for $\text{Bi}_{0.08}\text{Sb}_{0.92}\text{SI}$ (0.0041 eV).

4 — THEORETICAL MODEL

$\text{AV}_\text{VI}\text{CV}_\text{VII}$ crystals are generally thin needles, indicating highly anisotropic properties and its structure consists of chains formed by the charged groups $(\text{V}-\text{VI})^+$ and $(\text{VII})^-$ running parallel to the c -axis [10]. Bonding between neighbouring chains is weak, probably Van der Waals type, and so if interactions between chains can be

neglected, those compounds may approximately be represented by a linear chain of alternating groups of ions regularly spaced by a distance b as in figure 3. We represent the state in which an extra

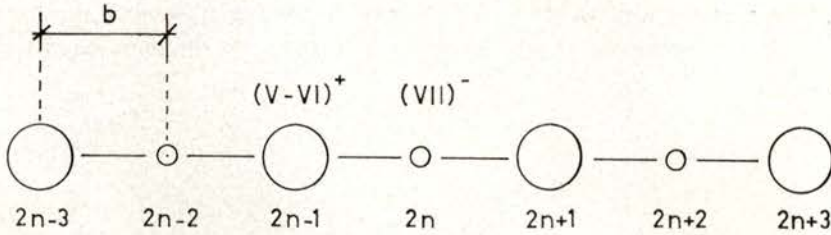


Fig. 3 — Schematic representation of one-dimensional lattice.

electron occupies the $2n$ site of the linear chain by the ket $|2n\rangle$ and we assume that $\{|2n\rangle\}$ form a complete set of orthonormal eigenfunctions of the Hamiltonian \hat{H} (n positive or negative integer) [11]. For the sake of simplicity we take the Hamiltonian of the system to satisfy:

$$\begin{aligned} \langle 2n | \hat{H} | 2n \rangle &= E_1 \\ \langle 2n+1 | \hat{H} | 2n+1 \rangle &= E_2 \\ \langle 2n | \hat{H} | 2n+m \rangle &= -A \quad \text{if } m = \pm 1 \\ \langle 2n | \hat{H} | 2n+m \rangle &= 0 \quad \text{otherwise} \end{aligned}$$

where E_1, E_2, A are real quantities and $E_1 < E_2$.

With these assumptions, we have two energy bands for the electronic states separated by an energy gap $E_g = E_2 - E_1$. If there is an electronic defect in the chain, e.g. an imperfection in the site 0, one matrix element becomes different, $\langle 0 | \hat{H} | 0 \rangle = E_1 + \Delta E$ ($\Delta E > 0$), the other elements remain unchanged.

We look for solutions of Schrödinger equation of the form

$$|\phi\rangle = \exp(-iEt/\hbar) \sum_n a_n |n\rangle,$$

with

$$a_n \text{ (for } n < 0, n \text{ even)} = \alpha e^{n\lambda b}; a_n \text{ (for } n > 0, n \text{ even)} = \alpha e^{-n\lambda b}$$

$$a_n \text{ (for } n < 0, n \text{ odd)} = \beta e^{n\lambda b}; a_n \text{ (for } n > 0, n \text{ odd)} = \beta e^{-n\lambda b}$$

where α and β are constants and λ a real positive number.

If we substitute this trial solution into Schrödinger's equation, we have:

$$\begin{array}{r} \cdot \\ \cdot \\ E \alpha e^{-2\lambda b} = E_1 \alpha e^{-2\lambda b} - A \beta e^{-\lambda b} - A \beta e^{-3\lambda b} \\ E \beta e^{-\lambda b} = E_2 \beta e^{-\lambda b} - A \alpha e^{-2\lambda b} - A \alpha \\ E \alpha = (E_1 + \Delta E) \alpha - A \beta e^{-\lambda b} - A \beta e^{-\lambda b} \\ E \beta e^{-\lambda b} = E_2 \beta e^{-\lambda b} - A \alpha - A \alpha e^{-2\lambda b} \\ E \alpha e^{-2\lambda b} = E_1 \alpha e^{-2\lambda b} - A \beta e^{-3\lambda b} - A \beta e^{-\lambda b} \\ \cdot \\ \cdot \end{array}$$

The middle five equations are satisfied provided that

$$\begin{aligned} \beta^2 (E - E_2) &= \alpha^2 (E - E_1) \\ e^{-\lambda b} &= -\alpha (E - E_1 - \Delta E) / (2 A \beta) \\ e^{+\lambda b} &= \alpha (E_1 - E - \Delta E) / (2 A \beta). \end{aligned}$$

These equations are consistent only if,

$$[(E - E_1)^2 - (\Delta E)^2] (E - E_2) = 4 A^2 (E - E_1).$$

The energy of the trapped electron is given by E in this expression if $0 < (E - E_1) < E_g$. Taking $E_2 - E_1 = E_g$ and $E - E_1 = x$, we have,

$$(x - E_g) [x^2 - (\Delta E)^2] = 4 A^2 x \quad (2)$$

We now suppose ΔE and A to be very slow varying functions of temperature as compared with E_g and x . This seems to be the

situation for A_V B_{VI} C_{VII} compounds. Taking the temperature derivative of the last equation, we find.

$$dx/dT = (dE_g/dT) \cdot [x^2 - (\Delta E)^2] / [3x^2 - 2E_g x - (\Delta E)^2 - 4A^2].$$

So the temperature derivative of the activation energy (x) depends on the temperature derivative of E_g , on the energy of the trapped electron in the lattice defect and on the probability amplitude, per unit time, for the electron to jump from one atom to the next one. If ΔE , $A \gg x$, then

$$dx/dT \approx (dE_g/dT) \cdot (\Delta E)^2 / [(\Delta E)^2 + 4A^2].$$

Therefore the thermal derivative of the impurity activation energy is smaller than the thermal derivative of the gap width E_g .

We have collected in table I values of x ($0 < x < E_g$) and dx/dT calculated for different values of $(\Delta E)^2$ and A^2 . We have taken $E_g = 1.9 - 0.003 \Delta T$ eV, where $\Delta T = T - T_c$ was assumed to be 1K; these values are suggested by the experimental data for Sb₃I [2].

TABLE I

$(\Delta E)^2$ [(eV) ²]	$4A^2$ [(eV) ²]	x [eV]	dx/dT [eVK ⁻¹]
0.05	0.01	0.221	0.059×10^{-4}
0.1	1	0.141	1.5
0.5	0.5	0.546	2.8
0.5	1	0.442	3.6
0.75	0.75	0.621	4.1
1.85	1	0.936	7.7
1.85	10	0.285	4.1
1.85	100	0.034	0.55
1.88	0.1	1.29	3.4
1.899	0.01	1.37	0.49
1.899	1	0.948	7.9
1.899	1.7	0.804	8.0
1.899	8	0.345	4.9
3	0.1	1.581	9.4
5	0.1	1.796	24

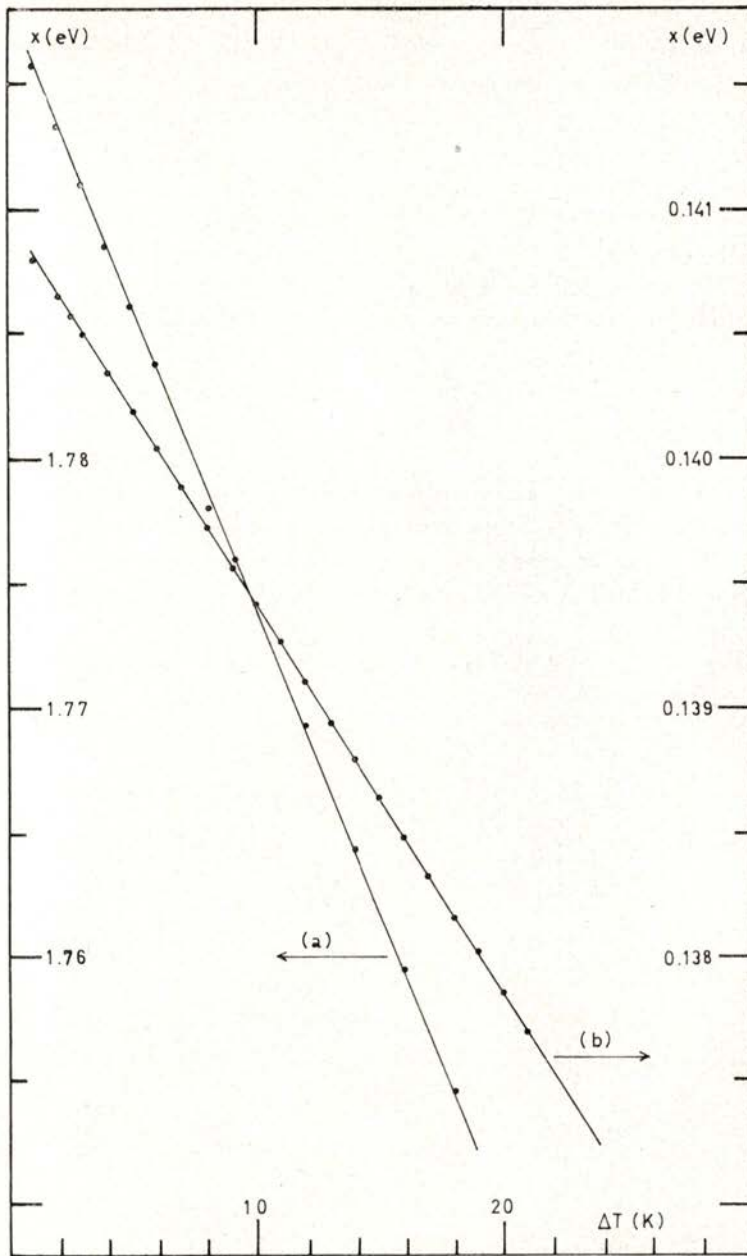


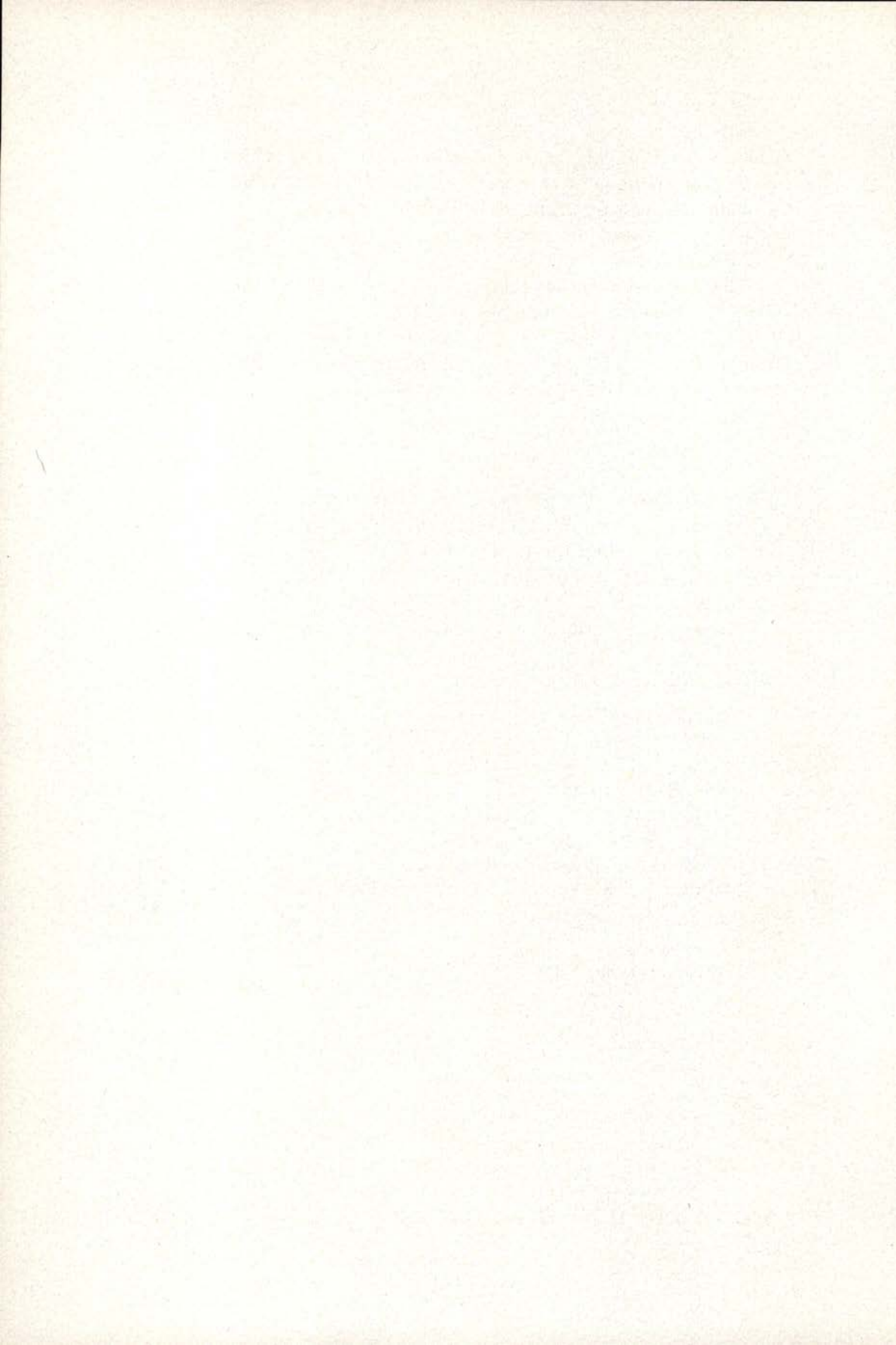
Fig. 4 — Theoretical values of x versus $\Delta T = T - T_c$ taken from eq. (2),
with $E_g = 1.9 - 0.003 \Delta T$ eV
curve a) $(\Delta E)^2 = 0.1 \text{ (eV)}^2$; $4A^2 = 1 \text{ (eV)}^2$.
curve b) $(\Delta E)^2 = 5 \text{ (eV)}^2$; $4A^2 = 0.1 \text{ (eV)}^2$.

In a range of $\Delta T = 20$ K, x varies linearly with temperature as can be seen in fig. 4. Hence our simple model seems to account for the main results concerning dark current behaviour in $SbSI$ and $Bi_{0.08}Sb_{0.92}SI$ near the critical region.

The authors wish to express their gratitude to Prof. M. Balkanski for helpful suggestions and to Prof. M. K. Teng and Dr. A. Levelut, for valuable discussions. Facilities from the 'Service Culturel, Scientifique et de Coopération Technique de l'Ambassade de France au Portugal' are gratefully acknowledged.

REFERENCES

- [1] G. HARBEKE — *J. Phys. Chem. Solids*, **24**, 957 (1963).
- [2] F. M. FRIDKIN, E. I. GERZANICH, I. I. GROSHIK, and V. A. LYAKHOVITSKAYA — *JETP Letters*, **4**, 139 (1966).
- [3] V. N. NOSOV and V. M. FRIDKIN — *Sov. Phys — Solid State*, **8**, 113 (1966).
- [4] R. CHAVES, H. AMARAL and S. ZIOLKIEWICZ, *J. Physique*, **41**, 259 (1980).
- [5] F. C. ZUMSTEG and R. D. PARKS, *Phys. Rev. Lett.*, **24**, 520 (1970).
- [6] A. KIKUCHI, Y. OKA and E. SAWAGUCHI, *J. Phys. Soc. Japan*, **23**, 337 (1967).
- [7] M. K. TENG, M. MASSOT, M. BALKANSKI and S. ZIOLKIEWICZ, *Phys. Rev.*, **B17**, 3695 (1978).
- [8] M. R. CHAVES, M. H. AMARAL and S. ZIOLKIEWICZ — *Europhysics Conference Abstracts*, **3G**, 283 (1980).
- [9] M. K. TENG, M. MASSOT, M. R. CHAVES, M. H. AMARAL, S. ZIOLKIEWICZ and W. YOUNG — *Phys. Stat. Sol.* (in press).
- [10] M. MATY'ÁŠ and J. HORÁK — *Phys. Stat. Sol. (a)*, **36**, K137 (1976).
- [11] R. FEYNMAN, *The Feynman Lectures on Physics*, vol. III, Addison-Wesley London, 1969.



DYNAMICAL BEHAVIOUR OF THE ALIPHATIC CHAINS OF 4,4'-DIHEXYLOXYAZOXYBENZENE IN THE NEMATIC PHASE. (*)

A. F. MARTINS, J. B. BONFIM

Centro de Física da Matéria Condensada (INIC)
Av. Prof. Gama Pinto, 2 - 1699 Lisboa Codex, Portugal

A. M. GIROUD-GODQUIN

Laboratoire de Chimie Organique Physique, ERA CNRS n° 20,
Département de Recherche Fondamentale, Centre d'Etudes Nucléaires
de Grenoble, 85 X, F.38041 Grenoble Cedex, France

(Received 27 November 1980)

ABSTRACT—The proton spin-lattice relaxation time T_1 has been measured as a function of frequency and temperature in the nematic phase of hexyloxyazoxybenzene completely deuterated on the benzene rings (6.OAB-D₈). The results show that the aliphatic chains are dynamically coupled to the nematic director in a rather strong fashion ($T_1 \sim \omega^{-1/2}$), and suggest that the average molecular conformation of 6.OAB-D₈ changes appreciably with temperature.

1—INTRODUCTION

Phenomenological properties of nematic liquid crystals have been extensively studied and are now rather well understood [1]. On the other hand, studies aimed to relate phenomenological properties to microscopic structure and dynamics are scarce.

In this paper, we pursue previous efforts to understand the internal order [2-4] and dynamics [5-9] of nematic materials, and concentrate our attention on the most studied homologous series of these mate-

(*) Work partially supported by the French Ministry of Foreign Affairs under the franco-portuguese scientific cooperation program. First presented as an oral communication at the Second National Conference of the Portuguese Physical Society (Porto, 16-18 April 1980).

rials, i.e., 4,4'-dialkoxyazoxybenzenes (m.OAB, for short, where $m=1, 2, \dots$ stands for the number of carbon atoms in the aliphatic chains).

In previous NMR studies related to the m.OAB series, only the first element (PAA, or 1.OAB) was considered, either normal or methyl-deuterated, and definite conclusions were only reached on the dynamics of the most rigid part of the molecule [6,7]. In particular, it was shown that the benzene skeleton of the molecule is strongly coupled to the long wavelength thermal fluctuations of the nematic director, which leads to a characteristic frequency dependence of the corresponding proton spin-lattice relaxation time $T_1 \sim \omega^{1/2}$. The dynamics of the terminal CH_3 groups was indirectly considered in refs. [5] and [6], where it was concluded that the relaxation of these groups should *not* depend appreciably on the long wavelength thermal fluctuations. This conclusion has been recently confirmed by direct measurements of the proton $T_1(T, \omega)$ on the same material, but now deuterated on the benzene rings (PAA- ϕD_8 , or simply PAA- D_8) so as to probe only the relaxation of the CH_3 groups [9].

In this paper we will discuss a set of results obtained from systematic measurements of the proton spin-lattice relaxation time T_1 as a function of Larmor frequency ω and temperature T , over the nematic range of the element with $m=6$, deuterated on the benzene rings (6.OAB- D_8). This selective deuteration ensures that the measured values of T_1 only contain contributions from the aliphatic chains, which are so *directly* probed.

In section 2 we give our experimental results and point out the techniques used in this work. In section 3 we discuss these results and try to answer the following questions: (i) how strong is the coupling of the flexible chains in higher homologs to the long-wavelength thermal fluctuations of the director; and (ii) can we get, from T_1 measurements, some insight on the changes (if any) of the average conformation of the chains with temperature? Finally, in Section 4, we present our conclusions.

2 — EXPERIMENTAL RESULTS

The synthesis of 4,4'-dihexyloxyazoxybenzene- D_8 was carried out as follows [10]. First, by nitration of phenol- D_6 we got p-nitrophenol- D_5 , which was purified from o-nitrophenol by column chro-

matography (alumina, benzene). Addition of hexylbromide on p-nitrophenol in presence of potassium carbonate produced p-hexyloxy nitrobenzene- D_4 . This compound was treated by lithium aluminium hydride in dry ether at -70°C . The excess of lithium aluminium hydride was then decomposed with sodium hydroxide and water. The residue was dissolved in acetic acid and after the addition of hydrogen peroxide, the solution was held at 65°C for 48 hours. The precipitate of 4,4'-dihexyloxyazoxybenzene- D_8 (yield = 75 %) was finally crystallised from ethanol giving pale yellow needles with melting point at 81°C and nematic-isotropic transition at 129.5°C .

After purification, the sample ($\sim 0.3 \text{ cm}^3$) was introduced in a NMR quartz tube, degased and sealed under vacuum.

Measurements of the proton spin-lattice relaxation time T_1 were performed at 25, 40, 56 and 90 MHz over the whole nematic range by using the $\pi - \tau - \pi/2$ pulse sequence on a Bruker SXP/4-1000 spectrometer. The temperature of the sample was controlled to within $\pm 0.3^\circ\text{C}$, and the estimated error in the absolute value was less than 1°C .

The results of the measurements of T_1 as a function of temperature are displayed in Fig. 1 for three working frequencies. The

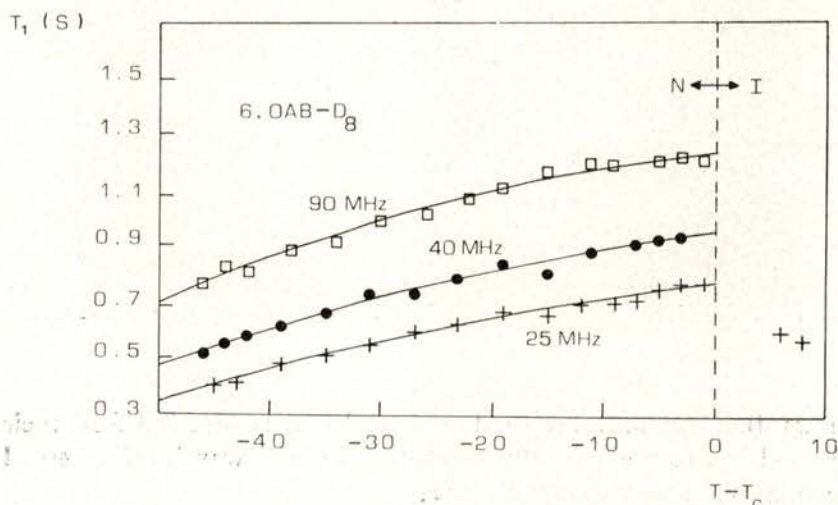


Fig. 1—Observed temperature dependence of proton spin-lattice relaxation time T_1 in the nematic phase of 6.OAB- D_8 at 25, 40 and 90 MHz.

results obtained at 56 MHz are omitted for the sake of clarity of the figure.

An example of the frequency dependence of T_1 is shown in Fig. 2, for $T=90$ and 118°C . It is seen that $1/T_1 \sim \omega^{-1/2}$; this same behaviour was found at any other temperature within the nematic phase.

3 — DISCUSSION

The most striking feature of the results in figs. 1 and 2 is their qualitative resemblance with the results previously obtained for PAA [5]. We recall that PAA is a rather rigid molecule and that the present results strictly refer to the *aliphatic chains* of 6.OAB. The characteristic frequency dependence $1/T_1 \sim \omega^{-1/2}$ displayed in fig. 2

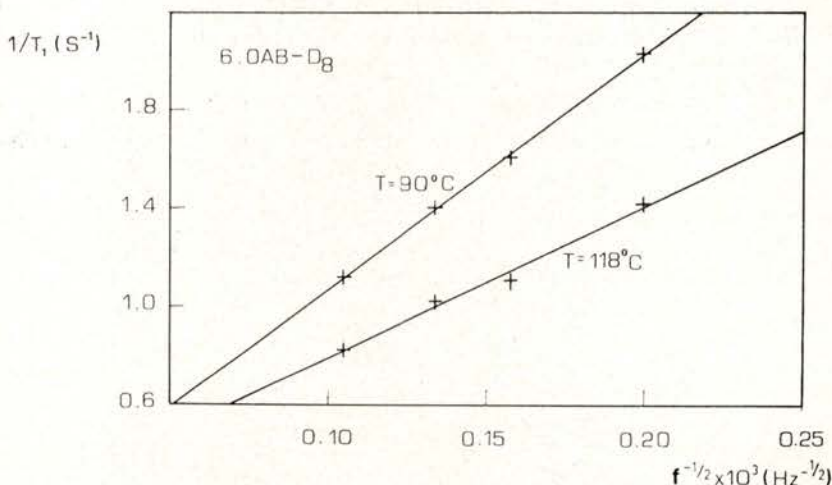


Fig. 2 — Observed frequency dependence of $1/T_1$ in the nematic phase of 6.OAB-D₈, at $T = 90$ and 118°C .

shows that not only the rigid core of the molecules but also their terminal chains are strongly coupled to the long-wavelength thermal fluctuations of the nematic director.

Assuming that the frequency-dependent part of the relaxation is mainly due to the modulation of dipolar interactions, the observed behaviour may be quantitatively explored in the framework of the

theory of spin-lattice relaxation in nematics developed in ref. [6]. This treatment contains the essential features of the more sophisticated theory proposed later on by Freed [8].

The relaxation rate due to dipolar interactions among the chain protons may be written :

$$\frac{1}{T_1} = \frac{9\sqrt{2}}{8\pi} \gamma^4 \hbar^2 \langle \Lambda(r_{ij}, \theta_{ij}) \rangle^2 \left(\frac{k_B T S^2}{K^{3/2}} \Gamma^{1/2} \right) \omega^{-1/2} + \frac{1}{T'_1} \quad (1)$$

where $\Lambda(r_{ij}, \theta_{ij})$ is a function of the chain configuration (θ_{ij} is the angle made by the interproton vector r_{ij} with the molecular axis), S is the Maier-Saupe degree of order, and Γ and K are respectively an effective viscosity and an effective Frank elastic constant, both defined in ref. [6]. The term $1/T'_1$, which is frequency independent, contains all the contributions to the relaxation rate that do not couple to the long-wavelength thermal modes.

In order to facilitate the following discussion, expression (1) may be written in the form :

$$1/T_1 = A(\Delta, T) \omega^{-1/2} + 1/T'_1 \quad (2)$$

Defining $C(K, S, \Gamma)$ as

$$C(K, S, \Gamma) = \frac{k_B T S^2}{K^{3/2}} \Gamma^{1/2} \quad (3)$$

we may write $A \sim \langle \Lambda \rangle^2 C$.

The coefficient $A(\Delta, T)$ may be obtained as a function of T from the slopes of linear least squares fits of T_1^{-1} as a function $\omega^{-1/2}$, at different temperatures (cf. fig. 2). The resulting values are displayed in fig. 3. We see that A is strongly dependent on T , in contrast to the case of PAA, where a negligible temperature dependence was found [6]. To understand this difference, we have to go into the details of $A(\Delta, T)$ and estimate separately the temperature dependence of $C(K, S, \Gamma)$ and $\langle \Lambda(r_{ij}, \theta_{ij}) \rangle$.

The value and temperature dependence of $C(K, S, \Gamma)$ may be estimated by taking

$$K \approx \frac{1}{3} K_{11} (1 + K_{22}/K_{11} + K_{33}/K_{11}) \quad (4)$$

(which is equivalent to assuming an isotropic distribution of the fluctuation wave-vectors) and $\Gamma \approx \gamma_1$ [6], and quoting from the literature the values of S [11], K_{11} [12, 13], K_{33}/K_{11} [12] and γ_1 [14], as a function of temperature. The absolute values of K_{22}/K_{11} have not been given so far for 6.OAB but we can estimate them by comparison with heptylazoxybenzene [12]. We find that the temperature variation of C (K, S, Γ) is much stronger here than in the case of PAA [6] (see

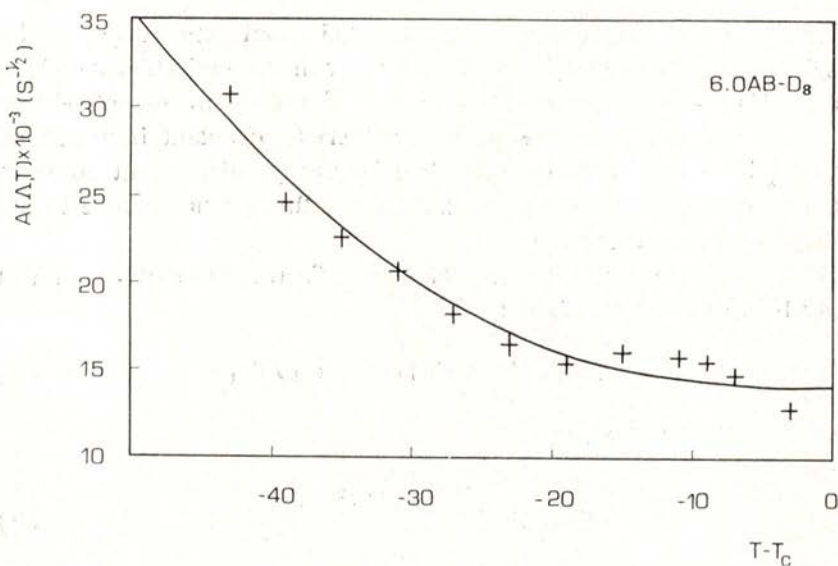


Fig. 3 — Observed temperature dependence of the function $A(\Delta, T)$ given by eq. (2) in the text.

fig. 4). This stands on the fact that both the elastic constant $K_{11}(T)$ and the twist viscosity $\gamma_1(T)$ increase much more strongly with decreasing temperature in 6.OAB than in PAA [12, 14]. The order parameters have similar behaviour, and in 6.OAB both K_{22}/K_{11} and K_{33}/K_{11} are practically independent of temperature [12].

The function $\Lambda(r_{ij}, \theta_{ij})$, in expression (1), is rather complex and may only be written down completely after a dynamic model for the chain is assumed, which is not the aim of this paper. Its average value, $\langle \Lambda(r_{ij}, \theta_{ij}) \rangle$ would vanish for a completely disordered chain. So, the fact that we observe experimentally the characteristic frequency

dependence $T_1 \sim \omega^{1/2}$ predicted by expression (1) is in agreement with direct measurements of a non-vanishing order along the chains [4].

The extent to which the chains are coupled to the director, at different temperatures and frequencies, can be evaluated by subtracting from the measured values of $1/T_1$ the values of $1/T'_1$ obtained from plots such as that in fig. 2. We find, e.g. at $\omega = 2\pi \times 40$ MHz and $T - T_c = 15^\circ\text{C}$, that the long-wavelength contribution to the relaxation

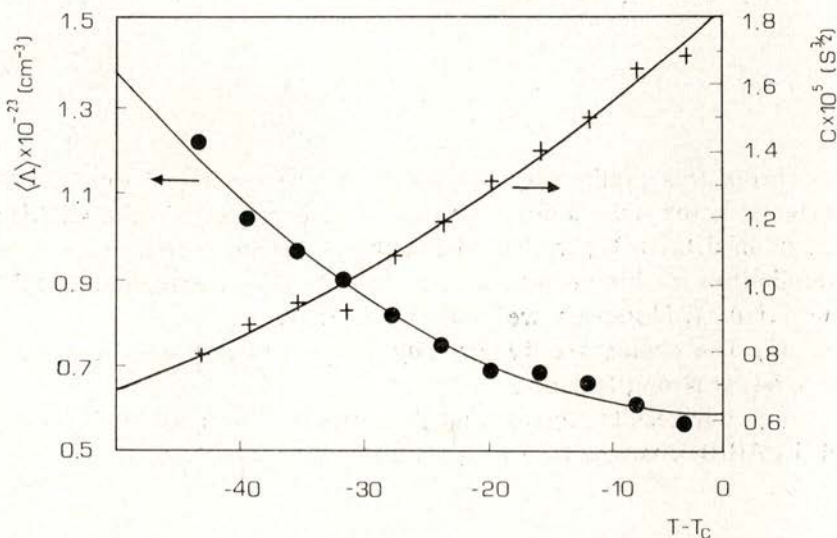


Fig. 4 — Estimated temperature dependence of the functions $C(K, S, F)$ and $\langle \Lambda(r_{ij}, \theta_{ij}) \rangle$ given by eqs. (3) and (5) in the text.

rate represents 83% of the total rate. This indeed reflects a strong coupling of the chains to the director, and it should be noted that this coupling increases with decreasing frequency (see expression (1)). On the other hand, as expected, it decreases as we approach the nematic to isotropic transition temperature T_c .

The temperature variation of $\langle \Lambda(r_{ij}, \theta_{ij}) \rangle$ can be estimated now from our knowledge of $A(\Lambda, T)$ and $C(K, S, \Gamma)$, through the expression

$$\langle \Lambda \rangle^2 = \frac{8\pi}{9\sqrt{2}} (\gamma^4 \hbar^2)^{-1} \cdot (A/C) \quad (5)$$

which comes directly from (1), (2) and (3). This is also shown in fig. 4, and we see that $\langle \Lambda(r_{ij}, \theta_{ij}) \rangle$ varies by more than a factor of two, through the nematic range of 6.0AB-D₈. This suggests that the average molecular conformation of 6.0AB-D₈ changes appreciably with temperature. Unfortunately the detailed nature of these conformation changes cannot be obtained, within this framework, before a detailed knowledge of the function $\Lambda(r_{ij}, \theta_{ij})$ is available. This point will be discussed in future work. We feel that some aspects of the theoretical model proposed in ref. [2] by one of us may be conveniently tested by detailed research along these lines.

4 — CONCLUSION

From this preliminary discussion of the results of our measurements of the spin-lattice relaxation time of protons in the aliphatic chains of 6.0AB-D₈, we have been able to disclose some microscopic peculiarities of this material as compared to its lowest homolog PAA (or 1.OAB). Moreover, we have shown that:

- (i) The chains are dynamically coupled to the nematic director in a rather strong fashion;
- (ii) our results suggest that the average molecular conformation of 6.0AB-D₈ changes with temperature.

The authors are indebted to Mrs. Inês S. Costa for helping in the synthesis and preparation of the samples.

REFERENCES

- [1] P. G. DE GENNES, *The Physics of Liquid Crystals* (Clarendon Press, Oxford, 1975).
- [2] A. F. MARTINS, *Phys. Rev. Lett.*, **43**, 158 (1980)
- [3] F. VOLINO, A. F. MARTINS, and A. J. DIANOUX, *Molec. Cryst. Liquid Cryst.* (in the press).
- [4] B. DELOCHE and J. CHARVOLIN, *J. Phys. (Paris)*, **37**, 1497 (1976).
- [5] A. F. MARTINS, *Phys. Rev. Lett.*, **28**, 289 (1972).
- [6] A. F. MARTINS, *Portgal. Phys.*, **8**, 1 (1972).

- [7] Most of the work on nuclear spin-lattice relaxation in nematics was recently reviewed by G. WADE, *Ann. Rev. Phys. Chem.*, **28**, 47 (1977); see also ref. [6].
- [8] J. H. FREED, *J. Chem. Phys.*, **66**, 4183 (1977).
- [9] J. J. VISINTAINER *et al.*, *J. Chem. Phys.*, **66**, 3347 (1977); J. B. BONFIM and A. F. MARTINS, to be published.
- [10] M. J. DEWAR, R. S. GOLDBERG, *Tetrahedron Lett.*, **24**, 2717 (1966).
- [11] E. G. HANSON and Y. R. SHEN, *Mol. Cryst. Liquid Cryst.*, **36**, 193 (1976).
- [12] W. H. de JEU and W. A. CLAASSEN, *J. Chem. Phys.*, **67**, 3705 (1977).
- [13] W. H. de JEU and W. A. CLAASSEN, *J. Chem. Phys.*, **68**, 102 (1978).
- [14] A. C. DIOGO and A. F. MARTINS, *Mol. Cryst. Liquid Cryst.* (in the press).



NUCLEAR SPIN-LATTICE RELAXATION IN THE COLUMNAR AND ISOTROPIC PHASES OF A DISCOTIC LIQUID CRYSTAL (H8.OTP). STRONG FREQUENCY DEPENDENT EFFECTS IN THE ISOTROPIC PHASE (*).

A. F. MARTINS and A. C. RIBEIRO

Centro de Física da Matéria Condensada (INIC)
Av. Prof. Gama Pinto, 2 - 1699 Lisboa Codex, Portugal

(Received 10 December 1980)

ABSTRACT—The dynamics of disc-like molecules in the isotropic and mesomorphic (columnar) states is studied by the NMR technique. The proton spin-lattice relaxation rate $1/T_1$ has been measured as a function of Larmor frequency between 10 and 90 MHz, and as a function of temperature over the whole mesomorphic state of hexa-n-octyloxytriphenilene (H8.OTP) and in the isotropic phase up to 90K above the clearing point T_{DI} . No discontinuity of $1/T_1$ is observed at T_{DI} , which reflects the incapacity of the lateral aliphatic chains to become significantly ordered on going from the isotropic to the mesomorphic state. $1/T_1$ is strongly dependent on the Larmor frequency over the whole range of temperatures covered. The frequency dependence of $1/T_1$ in the isotropic phase remains unchanged over more than 100K above T_{DI} and is shown to agree qualitatively with the predictions of available theories, but not quantitatively. The temperature dependence of $1/T_1$ is of the Arrhenius type, with an activation energy $W = 4.4$ kcal/mole.

(*) The results in this work were first presented in an oral communication at the Second National Conference of the Portuguese Physical Society (Porto, 16-18 April, 1980).

1 — INTRODUCTION

A rapidly growing interest on discotic liquid crystals has arisen since the appearance, three years ago, of the first report on the synthesis of a disc-like molecule capable of thermotropic mesomorphism [1].

Most of the papers published up to now describe the synthesis of new mesogens and the molecular arrangement, the optical, and thermodynamic properties of this new mesomorphic state [2].

The dynamics of disc-like molecules in the isotropic and mesomorphic states is also of considerable interest but has naturally received less attention so far. We have approached this problem by nuclear magnetic resonance (NMR) techniques, and we give here a set of results obtained from systematic measurements of the proton spin-lattice relaxation time T_1 , as a function of temperature T and Larmor frequency ω , in the mesomorphic (columnar) and isotropic phases of hexa-*n*-octyloxytriphenylene (hereafter abbreviated to H8.OTP). In this work, we comment on the whole set of results obtained but concentrate the discussion on the subset of results relative to the isotropic phase.

As it will appear below, the proton spin-lattice relaxation in the isotropic phase of H8.OTP shows a peculiar behaviour which is not common to the isotropic phases of usual liquid crystals (i.e. those composed of rod-like molecules).

In section 2 we mention the techniques used in this work. In section 3 we give a brief analysis of the whole experimental data obtained, with particular reference to the columnar phase and the columnar-isotropic transition. In section 4 we contrast the experimental data relative to the isotropic phase to those theoretical models so far proposed for the nuclear spin-lattice relaxation in isotropic liquids which can account for a frequency-dependent relaxation time. The results so obtained are discussed in section 5. Finally, in section 6 we present our conclusions.

An extension of this research including the full presentation and discussion of the results obtained for the columnar phase will be presented in a forthcoming paper [3].

2—EXPERIMENTAL TECHNIQUES

The synthesis of hexa-*n*-octyloxytriphenilene was described elsewhere [4]. Its molecular structure is given in figure 1.

After purification, the sample (0.5 cm³) used in our NMR experiments was degassed and sealed in an evacuated glass tube ($\phi=10$ mm). The degassing pressure was less than 10⁻⁴ mbar.

The clearing point of H8.OTP is $T_{D1}=358.8$ K, and the crystal-discotic transition is $T_{KD}=340$ K.

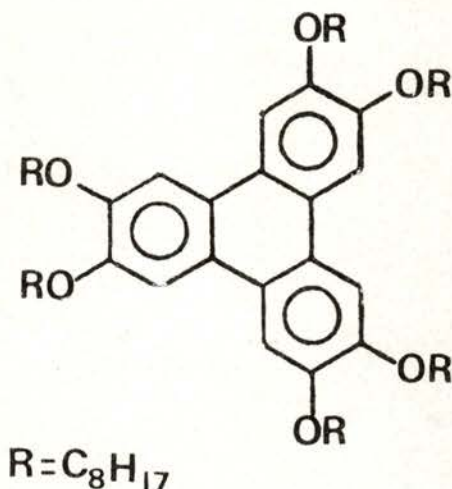


Fig. 1 — Structure of the hexa-*n*-octyloxytriphenilene (H8.OTP) molecule. Note its disc-like shape.

Measurements of the proton spin-lattice relaxation time T_1 were performed at eight different frequencies between 10 and 90 MHz. In each case the temperature was varied over the whole discotic (columnar) range and at least up to 10 K above the clearing point. In two cases, in fact, the isotropic phase was spanned up to 90 K above the clearing point (see below). T_1 was measured by the π - τ - $\pi/2$ pulse sequence with a Bruker SXP/4-100 spectrometer. The temperature of the sample was automatically controlled to within ± 0.3 K, and the estimated error in the absolute values of T was less than 1 K.

3—EXPERIMENTAL DATA AND GENERAL COMMENTS

The X-ray experiments of Levelut [5] suggest that the mesophase of H8.OTP is of the columnar type with regular stacking of molecules in the columns, their planes being normal to the columnar axis. The packing of the columns follows a two-dimensional hexagonal lattice. There is no correlation between molecular positions in neighbouring columns (longitudinal disorder).

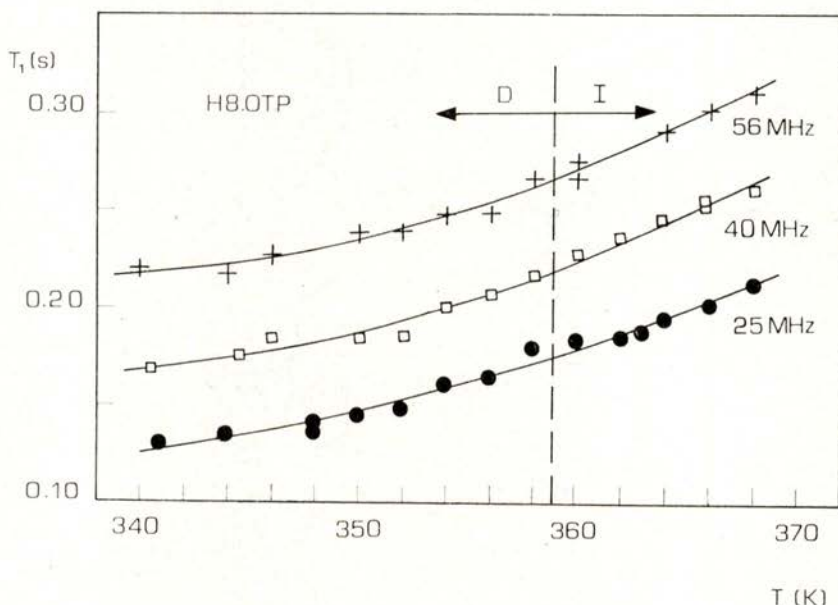


Fig. 2 — Observed temperature dependence of T_1 in the columnar (D) and isotropic (I) phase of H8.OTP, at 25, 40, and 56 MHz. The curves shown are simply guides to the eye, they have not a theoretical origin.

The results of our measurements of T_1 as a function of temperature are displayed in fig. 2 for three working frequencies. The results obtained at five other frequencies are omitted in this figure for the sake of clarity; they partially reappear in figures 4 and 5 (for one temperature). The subset of results referring to the isotropic

phase are best represented by figure 3, where $Lg(1/T_1)$ at 25 and 56 MHz is plotted as a function of $1/T$ over a much larger temperature range (from T_{DI} to $T_{DI} + 90$ K).

Two paramount features of our results are apparent in fig. 2, namely the absence of a discontinuity in $T_1(T)$ at the mesomorphic-isotropic transition temperature T_{DI} (up to the experimental

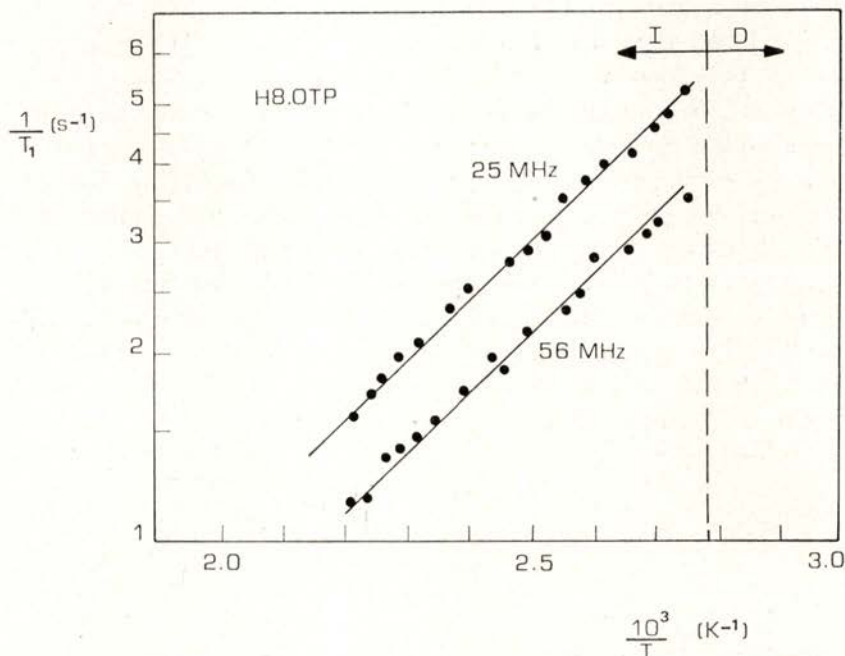


Fig. 3 — Arrhenius-type representation of the values of $1/T_1$ measured at 25 and 56 MHz, as a function of temperature, in the isotropic phase of H8.OTP. The activation energy is $W = 4.4$ Kcal/mole.

accuracy of our measurements), and the rather similar behaviour of $T_1(\omega)$ in both phases. The continuity of $T_1(T)$ at the isotropic-mesomorphic transition is in strong contrast to what is observed in liquid crystals composed of rod-like molecules [6].

We shall see [3] that the frequency behaviour of T_1 is only apparently similar in both phases. A quantitative analysis shows that we have $T_1^{-1} \sim \omega^{1/2}$ in the isotropic phase, as discussed in the

next section of this paper, and a different and more complex behaviour in the columnar phase. In this phase the overall behaviour at low temperatures is dominated by a new contribution of the type $T_1^{-1} \sim \omega^{-1/2}$, but our results [3] suggest that the previous one remains active. These two contributions may be explained in terms of molecular diffusion (section 4 below and ref. [3]) and thermal bending of the columns (long wave-length modes, see ref. [3]). Internal motions also play a role but do not contribute appreciably to the dispersion of the relaxation rate.

To understand the apparent continuity of $T_1(T)$ across T_{DI} we first note that we have measured the overall relaxation of a system of 108 proton spins, of which 102 belong to the lateral chains of the disc-like molecule and only 6 belong to the central core. If there is some short range order of the cores in the isotropic phase and the (dis)order of the chains does not change drastically at the transition, we indeed expect a quasi continuity of $T_1(T)$ at T_{DI} . Within the previous assumptions, only the contributions to the overall T_1 from the protons in the core are expected to change significantly at the transition, due to the onset of long range order, but these contributions will not affect the overall T_1 by more than a few percent. To be quantitative we expect, at T_{DI} :

$$\delta \left(\frac{1}{T_1} \right)_{\text{all}} = \frac{6}{108} \delta \left(\frac{1}{T_1} \right)_{\text{core}} + \frac{102}{108} \delta \left(\frac{1}{T_1} \right)_{\text{ch.}} \quad (1)$$

With $\delta(1/T_1)_{\text{ch}} \simeq 0$ and $\delta(1/T_1)_{\text{core}} \simeq -1$ the measured discontinuity in T_1 would be $\delta T_1 \simeq 0.056 T_1^2$, on going from the isotropic to the mesomorphic phase. Such a discontinuity could only be observed, within the accuracy of our present data, if $T_1 > 1$ s. As seen from fig. 2, this is not the case in the frequency range considered in this work.

4 — THEORETICAL ANALYSIS OF THE DATA RELATIVE TO THE ISOTROPIC PHASE

The most relevant feature of the results of our measurements of the proton spin-lattice relaxation time T_1 in the isotropic phase of HS.OTP is the rather strong Larmor frequency dependence observed

(figs. 2 and 3) over a wide temperature range above the clearing point T_{DI} . This behaviour of the relaxation time is not usual in the isotropic phases of liquid crystals formed by rod-like molecules, at least in the frequency range considered here. In the I-phases of these liquid crystals (sometimes called calamitic [2], as opposed to discotic) we only observe a significant dispersion of T_1 just above the clearing point, and this is due to collective (short range order) effects [6]. As we do not expect long-wavelength thermal modes of motion in HS.OTP over such a wide range of temperatures *above* T_{DI} , the observed behaviour is to be explained in terms of relative diffusion and internal motions of the molecules.

The basic theory of spin-lattice relaxation by translational diffusion (modulating the *intermolecular* spin-spin interactions) is due to Torrey [7]. Later on, several workers, particularly Harmon and Muller [8], and Freed [9], have introduced slight corrections to the theory of Torrey in order to incorporate, in different ways, the effects of boundary conditions (excluded volume due to a distance of minimum approach between the spin-bearing molecules) and the pair correlation function. We shall use below the theoretical expression proposed by Freed [9] for the spectral density $J(\omega)$ of molecular motion, in the isotropic jump model:

$$J(\omega) = \frac{4}{27} \frac{n}{Dd} \left[1 + \frac{3}{8} \frac{\langle r^2 \rangle}{d^2} - \frac{3}{8} \left(\frac{\omega d^2}{D} \right)^{1/2} + \right. \\ \left. + \frac{1}{2} \left(\frac{1}{9} + \frac{3}{32} \frac{\langle r^2 \rangle}{d^2} \right) \left(\frac{\omega d^2}{D} \right)^{3/2} + O(\omega^2) \right] \quad (2)$$

where n is the average number density of protons, $D = \langle r^2 \rangle / 6\tau$ is the absolute molecular diffusion coefficient, $\langle r^2 \rangle$ is the mean square jump distance, τ is the mean time between jumps, and d is the distance of closest approach.

The spin-lattice relaxation rate $1/T_1$ due to translational diffusion is related to $J(\omega)$ given above according to the following expression:

$$1/T_1 = \frac{4\pi}{5} \gamma_H^4 \hbar^2 I(I+1) [J(\omega) + 4J(2\omega)] \quad (3)$$

where γ_H is the proton gyromagnetic ratio and $I = 1/2$ is the proton spin quantum number. From (2) and (3) we get the proton relaxation rate:

$$\begin{aligned} 1/T_1 = \frac{4\pi}{9} (\gamma_H^4 h^2) \frac{n}{Dd} \left[1 + \frac{3}{8} \frac{\langle r^2 \rangle}{d^2} - \frac{3}{40} (1 + 4\sqrt{2}) \left(\frac{\omega d^2}{D} \right)^{1/2} + \right. \\ \left. + \frac{1}{90} (1 + 8\sqrt{2}) \left(1 + \frac{27}{32} \frac{\langle r^2 \rangle}{d^2} \right) \left(\frac{\omega d^2}{D} \right)^{3/2} + 0 (\omega^2) \right] \quad (4) \end{aligned}$$

To lowest order in ω , expression (4) may be written:

$$(1/T_1)_{\text{inter}} \sim \tau [1 - \alpha (\omega \tau)^{1/2}] \quad , \quad (5)$$

where α is a constant of order unity.

On the other hand, we expect the relaxation due to the modulation of intramolecular spin-spin interactions to be of the form

$$(1/T_1)_{\text{intra}} \sim \tau' [1 - \beta (\omega \tau')^2] \quad , \quad (6)$$

to the leading term in ω , where β is also a constant of order unity, and τ' is an appropriate correlation time [10].

Simple order of magnitude considerations allow us to expect $\omega \tau' \lesssim \omega \tau \sim 10^{-1} - 10^{-2}$ in the frequency range considered in this work. Then, it can be seen from equations (5) and (6) that the *intermolecular* relaxation will dominate the overall *frequency effect*. This is just what is suggested by our experimental data.

In fact, our data cannot be reasonably fitted to equation (6) at every temperature in the isotropic phase. On the other hand, fitting the data with equation (5), gives rather good qualitative agreement over the whole frequency range considered in this work, as shown in fig. 4 for one particular temperature ($T = 366\text{K}$). The straight line in fig. 4, as obtained by the least squares method, is given by

$$(1/T_1)_{\text{exp.}} = 7.773 - 2.372 \times 10^{-4} \omega^{1/2} \quad (7)$$

with a root mean square error

$$\varepsilon(\text{rms}) \equiv \left[(1/N) \sum_1^N (R - R_i)^2 \right]^{1/2} = 0.133 \text{ s}^{-1} \quad (8)$$

where $R \equiv 1/T_1$. So, it is clear that to lowest order in ω our data give $1/T_1 \sim \omega^{1/2}$, which is consistent with the predominance of a diffusion-controlled relaxation mechanism.

The next approximation in contrasting our data with theory is obtained by introducing a term proportional to $\omega^{3/2}$, according to eq. (4). In this case we find, by the least squares method, at $T = 366\text{ K}$:

$$(1/T_1)_{\text{exp.}} = 8.379 - 3.012 \times 10^{-4} \omega^{1/2} + 7.783 \times 10^{-14} \omega^{3/2} \quad (9)$$

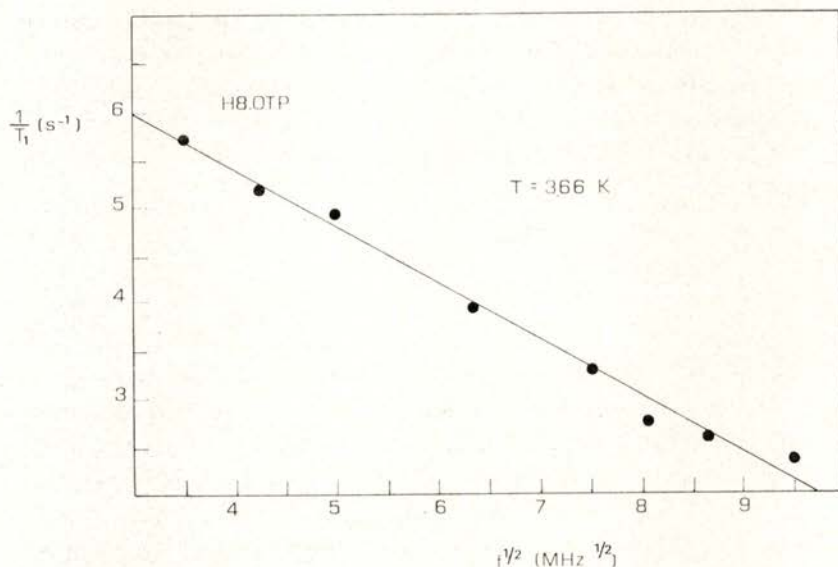


Fig. 4 — Linear least-squares fit of the data on $1/T_1$ versus $f^{1/2}$, where $f = \omega/2$; eq. (7) in the text.

with $\varepsilon(r \text{ m s}) = 0.108 \text{ s}^{-1}$. Terms of higher order in ω cannot introduce differences outside the experimental error of our measurements, in agreement with the foregoing order of magnitude considerations.

Now, by equating the terms proportional to $\omega^{1/2}$ in equations (4) and (9) we find:

$$D = 1.95 \times 10^{-7} \text{ cm}^2 \text{ s}^{-1} \quad (10)$$

Introducing this value of D in the coefficient of $\omega^{3/2}$ in eq. (4), and assuming some value for $\langle r^2 \rangle / d^2$, we find, by comparison with eq. (9),

$$d \leq 1.35 \text{ \AA} \quad (11)$$

The value of $\langle r^2 \rangle$ cannot be found because the frequency independent term in r.h.s. of eq. (9) contains both inter and intramolecular contributions, as given by the corresponding terms in equations (4) and (6) (and eventually a small contribution from other possible mechanisms of relaxation). The separation of these frequency-independent contributions to the overall relaxation rate would require measurements of T_1 on mixture samples prepared by progressively diluting completely deuterated H8.OTP with normal H8.OTP; unfortunately, deuterated samples of H8.OTP are not available at present.

5 — DISCUSSION OF RESULTS

Let us now discuss the results obtained in the previous section.

We have seen that expression (4) fits very well the experimental data. However, both the value of D , given by (10), and the value of d , given by (11), appear to be rather low. We can reasonably expect $d \approx 3 - 4 \text{ \AA}$ and $D \approx 10^{-6} \text{ cm}^2 \text{ s}^{-1}$. This value of D is an order of magnitude higher than the value found above. Similar discrepancies were found, by several researchers, for liquid crystals formed of elongated molecules, e.g. MBBA, between the values of D extracted from NMR-T analysis and those measured by direct techniques [11-13]. No explanation for these facts has been proposed so far.

It could be argued that in the general expression for $1/T_1$ a term proportional to ω^2 as predicted by eq. (6) may be non-negligible, in spite of the considerations about orders of magnitude developed in the preceding section. We have checked this point by fitting our data to the theoretical expression as developed to order ω^2 and have found that to the accuracy of our data the influence of such a term cannot be shown up.

On the other hand we have tried to fit our data with the full expression for $1/T_1$ given by Torrey [7] (after inclusion of the

proper weighting of the spectral densities), instead of the approximations such as eq. (4) or the equivalent one suggested by Harmon and Muller [8]. Figure 5 reproduces two examples of such fittings, where we have forced $d = 3.65 \text{ \AA}$, corresponding to the distance of closest approach of the discs (molecular cores) in the mesomorphic phase, as given by X-ray measurements [5] and semi-empirical calculations [14]. In this way we can get results which are physically sounder but not yet satisfactory.

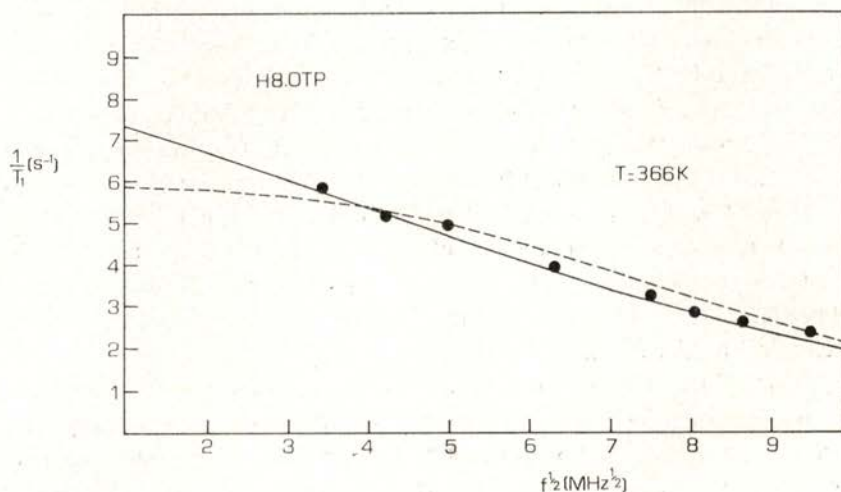


Fig. 5 — Fits of the full theoretical expression for $1/T_1$ given by Torrey [7] (corrected) with the data. Solid curve: $d^2 = \langle r^2 \rangle = (3.65 \text{ \AA})^2$, $D = 2.25 \times 10^{-7} \text{ cm}^2 \text{ s}^{-1}$. Dashed curve: $d = 3.65 \text{ \AA}$, $\langle r^2 \rangle = (10.9 \text{ \AA})^2$, $D = 1 \times 10^{-6} \text{ cm}^2 \text{ s}^{-1}$. The r.m.s. errors are respectively $\epsilon \text{ (rms)} = 0.157$ and 0.236 s^{-1} .

We suggest that the theories proposed so far [7-9] to account for the behaviour of the nuclear spin-lattice relaxation by translational diffusion do not apply to liquids formed by strong anisometric molecules, such as liquid crystals (in the isotropic phase), both of the calamitic and of the discotic types. We intend to discuss in a future publication the corrections to be introduced in the available theories in order to render them applicable to these cases too.

Let us finally remark that the relaxation rate $1/T_1$ varies with temperature according to an Arrhenius-type law (figure 3), as expected from eq. (5), to a good approximation, where

$$\tau = \langle r^2 \rangle / 6D = \tau_0 \exp(W/kT).$$

The activation energy, extracted from the least-squares fit in figure 3, is $W = 4.4$ kcal/mole. We did not observe pretransitional effects in the temperature range just above T_{DI} .

6—CONCLUSION

This work is, to our knowledge, the first report on the dynamics of disc-like molecules, in isotropic and mesomorphic (columnar) phases, as studied by nuclear magnetic relaxation techniques. Our results were obtained from measurements on a single material, hexaoctyloxy-triphenylene (H8.OTP), but most of them are presumably of general interest. Two of these results are particularly remarkable:

(i) No discontinuity of $1/T_1$ is observed on varying the temperature across the mesomorphic-isotropic transition point, which is interpreted as a consequence of the incapacity of the aliphatic chains in the molecule to become significantly ordered on going from the isotropic to the mesomorphic state. This behaviour differs from that observed with similar chains attached to the rod-like molecules of "classic" liquid crystals [15].

(ii) The proton spin-lattice relaxation rate $1/T_1$ is strongly dependent on the Larmor frequency ω over the whole temperature range covered in our experiments (up to 90K above the clearing point T_{DI}). The theories of relaxation proposed so far [7-9] hardly account for the observed behaviour. The discrepancy should originate in the strong anisometric form of the molecules, which couples molecular rotation to translational diffusion of spins. No short range order effects are observed just above T_{DI} .

We are indebted to Professor J. M. Araújo, of University of Porto, for pointing out a numerical error in the manuscript, and to Dr. Ch. Destrade and the chemical group of C.R.P.P., Bordeaux, for the preparation of the sample used in this work. The cooperation of Mrs. I. S. Costa is also acknowledged.

REFERENCES

- [1] S. CHANDRASEKHAR, B. K. SADASHIVA, and K. A. SURESH, *Pramàna* **9**, 471 (1977).
- [2] For a recent review see C. DESTRADE *et al.*, in *Liquid Crystals*, S. Chandrasekhar ed (Heyden & Son Ltd, London, 1980), and

- J. BILLARD, in *Liquid Crystals of One and Two-dimensional Order*, W. Helfrich and G. Heppke eds. (Springer-Verlag, Berlin, 1980).
- [3] A. F. MARTINS and A. C. RIBEIRO, in preparation.
- [4] J. BILLARD *et al.*, *Nouveau J. de Chimie*, **2**, (1978), 535; C. DESTRADE, M. C. MONDON and J. MALTHETE, *J. Phys. (Paris)* **40**, C3-17 (1979).
- [5] A. M. LEVELUT, *J. Phys. Lett. (Paris)* **40**, 81 (1979).
- [6] A. F. MARTINS, *Molec. Cryst. Liquid Cryst.*, **14**, 85 (1971); *Portgal. Phys.* **8**, 1 (1972).
- [7] H. C. TORREY, *Phys. Rev.* **92**, 962 (1953).
- [8] J. F. HARMON and B. H. MULLER, *Phys. Rev.* **182**, 400 (1969).
- [9] J. H. FREED, *J. Chem. Phys.* **68**, 4034 (1978).
- [10] A. ABRAGAM, *The principles of nuclear magnetism* (Oxford Univ. Press, London, 1961).
- [11] M. VILFAN, R. BLINC, and J. W. DOANE, *Solid State Commun.* **11**, 1073 (1972).
- [12] R. Y. DONG, E. TOMCHUK, and E. BOCK, *Can. J. Phys.* **53**, 610 (1975).
- [13] G. ROLLMANN, K. F. REINHART, and F. NOACK, *Z. Naturforsch.* **34a**, 964 (1979).
- [14] M. PESQUER *et al.*, *J. Physique* **41**, 1039 (1980).
- [15] A. F. MARTINS, A. J. BONFIM, and A. M. GIROUD-GODQUIN, *Portgal. Phys.* **11**, 159 (1980).



PROPRIETES PHYSIQUES DE POLYMERES ORGANIQUES SEMI-CONDUCTEURS ET METALLIQUES: LE CAS DU POLYACETYLENE(*)

P. BERNIER (1), M. ROLLAND (1), S. LEFRANT (2), A. MONTANER (1),
O. PARODI (1), C. BENOIT (1), M. GALTIER (1), F. SCHUE (3),
J. SLEDZ (3), J. M. FABRE (4), L. GIRAL (4), M. ALDISSI (3)

(Received 9 October 1980; revised version in 30 December 1980)

RÉSUMÉ — Dans cet article nous passons en revue certaines des propriétés physiques du polyacétylène non dopé et dopé, telles qu'elles ont été étudiées en France récemment. Nous insistons en particulier sur certains travaux concernant le matériau non dopé (isomérisation, évolution à l'air) qui sont essentiels avant d'aborder l'étude du dopage et de ses conséquences. Les propriétés physiques du polyacétylène dopé sont décrites en se limitant à quelques cas typiques d'espèces dopantes. Nous ne rentrons pas dans le détail des interprétations théoriques, concernant en particulier les propriétés électroniques et magnétiques de ces matériaux, qui sont l'objet de profondes controverses. Enfin nous essayons de dégager les caractéristiques de ces nouveaux matériaux qui permettent d'envisager leur utilisation à des fins industrielles.

ABSTRACT — Some physical properties of doped and undoped polyacetylene, $(CH)_x$ are reviewed, with special emphasis on authors' recent work in the field. Results for the undoped material (isomerization, effect of contact with air, etc.) are stressed since they are essential for studying effects of doping. Physical properties of doped $(CH)_x$ are discussed only for a few typical doping agents. No detailed theoretical interpretation of electronic and magnetic properties is presented, given the lack of agreement between different approaches. Characteristics of these new materials of possible interest for industrial applications are stressed.

(1) Groupe de Dynamique des Phases Condensées (*), USTL, Montpellier, France.

(2) Laboratoire de Physique Cristalline (*), 91405 ORSAY, France.

(3) Laboratoire de Chimie Macromoléculaire, USTL, Montpellier, France.

(4) Laboratoire de Synthèse Organique USTL, Montpellier, France.

(*) Laboratoire associé au C.N.R.S.

1 — INTRODUCTION

Le polyacétylène $(CH)_x$ est sûrement le plus simple des polymères organiques. Il présente une alternance de simples et doubles liaisons entre atomes de carbone. Le système des électrons π est donc non saturé et la structure de bande correspondante en fait un matériau semi-conducteur (fig. 1). Néanmoins, le polyacétylène est fonda-

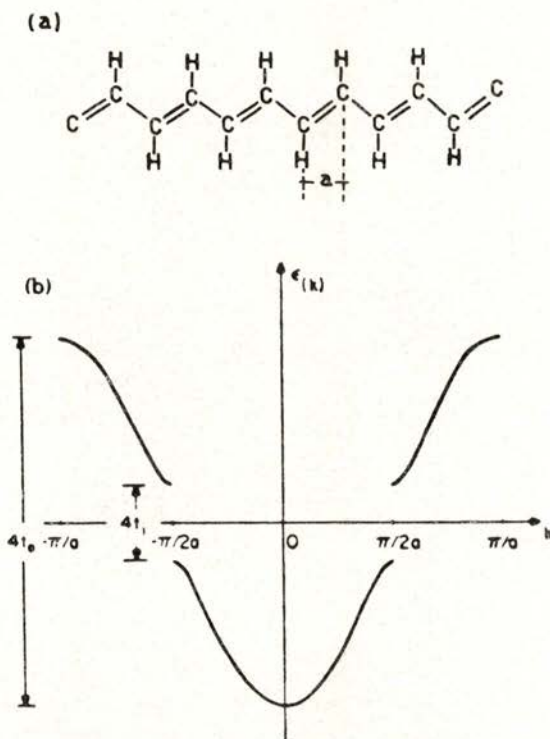


Fig. 1 — Le polyacétylène est constitué d'une chaîne hydrocarbonée avec simples et doubles liaisons alternées (a). La différences de longueur de ces liaisons en fait un système semi-conducteur avec une largeur de bande $4t_0 \sim 10$ eV et un gap $4t_1 \sim 1,4$ eV (b).

mentalement différent des semi-conducteurs organiques classiques, comme l'anthracène, qui sont constitués de molécules en faibles interactions. Il est par contre plus proche des semi-conducteurs inorganiques et, comme eux, peut être dopé avec des éléments chimiques

donneurs ou accepteurs d'électrons, conduisant à une conduction électronique de type n ou p. De plus, pour de très forts taux de dopage (supérieur à quelques pour cents molaire) on observe un comportement quasiment métallique.

Expérimentalement, le polyacétylène peut être obtenu sous forme de films de grandes surfaces, ce qui en rend l'utilisation particulièrement aisée.

Cette possibilité de couvrir une large gamme de comportements de pratiquement isolant à hautement conducteur (la conductivité est alors comparable à celle des mauvais métaux), alliée à la simplicité de sa synthèse, font du polyacétylène un matériau exemplaire, tant sur le plan fondamental qu'appliqué. Son étude passe par diverses étapes qui concernent en particulier la caractérisation du matériau non dopé, sa stabilité lorsqu'il est soumis à diverses contraintes chimiques, mécaniques ou thermiques, la compréhension des mécanismes de dopage, etc.

Ce matériau a fait l'objet, depuis maintenant trois ans, d'un grand nombre de travaux, en majorité expérimentaux, qui ont donné lieu à plus d'une centaine de publications, parmi lesquelles une dizaine font mention d'applications industrielles envisageables [1].

Dans cet article, nous voulons faire un bilan de certaines études qui ont été entreprises en France, en particulier dans le but de mieux comprendre les caractéristiques fondamentales du matériau, et décrire les propriétés physiques du polyacétylène non dopé et dopé, telles qu'elles apparaissent lors de l'utilisation de techniques expérimentales comme la conductivité électrique, la RPE et la RMN, et les spectroscopies infrarouge et Raman.

2 — SYNTHÈSE ET CARACTÉRISATION DU $(CH)_x$

La polymérisation de l'acétylène se fait par une réaction de type Ziegler-Natta. Le catalyseur utilisé est un mélange de $Ti(OBu)_4$ et de $Al(Et)_3$ en proportion $[Al]/[Ti] = 4$, solubilisé dans le toluène. La polymérisation se fait directement par contact du gaz avec la surface libre de la solution de catalyseur [2]. On obtient alors un film d'épaisseur variable (quelques microns à quelques mm dépendant des conditions de la polymérisation), de couleur brun-noir, et d'éclat métallique argenté une fois légèrement poli. La surface du

film obtenu n'est limitée que par la taille du réacteur de polymérisation. On peut donc envisager d'obtenir des quantités considérables de polyacétylène. Néanmoins la détermination de ses caractéristiques physico-chimiques est rendue compliquée par le fait qu'il est insoluble dans tous les solvants connus. Enfin, une fois correctement lavé, le polyacétylène présente un taux de résidus catalytique qui peut être inférieur à 0,1 %.

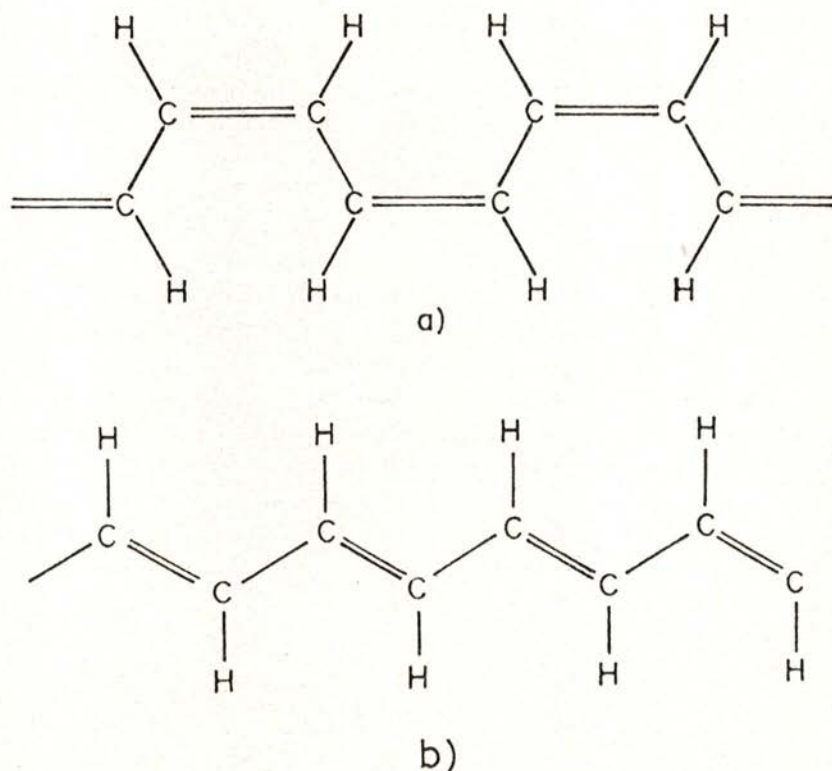


Fig. 2 — Géométrie des configurations cis (a) et trans (b) du polyacétylène. On notera un plus haut degré de dégénérescence pour la configuration trans que pour la configuration cis.

Si la polymérisation est faite à -78°C le matériau est de configuration principalement cis alors qu'à $+150^{\circ}\text{C}$ il est essentiellement trans (fig. 2). On peut identifier ces configurations par des techniques

expérimentales comme les spectroscopies Raman [3] et infrarouge [4] et la RMN du ^{13}C à l'état solide. Dans tous les cas, les fréquences des vibrations (IR et Raman) ou de la résonance (RMN) dépendent de la géométrie de la molécule, et dans le cas de la RMN on a une méthode assez fine pour estimer les quantités respectives de cis et de trans [5] (figures 3, 4 et 5).

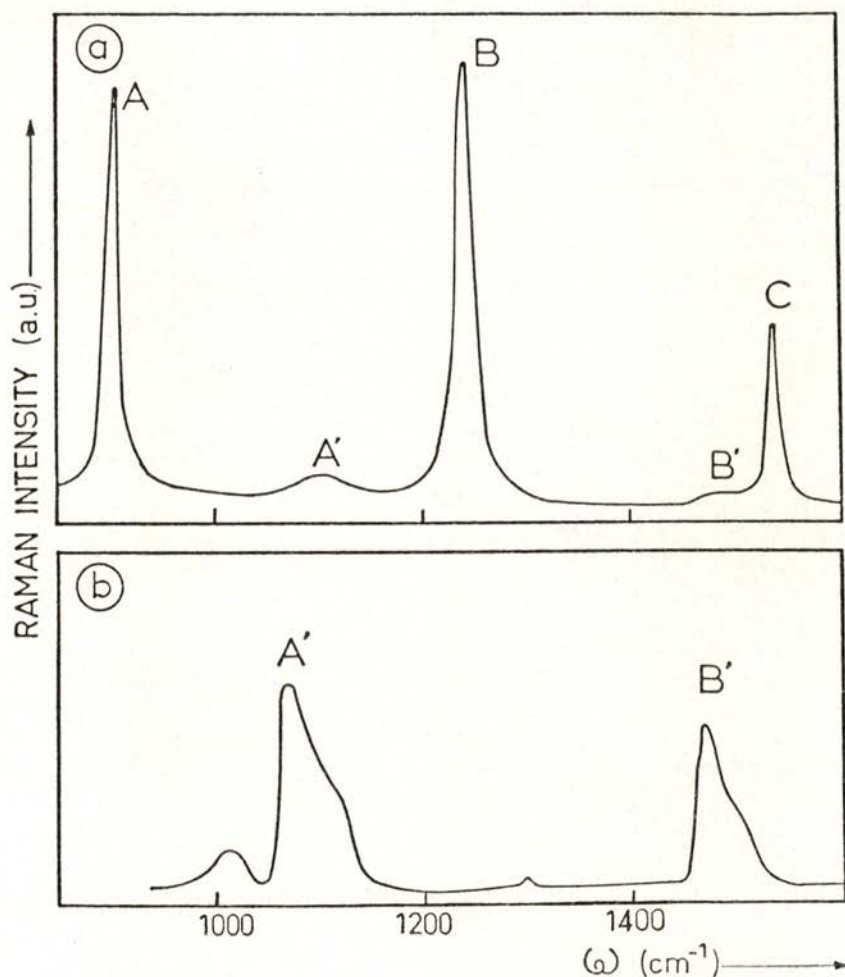


Fig. 3 — Spectres Raman obtenus avec les configurations cis (a) et trans (b) du polyacétylène. Le degré de pureté structurale est de l'ordre de 96 % dans le cas du cis et voisin de 100 % dans le cas du trans.

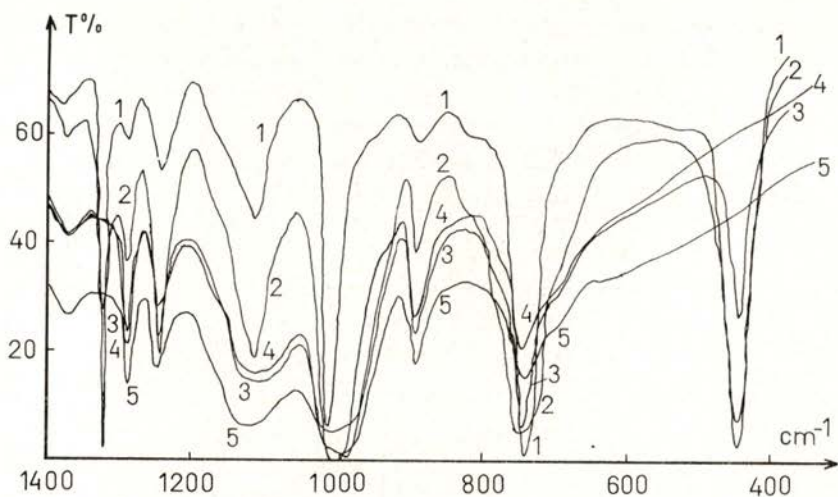


Fig. 4 — Spectres infrarouges obtenus dans le cas d'une configuration cis (à 96 %) (1) et d'une configuration trans (à ~ 100 %) (5), ainsi que pour trois situations intermédiaires (2, 3, et 4).

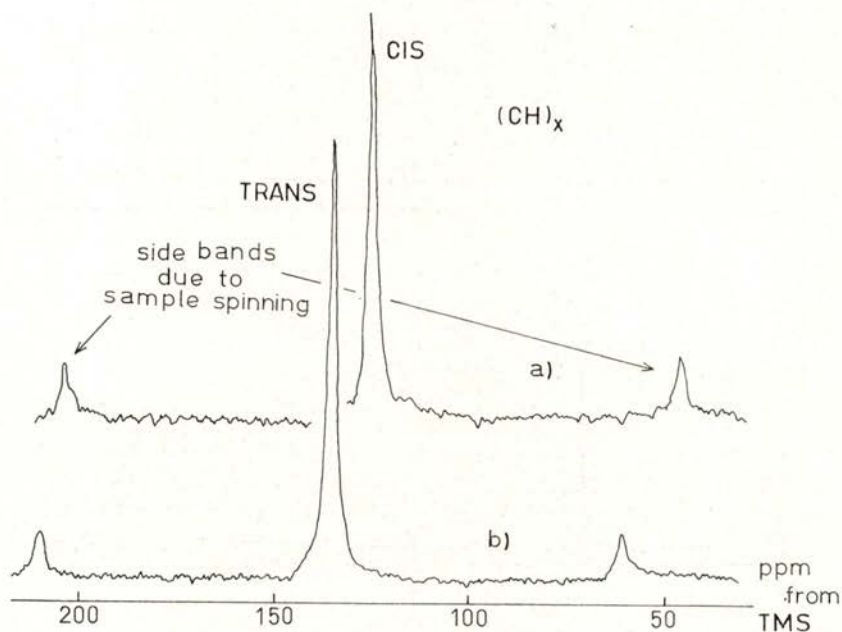


Fig. 5 — Spectres obtenus par RMN haute résolution du ^{13}C en abondance naturelle dans l'état solide des configurations cis (a) et trans (b) du polyacétylène. Dans une situation intermédiaire l'intensité relative des deux raies permet d'estimer le rapport [cis] / [trans].

Les films de polyacétylène, observés au microscope électronique à balayage, ont un aspect fibrillaire plus ou moins compact (Fig. 6).

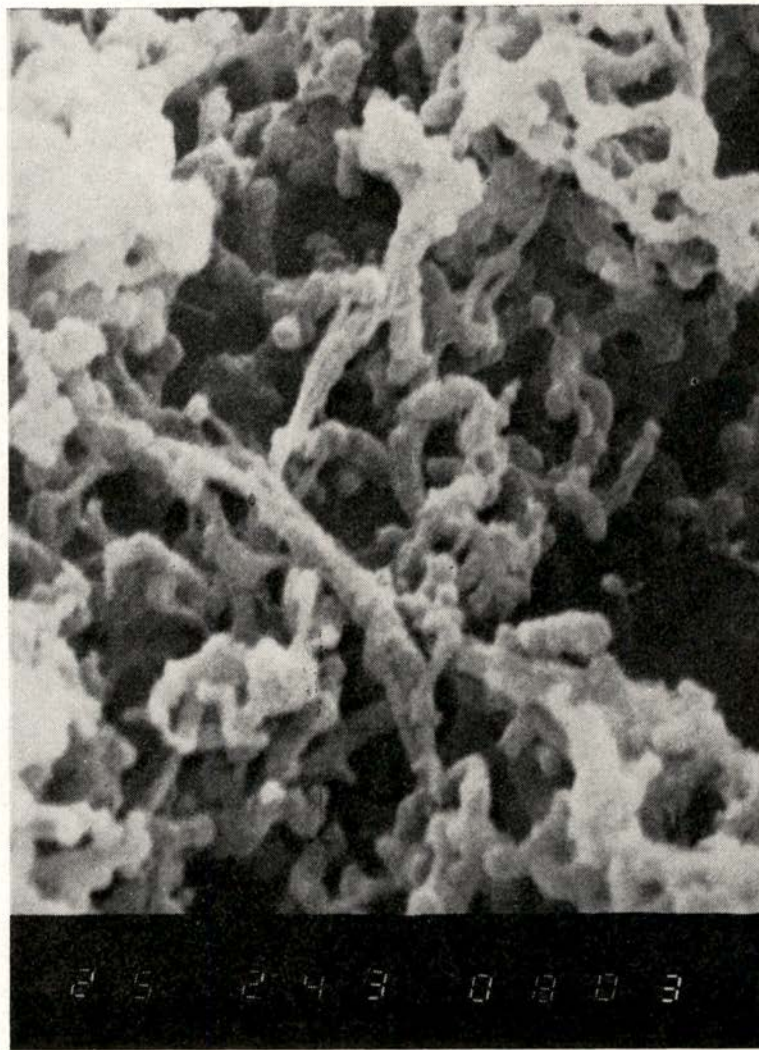


Fig. 6 — Cliché obtenu au microscope électronique à balayage d'un film de polyacétylène, montrant l'aspect fortement inhomogène du système, avec des fibres (épaisseur $\sim 200 \text{ \AA}$, longueur $\sim 1000 \text{ \AA}$) interconnectées les unes aux autres. La nature du cliché observé peut varier sensiblement suivant les conditions de la polymérisation et la zone observée.

Ces fibres qui ont des orientations aléatoires et sont interconnectées les unes aux autres ont typiquement quelques centaines d'Å d'épaisseur pour quelques milliers d'Å de long. Sur le plan cristallographique, des expériences de diffraction des rayons X ont montré [6] que le degré de cristallinité (qui dépend des conditions expérimentales lors de la polymérisation) pouvait être de l'ordre de 80 %. Le type de structure qui a pu être déterminé (maille orthorhombique avec huit unités CH par maille) conduit à un matériau de densité $1,16 \text{ gr/cm}^3$ en bon accord avec la valeur expérimentale de $1,165 \text{ gr/cm}^3$ mesurée par une technique de flottation. Néanmoins, du fait de sa nature fibrillaire, le matériau macroscopique a une densité apparente de $\sim 0,4 \text{ gr/cm}^3$ [1].

3 — PROPRIÉTÉS PHYSIQUES DU $(\text{CH})_x$ NON DOPÉ

Une caractéristique essentielle du polyacétylène est la possibilité de l'obtenir dans ses deux formes isomériques *cis* et *trans*. La forme *cis*, qui est obtenue par polymérisation à -78°C , est instable à plus haute température. Tout traitement thermique induit donc une isomérisation vers la configuration *trans* stable.

De plus, si ce traitement est fait à température assez élevée ($T > 130^\circ\text{C}$) on assiste à une dégradation du polymère qui modifie profondément ses caractéristiques.

a) — Etude de l'isomérisation *cis-trans*

La configuration *cis* obtenue à -78°C est caractérisée par l'absence d'électrons non appariés (absence de signal RPE) [7]. La structure des raies Raman caractéristiques du *cis* suggèrent que l'on a des chaînes longues avec une distribution de longueurs assez étroite. Ce point a été précisé quantitativement par Shirakawa [8] qui après hydrogénation du $(\text{CH})_x$ a mesuré la masse moléculaire du matériau soluble obtenu : les chaînes auraient en moyenne 600 unités (CH).

Dès que la température est élevée au dessus de -78°C apparaît un signal RPE à $g = 2,0023$ (facteur gyromagnétique des électrons libres) qui est dû à l'existence d'électrons non appariés sur les chaînes de $(\text{CH})_x$. A température ambiante (20°C) la largeur de la raie singulet observée est de 8 gauss et son intensité correspond

à 10^{18} spins / gr. On admet actuellement que ces électrons non appariés sont liés à l'existence de défauts dans l'alternance des doubles et simples liaisons dans la structure trans (fig. 7) [1]. L'absence

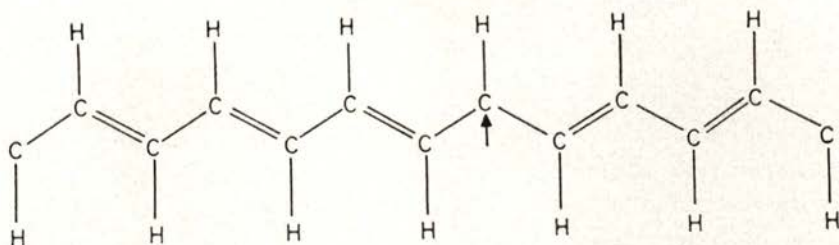


Fig. 7 — Structure du trans-polyacétylène présentant un défaut (flèche) dans l'alternance des simples et doubles liaisons. Un tel défaut est électriquement neutre mais paramagnétique.

de structure hyperfine dans le spectre RPE observé indique que de tels défauts sont mobiles: l'inverse de la largeur de raie ΔH_{pp} est alors une mesure indirecte de cette mobilité. Plus précisément on peut établir la relation suivante [9]:

$$\Delta H_{pp} = A D_{||}^{-1/3}$$

où A est un paramètre qui tient compte de l'amplitude des interactions entre les électrons non appariés et les spins nucléaires des hydrogènes ainsi que des interactions entre électrons eux-mêmes; $D_{||}$ est le taux de diffusion de l'électron non apparié le long d'une chaîne du polymère. On a donc un effet de rétrécissement par le mouvement, d'autant plus important que l'extension de la conjugaison est grande sur les séquences trans.

Les mesures en Raman [3] et IR [4] confirment qu'à température ambiante l'échantillon polymérisé à -78°C est déjà partiellement isomérisé avec un contenu en trans de $\sim 5\%$ (figures 3 et 4), cet état étant stationnaire au bout de quelques jours. Ce résultat suggère que l'isomérisation cis-trans est un processus progressif qui requiert un mouvement d'ensemble des molécules. L'existence d'une distribution des longueurs de chaînes ainsi que la possibilité de modifier cette distribution au cours du processus (brisures, réticulations, etc) rendent la cinétique de celui-ci difficile à décrire.

Au fur et à mesure que la température T_{tt} du traitement augmente, l'isomérisation devient de plus en plus rapide, mais conjointement, on doit tenir compte d'une dégradation de plus en plus importante du système. On distingue globalement trois domaines de températures [10]:

a) $T_{tt} < \sim 130^\circ\text{C}$.

L'isomérisation ne peut pas être complète, comme le montrent les expériences de RPE: la largeur de raie ΔH_{pp} décroît bien lorsque la température augmente (augmentation de longueur des séquences trans, donc de la mobilité des spins observés). Mais ΔH_{pp} atteint après un certain temps une valeur constante à T_{tt} donnée, cette constante pouvant à nouveau diminuer si T_{tt} est augmentée (figure 8).

b) $\sim 130^\circ\text{C} < T_{tt} < \sim 200^\circ\text{C}$.

Dans ces conditions l'isomérisation peut être totale (dans la limite de la précision des mesures), comme le montre l'indépendance de ΔH_{pp} avec T_{tt} qui atteint sa valeur minimale $\sim 0,7$ Gauss (fig. 8). Néanmoins il faut tenir compte d'une dégradation de plus en plus efficace. Cette superposition d'une dégradation à l'isomérisation est clairement mise en évidence par mesures de la résistivité électrique ρ au cours du traitement thermique (figure 9). Il apparaît clairement un minimum de résistivité pour un temps t_{\min} d'autant plus petit que la température est plus élevée [11]. L'isomérisation cis-trans est accompagnée d'une diminution de résistivité ($\rho_{\text{cis}} \sim 10^9 \Omega \text{ cm}$ et $\rho_{\text{trans}} \sim 10^5 \Omega \text{ cm}$ à température ambiante) alors que la dégradation provoque une augmentation de résistivité. Le minimum de ρ observé est alors lié à une compétition entre ces deux processus qui ont des énergies d'activation différentes: 18 kcal/mole pour l'isomérisation et ~ 30 kcal/mole pour la dégradation, valeurs approximatives déterminées à partir des cinétiques de variation de la résistivité et de la largeur de raie RPE respectivement. La nature de la dégradation est difficile à préciser, néanmoins on peut invoquer l'apparition de réticulations, de brisures de chaînes, etc., qui toutes ont pour effet de réduire l'extension de séquences de type trans le long d'une chaîne. Ce point est rendu particulièrement clair par l'observation d'une modification de la structure des raies Raman caractéristiques du trans qui indique que pour un temps de traitement thermique correspondant à t_{\min} la longueur des séquences trans passe par un maximum [3].

c) $T_{tt} > \sim 200^{\circ}\text{C}$.

A de telles températures, si l'isomérisation est très rapide (quelques dizaines de secondes suffisent à rendre le système pratiquement trans), la dégradation est très importante et se manifeste par une augmentation rapide et importante de la largeur de raie RPE (Fig. 8), de la résistivité (Fig. 9), ainsi que par des modifica-

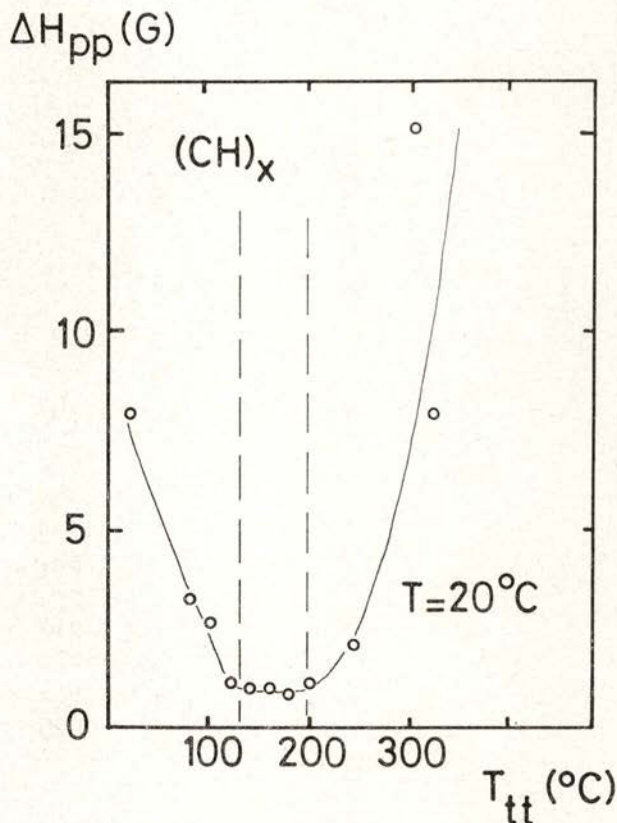


Fig. 8 — Dépendance de la largeur de raie RPE ΔH_{pp} (mesurée à température ambiante) avec la température T_{tt} auquel un échantillon cis $(\text{CH})_x$ a été soumis pendant un temps assez long afin d'atteindre un état stationnaire (sauf pour $T_{tt} > 200^{\circ}\text{C}$ où un état stationnaire n'est jamais atteint). Le comportement observé met clairement en évidence trois zones (voir texte):

- a) $T_{tt} < 130^{\circ}\text{C}$, zone d'isomérisation partielle.
- b) $130^{\circ}\text{C} < T_{tt} < 200^{\circ}\text{C}$, zone d'isomérisation totale.
- c) $T_{tt} > 200^{\circ}\text{C}$, zone où la dégradation est prépondérante.

tions notables de la structure des spectres Infrarouge et Raman. Finalement pour des températures supérieures à $\sim 325^{\circ}\text{C}$, le polyacétylène se décompose rapidement.

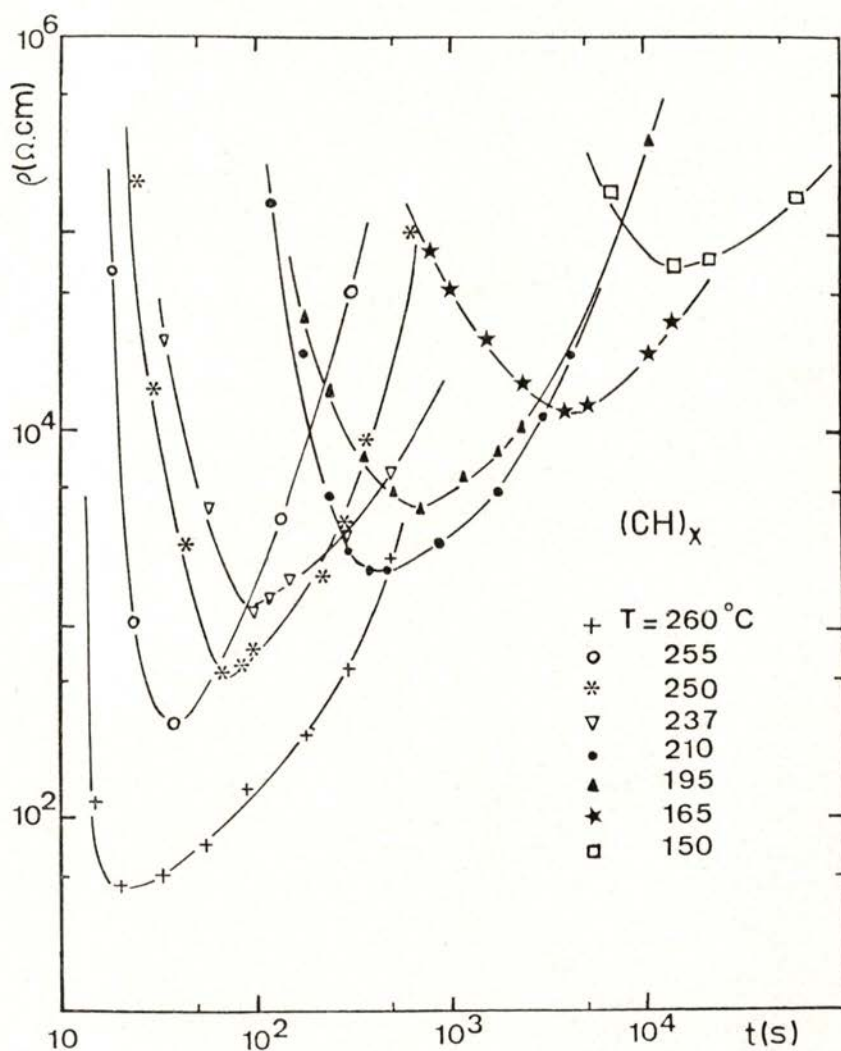


Fig. 9 — Dépendance de la résistivité ρ avec le temps t au cours du processus d'isomérisation induit par un traitement thermique à diverses températures. Le minimum observé est dû à une compétition entre le processus d'isomérisation (qui fait chuter la résistivité) et la dégradation du système (qui augmente la résistivité).

b) — Conclusion

Il faut noter que les bornes délimitant les intervalles de T_{tt} ci-dessus, ne sont pas définies de manière précise et ont été choisies principalement d'après les résultats obtenus en RPE. Il est évident que l'effet induit par la présence de défauts le long des chaînes de $(CH)_x$ ne sera pas ressenti avec la même intensité suivant la technique expérimentale utilisée. En particulier, les phénomènes de transports qui nécessitent un déplacement de charges à l'échelle macroscopique sont très sensibles à l'existence d'une faible concentration de défauts. L'intérêt de cette étude de l'isomérisation cis-trans est de montrer que le polyacétylène stable (donc de configuration trans) peut-être optimisé par un choix judicieux des conditions de l'isomérisation (température et durée) de manière à maximiser le contenu en trans tout en minimisant la quantité de défauts introduits [11].

4 — ACTION D'ESPÈCES CHIMIQUES DOPANTES

Il est maintenant bien établi, après les travaux de Mac Diarmid et Heeger [1] que le polyacétylène peut être dopé à l'aide de diverses espèces chimiques comme Br_2 , I_2 , AsF_5 , SbF_5 , H_2SO_4 , Na, K, etc. L'effet le plus spectaculaire observé est alors une diminution considérable de la résistivité (jusqu'à $\sim 10^{-3} \Omega \text{ cm}$) pour des taux de dopages de 10 à 20 % (molaires). Au contraire, une espèce chimique comme O_2 cause une augmentation de résistivité des films trans. Pour comprendre ces comportements, il faut invoquer, dans certains cas, un transfert de charge entre le dopant et la chaîne de $(CH)_x$ ionisés, dans d'autres cas une liaison covalente (rupture de double liaison) entre le dopant et la chaîne carbonée. Les questions principales qui se posent à l'heure actuelle concernent :

- la nature exacte de l'espèce chimique dopante au sein du matériau. Par exemple dans le cas du dopage avec I_2 des mesures de Raman ont clairement mis en évidence l'existence des espèces I_3^- et I_5^- [12]. La situation est moins claire en ce qui concerne les dopages avec AsF_5 par exemple où les espèces AsF_6^- , AsF_3 et As_2F_{10} semblent avoir été identifiées [1].

- l'homogénéité de distribution de l'espèce dopante au sein du matériau. La situation est rendue compliquée par la nature inhomogène du polyacétylène. Des expériences récentes de diffusion de l'iode dans $(CH)_x$ [13] tendent à prouver que celui-ci pénètre très peu dans le matériau et reste confiné près de la surface des fibres.

a) — *Influence de l'oxygène de l'air*

Toute application du polyacétylène a des fins industrielles suppose à priori, à un moment ou à un autre, le contact avec l'air. On recherche donc une bonne stabilité du matériau, en particulier soumis à l'oxygène de l'air.

L'expérience prouve que l'oxygène induit une détérioration notable du matériau: soumis à l'oxygène de l'air (l'azote n'ayant, lui, aucune influence) l'échantillon voit sa résistivité augmenter [14], la longueur des séquences trans diminuer [3] et son aptitude à être dopé (par d'autres espèces chimiques) amoindrie. D'une manière plus précise, l'action de l'oxygène, qui est de briser aléatoirement des doubles liaisons $C = C$, se manifeste différemment sur les isomères cis et trans:

- En ce qui concerne la configuration cis, l'oxygène agit comme un catalyseur d'isomérisation vers la configuration trans. Cet effet est clairement mis en évidence par spectroscopie Raman [3]: deux échantillons cis identiques, conservés plusieurs jours à température ambiante, l'un sous vide et l'autre à l'air voient leurs contenus en trans inchangé pour le premier et notablement augmenté pour le second.
- Sur la configuration trans l'effet précédent est sans objet, mais l'oxygène agit localement sur la chaîne en perturbant le système des électrons π ce qui se traduit par une diminution de la longueur effective des séquences trans. On observe alors une augmentation de la largeur de raie RPE (diminution de la mobilité des électrons non appariés) [14] et une modification notable de la structure des raies Raman [3].

Enfin l'effet de l'oxygène se manifeste par une détérioration rapide des propriétés plastiques du matériau: après quelques minutes de soumission à l'air celui-ci ne peut plus être étiré. [1].

b) — Influence des espèces dopantes I_2 , SbF_5 et $CF_3 SO_3H$

Le contact direct du $(CH)_x$ cis ou trans avec les phases gazeuses ou liquides des espèces chimiques I_2 , SbF_5 et $CF_3 SO_3H$ conduit à une augmentation considérable de la conductivité du matériau qui passe de $10^{-9} (\Omega \text{ cm})^{-1}$ (ou $10^{-5} (\Omega \text{ cm})^{-1}$ pour le trans) à environ $10^2 (\Omega \text{ cm})^{-1}$ [15]. Comme dans le cas de l'oxygène, le dopage du cis avec les espèces chimiques ci-dessus induit une isomérisation vers l'état trans, quoique moins prononcée. Les taux de dopages maximum qui peuvent être atteints sont de l'ordre de 15 à 25 % (molaire), ces taux pouvant subir ensuite des variations considérables suivant le traitement qui est soumis à l'échantillon.

Les variations de la résistivité en fonction de la température présentent dans tous les cas un comportement caractéristique d'un état semi-conducteur (voir la fig. 10 pour le cas du dopage avec SbF_5). Néanmoins pour les taux de dopage les plus élevés les variations observées sont particulièrement faibles et suggèrent un état quasi métallique. Ceci peut être mis en évidence de manière plus précise en étudiant la dépendance avec le taux de dopage y de l'énergie d'activation E_a tirée des lois expérimentales $\log \rho$ fonction de $10^3/T$. On constate que pour $y < \sim 1\%$, E_a varie rapidement (comportement semi-conducteur) alors que pour $y > \sim 1\%$, E_a reste pratiquement constant à une faible valeur (comportement quasi-métallique). On peut donc définir une transition «semi-conducteur – métal» aux alentours de $y \sim 1\%$. La même observation est faite dans le cas du dopage à l'iode mais pour $y \sim 3\%$ [1]. Comme l'espèce chimique dopante dans ce dernier cas a été identifiée comme étant I_3^- on constate que dans les deux cas la transition se produit pour $\sim 1\%$ de porteurs de charges. Ceci montre que cette transition dépend de la concentration en porteurs de charge et non de la nature de l'espèce chimique dopante.

En ce qui concerne les propriétés magnétiques on assiste après dopage à une diminution considérable (d'un facteur qui peut aller jusqu'à 10^{-2}) de l'intensité du signal RPE, indiquant une chute importante de la susceptibilité χ . D'autre part dans le cas non dopé χ suit une loi de Curie (comportement paramagnétique classique)

alors que pour des taux de dopage importants (I_2 ou SbF_5) la susceptibilité plus faible est pratiquement indépendante de la température (paramagnétisme de Pauli caractéristique de l'état métallique)

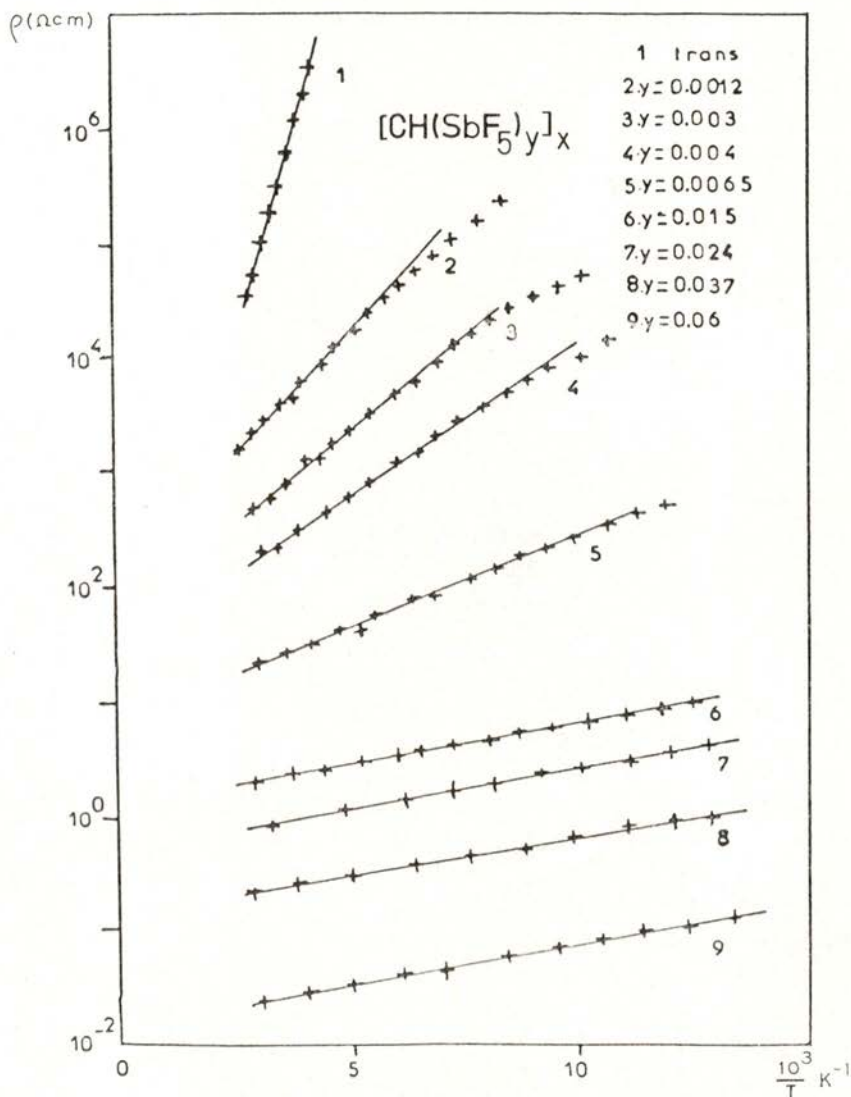


Fig. 10 — Dépendance de la résistivité ρ avec l'inverse de la température pour $(CH)_x$ dopé avec SbF_5 à différents taux de dopage γ . On note que pour $\gamma > \sim 1\%$ la dépendance avec T est faible avec une pente pratiquement indépendante de γ (comportement quasi-métallique).

(fig. 11) [16]. Une autre évidence de ce comportement métallique apparaît au vu de la forme dissymétrique de la raie RPE (forme de Dyson) et que l'on rencontre usuellement pour des plaques métalliques dont l'épaisseur n'est plus faible devant l'épaisseur de peau [16] [17].

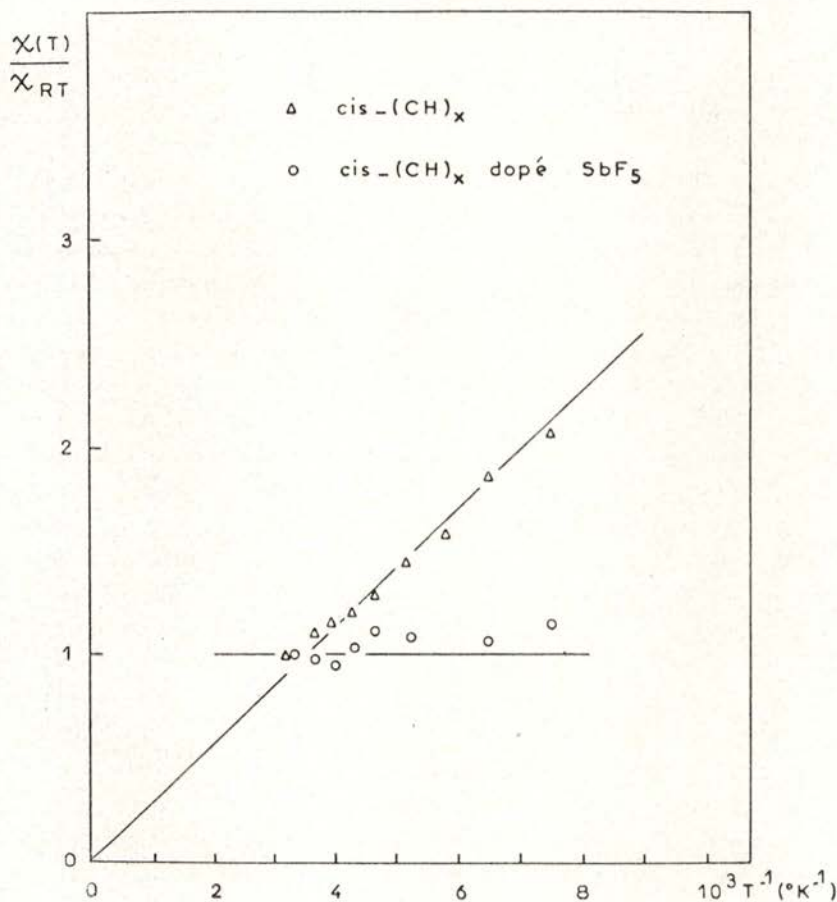


Fig. 11 — Dépendance avec T^{-1} de la susceptibilité électronique relative déduite des spectres RPE. Alors que la susceptibilité du $(\text{CH})_x$ non dopé (cis ou trans) suit une loi Curie, celle matériau dopé à saturation (régime quasi-métallique) est indépendante de T (paramagnétisme de Pauli).

Les espèces chimiques dopantes citées ici présentent une stabilité plus ou moins grande dans le système $(\text{CH})_x$. A température ambiante on peut par simple pompage faire chuter la concentration en Iode

de plus de 20 %, indiquant que beaucoup de molécules dopantes sont faiblement liées avec le système hôte. Par traitement thermique on peut accélérer le processus de dédopage. A 100°C par exemple le dopant I_2 a presque entièrement disparu du film de $(CH)_x$ au bout de quelques heures, alors que le dopant SbF_5 reste stationnaire à une concentration de $\sim 6\%$ [18].

c) — Optimisation de la conductivité électrique

Au chapitre III était clairement ressorti le rôle important joué par la dégradation du $(CH)_x$ au cours d'un traitement thermique à une température supérieure à $\sim 130^\circ C$. Or un tel traitement est nécessaire afin de porter le matériau cis dans sa configuration trans stable. Après dopage, on peut alors s'attendre à ce que la conductivité électrique dépende des conditions dans lesquelles l'isomérisation a été effectuée. Jusqu'à ce jour, ces conditions, telles qu'elles sont décrites dans la littérature [1], étaient: une ou deux heures de traitement thermique à $200^\circ C$. Les valeurs de la conductivité étaient alors ~ 100 à $200 (\Omega \text{ cm})^{-1}$ pour un dopage à l'iode par exemple. Nous avons montré qu'en utilisant les conditions propres à optimiser l'isomérisation (150 à $160^\circ C$, 30 à 60 minutes) la conductivité après dopage pouvait être augmentée d'une facteur 2 à 3 [11].

5 — QUELQUES APPLICATIONS DU POLYACÉTYLÈNE

Du fait de ses propriétés mécaniques et électriques, le polyacétylène a évidemment suscité beaucoup de recherches en vue d'applications industrielles. La possibilité de le polymériser en films de grandes surfaces est un atout appréciable.

Des fonctions redresseuses ont été obtenues en dopant deux films de $(CH)_x$, l'un de type n, l'autre de type p, et en les pressant l'un contre l'autre [1]. Néanmoins le système obtenu manque de stabilité et, par diffusion des dopants entre les fibres, on assiste à une compensation graduelle.

Des cellules solaires ont aussi été réalisées, en utilisant le $(CH)_x$ faiblement dopé comme matériau semi-conducteur, mais les rendements obtenus ($\sim 2\%$) ne sont pas encore assez élevés pour que l'on puisse envisager une utilisation à grande échelle [1].

Les applications qui sont actuellement développées mettent à profit une des caractéristiques les plus spectaculaires du $(CH)_x$: son énorme surface spécifique qui peut atteindre $100 \text{ m}^2 / \text{gr}$. D'autre part, son utilisation comme électrode dans un bain électrolytique atténue considérablement le problème posé par l'instabilité à l'air. Des chercheurs américains ont ainsi pu réaliser des cellules solaires photoélectrochimiques [19] ainsi que des microbatteries rechargeables de puissances raisonnables [20].

6 — CONCLUSION

Beaucoup de résultats obtenus sur le polyacétylène n'ont pas été décrits dans cet article. On en trouvera un bilan à peu près complet et récent dans la référence [1].

Nous avons voulu ici insister sur les propriétés du polyacétylène non dopé et montrer que celles-ci dépendent beaucoup de l'«histoire» de l'échantillon : conditions de polymérisation, soumission à l'air, traitement thermique, en particulier. Cette «histoire» de l'échantillon influe notablement sur les caractéristiques du système qui est obtenu après dopage. Ainsi, il est maintenant bien établi que par un choix judicieux des conditions de l'isomérisation, on peut optimiser la conductivité du matériau dopé.

Beaucoup de caractéristiques du polyacétylène rendent délicates la confrontation avec d'éventuels modèles théoriques : inhomogénéité, semicristallinité, instabilité. Si l'obtention d'un matériau homogène, stable et cristallin permettrait de mieux comprendre les propriétés physiques du polyacétylène, il n'en reste pas moins que certaines caractéristiques du système obtenu actuellement, comme la simplicité de sa synthèse et son énorme surface spécifique, en font un matériau de choix en vue d'applications industrielles.

REFERENCES

- [1] *The Physics and Chemistry of Low Dimensional Solids*. Proceedings of the NATO ASI, Tomar (Portugal), Sept. 1979, Ed. L. Alcazer, D. Reidel Pub.
- [2] ITO, T., SHIRAKAWA, H., IKEDA, S., *J. Polym. Sci.*, **12**, 11 (1974).
- [3] LEFRANT, S., RZEPKA, E., BERNIER, P., ROLLAND, M., ALDISSI, M., LINAYA, C., *Sol. St. Comm.*, à paraître.

- [4] MONTANER, A., GALTIER, M., BENOIT, C., ALDISSI, M., Soumis à *Polymer*.
- [5] BERNIER, P., SCHUE, F., SLEDZ, J., ROLLAND, M., GIRAL, L., *Chemica Scripta*, à paraître.
- [6] BAUGHMAN, R. H., HSU, S. L., PEZ, G. P., SIGNORELLI, A. J., *J. Chem. Phys.*, **68**, 5405 (1978).
- [7] BERNIER, P., ROLLAND, M., LINAYA, C., ALDISSI, M., *Polymer*, **21**, L7 (1980).
- [8] SOGA, K., KAWAKAMI, S., SHIRAKAWA, H., IKEDA, S., *Makromol. Chem.*, **1**, 523 (1980).
- [9] HOLCZER, K., BOUCHER, J. P., DEVREUX, F., NECHTSCHHEIN, M., à paraître.
- [10] BERNIER, P., ROLLAND, M., LINAYA, C., ALDISSI, M., à paraître.
- [11] ROLLAND, M., BERNIER, P., LEFRANT, S., ALDISSI, M. *Polymer*, à paraître.
- [12] LEFRANT, S., LITCHMANN, L. S., TEMKIN, H., FITCHEN, D. B., MILLER, D. C., WHITWELL, D. C., BURLITCH, J. M., *Sol. St. Comm.*, **29**, 191 (1979).
- [13] BENIERE, F., HARIDOSS, S., LOUBOUTIN, J. P., ALDISSI, M., FABRE, J. M., à paraître.
- [14] BERNIER, P., ROLLAND, M., LINAYA, C., ALDISSI, M., SLEDZ, J., FABRE, J. M., SCHUE, F., GIRAL, L., *Polymer Journal*, 1980, à paraître.
- [15] ROLLAND, M., BERNIER, P., ALDISSI, M., LINAYA, C., SLEDZ, J., SCHUE, F., FABRE, J. M., GIRAL, L., *J. de Physique, Lettres*, **41**, 165 (1980).
- [16] BERNIER, P., ROLLAND, M., GALTIER, M., MONTANER, A., REGIS, M., CANDILLE, M., BENOIT, C., ALDISSI, M., LINAYA, C., SCHUE, F., SLEDZ, J., FABRE, J. M., GIRAL, L., *J. de Physique, Lettres*, **40**, 297 (1979).
- [17] GOLDBERG, I. B., CROWE, H. R., NEWMAN, P. R., HEEGER, A. J., MACDIARMID, A. G., *J. Chem. Phys.*, **3**, 1132 (1979).
- [18] ROLLAND, M., BERNIER, P., ALDISSI, M., à paraître.
- [19] CHEN, S. N., HEEGER, A. J., KISS, Z., MACDIARMID, A. G., GAU, S. C., PEEBLES, D. L., *App. Phys. Lett.*, **36**, 96 (1980).
- [20] NIGREY, P., HEEGER, A. J., MACDIARMID, A. G., à paraître.

CONCENTRATION AND SOLVENT EFFECTS ON LUMINESCENCE OF MOLECULES CONTAINED IN RIGID MATRICES

L. C. PEREIRA, M. M. S. PINHEIRO and M. E. C. DIAS

Centro de Química Pura e Aplicada da Universidade do Minho,
Física Molecular, Av. João XXI, 4700 Braga

(Received 12 December 1980)

ABSTRACT — Fluorescence and phosphorescence of cumene and of tryptophan in rigid matrices of methylcyclohexane and ethanol were measured at 77 K as a function of concentration. Effects of photoselection were investigated at various concentrations. The results show that the phosphorescence lifetimes and phosphorescence quantum yields decrease upon concentration for cumene solutions, in which a correlation was established between phosphorescence depolarization and increasing concentration. Phosphorescence decay curves become non-exponential at higher concentrations in the case of cumene solutions.

1—INTRODUCTION

The understanding of environmental effects on luminescence of molecules contained in rigid glasses is fundamental in photophysical studies carried out at 77 K. Although phosphorescence spectroscopy is a current technique in the study of triplet states of aromatic molecules, the effects of the glassy media on the measured parameters is still open to question [1]. On the other hand, concentration effects [2-3] and photoselection [4] can also bring about new problems in the interpretation of the spectroscopic results. In the present work we have obtained luminescence spectra and phosphorescence lifetimes of isopropylbenzene (cumene) in methylcyclohexane and ethanol glasses at 77 K, changing the concentration from about 0.72 M down to 7.2×10^{-4} M. Special care was put on the investigation of the character of the phosphorescence decay curves as a function of either solute concentration, nature of the glassy environment and wavelength peak emission.

For its biological importance the same type of research was undertaken with tryptophan solutions.

The excitation wavelength λ_{ex} , was in general 255 nm for cumene emission spectra and $\lambda_{\text{ex}} = 280$ nm for tryptophan.

2 — EXPERIMENTAL DETAILS

Fluorescence, phosphorescence and excitation spectra were measured in a conventional Perkin-Elmer spectrometer. The changes of the degree of polarization, p , for fluorescence and phosphorescence were obtained with a proper set of UV polarizers. Under the experimental conditions used, the value of p is taken [5] as

$$p = \frac{I_{VV} - I_{VH} (I_{HV} / I_{HH})}{I_{VV} + I_{VH} (I_{HV} / I_{HH})}$$

The subscripts show the orientation of the electric vector (first letter) and emission (second letter), V and H representing the vertical and horizontal orientations. The expression accounts for the eigenpolarization of the apparatus [6] which under our experimental conditions is not negligible, particularly over the longer wavelength region.

The experimental arrangements and nomenclature used for polarization studies is illustrated in Fig. 1.

Dried gaseous nitrogen was circulated inside the sample compartment to avoid some possible condensation on the dewar walls. Most of the samples were uncracked and transparent at 77 K although this is not always the case at higher concentrations, in which signs of turbidity were apparent. Fast-cooled and slow-cooled samples did not produce any appreciable alteration on the measured photophysical parameters. Further details of the experimental procedure used for phosphorescence measurements were previously reported [3].

3 — RESULTS AND DISCUSSION

The kinetic scheme for the most probable unimolecular processes taking place after the excitation of the molecule can be written as follows:

	Process	Rate parameter
Fluorescence	$^1M^* \rightarrow ^1M + h\nu_{FM}$	K_{FM}
Internal conversion	$^1M^* \rightarrow ^1M$	K_{GM}
Intersystem crossing	$^1M^* \rightarrow ^3M^*$	K_{TM}
Phosphorescence	$^3M^* \rightarrow ^1M + h\nu_{PT}$	K_{PT}
Intersystem crossing	$^3M^* \rightarrow ^1M$	K_{GT}

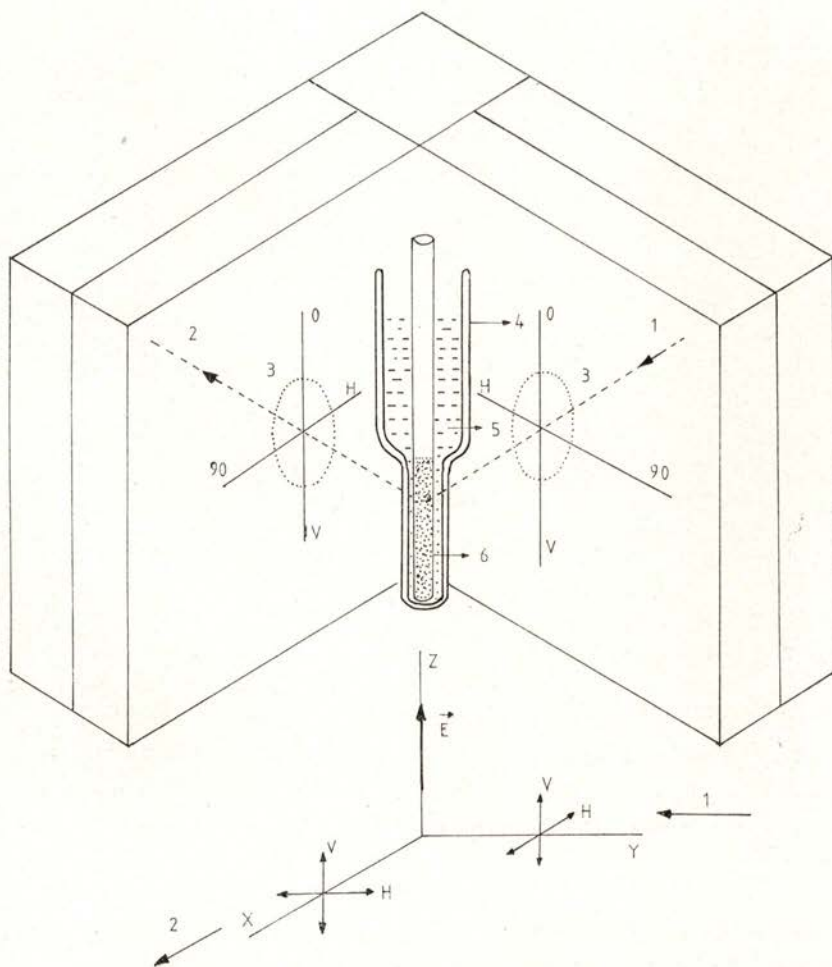


Fig. 1 — Experimental arrangement of the cell compartment for the measurement of polarization luminescence spectra; 1—excitation beam; 2—emission beam; 3—polarizer; 4—quartz dewar; 5—liquid nitrogen; 6—quartz cell; V—vertical orientation of the electric vector, \vec{E} ; H—horizontal orientation.

The notation used follows the one generally accepted in Organic Luminescence for characterizing the electronic and spin states [7-9].

An example of fluorescence and phosphorescence spectra of cumene in methylcyclohexane (7.2×10^{-4} M) is shown in Fig. 2,

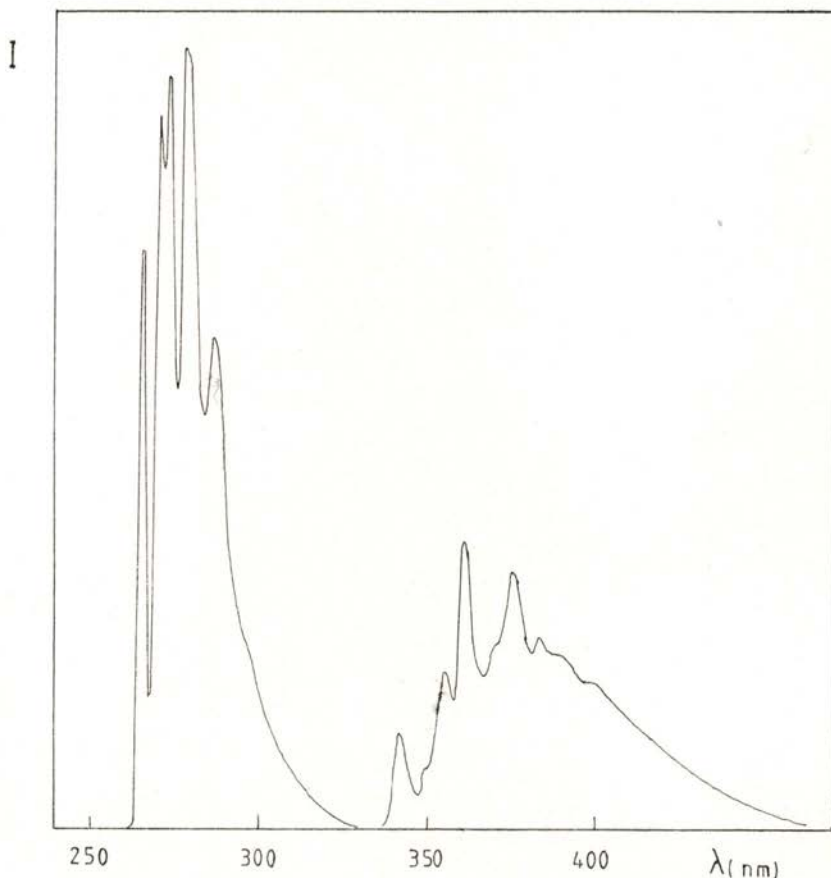


Fig. 2 — Fluorescence and phosphorescence spectra of cumene in methylcyclohexane (7.2×10^{-4} M) at 77 K.

obtained from a transparent sample, without polarizers. Phosphorescence spectra of the same sample, obtained with the various orientations of both polarizers, are presented in Fig. 3. From the spectra one can conclude that photoselection is not negligible for randomly orientated molecules at 77 K. This implies that the experimental ratio of the phosphorescence quantum yield to fluorescence quantum yield,

$\chi = \phi_{PT} / \phi_{FM}$, measured from spectra obtained without polarizers, can, in fact, introduce some errors as pointed out before [4], [10]. Experimental arrangements to correct for emission anisotropy are, in general, quite complicated for studies carried out at 77 K with glassy

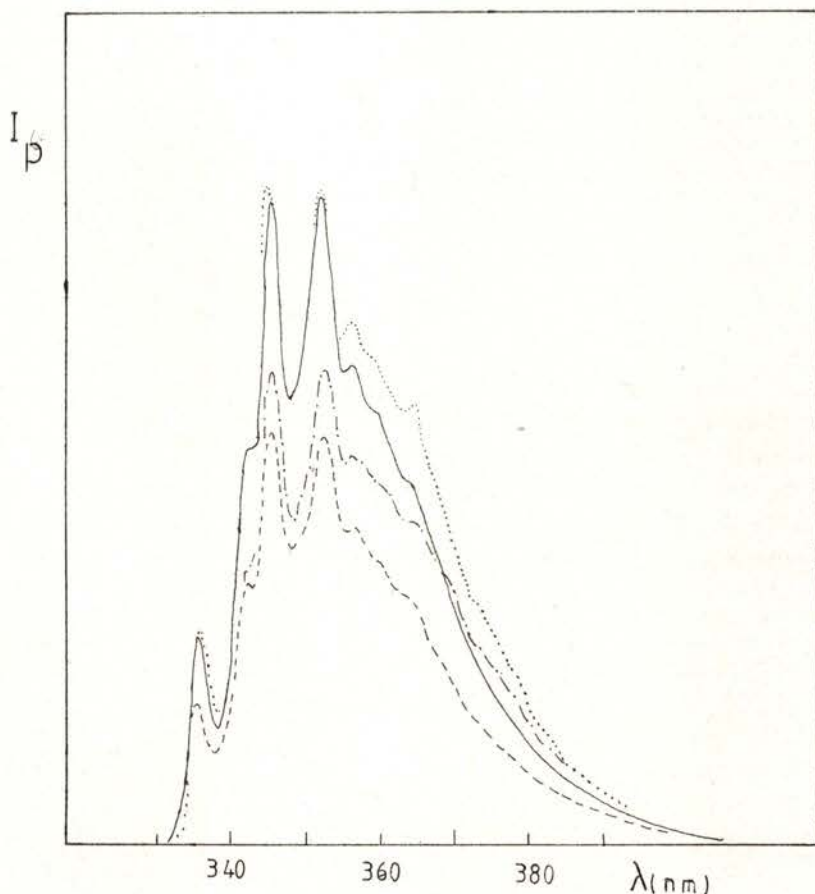


Fig. 3—Phosphorescence spectra of cumene in methylcyclohexane ($7.2 \times 10^{-4}M$) for various orientations of the polarizers: HV(—); HH(...); VH(- - -); VV(-.-).

solvents [10]. It is therefore advisable to get the correct luminescence values of I_{VH} and I_{VV} for a proper interpretation of the χ values obtained.

Results obtained for cumene solutions in ethanol are listed in Table I. The reported values of phosphorescence lifetimes, τ_p , are averages obtained from various recorded decays. The majority of log plots are exponential after the initial intensity has dropped about

TABLE I—Experimental values of χ , τ_p and χ/τ_p of cumene solutions in ethanol, at various concentrations.

C (M)	χ	τ_p (s)	χ/τ_p (s ⁻¹)
7.2	~ 0.1	—	—
3.6	~ 0.1	2.0	—
0.72	0.44	4.0	0.11
0.36	0.56	6.5	0.09
0.14	0.90	7.1	0.13
7.2×10^{-2}	0.94	7.2 ($\lambda_{em} = 376$ nm)	0.13
		7.3 ($\lambda_{em} = 342$ nm)	0.13
		7.0 ($\lambda_{em} = 362$ nm)	
7.2×10^{-3}	1.02	7.5	0.14
7.2×10^{-4}	0.96	7.5	0.13

10–20%. The reproducibility of values is within ± 0.2 s. Phosphorescence lifetimes are independent of emission wavelength, λ_{em} , as seen in Table I for 7.2×10^{-2} solutions. In the remaining cases the τ_p values are obtained at $\lambda_{em} = 376$ nm for cumene solutions. In table II we show the values of χ ratios and of τ_p , measured for cumene solutions in methylcyclohexane, as a function of concentra-

TABLE II—Experimental values of χ and τ_p of cumene solutions in ethanol, at various concentrations, without polarizers and with polarizers.

C (M)	χ	τ_p (s) without polarizers	τ_p (s) with polarizers
0.72	0.41		VH-2.8 HV-2.8 VV-2.9 HH-2.8
0.14	0.70	5.0 ($\lambda_{em} = 342$ nm) 5.1 ($\lambda_{em} = 362$ nm) 5.6 ($\lambda_{em} = 376$ nm)	
7.2×10^{-2}	0.74	5.9	
7.2×10^{-3}	0.73	5.9	
7.2×10^{-4}	0.73	6.0	HH-6.0 VH-6.0 VV-5.9 HV-6.0

tion. Results of τ_p obtained with and without polarizers and at various λ_{em} , show no major differences, at a common concentration.

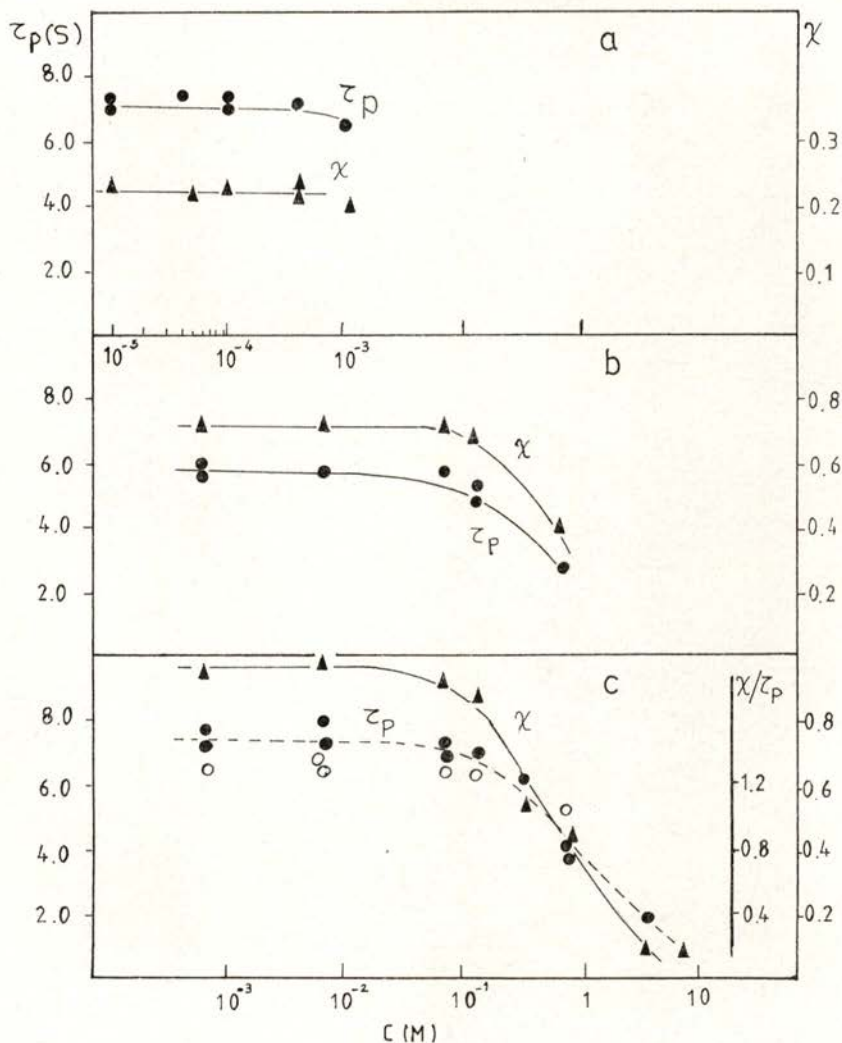


Fig. 4—Experimental values of χ and τ_p as a function of concentration; a—tryptophan in ethanol; b—cumene in methylcyclohexane; c—cumene in ethanol; (o) represent χ/τ_p .

The results obtained for χ , τ_p and χ/τ_p are summarized in Fig. 4 for tryptophan and cumene solutions, at various concentrations.

Values of τ_p at higher concentrations are of difficult assessment in our experimental set up. A proper phosphoroscope is being constructed in our laboratory for suitable measurements of lifetimes in

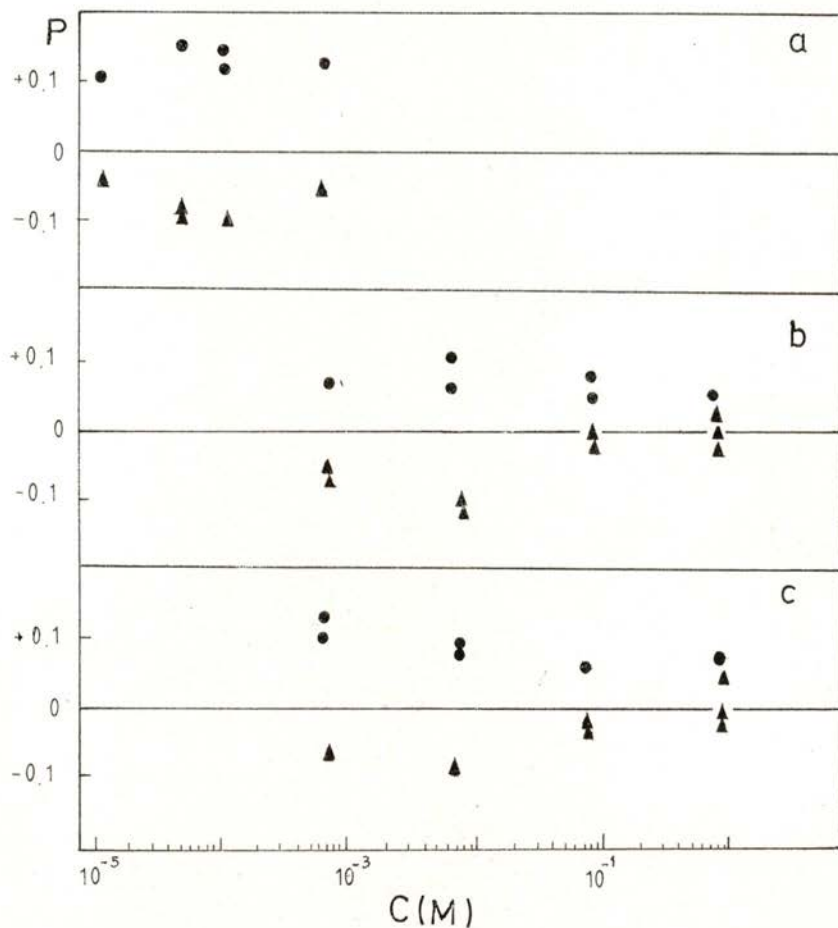


Fig. 5 — Values of luminescence polarization, p , vs concentration; a — tryptophan in ethanol, $\lambda_{ex} = 280$ nm, $\lambda_{em} = 311$ nm (\bullet) and $\lambda_{em} = 404$ nm (\blacktriangle); b — cumene in ethanol, $\lambda_{ex} = 260$ nm, $\lambda_{em} = 274$ nm (\bullet) and $\lambda_{em} = 362$ nm (\blacktriangle); c — the same as b, for cumene in methylcyclohexane.

the milisecond region. However we were able to demonstrate that a decrease of τ_p , ϕ_{PT} and exponentiality of the decays is taking place at higher solute concentrations.

The concentration variation of polarization of the same systems are presented in Fig. 5. The values were obtained upon well defined emission bands with weak vibrational overlap. Careful mea-

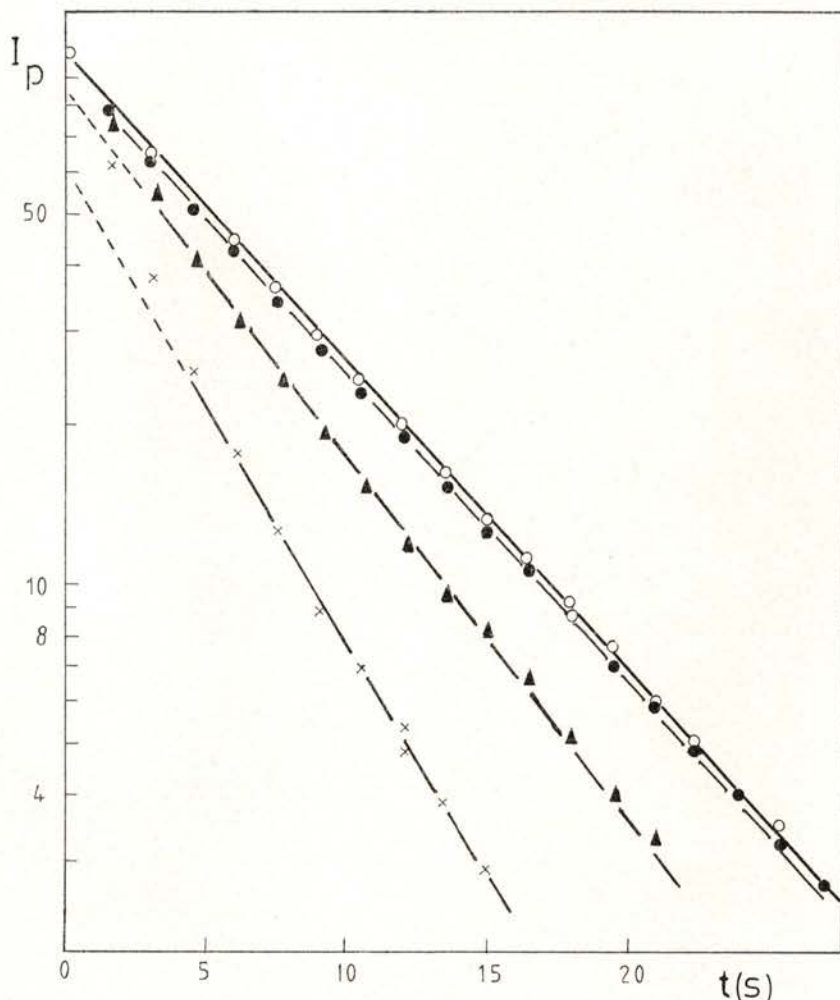


Fig. 6—Phosphorescence log decays of cumene in ethanol; (o) $7.2 \times 10^{-4}\text{M}$; (•) $7.2 \times 10^{-3}\text{M}$; (Δ) 0.36M ; (\times) 0.72M ; $I_p = 1(0)$ is a common value to all the decays.

surements must be taken to ensure good reproducibility during the period of a series of experiments. It was advisable to measure consecutively the luminescence from the various orientations (for example I_{VV} , I_{VH} , I_{HV} , I_{HH} , and then to check again I_{VV}) to be sure

that any alteration had occurred. We can see from Fig. 5 that fluorescence displays a typical «in plane» polarization while an «out of

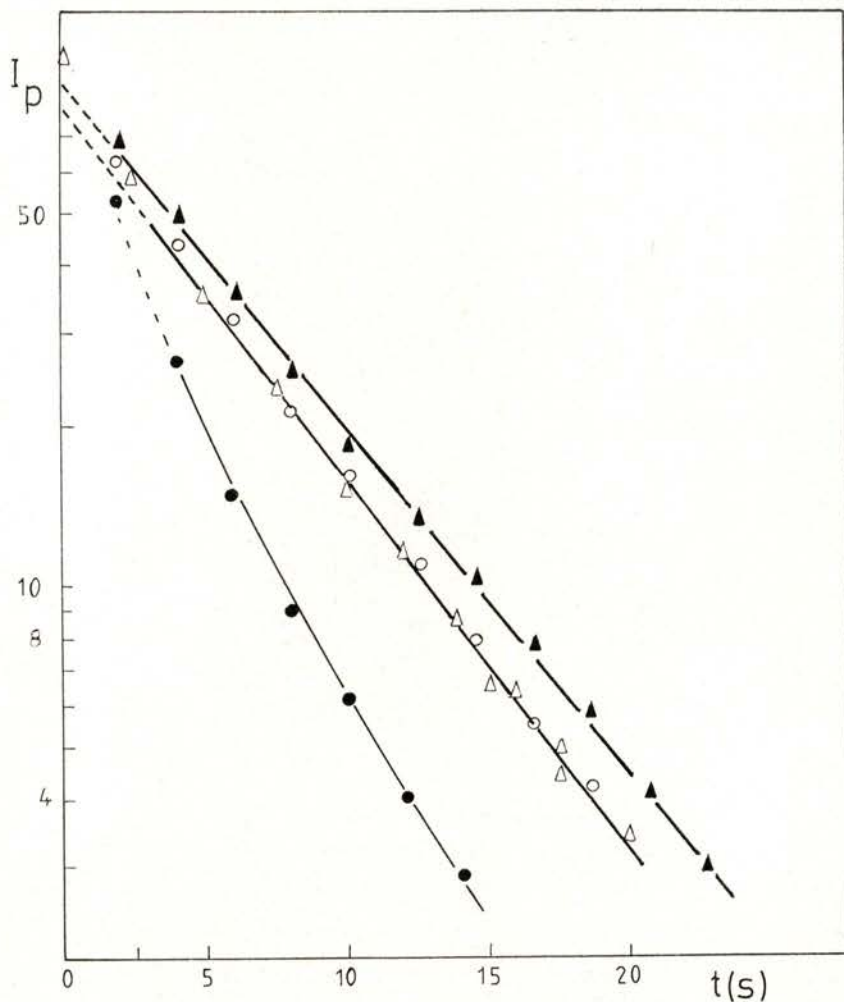


Fig. 7 — Phosphorescence log decays of cumene in methylcyclohexane; (▲) $7.2 \times 10^{-4}M$; (○) $7.2 \times 10^{-2}M$; (Δ) $0.14M$; (●) $0.72M$; $I_p = 100$ is a common value to all the decays.

plane» character is found for phosphorescence. However this negative polarization for phosphorescence disappears at higher concentrations in cumene solutions.

It is interesting to note that the correlation of phosphorescence depolarization upon concentration is accompanied by an increase of the non-exponential behaviour of the respective decay curves.

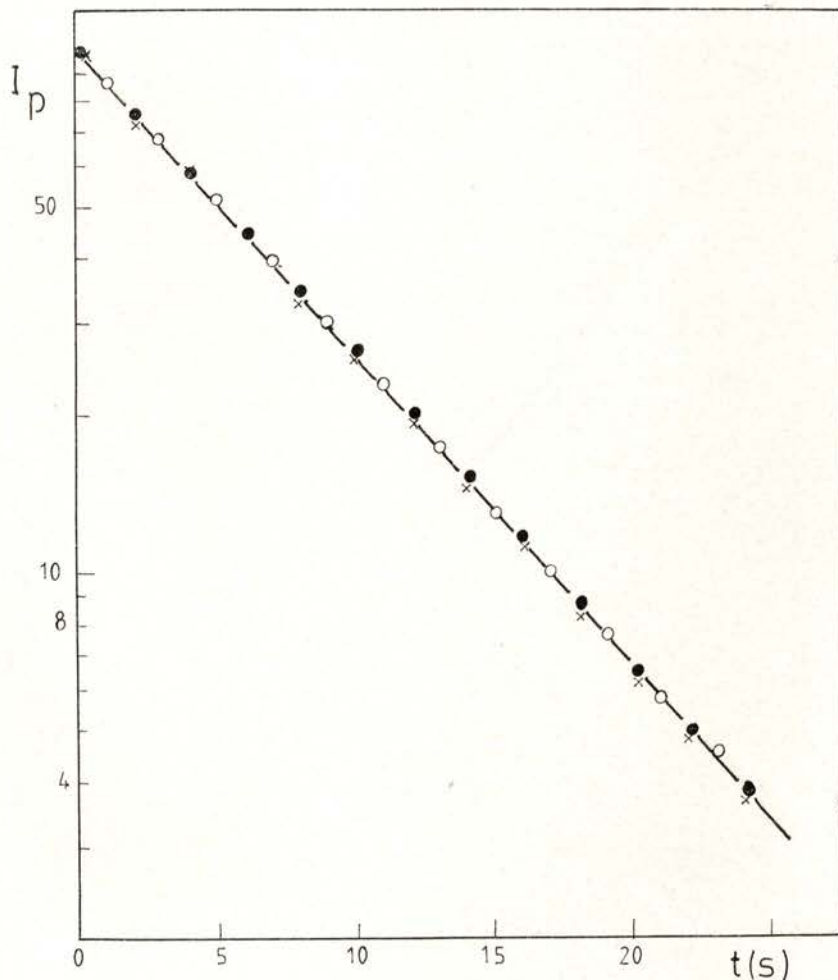


Fig. 8—Phosphorescence log decays of tryptophan in ethanol; (●) $5 \times 10^{-5}\text{M}$; (○) $1 \times 10^{-4}\text{M}$; (×) $1 \times 10^{-3}\text{M}$.

The character of the various decays as a function of concentration was investigated for cumene in ethanol, cumene in methylcyclohexane and tryptophan in ethanol as shown, respectively, in Fig-

res 6, 7 and 8. The decays displayed at different orientations of the polarizers, for a dilute solution of cumene in methylcyclohexane, show

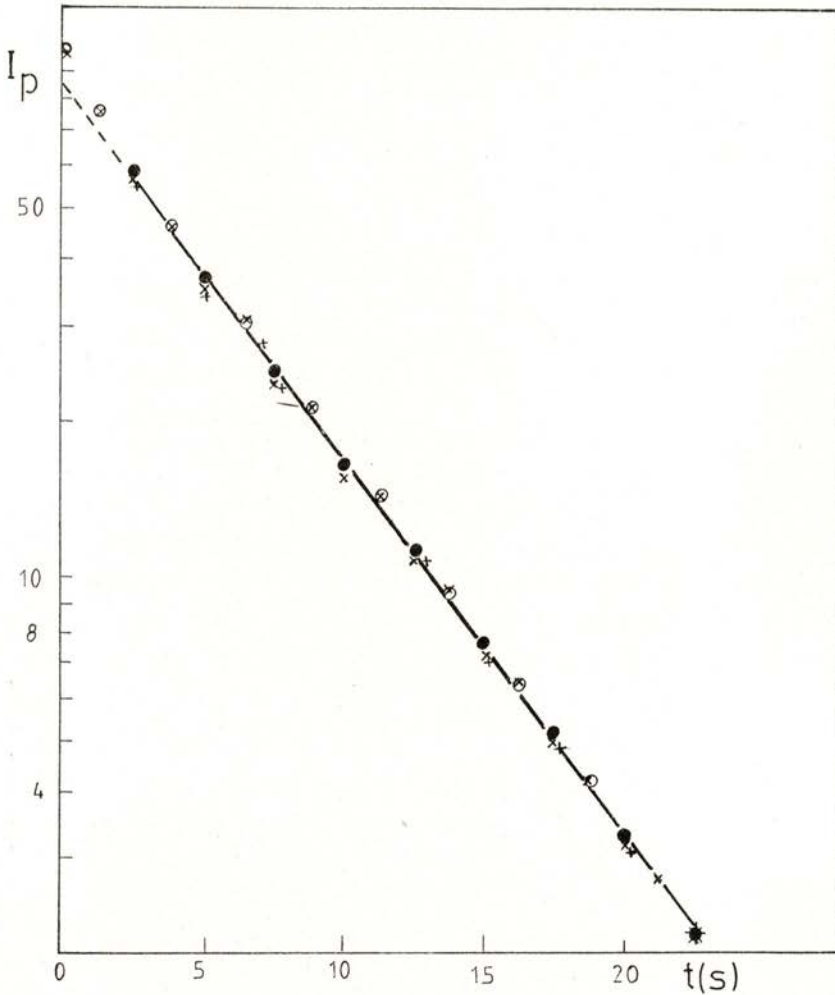


Fig. 9 — Phosphorescence log decays of cumene in methylcyclohexane ($7.2 \times 10^{-4}\text{M}$) at various orientations of the polarizers. HH(•); VH(×); HV(o); VV(+); $I_p = 100$ is common to all the decays.

the same type of behaviour, as illustrated in Fig. 9. One can conclude that the degree of polarization does not change during the phosphorescence decay.

The results of Table I, Table II and Fig. 4 show, for cumene solutions, that not only τ_p and λ decrease upon concentration but the same happens to λ/τ_p . Moreover the phosphorescence intensity drops down to zero at higher concentration. Similar results have been reported with benzene and benzene derivatives [3], [11–12]. In the absence of further deexcitation processes of $^1M^*$ and $^3M^*$ the ratio λ is given by

$$\lambda = K_{TM} K_{PT} \tau_p K_{FM}^{-1}$$

and the results would indicate that either K_{TM} , K_{PT} or K_{FM} could change upon concentration. An increase in the measured fluorescence quantum yield, ϕ_{FM} , vs concentration was reported [11] for a single crystal of benzene but the results obtained require a cautious interpretation. It should be said that an increase of ϕ_{FM} with a decrease of temperature, as found in benzene, is in good agreement with a similar variation of fluorescence lifetime, τ_M , vs temperature [13], which implies that K_{FM} is practically constant with temperature, except for its variation due to refractive index differences [14]. On the other hand our results have shown that the ratio λ does not represent the true ratio of phosphorescence to fluorescence yields, due to the fact that a different set of photoselected molecules is viewed from samples with different concentrations. Furthermore the values of τ_p at higher concentrations do not represent a single exponential decay in the case of cumene solutions. It should be noted that the results obtained for tryptophan solutions show that both λ and τ_p are unchanged with concentration and that the phosphorescence decays are all exponential. However the fact that concentrations used are much lower (10^{-3} M to 10^{-5} M) could explain the absence of concentration effects on λ and τ_p of this molecule. This is also true for the polarization results presented in Fig. 9. We can see that p is relatively constant for both fluorescence and phosphorescence of tryptophan solutions (10^{-3} M– 10^{-5} M), while, for cumene, a depolarization is taking place when concentration increases.

Concentration depolarization of phosphorescence has been reported elsewhere [15] for other aromatic molecules, in which the results could be attributed to a triplet-triplet energy transfer mechanism.

Some general conclusions can already be drawn from the results obtained although a proper kinetic analysis is complex and would need further studies at higher concentrations, including 100% solutions. The results illustrate that both concentration and environmental characteristics change considerably the behaviour for the emitting triplet of cumene. This is not the case of tryptophan solutions under our experimental conditions. For that reason we refer our conclusions to cumene results. Phosphorescence lifetimes and triplet decay curves are strongly dependent on concentration and, at a given concentration, they are also influenced by the solvent environment.

Very dilute solutions show a single exponential decay of the phosphorescent molecules in ethanol matrices, while in methylcyclohexane the decay deviates from exponentiality at the same concentration. On the other hand, the triplet is long lived in ethanol when compared to methylcyclohexane. This is probably due to differences of viscosity and or structure of the glasses. The results are compatible with the existence of other (or others) deexcitation channel apart from the usual unimolecular processes. As a matter of fact it seems reasonable to accept that K_{FM} , K_{PT} , K_{GT} and K_{TM} do not depend strongly on the environment, at 77K. Triplet-triplet migration at higher concentrations could well explain both the triplet quenching and luminescence depolarization. However one can not neglect the possibility of the existence of agregation of cumene molecules into microcrystalline regions in which excitonic migration can occur, thus reducing the phosphorescence signal. This hypothesis is also consistent with the non-exponential behaviour of the decays at higher concentrations for which phosphorescence could occur from molecules trapped in non-equivalent sites.

This possibility is in good agreement with the experimental detection of delayed fluorescence in benzene and toluene solid solutions [3] with a suitable phosphoroscope. Broadening of the phosphorescence spectra with increasing concentration, as found in the present work, is also compatible with emission arising from microcrystalline regions.

Financial support by INIC (National Institute for Scientific Research, Portugal) and NATO (Res. Grant no. 674) is gratefully acknowledged. We also thank E. Lenine and Nelson Almeida for technical assistance.

REFERENCES

- [1] R. B. CUNDALL, D. A. ROBINSON and L. C. PEREIRA, *Advances in Photochemistry*, John Wiley, Interscience, **10**, 147 (1977).
- [2] M. D. LUMB, C. L. BRAGA and L. C. PEREIRA, *Trans. Faraday Soc.*, **65**, 1992 (1969).
- [3] R. B. CUNDALL and L. C. PEREIRA, *Chem. Phys. Lett.*, **29**, 561 (1974).
- [4] E. D. CEHELNIK, K. D. MIELENZ and R. A. VELAPOLDI, *J. Res. of NBS-A Phys. and Chem.*, **79A**, 1 (1975) and references therein.
- [5] M. GRATZEL and J. K. THOMAS, *Modern Fluorescence Spectroscopy*, ed. E. L. Wehry, vol. 2, Heyden, London (1976).
- [6] M. ALMGREN, *Photochem. Photobiol.*, **8**, 231 (1968).
- [7] J. B. BIRKS, *Photophysics of Aromatic Molecules*, Wiley-Inter-Science, London (1970).
- [8] M. D. LUMB, *Luminescence Spectroscopy*, Academic Press (1978).
- [9] R. SANTUS, M. BAZIN and M. AUBAILLY, *Rev. Chem. Intermediates*, **3**, 231 (1980).
- [10] K. D. MIELENZ, E. D. CEHELNIK and R. L. MCKENZIE, *J. Chem. Phys.*, **64**, 370 (1976).
- [11] M. D. LUMB and L. C. PEREIRA, *Organic Scintillators and Liquid Scintillation Counting*, eds. D. L. Horrocks and C. Peng, Academic Press, New York, 239 (1971).
- [12] F. HIRAYAMA, *J. Chem. Phys.*, **42**, 3726 (1965).
- [13] A. O. AL-CHALABI, *Chem. Phys. Lett.*, **70**, 371 (1980).
- [14] Reference [7], p. 103.
- [15] N. K. CHAUDRURI and M. A. EL-SAYED, *J. Chem. Phys.*, **42**, 1947 (1965).



STRUCTURAL ANALYSIS OF LAVES PHASES WITH Ti

M. J. M. DE ALMEIDA, M. M. R. COSTA, L. ALTE DA VEIGA,
L. R. ANDRADE and A. MATOS BEJA

Grupo de Estruturas dos Materiais, FC1, INIC, Departamento de Física,
3000 Coimbra, Portugal

(Received 29 December 1980)

ABSTRACT — The atomic structure of the Laves phases TiFe_2 and TiMn_2 has been refined by X-ray diffraction from single crystals. The interatomic distances have been calculated and discussed in terms of the contraction of atoms in these structures.

1 — INTRODUCTION

A detailed description of the structures of the Laves phases has been given by Sinha [1] based on the original work of Laves and Witte [2].

These phases have generally a stoichiometric composition AB_2 and the closest packing of the constituent atoms occurs when the ratio of their atomic radii, R_A/R_B , is 1.225. If we consider that two atoms make a 'contact' when their interatomic distance is smaller than the sum of the corresponding atomic radii, then, under the above conditions, only A-A and B-B contacts are possible.

However, several binary alloys with a Laves phase structure for which R_A/R_B deviates from that ideal value have been found, R_A/R_B varying between 1.05 and 1.68. In these cases, adjustments in the atomic dimensions can be observed, so as to preserve the closest possible packing of the atoms in the structure; these can possibly be attributed to changes in the valences of the constituent elements. Thus, when $R_A/R_B > 1.225$ the A atom and hence the interatomic distance A-A undergo an apparent contraction [3]. In some of these Laves phases Pearson [4] has observed the occurrence not only of

A-A and B-B but also of A-B contacts. When $R_A/R_B < 1.225$, B-B contacts are predominant.

Values of R_A/R_B favouring the structure of the Laves phases occur frequently when A is a transition metal to the left of chromium in the periodic table and B is an element to the right of this metal, either in the same or in a different series.

The structural study of three Laves phases, $TiMn_2$, $TiFe_2$ and $TiCo_2$ was undertaken in this Laboratory. In the present paper the results obtained by X-ray diffraction for the two first alloys are reported. The aim of this work is the accurate determination of interatomic distances and the analysis of their variation in a set of AB_2 alloys whose B atom varies along a transition series in the periodic table.

2—EXPERIMENTAL

The Laves phases are homogenous over the ranges 22.5–35.0 at% Ti (Murakami *et al*, [5]) and 31.6–42.0 at% Ti (Murakami *et al*, [6]), respectively.

Both phases have the $MgZn_2$ (C14) hexagonal type structure. Ingots of $TiFe_2$ and $TiMn_2$, containing both 33.33 at% Ti were kindly supplied by Dr. M. Nevitt, Argonne National Laboratory, Illinois, U. S. A..

Single crystals of $TiFe_2$ and $TiMn_2$ with regular shape and dimensions of the order of 0.2 and 0.4 mm, respectively, were selected for the subsequent diffraction experiments.

The lattice parameters obtained by the method of Farquhar and Lipson [7] for the specimen of $TiFe_2$ are:

$$a = 4.7942 \pm 0.0003 \text{ \AA} \quad c = 7.8238 \pm 0.0003 \text{ \AA} \quad c/a = 1.632$$

Measurements of the lattice parameters of both crystals were carried out in an automatic 4-circle diffractometer, yielding the results:

$$TiFe_2: \quad a = 4.7870 \pm 0.0004 \text{ \AA} \quad c = 7.8150 \pm 0.0007 \text{ \AA} \quad c/a = 1.633$$

$$TiMn_2: \quad a = 4.8310 \pm 0.0005 \text{ \AA} \quad c = 7.9390 \pm 0.0008 \text{ \AA} \quad c/a = 1.643$$

No reason could be found for the significant difference in the lattice parameters of $TiFe_2$ obtained by the two methods.

A preliminary study of both structures, based on Laue and oscillation photographs, has justified the choice of the spatial group $P6_3/mmc$ attributed to both structures; this is in agreement with previous investigations (Wallbaum, [8]; Duwez and Taylor, [9]).

The integrated intensities of a large number of reflections from both crystals were collected, using filtered Mo-K α radiation, on a Philips automatic diffractometer of the Instituto de Química-Física «Rocasolano» of the Consejo Superior de Investigaciones Científicas, Madrid (Spain).

A set of independent $0k.l$ reflections from either crystal out to $(\sin \theta)/\lambda = 1.15 \text{ \AA}^{-1}$ were selected; of these, approximately 100 from TiFe_2 and 86 from TiMn_2 , for which $F_o > 3\sigma_{F_o}$ were used in subsequent structure refinements, F_o and σ_{F_o} standing for the observed structure factor amplitude and the corresponding standard deviation.

3 — STRUCTURE REFINEMENT

The atomic positions in the hexagonal unit cell of the C14 type of structure can be determined using the reflection intensities from the zero layer line of the $[2\bar{1}.0]$ projection.

For simplicity, a non-primitive orthorhombic unit cell with dimensions a , $a\sqrt{3}$ and c was chosen, which is equivalent to the primitive hexagonal cell; hence, the hexagonal indices $0k.l$ were transformed into orthorhombic indices, $02k.l$.

The reflection intensities were corrected in the usual way for Lorentz and polarization factors. Allowance was made for the resolution of the $\alpha_1 \alpha_2$ doublet by scaling observed and calculated structure factor amplitudes, F_o and F_c , in regions of $(\sin \theta)/\lambda$. This procedure also takes into account the variation of absorption in the crystal: owing to the regular shape and small dimensions of both TiFe_2 and TiMn_2 specimens no further absorption correction was applied.

Atomic scattering factors were calculated from the set of analytical constants given by Forsyth and Wells [10] for Fe, Ti^{2+} and Mn^{2+} .

The refinement of atomic and temperature parameters was based on two-dimensional Fourier syntheses, $(F_o - F_c)$; the atomic parameters x and z known for the MgZn_2 structure were initially postulated in both cases. The final stages of the refinement will now be described for TiFe_2 and TiMn_2 separately.

TiFe₂

An isotropic temperature factor, $B = 0.439$, obtained by the Wilson method, was used for the calculation of F_o in the first Fourier syntheses. The refinement of this factor was carried out in the following way: values of B , varying between 0.3 and 0.5 were attributed to the iron and titanium atoms separately, while the atomic parameters were kept fixed. The best difference maps and lowest R-factors were obtained for the value initially postulated for B .

In the final stages of the refinement, extinction was found to affect two of the strongest reflections, namely 400 and 401. An empirical extinction correction (Damjanovick and Black, [11]) was applied. The Fourier difference maps did not evidence any significant alteration and the R-factor decreased from 0.054 to 0.052.

The final values of the atomic parameters, their standard deviations and temperature factors are shown in table 1, together with the corresponding R-factor. Figures 1(a) and 1(b) show the final F_o and $(F_o - F_c)$ maps.

Table 1 — Atomic parameters and their standard deviations, temperature factors and R-factors for the structures TiFe₂ and TiMn₂.

Position	Atom		MgZn ₂ (AB ₂)	TiFe ₂ (AB ₂)	TiMn ₂ (AB ₂)
2 (a) (0, 0, 0)	B	—	—	—	—
6 (h) (x, 2x, 1/4)	B	x	0.1667	0.1710 ± 0.0002	0.1701 ± 0.0004
4 (f) (1/3, 2/3, z)	A	z	0.0625	0.0640 ± 0.0003	0.0642 ± 0.0005
				B _{Ti} = 0.439	B _{Ti} = 0.50
				B _{Fe} = 0.439	B _{Mn} = 0.30
				R = 0.052	R = 0.051

TiMn₂

An isotropic temperature factor, $B = 0.4$, was initially used in the calculation of F_o . The Fourier difference maps were found to be sensitive to variations of this value, and suggested the use of different temperature factors for Ti and Mn.

No extinction correction was applied to the reflection intensities, since the observed structure amplitudes, F_o , were not significantly lower than the corresponding F_c , even for the strongest reflections.

The refined atomic parameters, their standard deviations and the temperature factors, as well as the corresponding R-factor, are listed in table 1. Figures 2(a) and 2(b) show the final F_o and $(F_o - F_c)$ maps.

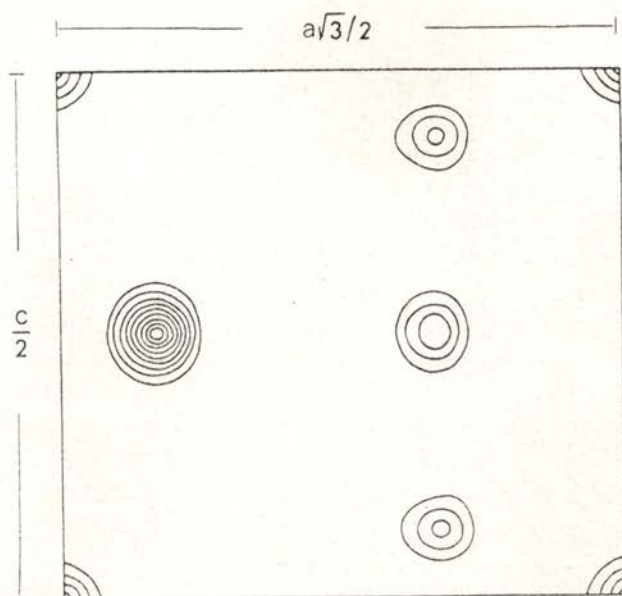
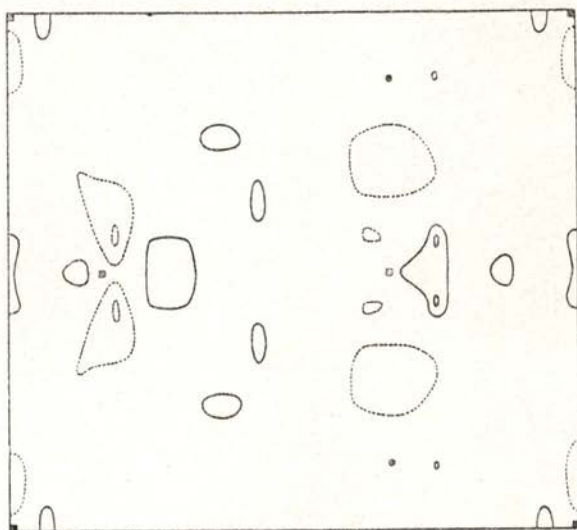


Fig. 1 — Fourier syntheses for the $[2\bar{1}0]$ projection of TiFe_2 .
 (a) F_0 ; contours are at arbitrary equal intervals;



(b) $(F_0 - F_c)$; contours at $1/15$ those of F_0 ; dashed lines represent negative contours;
 ■ positions occupied by Ti atoms
 • positions occupied by Fe atoms

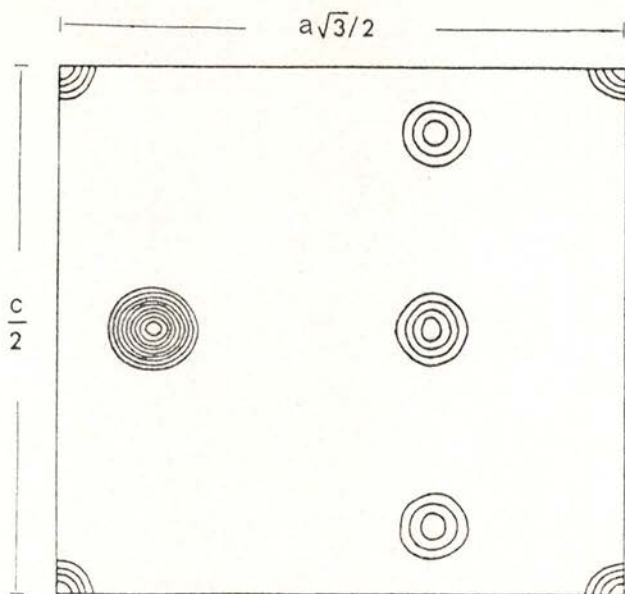
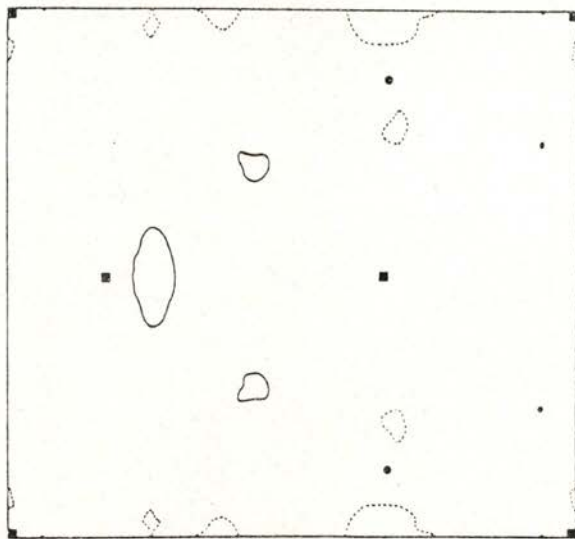


Fig. 2—Fourier syntheses for the $[2\bar{1}0]$ projection of TiMn_2 .
(a) F_0 ; contours are at arbitrary equal intervals;



(b) $(F_0 - F_c)$; contours at $1/10$ those of F_0 ; dashed lines represent negative contours;
 ■ positions occupied by Ti atoms
 ● positions occupied by Mn atoms

4-- CONCLUSIONS

The atomic radii of the constituents of binary transition metal alloys with the $MgZn_2$ type structure are in general markedly different. This fact, together with the occurrence of compositions very close to the stoichiometry, suggests that these structures should be fully ordered; the lack of experimental results confirming such conclusion has been pointed out by Sinha [1].

The order of magnitude of the reliability factors, as well as the Fourier maps obtained in the present work show that complete ordering occurs in the case of $TiFe_2$ and $TiMn_2$.

Analysis of table 1 shows that the atomic parameters x and z obtained for the two alloys deviate, beyond the error limits, from the ideal values, $1/6$ and $1/16$ respectively, in these structures.

In the case of $TiFe_2$ the present results agree, within the experimental uncertainty, with those determined by Brückner *et al.* [12]. Their results were obtained by powder neutron diffraction from the observed intensities of 13 reflections and the composition of the specimen used was not stoichiometric. It should be pointed out that a considerably smaller standard deviation for the z -parameter is given in the present work.

The ratio R_A/R_B for the two alloys, $TiFe_2$ and $TiMn_2$, are respectively 1.14 and 1.11₅. Two distinct values were found for the interatomic distance A-A (Ti-Ti), as well as for the B-B distance (Fe-Fe or Mn-Mn), as can be seen in table 2. This has already been pointed

Table 2—Interatomic distances in the Laves phases $TiFe_2$ and $TiMn_2$.

Position	Atom	Neighbours	Distances		Other neighbours
			$TiFe_2$ (AB_2)	$TiMn_2$ (AB_2)	
f	A (Ti)	1 f	2.939	2.950	1 f, 1 f
		1 f	2.907	2.970	
		3 h	2.799	2.844	2a, 1a
		6 h	2.783	2.830	
a	B	6 h	2.414	2.442	6 f
h	B	2 h	2.336	2.366	6 f, 2a 2 f, 2 f, 2 f
Atomic radii (CN12)			Ti	Fe	Mn
			1.45	1.27	1.30

out for other Laves phases when the axial ratio deviates from 1.63. One of the two Ti-Ti interatomic distances only depends on c and z whereas the calculation of the other involves, besides the z -coordinate, both lattice parameters a and c . The z -parameter is the same for both structures, within the experimental error; hence the difference between Ti-Ti distances, which occurs in TiFe_2 and in TiMn_2 , should be attributed to their significantly different lattice parameters a and c .

The calculated contraction of the B-B interatomic distance based on the structure geometry and on the parameters a and c known for a large number of C14 Laves phases decreases with increasing R_A/R_B . When these contractions are plotted against the atomic radii they fall on a band with a well defined slope (Nevitt, [3], fig. 15). If the B-B contraction were determined by geometrical factors only, the mentioned values should fall on a straight line intersecting the horizontal axis at $R_A/R_B = 1.225$.

Plotting, as above, the contractions of the distances Fe-Fe and Mn-Mn calculated from the results shown in table 2, they fall well above that straight line; this indicates an additional contraction of the Fe and Mn atoms, which cannot be attributed to geometrical factors. Furthermore, this contribution is not the same in the two alloys, but appears to decrease with increasing atomic number of the B element (5.1% and 7.8% for the two Fe-Fe distances; 6.1% and 8.8% for the two Mn-Mn distances).

Berry and Raynor [13] suggested that an additional contraction dependent on the position of B in the periodic table, and hence on its electronic configuration, can occur in some Laves phases (AB_2) as a result of an interaction between A and B atoms.

The contractions observed in both TiFe_2 and TiMn_2 alloys appear to confirm the above assumption; furthermore, they indicate that the contraction associated with the B element decreases with increasing number of 3d electrons. Since cobalt follows manganese and iron along the same transition series the study of the TiCo_2 structure would be of great interest.

We would like to thank Prof. S. Garcia-Blanco and Prof. S. Martínez-Carrera of "Instituto de Química-Física Rocasolano, Consejo Superior de Investigaciones Científicas", Madrid, Spain, for the provision of facilities on the automatic diffractometer and processing of the data.

REFERENCES

- [1] SINHA A. K. — *Progress in Materials Science* **15**, 93 (1972).
- [2] LAVES F. and WITTE H. — *Metallwirt.* **15**, 840 (1936).
- [3] NEVITT, M. V. — «*Electronic Structure and Alloy Chemistry of the Transition Elements*» — (ed. P. A. Beck); Interscience; New York (1968).
- [4] PEARSON W. B. — *Acta Cryst.* **B 24**, 7 (1968).
- [5] MURAKAMI Y. and ENJYO T. — *J. Japan Inst. Metals* **22**, 261 (1958).
- [6] MURAKAMI Y., KIMURA H. and NISHIMURA Y. — *Trans. Nat. Res. Inst. Met. Japan* **1**, 7 (1958).
- [7] FARQUAR M. C. M. and LIPSON H. — *Proc. Phys. Soc.* **58**, 200 (1946).
- [8] WALLBAUM H. J. — *Z. Krist.* **A 103**, 391 (1941).
- [9] DUWEZ P. and TAYLOR J. L. — *J. Metals* **2**, 1173 (1950).
- [10] FORSYTH J. B. and WELLS M. — *Acta Cryst.* **12**, 412 (1959).
- [11] DAMJANOVICK A. and BLACK P. J. — *Acta Cryst.* **14**, 987 (1961).
- [12] BRÜCKNER W., KLEINSTÜCK K. and SCHULZE G. E. R. — *Phys. Stat. Sol.* **23**, 475 (1967).
- [13] BERRY R. L. and RAYNOR G. N. — *Acta Cryst.* **6**, 178 (1953).



CONTENTS
FASCÍCULO 1-2

NUCLEAR PHYSICS

Improved Experimental Method for Half-Life Measurements by Electron — Electron Delayed Coincidences M. C. ABREU, J. P. RIBEIRO, F. B. GIL	1
The L_1 Subshell Fluorescence Yield of Tl M. I. MARQUES, M. C. MARTINS, J. G. FERREIRA	9
Proton-Induced K-Shell Hole Production on Ar and Kr J. S. LOPES, K. KRIEN, J. C. SOARES, F. B. GIL	13

MOLECULAR AND CONDENSED MATTER PHYSICS

Ultrasonic Study of Antiferromagnetic Domains in Dysprosium G. N. BLACKIE, S. B. PALMER	23
Magnetic Phase Transitions in Terbium Single Crystals M. M. AMADO, J. B. SOUSA, M. F. PINHEIRO, R. P. PINTO, M. E. BRAGA, J. M. MOREIRA, D. HUKIN, G. GARTON, P. WALKER	33
Thermopower in Rare Earth Intermetallic Compounds and the Validity of s-f Scattering Models R. P. PINTO, J. B. SOUSA, J. M. MOREIRA, M. M. AMADO, M. F. PINHEIRO, M. E. BRAGA, P. MORIN	41
Correlation Between Twist Viscosity and Dielectric Relaxation in Nematic Liquid Crystals A. C. DIOGO, A. F. MARTINS	47
Radioluminescence of Rare Gases (review article) M. SALETE S. C. P. LEITE	53

CONTENTS
FASCICULO 3-4

NUCLEAR PHYSICS

A Set of Nuclear Stopping Correction Factors M. F. DA SILVA, P. BORDALO, J. VARELA, P. M. CORRÊA and J. M. G. CARAÇA	101
The Position Linearity of Photo-Ionization Detectors M. ALEGRIA FEIO and A. J. P. L. POLICARPO	107
K- and L-Shell Ionization in Alpha Decay J. P. RIBEIRO and F. B. GIL	119

MOLECULAR AND CONDENSED MATTER PHYSICS

Enhanced Nuclear Magnetism in HoVO_4 B. BLEANEY	129
Critical Behaviour of Dark Current in Ferroelectric $\text{Bi}_{0.08}\text{Sb}_{0.92}\text{SI}$ M. RENATA CHAVES, M. HELENA AMARAL and S. ZIOLKIEWICZ	147
Dynamical Behaviour of the Aliphatic Chains of 4,4'-Dihexyloxyazoxy- benzene in the Nematic Phase. A. F. MARTINS, J. B. BONFIM, A. M. GIROUD-GODQUIN	159
Nuclear Spin-Lattice Relaxation in the Columnar and Isotropic Phases of a Discotic Liquid Crystal (H8.OTP). Strong Frequency Dependent Effects in the Isotropic Phase A. F. MARTINS and A. C. RIBEIRO	169
Proprietes Physiques de Polymeres Organiques Semi-Conducteurs et Metalliques: le cas du Polyacetylene P. BERNIER, M. ROLLAND, S. LEFRANT, A. MONTANER, O. PARODI, C. BENOIT, M. GALTIER, F. SCHUE, J. SLEDZ, J. M. FABRE, L. GIRAL, M. ALDISSI	183
Concentration and Solvent Effects on Luminescence of Molecules Con- tained in Rigid Matrices L. C. PEREIRA, M. M. S. PINHEIRO and M. E. C. DIAS	203
Structural Analysis of Laves Phases with Ti M. J. M. DE ALMEIDA, M. M. R. COSTA, L. ALTE DA VEIGA, L. R. ANDRADE and A. MATOS BEJA	219

AUTHOR INDEX

<p>ABREU, M. C., RIBEIRO, J. P., GIL, F. B. — Improved Experimental Method for Half-Life Measurements by Electron-Electron Delayed Coincidences</p>	1
<p>ALDISSI, M. — See P. BERNIER</p>	
<p>ALMEIDA, M. J. M. de, COSTA, M. M. R., ALTE DA VEIGA, L., ANDRADE, L. R., MATOS BEJA, A. — Structural Analysis of Laves Phases With Ti</p>	219
<p>ALTE DA VEIGA, L. — See M. J. M. de ALMEIDA</p>	
<p>AMADO, M. M., SOUSA, J. B., PINHEIRO, M. F., PINTO, R. P., BRAGA, M. E., MOREIRA, J. M., HUKIN, D., GARTON, G., WALKER, P. — Magnetic Phase Transitions in Terbium Single Crystals</p>	33
<p>AMADO, M. M. — See R. P. PINTO</p>	
<p>AMARAL, M. H. — See M. R. CHAVES</p>	
<p>ANDRADE, L. R. — See M. J. M. de ALMEIDA</p>	
<p>BENOIT, C. — See P. BERNIER</p>	
<p>BERNIER, P., ROLLAND, M., LEFRANT, S., MONTANER, A., PARODI, O., BENOIT, C., GALTIER, M., SCHUE, F., SLEDZ, J., FABRE, J. M., GIRAL, L., ALDISSI, M. — Propriétés Physiques de Polymères Organiques Semiconducteurs et Metalliques: Le cas du Polyacétylène</p>	183
<p>BLACKIE, G. N., PALMER, S. B. — Ultrasonic Study of Antiferromagnetic Domains in Dysprosium</p>	23
<p>BLEANEY, B. — Enhanced Nuclear Magnetism in HoVO_4</p>	129
<p>BONFIM, J. B. — See A. F. MARTINS</p>	
<p>BORDALO, P. — See M. F. da SILVA</p>	
<p>BRAGA, M. E. — See M. M. AMADO and R. P. PINTO</p>	
<p>CARAÇA, J. M. G. — See M. F. da SILVA</p>	
<p>CHAVES, M. R., AMARAL, M. H., ZIOLKIEWICZ, S. — Critical Behaviour of Dark Current in Ferroelectric $\text{Bi}_{0.08}\text{Sb}_{0.92}\text{SI}$</p>	147
<p>CORRÊA, P. M. — See M. F. da SILVA</p>	
<p>COSTA, M. M. R. — See M. J. M. de ALMEIDA</p>	
<p>DIAS, M. E. C. — See L. C. PEREIRA</p>	
<p>DIOGO, A. C., MARTINS, A. F. — Correlation Between Twist Viscosity and Dielectric Relaxation in Nematic Liquid Crystals</p>	47

FABRE, J. M. — See P. BERNIER	
FEIO, M. A., POLICARPO, A. J. P. L. — The Position Linearity of Photo-Ionization Detectors	107
FERREIRA, J. G. — See M. I. MARQUES	
GALTIER, M. — See P. BERNIER	
GARTON, G. — See M. M. AMADO	
GIL, F. B. — See: M. C. ABREU; J. S. LOPES; J. P. RIBEIRO	
GIRAL, L. — See P. BERNIER	
GIROUD-GODQUIN, A. M. — See A. F. MARTINS	
HUKIN, D. — See M. M. AMADO	
KRIEN, K. — See J. S. LOPES	
LEFRANT, S. — See P. BERNIER	
LEITE, M. S. S. C. P. — Radioluminescence of Rare Gases	53
LOPES, J. S., KRIEN, K., SOARES, J. C., GIL, F. B. — Proton-Induced K-Shell Hole Production on Ar and Kr	13
MARQUES, M. I., MARTINS, M. C., FERREIRA, J. G. — The L_1 Subshell Fluorescence Yield of Tl	9
MARTINS, A. F., BONFIM, J. B., GIROUD-GODQUIN, A. M. — Dynamical Behaviour of the Aliphatic Chains of 4,4'-Dihexyloxyazoxybenzene in the Nematic Phase	159
MARTINS, A. F., RIBEIRO, A. C. — Nuclear Spin-Lattice Relaxation in the Columnar and Isotropic Phases of a Discotic Liquid Crystal (H8.OTP). Strong Frequency Dependent Effects in the Isotropic Phase	169
MARTINS, A. F. — See A. C. DIOGO	
MARTINS, M. C. — See M. I. MARQUES	
MATOS BEJA, A. — See M. J. M. de ALMEIDA	
MONTANER, A. — See P. BERNIER	
MOREIRA, J. M. — See M. M. AMADO and R. P. PINTO	
MORIN, P. — See R. P. PINTO	
PALMER, S. B. — See G. N. BLACKIE	
PARODI, O. — See P. BERNIER	

PEREIRA, L. C., PINHEIRO, M. M. S., DIAS, M. E. C. — Concentration and Solvent Effects on Luminescence of Molecules Contained in Rigid Matrices	203
PINHEIRO, M. F. — See M. M. AMADO and R. P. PINTO	
PINHEIRO, M. M. S. — See L. C. PEREIRA	
PINTO, R. P., SOUSA, J. B., MOREIRA, J. M., AMADO, M. M., PINHEIRO, M. F., BRAGA, M. E., MORIN, P. — Thermopower in Rare Earth Intermetallic Compounds and the Validity of s-f Scattering Models	41
PINTO, R. P. — See M. M. AMADO	
POLICARPO, A. J. P. L. — See M. A. FEIO	
RIBEIRO, A. C. — See A. F. MARTINS	
RIBEIRO, J. P., GIL, F. B. — K and L Shell Ionization in Alpha Decay	119
RIBEIRO, J. P. — See M. C. ABREU	
ROLLAND, M. — See P. BERNIER	
SCHUE, F. — See P. BERNIER	
SILVA, M. F. da, BORDALO, P., VARELA, J., CORRÊA, P. M., CARAÇA, J. M. G. — A Set of Nuclear Stopping Correction Factors	101
SIEDZ, J. — See P. BERNIER	
SOARES, J. C. — See J. S. LOPES	
SOUSA, J. B. — See M. M. AMADO and R. P. PINTO	
VARELA, J. — See M. F. da SILVA	
WALKER, P. — See M. M. AMADO	
ZIOLKIEWICZ, S. — See M. R. CHAVES	

SOCIEDADE PORTUGUESA DE FÍSICA
AV. REPÚBLICA 37-4.º, 1000 LISBOA, PORTUGAL

PORTUGALIAE PHYSICA publishes articles or research notes with original results in theoretical, experimental or applied physics; invited review articles may also be included.

Manuscripts, with an abstract, may be written in English or French; they should be typewritten with two spaces and in duplicate. Figures or photographs must be presented in separate sheets and be suitable for reproduction with eventual reduction in size; captions should make the figures intelligible without reference to the text. Authors are requested to comply with the accepted codes concerning references.

There is no page charge. Author(s) will get 50 free reprints (without covers); these are to be shared among all the authors of the article. Authors interested in more reprints should say so when sending their manuscripts; quotations shall be sent with the proofs.

Subscription rates for volume 11:

1,000 Escudos (US\$20) — individuals
2,500 Escudos (US\$50) — libraries

PORTUGALIAE PHYSICA may also be sent on an exchange basis; we welcome all suggestions to such effect.

All mail to be addressed to

PORTUGALIAE PHYSICA

C/O LABORATÓRIO DE FÍSICA, FACULDADE DE CIÊNCIAS
PRAÇA GOMES TEIXEIRA
4000 PORTO PORTUGAL

PORTUGALIAE PHYSICA

VOL. 11 · NUMB 3/4 · 1980

CONTENTS

NUCLEAR PHYSICS

A Set of Nuclear Stopping Correction Factors M. F. DA SILVA, P. BORDALO, J. VARELA, P. M. CORRÊA and J. M. G. CARAÇA	101
The Position Linearity of Photo-Ionization Detectors M. ALEGRIA FEIO and A. J. P. L. POLICARPO	107
K- and L-Shell Ionization in Alpha Decay J. P. RIBEIRO and F. B. GIL	119

MOLECULAR AND CONDENSED MATTER PHYSICS

Enhanced Nuclear Magnetism in HoVO_4 B. BLEANEY	129
Critical Behaviour of Dark Current in Ferroelectric $\text{Bi}_{0.08}\text{Sb}_{0.92}\text{SI}$ M. RENATA CHAVES, M. HELENA AMARAL and S. ZIOLKIEWICZ	147
Dynamical Behaviour of the Aliphatic Chains of 4,4'-Dihexyloxyazoxy- benzene in the Nematic Phase. A. F. MARTINS, J. B. BONFIM, A. M. GIROUD-GODQUIN	159
Nuclear Spin-Lattice Relaxation in the Columnar and Isotropic Phases of a Discotic Liquid Crystal (H8.OTP). Strong Frequency Dependent Effects in the Isotropic Phase A. F. MARTINS and A. C. RIBEIRO	169
Proprietes Physiques de Polymeres Organiques Semi-Conducteurs et Metalliques: le cas du Polyacetylene P. BERNIER, M. ROLLAND, S. LEFRANT, A. MONTANER, O. PARODI, C. BENOIT, M. GALTIER, F. SCHUE, J. SLEDZ, J. M. FABRE, L. GIRAL, M. ALDISSI	183
Concentration and Solvent Effects on Luminescence of Molecules Con- tained in Rigid Matrices L. C. PEREIRA, M. M. S. PINHEIRO and M. E. C. DIAS	203
Structural Analysis of Laves Phases with Ti M. J. M. DE ALMEIDA, M. M. R. COSTA, L. ALTE DA VEIGA, L. R. ANDRADE and A. MATOS BEJA	219
CONTENTS AND AUTHOR INDEX (VOL. 11)	229